THE APPLICATION OF LASER-GENERATED ULTRASOUND TO THE STUDY OF ALUMINIUM-EPOXY BONDED SYSTEMS

by

ANDREW CHARLES BUSHELL. B.A.

A thesis submitted for the degree of Doctor of Philosophy

UNIVERSITY OF WARWICK

DEPARTMENT OF PHYSICS

September 1993

TABLE OF CONTENTS

LIST OF ILLUSTRATIONS

ACKNOWLEDGEMENTS

The research described in this thesis was wholly funded by the Materials and Structures Department of DRA (Aerospace Division). I wish to express my gratitude to the Agency and those responsible for the collaboration in general, both financing and supplying the adhesively-bonded samples around which the project has revolved. I particularly appreciate the support offered to me by my liaising supervisor Dr. S. P. Wilford and the work of Richard Clark and Martin Stone in producing bonded joints for me.

I also owe thanks to staff, both academic and technical, at the University of Warwick, where I was based while carrying out experimental research for the project. My supervisor, Professor S. B. Palmer, deserves credit for an infectious optimism in the face of some of physics' more intractable problems, balanced by a sharp eye for the concise. A warm thank you is also due to Dr. C. Edwards, my 'second supervisor', whose day-to-day involvement was a constant reassurance, despite the repeated offers of suspect fungi. I am grateful for moral support, and freely donated computer expertise, from Dr. D. McK. Paul, not forgetting Dr. D. Hutchins and his NDT group in engineering. John Reed and Dr. Roger Eccleston are owed a mention as the only other members of the laser ultrasound group to survive all three years in the same room with me. The Chapter 6 interference source was set up with initial assistance from the visiting Dr. H. Nakano.

Finally, I should like to thank those who have made life less difficult for me since I left Warwick, in particular my parents who have adopted a resident hermit with great fortitude. I am deeply grateful to my present employers, the UK Meteorological Office, for considerable understanding and a generous flexibility that has allowed me to bring this project to a satisfactory conclusion.

DECLARATION

Work contained in this thesis is my own except where specifically stated as otherwise, and was carried out primarily in the Department of Physics, at the University of Warwick, during the period from October 1988 to October 1991. No part of this work has been submitted previously to the University of Warwick, nor any other academic institution, for admission to a higher degree. Some of the work has already appeared in the form of publications which are listed in the bibliography section.

SUMMARY

The poor performance of acoustic wave techniques in predicting adhesively-bonded joint failure under destructive loading is a long-standing problem, known to derive from unreliable adhesive defect detection. This thesis examines the feasibility of applying a relatively new technique, generating ultrasound with pulsed Nd:YAG lasers, to the study of aluminium alloy adherends joined by epoxy layer bonds. Laser generation is a non-contacting method which produces highly repeatable ultrasonic sources in metals, without damping motion at the sample surface. Pulses created in this fashion have bandwidths around 20 MHz and radiate both along the sample surface and into the material bulk. Displacements at the sample surface recorded by a broad bandwidth non-contact detector, such as a 532 nm wavelength laser Michelson interferometer, are therefore able to resolve details in time-varying traces which are not visible when narrowband transducers are used. In particular, individual reverberations between the interfaces of epoxy layers less than 100 μm thick are detected in transmission through adhesively bonded joints, on time domain traces.

An epoxy layer sandwiched between two thick aluminium adherends presents a three layer case which is seldom discussed in the literature. I have therefore adapted theory developed for surface waves in thin layers overlying deep substrates, and for waves transmitted through multilayer structures, into an explicit formulation for an elastic layer embedded in adherend half-spaces that can be used for both through-transmission and interface-parallel waves. The case of travelling waves in a viscoelastic layer has not yet been examined as the current formulation requires unfeasibly long computation times. A numerical solution assuming elastic behaviour, gives strong indications that embedded epoxy layers support travelling waves directed along the interfaces, despite the fact that a single interface between epoxy and aluminium will not support non-dispersive Stoneley interface waves.

Experimental work presented in Chapters 4 to 7 is preceded by a review of laser generation and non-contact detection methods, which introduces techniques that I have employed. As well as using laser interferometers, I have also built my own electromagnetic acoustic transducers (EMATs), to provide a cheaper alternative detection scheme. Chapter 4 concentrates upon on-epicentre detection of direct through transmission pulse arrivals, using analysis both of the entire reverberation wavetrain following the main arrival and of consecutive pulses within it, in order to extract information on the bonds' cohesive and adhesive properties. Chapter Five examines variations in surface-travelling waveforms on unbonded, free-surface aluminium plates with thicknesses varying from 63 mm down 28 μm, in a search for non-dispersive waves that would be suitable for probing adhesive bonds. Rayleigh arrivals on samples over 10 mm thick and the symmetric zero-order Lamb mode on plates under 200 μm thick both propagate from the Nd:YAG laser source as sharp pulses, but intermediate plate thicknesses only allow waves with highly dispersive characteristics, which tend to mask any dispersion due to bonds. The plate wave experiments allow a full intercomparison between interferometer and EMATs, both out-of-plane motion sensitive and in-plane motion sensitive. Chapter 6 uses Rayleigh-like surface waves travelling along 25 mm thick adherends to initiate interface-parallel travelling waves in an adhesive layer bonding a second adherend to the surface, which are subsequently detected on emerging at the free surface beyond the bond. These surface-interface-surface travelling (SIST) waves penetrate under increasingly longer bonds as the wave frequency decreases, a fact confirmed by the behaviour of pulses given a narrowband frequency modulation when generating laser beams interfere to produce a spatially modulated source. The interference source optical arrangement, described in Chapter 5, can be altered to give Rayleigh arrival modulation frequencies from 20 MHz to below 1 MHz. Finally, Chapter 7 examines alternative pathways for surface waves incident upon the edge of a bonded joint region, and demonstrates that SIST waves are an efficient mechanism for transferring ultrasound between the two adhesive-adherend interfaces, given the observed emergence of clearly discernible SIST waves on the second adherend of a lapped bond joint.

I conclude that through transmission pulse analyses are capable of extracting quantitative information about bond properties and should be developed as the basis for laser generated ultrasonic bond testing. SIST waves, however, require further research before they can be employed in a practical manner.

... And all for want of a nail. (Anon.)

CHAPTER 1.

INTRODUCTION

For anybody who likes their science neatly catagorized between physics, chemistry and engineering, the ultrasonic study of adhesively bonded joints will set something of a challenge. Although the laser generation technique, used throughout this thesis to create sharply-pulsed ultrasonic waves, is still too new to have emerged from the confines of physics or engineering laboratories, ultrasonics is a field which embraces medicine, geology and electronics. The concept of adhesive bonding as a means of joining components has been widespread since prehistoric times and the range of adhesives available is as wide as that of the purposes for which they are used. Adhesives have a number of highly desirable characteristics. They are able to join dissimilar materials with irregular surface geometries and generally cause far less damage to the components either side of the joint than alternative methods like stitching, pinning, welding or riveting. The presence of an adhesive layer with submillimetre thickness adds little weight to the bonded structure, and the relative uniformity of adhesion over potentially large areas leads to more even stress distributions across a loaded joint. These traits, taken together, explain the keen interest in such fastening methods shown by aerospace engineers, whose structures require a critical combination of high strength and low mass.

Unfortunately, adhesives have the undesirable characteristic that apparently acceptable joints can contain weaknesses which lead to catastrophic failure of the bond under load. This is as true for state-of-the-art aerospace components, manufactured under controlled conditions, as it is for simple household repairs. An inappropriate choice or inhomogeneous mixing of the adhesive, impurities it absorbs while fluid, contamination or inadequate preparation of the surfaces to be bonded, errors or interruptions in the curing process, sudden or extreme changes in temperature, ingress of moisture or other forms of environmental degradation encountered in service can all weaken and finally destroy the bond. Until a reliable, non-destructive technique is found by which such weaknesses can be detected and then monitored, it will never be acceptable to risk the exclusive use of adhesive bonds in joints where failure could result in the collapse of an entire structure.

The work presented in this thesis was carried out as part of a continuing project which embraces a set of linked stages aimed at the development of ultrasonic methods for the non-destructive evaluation of adhesive bond strengths. At one end of the chain lies a formal verification of the tacit assumption that changes in bond strength affect the ultrasonic properties of the sample in a systematic and consistent manner. There is clear evidence for ultrasonic velocity changes in adhesives during the cure process [Rokhlin, 1983 & 1987] as extensive crosslinks transform the viscous epoxy fluid into a viscoelastic glass. But relating alterations in ultrasonic behaviour to bond strength variations is much more difficult when trying to compare different bonded samples. The source of this uncertainty is the tendency of bonded joints to fail at localized sites, usually near the edge of the bond and frequently along an adhesive-adherend interface. The correlation between bulk properties of the materials involved and strength, measured in a test to destruction, may thus be rather poor and joints are expected to fail at different strengths under peel, shear or tensile stresses.

However, despite doubts concerning the positive, nondestructive confirmation of high strength bonds, testing with pulsed ultrasound is worth examining for its ability to reject particular classes of low strength bonds. For instance, ultrasonic pulses are sensitive to density changes caused by an error in the cure process, or the presence of voids in the adhesive layer, both of which are properties of a bonded system associated with loss of strength in the joint. Therefore, the second stage in the project is to decide which property changes, if any, pulsed ultrasound will actually detect. I have invested the greatest amount of effort in this area, owing to a dearth of extant information surrounding the laser-generated acoustic study of bonded systems. This scarcity might seem surprising, given substantial scrutiny of the problem by researchers with piezoelectric transducer sources, which use the same underlying ultrasonic theory. However, pulsed laser generated ultrasound is extremely broadband in nature (up to 30 MHz), and the source areas involved can be made less than 1 mm^2, creating signal waveforms that are substantially different from those obtained by standard techniques. The contrast is enhanced when using a displacement sensitive laser Michelson interferometer because both source and detector are then remote, eliminating signal distortions arising from surface damping. However, as a penalty for shedding new light on an investigation, the optical generation and detection of ultrasound requires remeasurement of the detection limits for ultrasonic signals,

which are poorer than those encountered with the more sensitive piezoelectric transducers [Dewhurst et al., 1987].

Having determined a series of features on the ultrasonic signals which may be used to differentiate between different samples, the next hurdle is to isolate those features which say most about the state of the adhesive layer. Adhesive property information on epoxy bonded aerospace joints is difficult to extract from ultrasonic data because even the simplest models require three layers; the two outer adherends, comprising most of the mass of the system, surrounding a layer of bonding material only the order of 0.1 mm thick. The central adhesive layer is poorly characterized, as thin-layer and bulk properties of the constituent epoxy resin may differ markedly, and the thickness is critically dependent upon local stress distributions in the joint during the curing process, varying even over the area of an individual sample. Measurements of bond thickness, taken as the difference between total joint and total adherend thicknesses, are generally subject to large percentage errors and may well be inaccurate if the surfaces are irregular, as the glue will tend to spread to give a constant overall thickness to the joint. A useful bond-testing method must be able to detect changes in the adhesive layer in such a way that thickness variations may be separated from other properties of the layer or its adherend interfaces. However, the calibration of adhesive layer thickness, addressed within this thesis, is in truth only the most obvious starting-point in the much wider problem concerning the extraction of data from a patently multi-parameter system. And the interdependent nature of the parameters suggests that a large body of theoretical work on bonded systems remains to be tackled, if numerical representations of the experimentally observed laser generated ultrasonic waveforms are to be computed with accuracy.

Finally, the question of automation will need to be taken into account if any systems which are developed are to be of practical use outside the research laboratory. The problems involved are technological, not fundamental, and mainly concern detector stabilities towards variations in sample surface displacement and tilt, which occur under rapid scanning conditions. If these are once overcome, automated systems superior to those using piezoelectric transducers can be expected, as the excellent repeatability of laser generated acoustic pulses when samples are scanned is one of the distinguishing features of this method of producing ultrasound. Given

the main thrust of this thesis, however, towards exploration of the various approaches to ultrasonic bond testing, frequent configurational changes were required and measurements were taken manually, with automation barely touched upon here.

1.1 A Schedule of the Thesis Chapters.

Chapter One has begun with a brief description of the framework within which the research presented here is set. This section therefore introduces the remaining chapters with an outline of their contents, as a guide to the way in which the thesis is arranged.

Chapter Two provides the basis for analysis of pulsed ultrasonic data used to interrogate bonded layer structures. A detailed investigation of either temporal or spatial distributions for the laser-generated acoustic pulse would be inappropriate to the theme of this thesis. Instead, section 2.1 reviews the range of work which has been applied to provide numerical descriptions of waveforms generated by lasers under varying conditions of incident power and energy. The remaining sections assume sharply-pulsed ultrasound, but do not specify any particular generation mechanism. A general description of the adhesive layer model and parametrization of adhesion at the adhesive-adherend interfaces leads into the transmission matrix method, a convenient way of describing the passage of plane-wave ultrasound within an arbitrary number of layers. The approach that I have taken is equally applicable to experimental configurations in which ultrasound is detected epicentrally in through-transmission, or on the same side as the incoming pulse at surface-parallel angles of incidence. This flexibility is designed to mirror that of the laser source, which generates longitudinal, shear and surface-travelling waves simultaneously with each shot. Since, however, the detectors only monitor one position at a time, the through-transmission and surface-travelling cases are dealt with in separate sections, with approximations reflecting the different geometries traversed by the ultrasonic arrivals. Detailed calculations, consigned to Appendix A, are consistent with an inverse approach to the through-transmission problem [Challis et al., 1991], allowing frequency dependent phase velocity and attenuation curves to be extracted from transmitted waveforms. Surface-travelling waves, however, require time-consuming numerical analysis for the forward calculation of wave modes, making inversion unfeasible, although useful insight into the observed behaviour can still be gained from modelled dispersion curves.

Chapter Three begins by describing which defects are most likely to have an effect on the bond strength and thus have to be detected reliably. Defects occur largely as a result of joint processing irregularities during, or immediately prior to, the cure cycle in which an adhesive bond forms. This has the possible advantage that a defect may be accompanied by symptomatic changes in the epoxy composition and thus detected from a general consideration of the thin adhesive layer properties. Alternative methods currently used for predicting bond failure, with an emphasis on acoustic results, are outlined before the experimental methods employed in the laser generation and non-contacting detection of pulsed ultrasound. The use of generation and detection techniques which do not require physical contact with the surface of the sample under test is an important step forward in the study of adhesive systems, as surface coupling problems are eliminated. However, though continuing developments in laser technology are making optical detection techniques increasingly viable, the alternatives are usually cheaper and frequently more sensitive, factors which might outweigh advantages of tighter spatial and temporal resolution for specific applications. Discussion of acoustic pulse generation by laser is thus followed by a review of broadband ultrasonic receivers before, finally, detailed descriptions of the Michelson laser interferometer and electromagnetic acoustic transducer (EMAT) detection systems used.

Following Chapter Three are the four experimental thesis chapters, each examining aspects of ultrasonic pulse propagation from laser generated sources at aluminium alloy surfaces. Chapter Four presents acoustic data detected in a through-transmission arrangement epicentral with the laser source, whilst Chapters Five, Six and Seven share a common approach in the study of samples with surface-travelling ultrasound. The same laser, generating ultrasound that radiates simultaneously into the bulk and along the surface of a metallic sample, acts as a source for both transmission and interface wave experiments simply by altering the detector configuration. Oblique incidence measurements are avoided, due to the complicated ultrasonic directivity patterns generated by laser sources [Hutchins, 1988], although they may be viable in future, following recent developments in phased arrays that have produced steered beams [Noray et al., 1993]. The preferential interest in Rayleigh-Lamb (homogeneous plate) waves, or their interface-travelling equivalents in layered specimens, stems from the retrograde elliptical particle motions that they produce. Interactions at the adhesive layer interface, to which in-plane displacements show the maximum sensitivity, thus alter particle motions normal to the adhesive

plane, allowing them to be observed at the sample surface by detectors sensitive to out-of-plane displacements. In addition, acoustic waves travelling along the bonding layer interact with the epoxy over distances much longer than the layer thickness, which is the characteristic interaction length for bulk waves crossing the bonded region.

Chapter Four, however, considers laser generated ultrasonic pulses which are transmitted through the joint, perpendicular to the adhesive layer, and detected on-epicentre with respect to the source. The practicalities of generating ultrasound with a focussed Nd:YAG laser beam, which requires a line of sight to the sample surface, strongly favour through-transmission over pulse-echo configurations for the interrogation of adhesively bonded layers. This is contrary to the majority of results published using piezoelectric transducers, where the pulse-echo mode is more natural. The main advantage in replacing a piezoelectric system with laser generation is the improvement in temporal resolution, which even allows the observation on amplitude-time traces of a series of distinct reverberation pulses, following the first signal arrival, within epoxy layers as thin as 70 μm. The system may thus be analysed in both time and frequency domains. Nearly monopolar, longitudinal acoustic pulses are generated with maximum amplitudes by weakly ablating sources, obtained by adjusting the power density of the incoming laser beam. Shear waves generated by the laser have vanishing amplitudes, due to symmetry, on the epicentral axis so that other means (perhaps spiral coil EMATs) are recommended for on-epicentre transverse wave generation. After a brief outline of the experimental arrangement for through-transmission measurements and the analysis used to extract phase velocity dispersion curves for epoxy layers in rigid bonds, experiments upon well-prepared joints are examined. Pulsed laser ultrasound is particularly sensitive to relative thickness changes along an epoxy layer and a study of a joint with varying dimensions down its length emphasizes the technique's potential for quality control. The chapter finishes with a set of bonds incorporating particularly gross defects, all of which a nondestructive test system would need to detect. Sure identification of pronounced defects is merely the baseline requirement for a reliable test procedure, as failure in a bonded joint may occur from relatively minor faults. A systematic assessment of the minimum detectable levels for various defect types is an obvious candidate for future investigation.

Chapter Five presents a series of experiments carried out upon aluminium alloy plates

in order to characterize the free surface behaviour of surface-travelling ultrasonic pulses. The principal aim was to observe variations in the waveforms detected when the plate thicknesses were reduced from those appropriate to the Rayleigh regime down to those in which the zero order Lamb modes appeared. Analysis of the surface-interface-surface travelling (SIST) waves seen in bonded joint tests (Figure 1.1.a,b) simplifies considerably if the free surface portions are sharply-pulsed and non-dispersive. Such conditions are shared by the Rayleigh wave, on thick adherends, and the zero order symmetric Lamb mode, on thin. However, for a range of plate thicknesses, dependent on the plate material and the ultrasonic frequencies used, neither of these waves is observed and complex behaviour seen in SIST waves is no longer attributable solely to the interfacial segments. The surface wave behaviour on plates ranging from 63 mm to 28 μm thick was surveyed with a number of non-contacting detectors, allowing as a bonus a comparison between the various devices. Finally, the Rayleigh surface wave was used to investigate aluminium alloy bars for acoustic effects which seem to originate from work hardening, occurring when the bars were first extruded. Milling 1.5 mm off the bar.surface removes the effects but is not always convenient when preparing epoxy joints. Experimental runs in later chapters instead keep surface effects constant by using fixed source to detector distances wherever possible.

Chapter Six details experiments in adhesively bonded reinforcement joints (Figure 1.1.a) to determine bond lengths from the attenuation of SIST waves passed along them. The calculated bond lengths may be compared with externally measured dimensions of the bond and discrepancies would strongly indicate defects in the adhesive. However, sharply-pulsed ultrasonic signals, used to enable minor waveform modifications to be identified, contain a broad range of frequencies each damped to a different extent by a length of adhesive interface. To obtain length estimates from the pulsed data thus requires some knowledge of the behaviour of individual frequencies. Accordingly, a spatially periodic laser source was created, by splitting the laser beam in two and recombining it to form an interference pattern on the sample surface. The spatial periodicity was varied to enhance a range of single frequencies in free surface Rayleigh waves, propagating on aluminium alloy samples. SIST waves, formed from similar sources on exposed surfaces of epoxy-bonded aluminium joints, enabled the progress of individual frequencies passing along the adhesive bond interface to be monitored. Waves in the

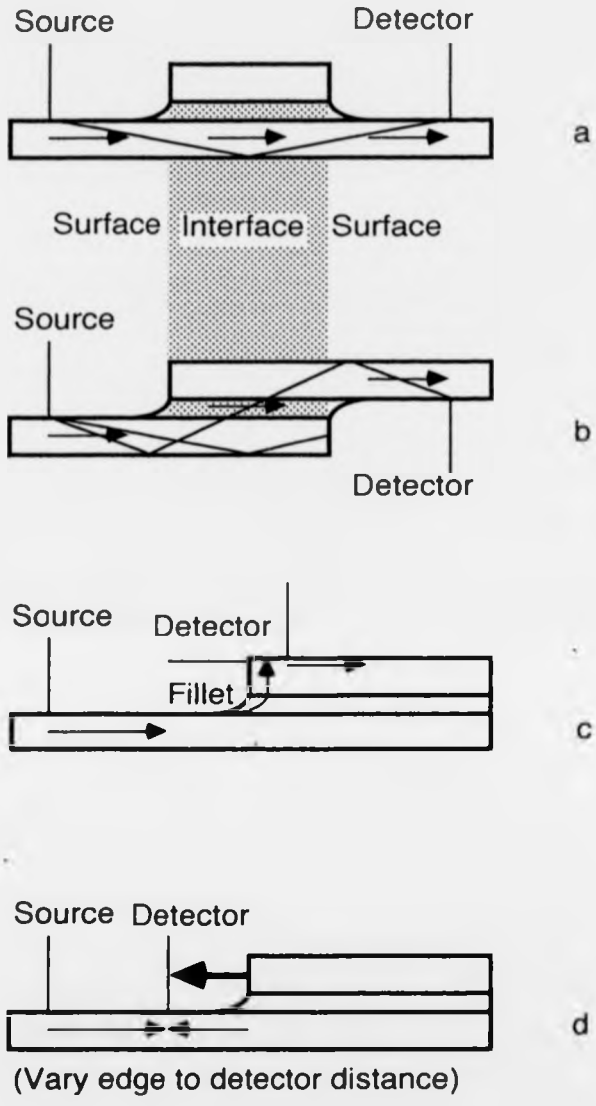

Figure 1.1 Possible pathways for acoustic waves. a) SIST wave on reinforcement joint. b) SIST wave on lap joint. c) Wave diverted by fillet. d) Reflected wave at bond edge. Surface waves - arrowed, bulk waves - solid lines.

2-3 MHz frequency range emerged as the most sensitive to adhesive bond length and were used to examine defect containing reinforcement joints in order to estimate the method's ability to pick out poor quality bonds.

Chapter Seven returns to sharply pulsed surface-travelling waves and examines the various routes available to the acoustic energy of a surface wave as it encounters the edge of a bonded interface. One route is the SIST wave encountered in the Chapter Six studies of reinforcement joints (Figure 1.1.a). However, energy is also reflected at the corner formed where the second adherend bonds and a detector placed between the source and the bond edge (Figure 1.1.d) observes, as well as the incident surface wave, a reflected wave the amplitude of which may be compared directly with the incoming amplitude. The reflection is so weak that a series of measurements are necessary, fixing the source and detector and varying the distance to the bond edge, in order to identify it unambiguously. Another possibility for surface-travelling waves is a coupling via the adhesive fillet to the outside edge of the second adherend (Figure 1.1.c), where they continue to propagate as surface waves. In theory, these waves should contain information about the fillet, an area in which the presence of defects is likely to be critical. Unfortunately, the wave amplitudes are again too low to be useful. The final case to be examined is that of SIST waves in lapped joints (Figure 1.1.b), where the transmitted surface wave emerges on the opposite adherend from the incident wave after coupling through the epoxy layer. This fortuitously cuts out a number of the bulk-travelling waves, which are also detected at sample surfaces, since some bulk waves are not reflected onto the adhesive layer "window" into the other adherend (Figure 1.1.b). More importantly, this arrangement ensures that all the ultrasound which reaches the detector has interacted at least once with the adhesive layer, thereby optimizing the chances of detecting any defects.

Chapter Eight, the final chapter of the thesis, offers a brief summary drawing together the experimental work laid out in the previous four chapters, and the overall conclusions which have been reached. In line with the ongoing nature of research in this area, the closing remarks also include a discussion of the more obvious gaps in present knowledge, suggesting the directions along which future advances are most likely to proceed, with a wider glance at the ultimate applications for the technique.

1.2 Summary.

Laser generated ultrasound is still a relatively young technique and its application to the problems of adhesion in epoxy-bonded joints is previously undemonstrated. The main thrust of this thesis will be a thorough examination of the way in which ultrasound generated by a pulsed laser, and detected by non-contact methods at the sample surface, may be used to differentiate individual aluminium-epoxy bonded samples. The aim of these studies is to extract reliable information from the ultrasonic waveforms, which will enable random samples to be catagorized according to the presence or absence of defects in the epoxy bond. The extent to which the presence of such defects may be used to predict adhesive bond strengths requires a programme of destructive testing, suggested for future work. At this moment, laser generated ultrasound is still predominantly a laboratory technique, being expensive, labour intensive and requiring equipment that is neither robust nor of exceptional acoustic sensitivity. However, as this thesis will show, the ability to generate highly repeatable, broad frequency bandwidth ultrasonic pulses is a considerable asset in the study of adhesively bonded joints. More importantly, the remote, noncontact nature of laser generation and interferometric detection suggest strongly that, once the present, mainly technical, hurdles to full automation are overcome, laser ultrasonics will provide a rapid and reliable industrial tool for in-service testing of bonded joints.

CHAPTER 2.

ULTRASONIC ANALYSIS OF BONDED EPOXY-ADHEREND LAYERS

The experimental generation of ultrasound by high energy pulsed lasers will be described in more detail in Chapter Three (Experimental Preparations and Methods). This chapter aims to present a theoretical basis against which the results of later chapters may be assessed.

Ultrasonic pulses with sharply confined time-duration have the advantage of providing accurate time-of-flight data in the time domain and broad bandwidth spectra in the frequency domain. The penalties include a corresponding increase in the noise bandwidth, highly complicated signals in strongly dispersive situations and involved source structures. Section 2.1 outlines the increasingly intricate configurations modelled for sources located at plate or half-space surfaces. This thesis, however, is interested mainly in source-independent quantities, such as the complex acoustic transmission coefficients which are used to extract information about the interior of epoxy-bonded layer systems.

The most useful time domain data obtained from pulses directed across a bonded layer are the time interval and attenuation between consecutive transits. These may be used in one of two ways. If the cohesive properties of the bond layer are known, the time gives the layer thickness and the measured attenuation factors may be compared with those expected for signs of bond defects. When the adhesive's properties are unknown, the attenuation factors yield Z^*, the epoxy to adherend acoustic impedance ratio, and hence a handle on the epoxy layer cohesive properties, provided that the value for Z^* does not deviate so wildly that the assumption of perfect adhesion must be dropped. The group velocity from Z^* and reverberation time between successive pulses give the adhesive layer thickness, which is usually controlled to within ~10% and thus a useful indicator of Z^* accuracy. Frequency domain analysis provides more detailed information about phase velocity dispersion and absorption in the epoxy, which may exhibit marked frequency dependence. Thus, sections 2.2 and 2.3 set up a simple model of plane-wave ultrasound interacting with an adhesive layer embedded between two semi-infinite half-space adherends. This is then applied in section 2.4 to the epicentral case, where ultrasound crosses perpendicular to the adhesive layer, and in section 2.5 to the passage of ultrasonic

waves along and parallel with the layer. The aim of these calculations is to examine the relationships between bond properties, which it is desirable to know, and measurable ultrasonic quantities. Where simple relations occur, information may be obtained experimentally by direct inversion of the problem, while more convoluted links suggest a trial and error approach of changing the assumed properties to optimize the match with observation.

2.1 Ab Initio Ultrasonic Source Calculations.

Theoretical results for the propagation in plates of monochromatic, infinitely extending, plane, ultrasonic waves were first presented over a century ago [Rayleigh, 1889]. In practice, however, real sources have finite spatial extent and even transducers driven at resonant frequencies yield measurable bandwidth signals lasting a finite length of time. Nonetheless, standard piezoelectric transducers may be treated as continuous, monochromatic emitters when the wavetrains permeating systems under study last considerably longer than any ultrasonic interactions and contain insufficient bandwidth to excite the majority of resonances. This is no longer true when thick, broadband resonant crystals, stimulated by preprocessed electrical impulses, generate signals with only a few cycles per pulse [Dewhurst et al., 1983] nor in the context of seismic tremors, for which the impulse source problem on the surface of a two-dimensional elastic half-space was first tackled [Lamb, 1904]. Seismic shocks fall into a non-resonant class of spatially confined ultrasonic sources, often occuring naturally, with short duration and, therefore, extremely broad bandwidth. Also included are acoustic emission and techniques developed to mimic such sources, such as pencil-breaking and, in the last thirty years, laser ultrasound. Solutions to these pulse problems are arrived at by double integrals, over time and space, of monochromatic waves which are not planar, but instead adopt the geometry of the source through spherical Bessel or cylindrical Hankel functions.

Despite considerable work [Cooper, 1985; Aindow, 1986; Spicer, 1991], the laser acoustic source is poorly characterized in terms of the input laser pulse, especially at power densities where material ablation results and energy transfer into the sample is governed by local material properties under rapidly varying temperature and pressure conditions. However, under the conditions for pulsed laser generation in metals, sources (in the most usual geometries) approximate well to idealized point or line forces acting at the metal surface. Locating the

source at the sample surface enables the forces to be treated as part of the problem's boundary conditions. The surface forces applied are inferred from the waveforms detected, so that thermoelastic laser sources are modelled by dipolar Heaviside forces acting in the surface plane, while higher energy ablation sources are represented by impulses directed normal to the surface. Agreement is facilitated by the lack of direct contact with the sample, eliminating both surface coupling and surface damping problems, inherent to close contact generation.

The technique developed by Cagniard and deHoop enables calculation of analytical solutions to the pulsed source problem in simple geometry cases. Put briefly, the pulse is expressed as a double integral transform over time and space. The ultrasonic equations and boundary conditions are expressed in the transform variables to obtain a transformed solution, which is inverted by finessing the inverse spatial transform integral into the integral form of a temporal transform, allowing time transform inversion by inspection. Numerical solutions have been found in this manner for a compressional pulse line source buried beneath a half-space surface [Garvin, 1956] and for a similarly buried vertical point force with Heaviside time dependence [Pekeris & Lifson, 1957]. Motion beneath the epicentre of a normal, impulsive line source in an infinite plane plate has also been calculated explicitly [Knopoff, 1958], although a numerical model was used for off-axis motions on the reverse side. Analytical solutions for surface and epicentral displacements have been found both, in two-dimensions, for vertical line impulses [Pilant, 1979] and, in axisymmetric conditions, for surface-tangent point dipoles [Cooper, 1985] or wide disc sources [Bresse & Hutchins, 1989] acting on the surface of a semi-infinite half-space with Heaviside time dependence.

Transient solutions to a number of source geometries in and on the surface of an infinite plate have been presented [Pao et al., 1979], using the alternative method of generalized ray integrals. These are used to evaluate plate responses numerically at distances away from the source epicentre of under 10 plate thicknesses, by which time the number of calculations needed becomes exorbitant. A numerical approximation valid for wider distances off-epicentre uses asymptotic normal mode expansions to compute the infinite axisymmetric plate response to a point source [Weaver & Pao, 1982]. On-epicentre computations based on the generalized ray approach have also been used to model dipole shear sources extending a finite distance

below the sample surface [Doyle, 1986]. Thus, despite the problems to which I alluded above, the main theoretical outlines for standard geometry laser-generated sources on metals are broadly understood and numerical approaches of increasing complexity are enabling progressively more detailed descriptions of experimental observations.

2.2 Describing Ultrasonic Wave Interactions with Adhesively Bonded Layers.

A full ultrasonic study of adhesively bonded joints introduces two principal complications, the presence of multiple layers with variable adhesion properties at the interfaces and the problem of viscoelasticity in the epoxy layer. Thus, when transferring from half-space or plate problems to a consideration of adhesively-bonded layer structures, analytical solutions become exceedingly unlikely. However, attempting a full, numerical computer model, in the style of those that geophysicists use for seismology, requires some foreknowledge of the system's behaviour to interpret the output correctly and extract useful data from real waveforms.

Separating information relating to the adhesive, to the material it adheres and to the interfaces between them may well not be strictly possible. Epoxy layers in aerospace bonds are extremely efficient at damping ultrasonic frequencies above the 10 MHz range and have thicknesses comparable to or smaller than the wavelengths associated with lower frequency ultrasound. Motions of the two interfaces and, by inference, of the adhesive bridging the gap between them are therefore strongly correlated. There is also the difficulty of defining the term "interface". Considerations of molecular scale roughness apart, the epoxy surface will inevitably have impurities which differentiate it from the bulk, while the aluminium adherends are deliberately anodized to enhance their oxide layers. The interface also includes a bonding layer of alumina-epoxy compound (Figure 2.1.a), bringing the layer total for each interface zone to three, a number which can increase arbitrarily to model progressively finer gradations.

Drastic pruning reduces the model to a single epoxy layer, sandwiched between two semi-infinite aluminium half-spaces (Figure 2.1.b). Assuming half-spaces simplifies the system but also accords with experimental observations of Rayleigh-like surface-travelling, ultrasonic pulses on aluminium pieces from which adherends in my test bonds were cut. Taking a forward problem approach, the epoxy layer properties are chosen to represent as simply as

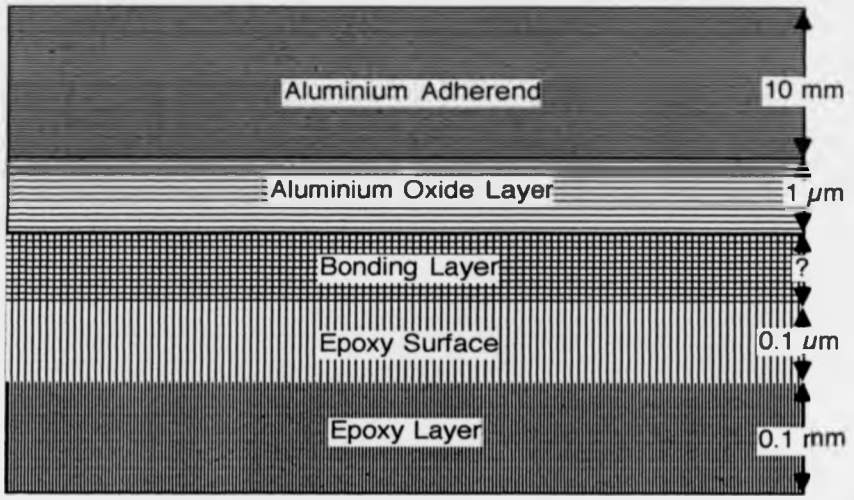

a). Each aluminium-epoxy interface may be subdivided into a series of layers in order to model the bonded region more closely.

b). For simplicity, however, consider a single epoxy layer between two aluminium half-spaces.

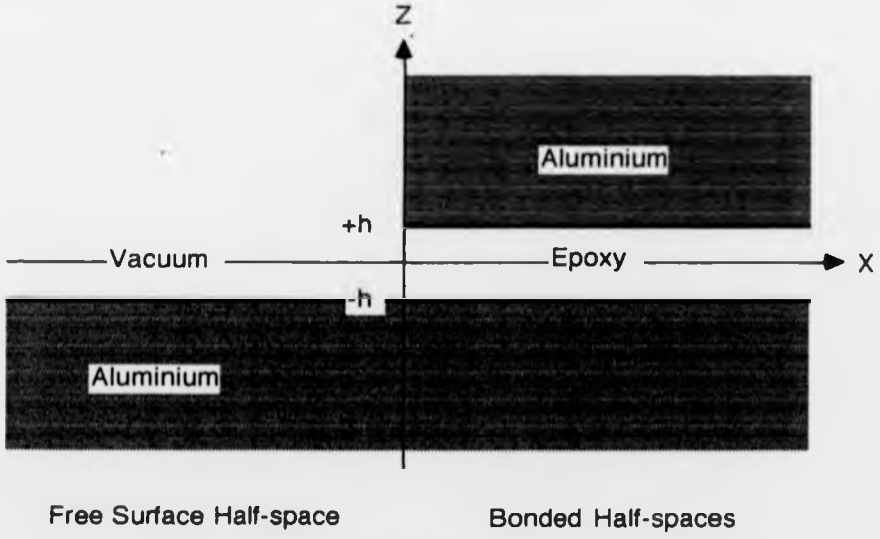

Figure 2.1 Representing an epoxy-bonded adhesive joint. The interfaces form planes seen edge-on in these cross-sections.

possible those which are observed. Despite careful process control, each bond is unique and the ultrasonic data varies between samples accordingly. The epoxy layer thickness also requires individual measurement for different locations along a sample, which has proved problematic as dissection and examination under an optical microscope provides accurate thicknesses within the joint but destroys the sample. Subtracting the total adherend thickness from the total joint thickness is imprecise but has nevertheless provided the most reliable non-destructive estimates for comparison with ultrasonic data. Treating the epoxy as homogeneous, isotropic and elastic is a patent oversimplification. Inhomogeneities arise from the nature of the pre-cure epoxy compound and the presence of embedded woven mesh carrier, designed both to hold the compound together and to prevent molten mix squeezing out of the bond during cure. That observations have consistently failed to distinguish similar bonds in which plastic carrier is either present or absent, however, suggests that this kind of inhomogeneity is unimportant in the present context. Presuming elastic behaviour is more likely to provide problems, as epoxy resins exhibit viscoelastic properties, with complex ultrasonic velocities (implying material attenuation) that are highly frequency sensitive. However, in order to incorporate viscoelastic behaviour into an analysis it is necessary to make a series of assumptions about the frequency dependences which will be observed [Rokhlin et al.,1980; Sachse & Pao, 1978], suggesting that a first order analysis assuming elasticity is the best place to start. It should be borne in mind that real epoxy will tend to damp ultrasound at high frequencies progressively more severely than in the simplified elastic case.

Given knowledge of the detailed properties of each layer, the problem breaks down into solving the ultrasonic wave equation within the layers, and coupling layer solutions together via the boundary equations at each interface. A formal approach would adopt solutions applicable to the variable laser source geometry (cylindrical for a line source, spherical for a point source) but the usually large ratio between adherend and adhesive thicknesses suggests waves crossing the bond layer with relatively large radii of curvature. Thus, for simplicity, I will take plane-wave solutions to the basic equation and assume pulses constructed by superposition of individual frequency waveforms. At a well-bonded interface, the 'stiff' boundary conditions are continuity of the three stress and three displacement components of ultrasonic motion. Across solid-liquid interfaces, stress components parallel with the interface vanish, while at a solid-vacuum 'free'

boundary all stress components are zero. In principle, breaking each epoxy-aluminium interface into a series of sub-layers with differing acoustic properties allows a wide range of bond strengths to be simulated [Rokhlin et al., 1981]. Another way of introducing interfacial weakness is by substituting the stiff boundary conditions with the constraints that stress is conserved but proportional to a finite displacement jump [Smith & Yang, 1989]. This is equivalent to a model in which adhesive and adherend are imagined to be linked by reduced stiffness springs in each component direction. Increasing the stiffness reduces the displacement difference until the continuous displacement stiff boundary conditions are retained. Setting either the tangential or normal stiffness component to zero causes the associated stress condition at the interface to vanish, retrieving the liquid and free surface constraints. I adopt this linear slip approach [Pilarski & Rose, 1988] because it enables the number of layers treated to be kept to a minimum, but still allows bonds to vary from perfect to non-existent as required.

2.3 Matrix Representations of Acoustic Wave Motion in Multiple Layers.

The fundamental ultrasonic wave equations yield two solution sets in each homogeneous, isotropic, linear elastic medium, denoting plane waves travelling with longitudinal (compressional wave) and transverse (shear wave) velocities respectively. Possible solutions are weighted with individually assigned frequency dependent coefficients and superposed to calculate the displacement and stress components. The coefficient values are found from the interface boundary conditions and from the requirement that solutions within the half-spaces remain finite at all distances from the centre layer. The resulting set of simultaneous equations linking the coefficients is most readily expressed in a matrix format and, for plane wave solutions, immediately breaks down into a transverse case linking y-component terms and a sagittal case in which x and z components interact (Figure 2.1.b). The latter case is of interest here as it concerns the vertical displacements detected by Michelson laser interferometry, and anyway the laser line source commonly used greatly reduces motion in the y-direction, parallel with the line.

For the sagittal case, coefficients from every layer may be linked by a single matrix equation, as in the case of a solitary layer upon a half-space [Farnell & Adler, 1972]. Off-axis matrix terms cater for reflection, refraction and for mode-conversion effects, appearing when the ultrasound travels at non-normal incidence to the bonded layer. It takes little imagination to

realize that increasing the number of layers rapidly generates unwieldy matrices, 8 x 8 being required for the single epoxy layer between two half-spaces. Fortunately, the boundary conditions only link neighbouring layers, allowing relations between coefficients in media many layers apart to be built up by stepping sequentially from one layer to the next. This is the transfer matrix method, used to analyse structures composed of multiple homogeneous, isotropic layers [Bresse, 1988; Nayfeh & Taylor, 1988a]. The aim is to link the two outermost layers' coefficients and thus express the total outgoing radiation in terms of the input values. Since observational measurements are invariably made at the outermost surfaces, the method has the obvious advantage of yielding surface displacements without requiring explicit calculation of all the intervening layer coefficients. In addition, matrix sizes are limited to the number of boundary conditions at each individual interface.

Thus, 4 x 4 matrices represent the four sagittal stress and displacement conditions either side of an interface:-

Stress $\sigma_{zz} = \rho_i [C_{Li}^2 (\partial u_x/\partial x + \partial u_z/\partial z) - 2C_{Ti}^2 \partial u_x/\partial x]$ is continuous at $z = z_{i-0.5}$ ... 2.3.B1

Stress $\sigma_{xz} = \rho_i C_{Ti}^2 [\partial u_x/\partial z + \partial u_z/\partial x]$ is continuous at $z = z_{i-0.5}$ ... 2.3.B2

Displacement $\Delta u_x = u_{xi} - u_{x,i-1} = \eta_T \sigma_{xz}$ across $z = z_{i-0.5}$ (continuity if $\eta_T = 0$) ... 2.3.B3

Displacement $\Delta u_z = u_{zi} - u_{z,i-1} = \eta_N \sigma_{zz}$ across $z = z_{i-0.5}$ (continuity if $\eta_N = 0$) ... 2.3.B4

where C_{Li}, C_{Ti}, ρ_i are the longitudinal, shear velocities and density in layer i, and the η are compliances which vary from 0 for perfect bonding to ∞ for smooth debonded surfaces.

Coefficients arrayed in vectors $\mathbf{x}_i$ for layers n and 1 are related by the matrix expression

$$\mathbf{x}_{i=n} = \prod_i (E_i^{-1}(z_{i-0.5}) J_i^{-1} A^{-1}_{i-0.5} J_{i-1} E_{i-1}(z_{i-0.5})) \mathbf{x}_{i=1}. \quad \text{... 2.3.1}$$

where the product runs from i = 2 to n. The E matrices propagate ultrasound within individual layers between the interfaces at $z_{i\pm0.5}$, where the stiff boundary conditions on either side are represented by the respective J matrices. By including adhesion matrices A to describe flow across interfaces, it is a relatively simple matter to examine the effects of interfacial weakness as the boundary conditions alter [Nayfeh & Taylor, 1987; 1988b]. A stiff boundary is obtained by setting the adhesion matrix to the identity *I*. A weakened adhesive bond is most plausibly

modelled by a tangential slip interface [Ngoc et al., 1988], with continuous stresses and normal displacement ($\eta_N = 0$) but tangential displacement slip (for smooth disbonds η_T tends to ∞, $\sigma_{xz} = 0$) proportional to the shear stress.

The advantage of this approach is that any number of layers may be considered by straightforward premultiplication of the product transmission matrix with the transmission matrix for the individual layers, a process which readily adapts to numerical treatment. However the authors mentioned above were interested primarily in non-normal incidences and couched many of their matrices in terms which diverge for on-epicentre calculations, rendering computation impracticable even though the end results are expected to behave. I will therefore treat separately the two situations with which I am concerned, through-transmission measurements detected under the source epicentre and waves detected on the same surface as the source after travelling parallel to the bond interfaces. Please remember, however, that a laser-generated source will generally be emitting radiation in both directions simultaneously.

2.4 Ultrasonic Transmission Through the Layer Perpendicular to the Interfaces.

The half-space assumption ensures consideration of only the first, direct arrival, laser-generated ultrasonic pulse transmitted through the bonded layer, followed immediately by a series of associated reverberations due to reflection at the two adhesive-adherend interfaces. Real joints show subsequent arrivals due to reflections at the outer joint surfaces, but the reverberations which follow them are suspect if the pulses reflected within top and bottom adherends arrive nearly simultaneously and interfere, as generally occurs because most joints have similar adherend thicknesses.

A general matrix approach amenable to epicentral configurations [Schoenberg, 1980] uses an input plane wave with displacements

$$u_{x\,i=1} = \sin\theta_{L,i}\, U\, e^{i z \omega \cos\theta_{L,i} / C_{L,i}} - \cos\theta_{T,i}\, V\, e^{i z \omega \cos\theta_{T,i} / C_{T,i}}$$

$$u_{z\,i=1} = \cos\theta_{L,i}\, U\, e^{i z \omega \cos\theta_{L,i} / C_{L,i}} + \sin\theta_{T,i}\, V\, e^{i z \omega \cos\theta_{T,i} / C_{T,i}} \qquad \ldots 2.4.1$$

where $\theta_{L\,i=1}$, $\theta_{T\,i=1}$ are incident angles for P and SV waves, $\sin\theta_{L,i} / C_{L,i} = \sin\theta_{T,i} / C_{T,i} = k^* / \omega$ (Snell's law), $C_{L,i}$, $C_{T,i}$ are longitudinal and shear velocities and U, V contain terms $e^{i(k^* x - \omega t)}$

and constants to set the relative contributions of the two waves.

Given plane wave solutions of this form, the matrices in 2.3.1 may be calculated (see Appendix A.1) for an epoxy layer bounded by z = ±h between two semi-infinite aluminium half-spaces. Equation 2.3.1 gives

$$\mathbf{x}_3 = E_3^{-1}(h)\, J_3^{-1} A_{2,3}^{-1} J_2 E_2(h) E_2^{-1}(-h) J_2^{-1} A_{1,2}^{-1} J_1 E_1(-h)\, \mathbf{x}_1 \qquad \ldots 2.4.2$$

where $\mathbf{x}_1 = (U, V, R_L, R_T)$ and $\mathbf{x}_3 = (T_L, T_T, 0, 0)$.

Assuming identical adherends ($J_1 = J_3$, ...), and noting that $E_2(h) = E_2^{-1}(-h)$

$$J_2^{-1} A_{2,3} J_1 \mathbf{X}_3 = E_2(2h)\, J_2^{-1} A_{1,3}^{-1} J_1 \mathbf{X}_1 \qquad \ldots 2.4.3$$

where $\mathbf{X}_1 = E_1(-h)\, \mathbf{x}_1 = (u, v, r_L, r_T)$ and $\mathbf{X}_3 = E_1(h)\, \mathbf{x}_3 = (t_L, t_T, 0, 0)$.

The equation may be dramatically simplified at this stage by taking the epicentral condition $\theta_{L,T=1} = \theta_{T,T=1} = 0$, which has the effect of completely decoupling longitudinal motions (u, r_L and t_L) and shear motions (v, r_T and t_T) in the system (Appendix A.2). Concentrating upon the longitudinal solution, although the shear has an identical form, and eliminating the reflected component,

$$t_L = 2u / ([(2 + Z^* + Z^{*-1}) - F_1 F_3 Z^* - i (Z^* + 1) (F_1 + F_3)] e^{i 2h\omega C_L} + [(2 - Z^* - Z^{*-1}) + F_1 F_3 Z^* - i (1 - Z^*) (F_1 + F_3)] e^{i 2h\omega C_L}) \qquad \ldots 2.4.4$$

where $Z^* = \rho C_L / \rho_A C_{LA}$, $F_1 = \omega \eta_{N1} \rho_A C_{LA}$, $F_3 = \omega \eta_{N3} \rho_A C_{LA}$,

ρ = epoxy density, C_L = epoxy longitudinal speed, $2h$ = epoxy layer thickness,

ρ_A = aluminium density, C_{LA} = aluminium speed, $\eta_{N1,3}$ = compliance at -/+ h interface.

For both rigid and tangential slip interface [Ngoc et al., 1988] bonds, $\eta_N = 0$ which is a reminder that longitudinal plane waves directed normal to the interface are relatively insensitive to adhesive properties, although shear waves are more responsive. Laser ultrasound produces longitudinal and shear waves, the latter admittedly at lower amplitudes, but since both are non-planar both produce adhesion-sensitive displacements parallel to the interface and insensitive displacements perpendicular to it.

It is immediately obvious that the system will resonate at frequencies for which

$$\tan(2h\omega/c_L) = 2 / (Z^* + Z^{*-1}) = 2\,\rho_A C_{LA}\,\rho\, C_L / [\rho^2 C_L^2 + \rho_A^2 C_{LA}^2] \qquad \ldots 2.4.5$$

as long as adhesion defect effects remain negligible. The perfectly adhered bond therefore has a cyclical, frequency dependent transmissivity (t_L / u) with a repeat period of $4h / C_L$, exactly the time 2T required for a wave with phase velocity $C_L(\omega)$ to cross the bond and back. Equation 2.4.3 can be further manipulated by setting $i\omega = s$, so that

$$t_L / u = (2 / [\,(2 - Z^* - Z^{*-1}) + F_1F_3Z^* - i\,(1 - Z^*)\,(F_1 + F_3)]\,)\, e^{-sT} / (1 - e^{-2sT} \bullet \qquad \ldots 2.4.6$$

$$([F_1F_3Z^* + i(Z^*+1)(F_1 + F_3) - (2 + Z^* + Z^{*-1})] / [(2 - Z^* - Z^{*-1}) + F_1F_3Z^* - i(1-Z^*)(F_1 + F_3)]))$$

which takes the form

$$t_L / u = t_L(-h)\, t_L(+h)\, H(s)\, e^{-sT(0)} / (1 - r_L(-h)\, r_L(+h)\, H^2(s)\, e^{-2sT(0)}) \qquad \ldots 2.4.7$$

when $t_L(-h)\, t_L(+h) = 2 / D$, $D = [\,(2 - Z^* - Z^{*-1}) + F_1F_3Z^* - i\,(1 - Z^*)\,(F_1 + F_3)]$,

$r_L(-h)\, r_L(+h) = [F_1F_3Z^* + i(Z^*+1)(F_1 + F_3) - (2 + Z^* + Z^{*-1})] / D$

$T(0) = 2h / C_L(0)$ and $H(s) = e^{-s\,[(2h / C_L(w)) - T(0)]}$.

If C_L is frequency independent, $H(s) = 1$ and Z^* is also frequency independent. In a viscoelastic epoxy, complex wavenumber wave motions are permitted and C_L becomes

$$C_{Visc} = C_L(\omega) / [\,1 - i\,(\alpha(\omega)\, C_L(\omega) / \omega)\,] \qquad \ldots 2.4.8$$

where $C_L(\omega)$ is the dispersive phase velocity and $\alpha(\omega)$ the wave attenuation.

$$\Rightarrow \qquad H(s) = e^{-2h\,\alpha(\omega)}\, e^{-s\,(T(\omega) - T(0))} \qquad \ldots 2.4.9$$

Equation 2.4.6 is significant in that a binomial expansion of the denominator gives a series

$$t_L / u = t_L(-h)\, t_L(+h)\, H(s)\, e^{-sT(0)} \sum_{n=0\,to\,\infty} [\, r_L(-h)\, r_L(+h)\, H^2(s)\, e^{-2sT(0)}\,]^n \qquad \ldots 2.4.10$$

in which each term represents a wave which has travelled one extra circuit reflected between the interfaces than the wave of the previous term, starting with the directly transmitted wave that is not reflected at all. If the epoxy velocity remains sufficiently close to its zero frequency value that Z^* can be considered frequency independent, all the frequencies in a pulse will be affected equally by passage through the bond layer and a train of pulses will emerge a time 2T(0) apart. Pulses crossing thin adhesive layers will merge and interfere if the pulse widths are greater than 2T(0), but 2.4.6 shows that the transmissivity will still exhibit a periodicity characteristic to the layer. Frequency dependence, altering the pulse shape, may result from either the layer's adhesive (F_1 and F_3) or cohesive (C_{Visc}) properties.

In well-adhered bonds, information on epoxy phase velocity dispersion and absorption may be obtained via Fourier transform of consecutive pulses [Challis et al., 1991]. The transformed displacement $\hat{U}$ detected by a broadband receiver depends upon the source transform S, adherend transfer functions A_i and the epoxy transfer function T_{123}:

$$\hat{U}(i\omega) = S(i\omega) \, . \, A_1(i\omega) \, . \, T_{123}(i\omega) \, . \, A_3(i\omega) \qquad \ldots 2.4.11$$

From equation 2.4.9, $T_{123}(s) = (t_L / u)$ which represents a series of multiple reverberations. Taking a ratio of the Fast Fourier transforms of two consecutive reverberation arrivals gives:-

$$\hat{U}_n / \hat{U}_{n-1} = | \, r_L(-h) \, r_L(+h) \, H^2(s) \, e^{-2sT(0)} \, | \qquad \ldots 2.4.12$$

Thus $$|\hat{U}_n / \hat{U}_{n-1}| = | \, r_L(-h) \, r_L(+h) \, | \, e^{-4h\alpha(\omega)} \approx | \, \hat{U}_n(0) / \hat{U}_{n-1}(0) \, | \, e^{-4h\alpha(\omega)} \qquad \ldots 2.4.13$$

as long as $r_L(-h)$ and $r_L(+h)$ are approximately frequency independent so that variations in their moduli are small compared with variations in the attenuation term.

$$\Rightarrow \quad \alpha(\omega) = (1 / 4h) \, \mathrm{Ln} \, | (\, \hat{U}_n(0) \, . \, \hat{U}_{n-1}(\omega) \,) / (\, \hat{U}_{n-1}(0) \, . \, \hat{U}_n(\omega) \,) | \qquad \ldots 2.4.14$$

And $$\mathrm{Phase}(\hat{U}_n / \hat{U}_{n-1}) = \mathrm{Phase}(r_L(-h) \, r_L(+h)) - 4h\omega / C_L(\omega) \approx -4h\omega / C_L(\omega) \qquad \ldots 2.4.15$$

setting the zero frequency phase to zero. Individual pulses are often aligned, in order to apply identical transform windows, by shifting the nth pulse back relative to the n-1th by the pulse reverberation time 2T(0) [Challis et al., 1991]. Hence,

$$\mathrm{Phase}'(\hat{U}_n / \hat{U}_{n-1}) = 2\omega T(0) - 2\omega T(\omega) = 4h\omega (\, 1 / C_L(0) - 1 / C_L(\omega) \,) \qquad \ldots 2.4.16$$

$$\Rightarrow \quad C_L(\omega) = 4h / (\, 2T(0) - (\mathrm{Phase}'(\hat{U}_n / \hat{U}_{n-1}) / \omega) \,) \qquad \ldots 2.4.17$$

On-epicentre arrival data from a through-transmission experiment, described in detail in chapter 4.1, on a 210 μm thick CG312/5 epoxy layer provides direct and first reverberation longitudinal pulse Fourier transforms for equations 2.4.14 and 2.4.17 (Figure 2.2). Data extraction below 1 MHz is distorted by windowing effects. Padding the original signal front ends with zeros to widen the windows beyond the current 4096 point value allows retrieval of lower frequency information but increases computation costs. Up to 5 MHz the epoxy phase velocity rises rapidly and can be modelled [Challis et al., 1992] as a single relaxation process consisting of 1 elastic element in parallel with a smaller elastic element and dashpot in series. The resulting viscoelastic dispersion relation, with 0.2 μs time constant and 1850 m/s zero frequency velocity, is fitted to the first 3.5 MHz of the extracted epoxy phase velocity curve

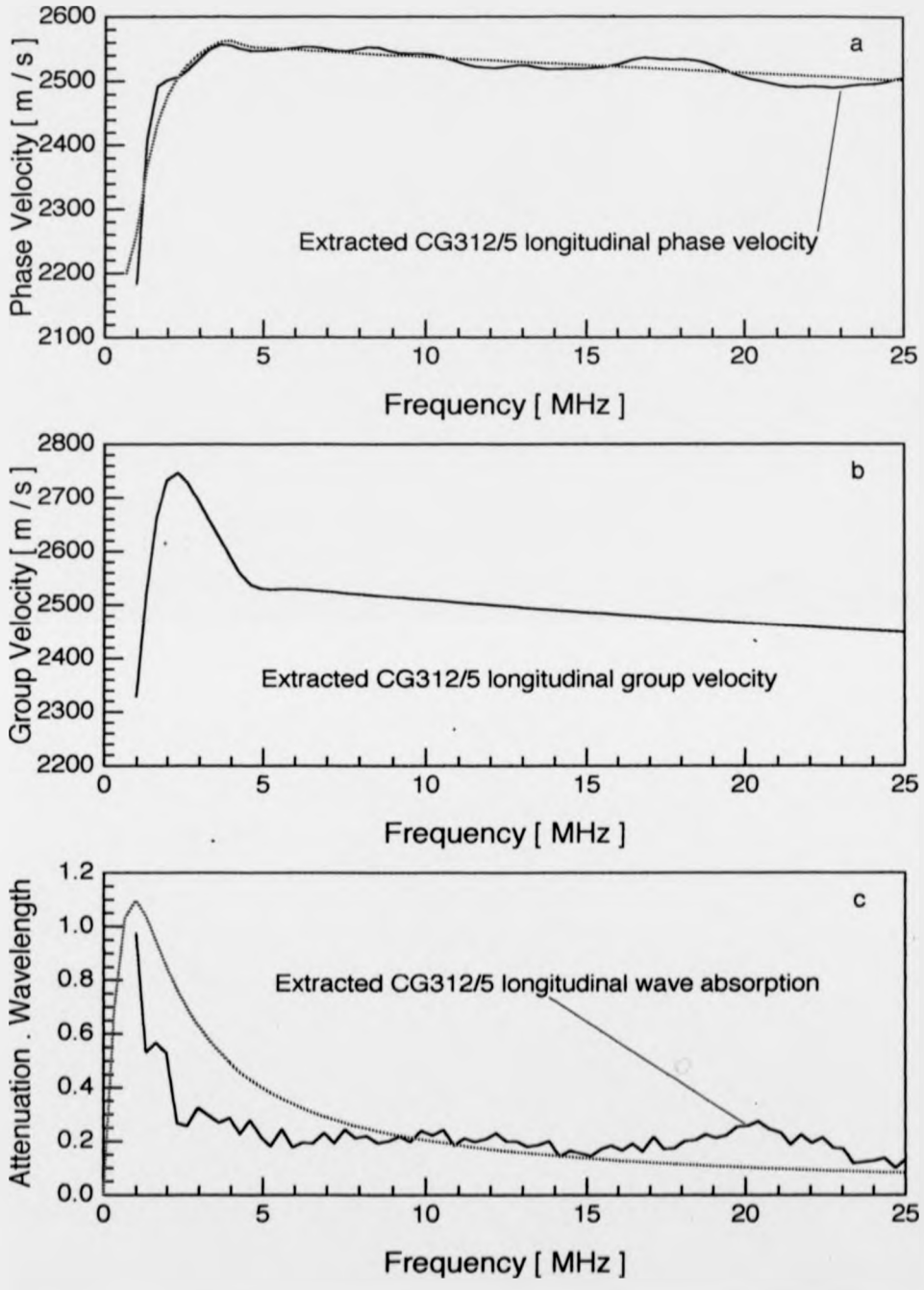

Figure 2.2 a). Phase velocity, b). group velocity, c). attenuation extracted by comparing the direct and 1st reverberation arrivals on 210 μm thick CG312/5 epoxy bond layer. (For experimental details see chapter 4.1).

(Figure 2.2.a) using software in Wavemetric's **Igor** package (see algorithm in Appendix A.2). Above 5 MHz the extracted velocity is roughly constant, decreasing linearly by ~2% before starting to oscillate at 17 MHz when signal amplitudes in the first reverberation pulse hit noise level. A group velocity is easily obtained from the fitted phase velocity (Figure 2.2.b), but this departure from viscoelastic behaviour is unexpected. One possible reason is the 8-bit digitization limit on data from the Lecroy 6880A, giving unreliable results at frequencies over 10 MHz, although this could be improved by summing 256 repeated shots to create 16-bit data, at the expense of increased laser ablation damage to sample surfaces. The viscoelastic model uses the same parameters with which the low frequency phase velocity was fitted to predict a frequency dependent absorption coefficient for the epoxy, and gives good agreement with the extracted absorption coefficient right up to 17 MHz (Figure 2.2.c).

A problem in evaluating equations 2.4.14 and 2.4.17 is the acquisition of accurate spectra from consecutive pulses $\hat{U}_n$. If $T(0) > T_{pw}$, the acoustic probe pulse width, and if bond layer attenuation is negligible, reverberation pulses will be well-separated in time and similar enough in shape to allow ready identification. As the attenuation increases, pulses broaden with each transit through the bond, until deciding a value for T(0) is a matter for debate. Laser-generated ultrasonic pulses tend to be asymmetric, rising much faster than they fall, with the result that although the pulse tails tend to overlap, individual pulses have been detected reverberating in epoxy bond layers under 0.1 mm thick (Chapter 4). When the bonded interfaces are close to each other, consecutive acoustic pulses overlap and assumptions about the pulse shapes have to be made in order to separate them. Strictly, equation 2.4.3 should be used under such conditions, requiring knowledge of source transform and adherend transfer functions, in equation 2.4.10, which are most readily obtained from parallel experiments using single unbonded adherend samples with the same total adherend thickness as the joints. Calculations at this point become messy and a forward approach using tunable estimates of the bond properties is preferred.

If the epoxy velocity and attenuation are known as functions of frequency, equation 2.4.7 gives $|r_L(-h)\, r_L(+h)|$ which may be compared with the value extracted from a sample using 2.4.13 to deduce the bond's adhesion properties. However, unless it is known which of the two interfaces is likely to be weak, extraction of adhesion data is not simple, intimating a

trial and error approach. One straightforward method is to return to the frequency dependent transmission coefficient of 2.4.4, which may be estimated from the experimental displacement transform in 2.4.11, by deducing forms for the remaining transfer function terms. The transmission is readily calculated and a number of computed traces are shown (Figure 2.3) using the same 210 μm CG312/5 epoxy bond data from which the longitudinal phase velocity and attenuation above were extracted. Values for a joint with rigid bonds (Figure 2.3.a -solid) are obtained by setting the compliance terms η_1 and η_3 in 2.4.4 to zero, but differences from the rigid case (Figure 2.3.a -dotted) only appear for compliances above 10^{-15} m^3 N^{-1}. The initial effect of reducing the bond strength is to reduce the reverberation frequency, associated with a slowing of the ultrasound across the interface. In well-bonded joints, this effect is only detectable when both the layer thickness and adhesive acoustic velocity are accurately known to high precision. As the joint quality deteriorates further (Figure 2.3.b) to compliances of 10^{-14} m^3 N^{-1} at either interface, the discrepancy between rigid and weak bond reverberation frequencies becomes measurable. In addition, the higher frequency reverberation harmonics appear progressively damped and with increasingly narrow widths, although this is more obvious in these examples, where epoxy attenuation is neglected, than would be the case in practice. Bonds with compliances below 10^{-12} m^3 N^{-1} are severely weakened and transmit so little energy that the problem would be immediately obvious in the raw data as a significant loss in signal. The combination of both forward and inverse treatments to the on-epicentre through transmission problem thus provides a theoretical basis for extracting both cohesive and adhesive bond properties that are mutually consistent: Chapter 4 tackles the practical application of these ideas.

2.5 Ultrasonic Layer Waves Travelling Parallel to the Bonding Epoxy Interfaces.

In contrast to through transmission calculations, the analysis of waves travelling parallel with the interfaces of a bonding layer does not lend itself to an inversion procedure. The emphasis is therefore more towards calculation of such modes as may be expected in the specific case of a 210 μm thick CG312/5 bond layer, using the through transmission data extracted in section 2.4. General conclusions drawn from this well-studied example may then be used to ellucidate experimental observations on other samples. Interface-travelling mode calculations in this section precede a discussion in section 2.6 of the results and their significance.

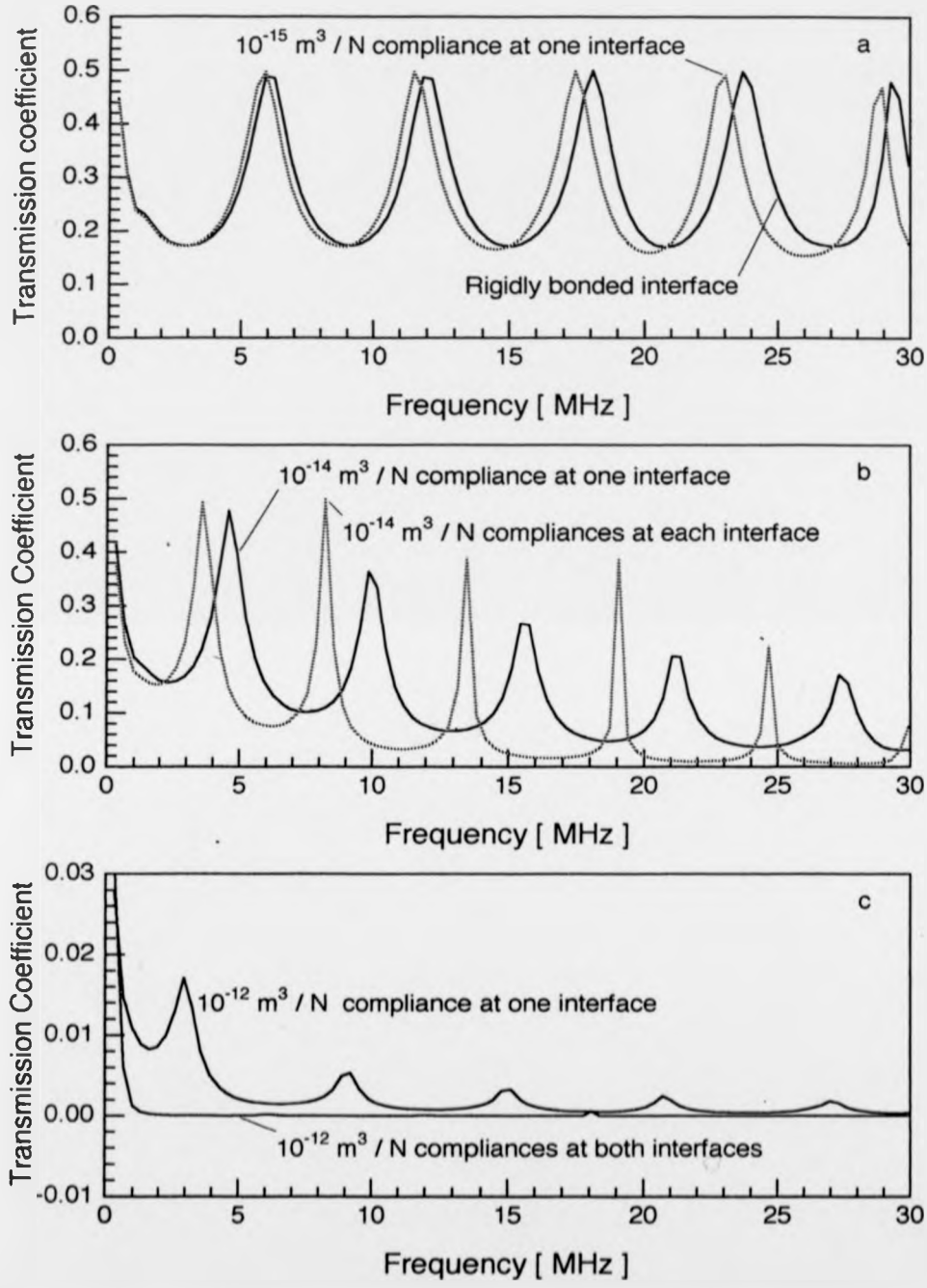

Figure 2.3 Calculated transmission coefficient magnitudes 210 μm thick CG312/5 epoxy layer bonding aluminium. Attenuation neglected (see 4.1) to illustrate differences in a). rigid, b). intermediate, c). weak strength bonds.

The plane wave layer displacement components of section 2.4 [Schoenberg, 1980] degenerate when the waves travel parallel with the layer interfaces [Farnell & Adler, 1972] into

$$U_j = (\Sigma_m c_m a_{jm} e^{ikb_m z}) e^{ik(x-vt)} \qquad \ldots 2.5.1$$

where, v and k are the velocity and wavenumber of a wave travelling parallel with the interface

c_m are the wave coefficients, set to zero where the z term diverges as z tends to $\pm\infty$,

$b_m = \pm i \sqrt{[1 - (v / C_{Ld})^2]}$ and $\mathbf{a}_m = (1, 0, \pm i \sqrt{[1 - (v / C_{Ld})^2]})$,

or $b_m = \pm i \sqrt{[1 - (v / C_{Td})^2]}$ and $\mathbf{a}_m = (- (\pm i \sqrt{[1 - (v / C_{Td})^2]}), 0, 1)$.

Given plane wave solutions of this form, the matrices in 2.3.1 may be calculated (see Appendix A.3). A check on the method in the case of a free surface half-space yields the Rayleigh wave equation for the material as expected. I am interested, however, in an epoxy layer bounded by z = ±h between two semi-infinite aluminium half-spaces (Figure 2.1.b). Equation 2.3.1 gives

$$\mathbf{x}_3 = E_3^{-1}(h) J_3^{-1} A_{2,3}^{-1} J_2 E_2(h) E_2^{-1}(-h) J_2^{-1} A_{1,2}^{-1} J_1 E_1(-h) \mathbf{x}_1 \qquad \ldots 2.5.2$$

where $\mathbf{x}_1 = (0, 0, c_a, c_b)$ and $\mathbf{x}_3 = (c_c, c_d, 0, 0)$.

Assuming perfect adhesion ($A_{2,3} = A_{1,2} = I$), identical adherends ($J_1 = J_3$, ...), and noting that $E_2(h) = E_2^{-1}(-h)$

$$J_2^{-1} J_1 \mathbf{X}_3 = E_2(2h) J_2^{-1} J_1 \mathbf{X}_1 \qquad \ldots 2.5.3$$

where $\mathbf{X}_1 = E_1(-h) \mathbf{x}_1 = (0, 0, c_A, c_B)$ and $\mathbf{X}_3 = E_1(h) \mathbf{x}_3 = (c_C, c_D, 0, 0)$.

Up to this point, apart fom the implicit plane-wave assumption, no restraints have been placed upon the velocities, known or otherwise, so that viscoelastic behaviour in the epoxy is allowed. From the system symmetry about the epoxy layer centre plane, it is tempting to imitate Lamb waves on a free plate and choose solutions that are either symmetric ($c_C = c_A$; $c_D = -c_B$) or antisymmetric ($c_C = -c_A$; $c_D = c_B$) about the middle. On doing this, however, the interface wave amplitude is forced to zero, unless the adherend shear velocities vanish, a situation which is fine for a layer surrounded by liquid or gas, but hardly applicable to aluminium!

Conditions on the interface wave velocity are relaxed slightly if the wave is allowed to travel at different speeds within the two media, in which case symmetric and antisymmetric waves may propagate, entirely within the epoxy layer, as long as the epoxy shear speed exceeds that in aluminium. Thus, if the epoxy were high ultrasonic velocity material, the wave

energy would be guided out of the aluminium to produce an interface wave running through the centre layer. In fact, epoxy resins have speeds of the order of a half those seen in aluminium alloys. Therefore ultrasound travels preferentially within the aluminium, albeit decaying with distance from the interface, and displacements within the epoxy are forced by the interfacial motion, resulting in a wave which travels at the same speed in both materials.

Abandoning the conditions for symmetric and antisymmetric internal layer waves but retaining a single interfacial wave velocity results in an eigenvalue-type problem, where the four equations linking c_A,c_B,c_C,c_D are used to relate three coefficients to the fourth and the remaining unknown is the velocity, found by setting the eigenmatrix determinant (see Appendix A.4) to zero. The velocity is implicit within the determinant, requiring a numerical solution, and it is at this point, in order to keep the problem manageable, that viscoelasticity is ignored and a real (but still dispersive) speed stipulated. Under such constraints the determinant rarely vanishes entirely and solutions are found by fixing the frequency, assuming a series of interface velocities spaced equidistantly between two limits and searching for minimum magnitudes in the values of the determinants thus obtained. Take the following experimental values (C_R is the Rayleigh speed):

	C_L [m/s]	C_T [m/s]	C_R [m/s]	Density [kg/m^3]
Aluminium	6370 (±0.05%)	3142 (±0.05%)	2930 (±1%)	2700
Epoxy	2500 (±7%)	1190 (±7%)	1010	1200

The section 2.4 analysis of a 210 μm thick CG312/5 layer gives a dispersion curve for the longitudinal velocity and the definition of 2.4.7 the zero frequency velocity quoted above. I do not have similar quality data for the shear velocity and have therefore modelled the shear dispersion curve by assuming a constant (experimentally determined) factor of 2.1 between longitudinal and shear speeds. By feeding these values into the determinant for a 210 μm thick layer, and looking in the frequency range 0 to 20 MHz, a number of frequency-dependent velocity modes may be traced out (Figure 2.4). The determinant actually yields phase velocities (Figure 2.4.a), which are differentiated with respect to frequency and then manipulated to calculate the group velocities (Figure 2.2.b). One mode has a dispersion curve which starts at the aluminium shear velocity and approaches the epoxy longitudinal velocity from above, while the remainder all have phase velocities with low frequency cutoff points, by which they are

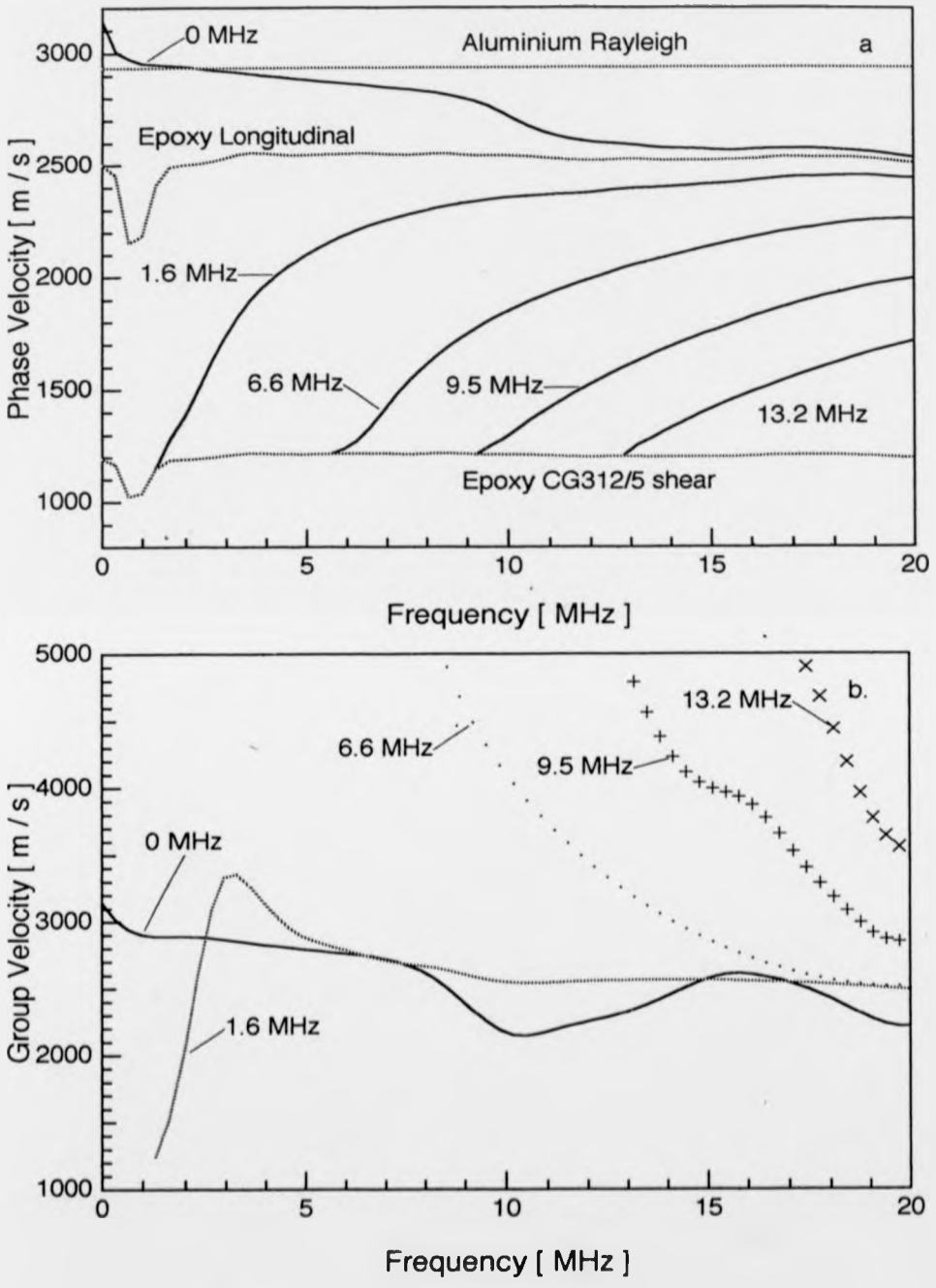

Figure 2.4 Calculated modes for ultrasonic waves travelling parallel to the interfaces of a 210 μm epoxy layer bonding two aluminium half-spaces. a). Phase velocity. b). Group velocity. All modes cause approximately antisymmetric displacements.

identified, rising to the epoxy longitudinal velocity from below. Despite the fact that epoxy and aluminium are not a material combination which can sustain non-dispersive Stoneley waves along an interface between them [Victorov,1967], there is no a priori reason why an epoxy layer between two aluminium adherends should not support travelling waves. The mechanism by which interface waves lose energy is shear wave radiation into the low velocity partner (epoxy) of the material pair. Since this radiation is unlimited in a semi-infinite medium, the interface wave is starved of energy and collapses. In the embedded epoxy layer case, however, it is possible to initiate parallel travelling waves simultaneously at both interfaces. Energy radiated from one wave will feed the wave on the opposite interface and vice-versa, creating a self-supporting disturbance which can propagate along the bond. An analogy would be the planetary Kelvin waves observed in atmospheric dynamics, which can only propagate around the equator when Northern and Southern hemisphere pairs travel back-to-back.

2.6 Ultrasonic Travelling Interfacial Wave Modes.

Examining the mode calculations in the light of the last remark, 2.5.1 shows that all the layer waves have components in the aluminium adherends which decay with distance from the interfaces and components ($i\, b_m = \pm i \sqrt{|(v / C_{l+p})^2 - 1|}$) associated with shear motion radiating in the epoxy. However, there is an immediate difference between the cutoff modes, where longitudinal motion in the epoxy ($i\, b_m = \pm \sqrt{|1 - (v / C_{l+p})^2|}$) is damped away from the interfaces, and the high velocity ($v > C_{l+p}$) zero frequency mode in which the longitudinal component also radiates into the adhesive. The latter mode formally reaches the aluminium shear velocity at zero frequency, the rigid bonding, zero layer thickness solution, but this is the only circumstance in which the interface wave is not trapped near the adherend interfaces.

Interest in the 0 MHz mode arises because it is the least dispersive and does not deviate greatly from the aluminium Rayleigh velocity between 0.5 and 9 MHz, when it drops sharply towards the epoxy longitudinal velocity. In fact between 1 and 2.3 MHz the mode appears to travel along the layer at exactly the aluminium Rayleigh velocity. Experimental observations on pulses travelling along bonded layers (Chapter 6) produced speeds indistinguishably close to the adherend Rayleigh speed for pulses having frequencies in the 1 to 10 MHz range, confirming that the 0 MHz mode carries a significant proportion of the interface wave energy. The flip

between aluminium Rayleigh and epoxy longitudinal velocities culminates around 11 MHz, when the associated longitudinal wavelength in epoxy drops below the bond layer thickness. At low frequencies, the bond layer is thin compared with the interface wavelength, allowing ultrasonic energy to propagate mainly within the aluminium adherends as long as displacements transmitted into the epoxy from both interfaces can interfere destructively. The mode phase velocity may be inserted back into the original matrix equation to calculate the c-coefficients, and hence displacement values, at the upper and lower interfaces. This is only an approximate method, unless the matrix determinant was truly zero at the minimum value from which the velocity was deduced. Displacements in the x and z directions at the z = -h interface (incident ultrasound) and at the z = h interface (outgoing ultrasound) were calculated for the 0 MHz mode (Figure 2.5). At each interface the two components are in phase quadrature, although this will probably not hold when attenuation is included and complex velocities are used. As predicted, the displacements are neither symmetric nor antisymmetric. However, the x-displacements appear roughly out of phase either side of the adhesive layer and the z-displacements almost in phase, making the layer mode, with its elliptical interface motions, somewhat akin to a free plate antisymmetric Lamb wave. The wave passage does not alter the layer thickness, as the z displacements at each interface are almost identical, and the adhesive therefore undergoes pure shear deformation, reducing the energy present in the S_0 symmetric mode to a minimum [Rokhlin & Rosen, 1982]. Thus, even when attenuation in the epoxy is included, the zero frequency mode should provide an efficient mechanism below 9 MHz for partitioning acoustic energy between the two adherends and transporting it along the bonding layer. Above 12 MHz, the layer is no longer thinner than the 0 MHz mode wavelength and both extensional and shear deformations are possible within the adhesive layer, even though the z displacements at the interfaces remain in phase. As a result displacements inside the epoxy are enhanced and the mode attenuation increases. Energy transfer between the interfaces is thus reduced through additional losses in the epoxy until, at some maximum frequency, the mode vanishes because displacements at the far interface are no longer sustainable and the non-propagating single epoxy-aluminium interface conditions are retrieved [Pilarski, 1985].

Finally, inspection of 1.6 MHz mode displacements (Figure 2.6) and the other cutoff modes also indicates x and z components $\pi / 2$ out of phase. However, by comparison with the

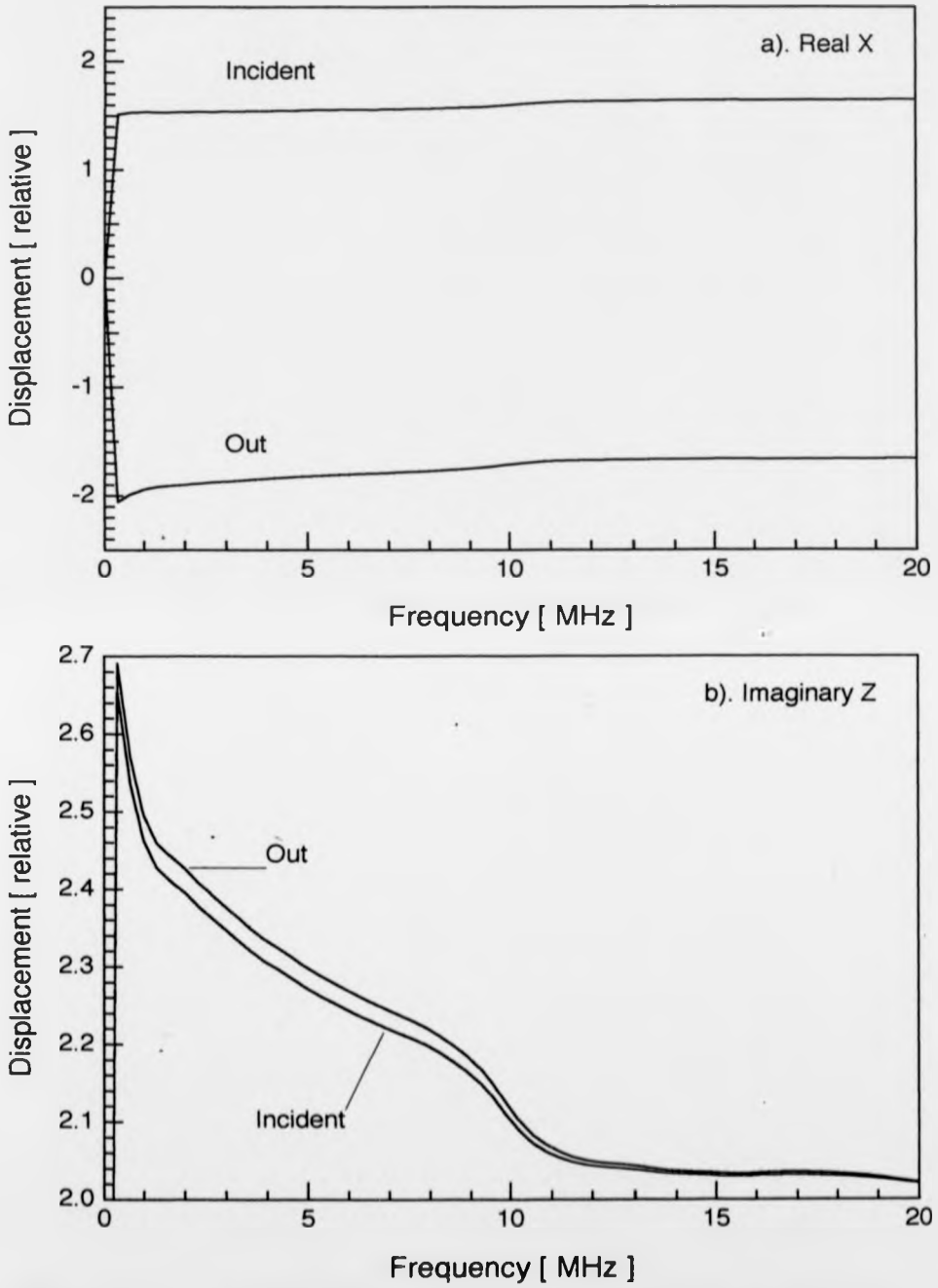

Figure 2.5 Relative displacement components parallel (X) and perpendicular (Z) to 210 μm thick epoxy bond layer embedded in aluminium due to quasi-antisymmetric interface travelling wave (zero frequency mode).

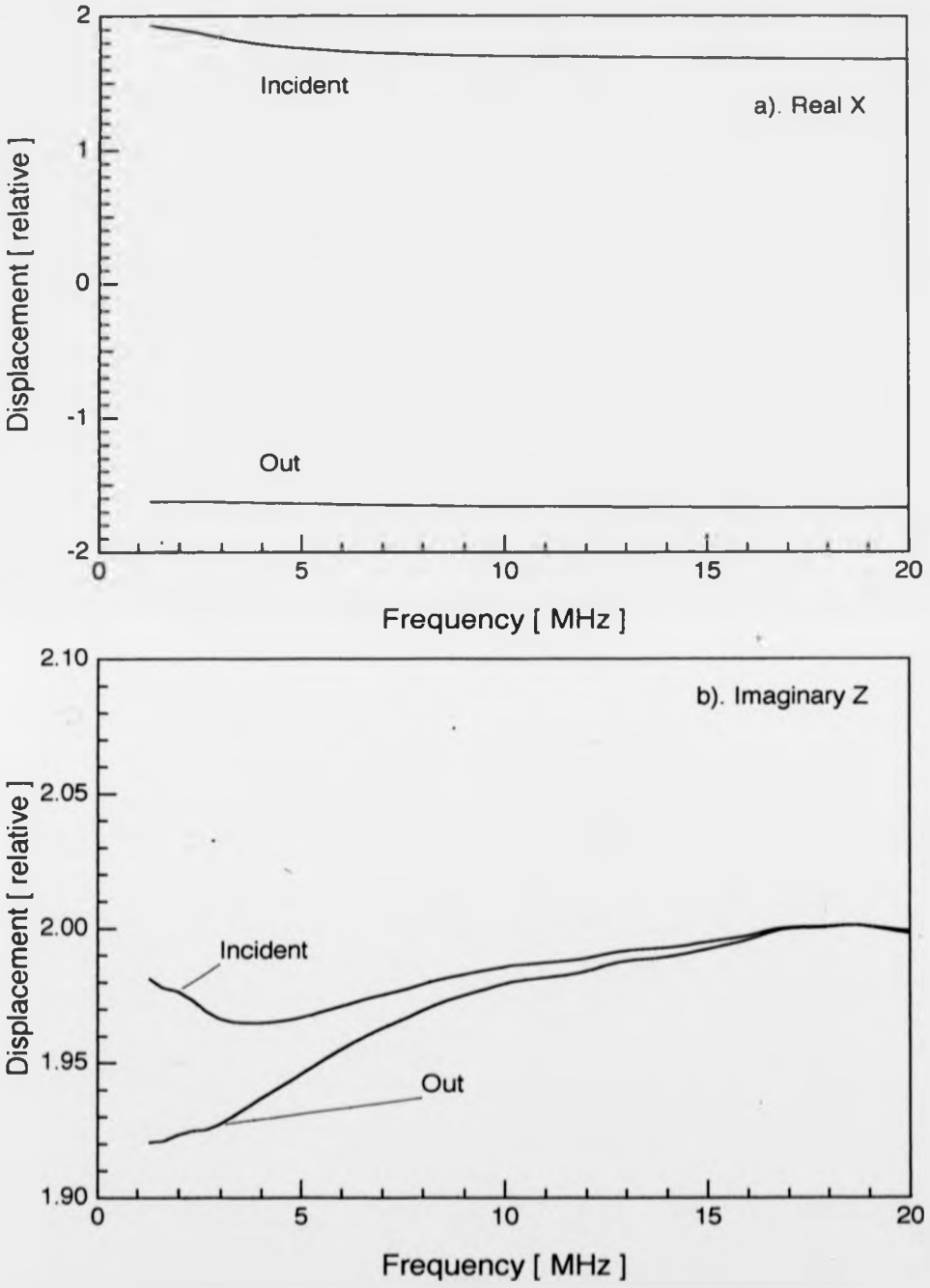

Figure 2.6 Relative displacement components parallel (X) and perpendicular (Z) to 210 μm thick epoxy bond layer embedded in aluminium due to quasi-antisymmetric interface travelling wave (2 MHz frequency mode).

0 MHz mode (Figure 2.5) the incident x and z components are increased in amplitude over the outgoing components. At high frequencies, the modes again exhibit quasi-antisymmetric behaviour, but close to cutoff there is a significant deviation between the imaginary z displacement components which increases with cutoff frequency. This may, however, result from inaccuracies in plotting the mode behaviour close to cutoff, as it is not clear from the numerical solutions whether the modes drop increasingly sharply, giving infinite group velocities at cutoff, or whether they flatten off to merge with the epoxy shear velocity (Figure 2.6.b). Any solution below the epoxy shear velocity will be highly attenuating, but until a computation with complex longitudinal and shear wave input can be made, to search for determinant zeros (section 2.5) in frequency, phase velocity and also attenuation coordinates, the onset of such solutions is hard to quantify. Even so, the cutoff modes' phase velocity range, between the epoxy shear and longitudinal velocities, suggests that the epoxy plays a far more prominent role in the transport of ultrasound in these modes. This in turn implies that attenuation will be more severe in the low velocity modes, at least below 10 MHz.

In conclusion, the interface-parallel layer wave analysis suggests the existence of travelling waves trapped in the neighbourhood of an epoxy layer bonding two aluminium half-spaces. The phase velocity of such waves is obtained by setting the matrix determinant in Appendix A.4 to zero, a process which requires numerical calculation. The computer macro which I have written is too time-consuming to use for producing exact zeros, but modes can be estimated by tracing minima in the determinant values as the frequency and mode phase velocity are varied. The significance of such modes is that motion along one adhesive-adherend interface is supported by a correlated motion along the other, implying that ultrasonic energy fed into the bond region will be distributed between the two interfaces as it propagates along the joint.

CHAPTER THREE

EXPERIMENTAL PREPARATIONS AND METHODS

This chapter describes experimental techniques, common to the remaining chapters in the thesis, which can be divided between the basic apparatus required to generate ultrasonic pulses and the methods chosen to detect ultrasound on metal surfaces. In section 3.1, however, I begin by describing the epoxy-bonded joints which are the subject of this thesis. Bonded samples were manufactured for me by my sponsors at DRA (Aerospace Division) using a process outlined in Appendix B.1 for completeness. Some of these bonds contained defects representative of those commonly appearing in adhesive joints. Section 3.1 therefore catalogues the defects which bond manufacturers are most anxious to spot and 3.2 mentions some of the nondestructive methods, mainly ultrasonic, previously applied for this purpose.

Laser generation is one of the more esoteric acoustic sources. Section 3.3 therefore outlines the technique's mechanisms and peculiarities, as they have emerged over the three decades since the effect was first reported. Section 3.4 describes various broad bandwidth, non-contacting detectors which can be used to receive laser-generated acoustic signals, while sections 3.5 and 3.6 concentrate upon the two types of detector which I used. These are electromagnetic acoustic transducers (EMATs), which have output related to the rate of change of displacement, and modified Michelson laser interferometers, where the signal is approximately linear with displacement at the sample surface. For ease of calibration, the quantitative work described in this thesis favours interferometers over the EMATs. This may be satisfactory for research, but it should be noted that industrial users are more likely to prefer EMATs, which are cheaper, simpler in design and environmentally more robust than interferometers.

3.1 Properties and Defects of Joints Adhesively Bonded by Epoxy Resins.

If two pieces of adherend material sandwiching an adhesive layer actually bond, they form an adhesive joint (Figure 3.1). DRA (Aerospace) use thermosetting epoxy adhesives, obtained from the manufacturers (Ciba Geigy) in large rolls of cold pressed resin, protected from contamination by polythene backing films which are removed prior to use. The epoxy consists of filler materials and long chain organic polymers which, as the adhesive melts under

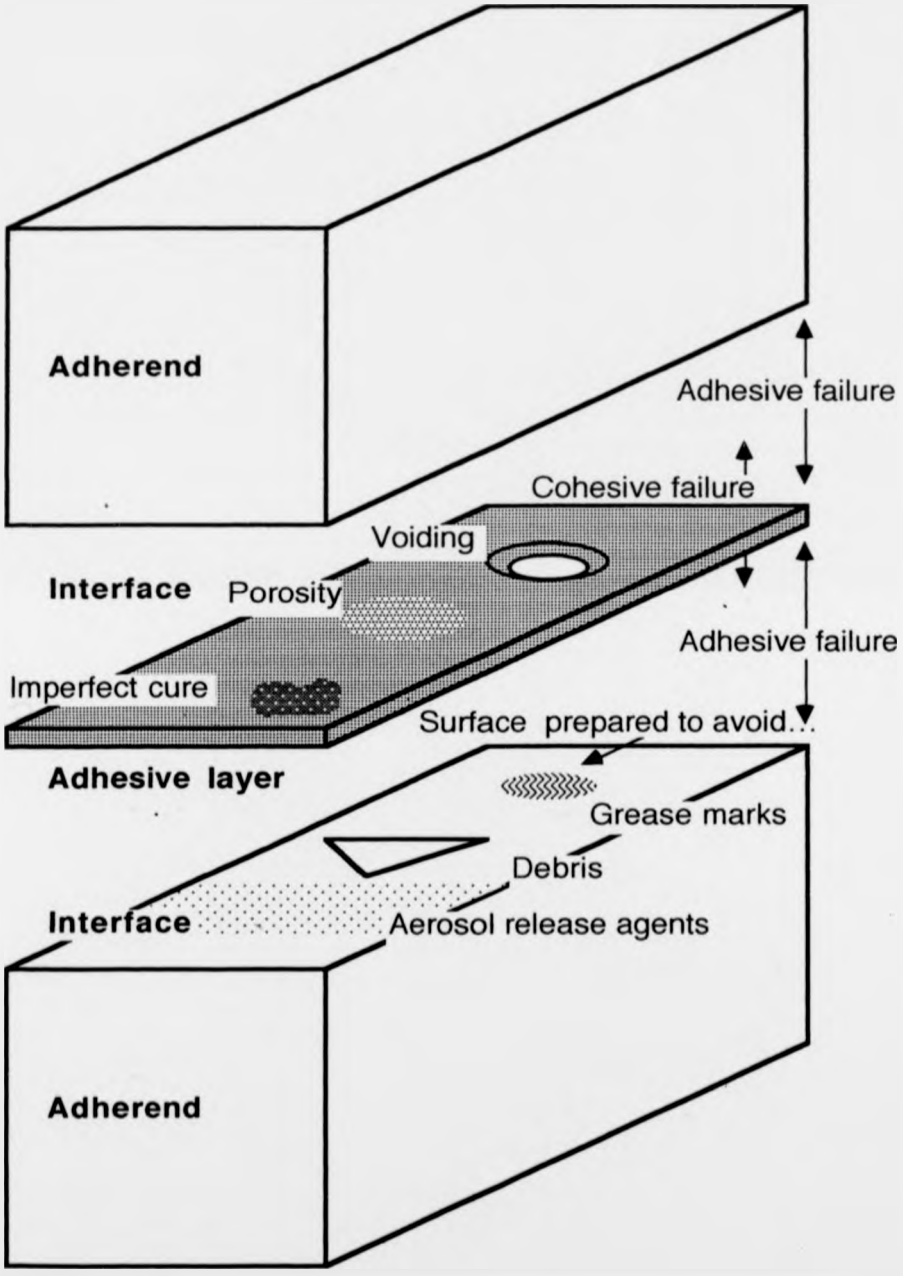

Figure 3.1 Illustration of a dissected epoxy bonded joint, typically with 1 to 50 mm thick aluminium alloy adherends and a 0.1 mm thick adhesive layer of CibaGeigy 312/5 epoxy.

pressure at cure temperatures between 100-200 °C, unwind and then cross-link extensively to form a glass. The resin is often pressed onto a woven polythene carrier which consolidates the prepreg (as precure epoxy is known). The DRA bonds had nominal 0.1 mm thick epoxy layers, set during cure by flanking the joint with blank adherends shimmed to the desired thickness, and relying on the carrier for a constant joint thickness under compression. The observed DRA bond thickness range is 0.05 - 0.25 mm. Variations occur because carrier is soft enough to deform under pressure, or may even be absent, so that edge thicknesses, where the shims lie, are regulated more closely than at the unsupported bond centre. Parallel wires, spaced at regular intervals along the joint, set the thickness more precisely, but disrupt bonds by providing a host of crack propagation sites.

Adhesive material is characterized by its cohesive strength, a measure of the stress needed to pull apart a bulk sample of the cured glue. Aerospace engineers prefer the strengths of joints, with known adherend properties and geometry, to be calculable from this cohesive strength alone. The best adhesives, however, must also bind strongly to the adherends they join. Weaknesses at the adhesive-adherend interfaces make cohesive failure within the epoxy less likely than adhesive failure, with low predictability, at its boundaries (Figure 3.1). In practice, the latter failure type is commoner and prevented only by elaborate preparation procedures (Appendix B.1). Cleaned and etched aluminium samples improve their adhesion properties when anodized to form aluminium oxide surface layers about 1 μm thick. Whether adhesion in aluminium-epoxy systems stems from chemical reaction at the epoxy alumina interface is still uncertain. Adhesives may only wet the adherend surfaces, forming weak hydrogen bonds, while the porous alumina provides tunnels which become impregnated with epoxy and form a physical key. Either way, increasing the oxide layer depth leads finally to the formation of brittle alumina columns, decreasing the adhesive strength. At the molecular scale, the interface is thus highly complex and the fundamental uncertainty as to the nature of adhesion plagues any attempt at nondestructive evaluation.

Review papers describe the commonest defect types encountered in adhesively bonded joints [Guyott et al., 1986; Adams & Cawley, 1988]. Starting with defects responsible for cohesive failure, the easiest to detect is voiding (Figure 3.1), a complete absence of adhesive

which occurs when the prepreg either fails to cover the entire bond area or traps an air pocket as it is laid out. Cohesive failure may also occur as a result of porosity, small bubbles in the adhesive caused by air, water or volatile constituents, which vaporize during the cure cycle. Moisture is a particular problem and great care is taken to keep both adherends and adhesive desiccated until fully cured. Although individual bubbles are too small to detect, their occurrence en masse can scatter ultrasound sufficiently to register on a detector. Partial cure, due to interruptions in the thermal cycle or inhomogeneity in the adhesive, and cracking due to thermal contraction are also liable to affect a large proportion of the epoxy and are observed where solitary defects would pass undetected. A void sited at one interface can induce adhesive failure, the so-called volume disbond. Adhesion problems, however, are more usually associated with bonds disrupted by pre-cure surface contamination. Thorough degreasing of the adherend surfaces is essential, to remove stray material, fingerprints or identifying crayon marks, and on an industrial production line even the use of aerosols will be strictly controlled. Surface contamination defects are notoriously hard to detect, even when severe enough to form zero-volume disbonds, where epoxy is in intimate contact with the adherend but not adhered. In practice, the epoxy will actually dissolve some surface contaminants when it melts during cure, so that the presence of releasing agents at the interface may result merely in the formation of a weakened epoxy layer. In this case bonding is good enough to transfer transverse acoustic waves across the interface, although adhesive failure will still occur at reduced loads. Defective bonding may also result from environmental attack, in particular moisture ingress from the joint edges. Water makes cured epoxy more plastic, thus reducing the strength of the joint, although its resistance to fracture may improve. Other chemicals may attack the interface by corroding the adherend surface. Adhesive strength can thus depend critically on the state of the bonding region's exposed perimeter, in particular the adhesive fillet, or frozen meniscus formed where the fluid adhesive escapes the joint edges during cure. Stresses applied to an adhesive joint are generally highest at the joint edges and the fillet reduces the stress gradients in these areas. The absence of fillet, or damage to it, significantly reduces the strength of a bonded joint.

Adhesively bonded joint strengths are ultimately defined in tests to destruction. Non-destructive testing, however, is widely used to infer bond strengths by detecting those defects described above which can significantly reduce the load-bearing capability of a joint. The main

problems in detecting bond defects are how to separate data relating to known adherend properties from those of the adhesive and how to distinguish the effects of defects from the variations in thin layer properties which arise normally when processing individual joints.

3.2 Non-Destructive Adhesive Bond Evaluation Experiments.

Any single technique is more responsive to some defect types than others, and the size and number of defects examined also determines their detectability. However the zero volume disbond and weakened adhesive layer are uniformly difficult to detect and reliable observation methods for these defects are needed if in-service monitoring of bonded joints is to be feasible. The task is made more difficult by the relative inaccessibility of an adhesive layer, which is protected from external influences by the adherends that it binds. X-Radiography, for instance, is totally ruled out because the epoxy layer is masked by the aluminium adherends, which absorb the radiation considerably better, although fibre reinforced composite components might be amenable to the technique. Passive thermography stands out as a possibility for employing pulsed lasers similar to those in this thesis, albeit as thermal rather than acoustic sources. Thermal imaging video cameras have detected transient 'cold shadows', on the opposite surface to the source, due to voids in 0.5 mm thick aluminium bonded samples [Guyott et al., 1986]. But the technique is more efficient in lower conductivity composites as the heat conduction rate limits the depth below the adherend surface at which a given size defect may be detected. More significantly, defects in which the adherend and adhesive remain in intimate contact conduct heat as well as their surroundings and pass undetected. Coin tap methods [Adams & Cawley, 1988] or sound probes, used to transfer acoustic energy at audible frequencies (< 20 kHz) into the joint without liquid couplants, are again most effective at detecting large voids in composites or disbonds in honeycomb structures.

However, ultrasonic frequency acoustics are commonly used for nondestructive evaluation of adhesive joints over the range 50 kHz to 50 MHz, corresponding in aluminium to longitudinal wavelengths between 10 cm and 0.1 mm or Rayleigh wavelengths from 6 cm to 60 μm. Reducing the wavelength increases the ability to resolve small features, such as porosity defects in the epoxy, but makes measurements increasingly difficult because ultrasonic attenuation damps the waves in correspondingly shorter distances. And as surface waves only

penetrate to depths comparable with their wavelengths. 100 MHz to 10 GHz acoustic microscope frequencies are useful only when examining adhesion properties of <1 μm thick layers [Weglein & Mal, 1987]. The studies in chapters 4 to 7 use ultrasonic pulses with DC to 30 MHz bandwidths. Optical manipulation of the laser beam controls the spatial character of laser generated ultrasonic sources, enabling enhancement of either shear or longitudinal wave components or production of directional Rayleigh-Lamb surface-travelling waves. Source and detector configurations in chapters 4 to7 are chosen to match arrangements commonly used for piezoelectric transducer investigations of bonded joints (Figure 3.2).

In the simplest, pulse-echo, test configuration a single transducer sends ultrasound and receives back on-epicentre reflections from either of the two adhesive-adherend interfaces or the bottom adherend surface (Figure 3.2.a). Since a generating pulsed laser does not act as an ultrasonic receiver (see section 3.3), a preferred arrangement is the on-epicentre through transmission configuration (Figure 3.2.b), which provides information complementary to the pulse-echo mode, extracted from transmitted rather than reflected ultrasound. Broadband transducers have distinguished individual bond layer reverberations in through transmission absorption and dispersion experiments on 0.3 mm thick epoxy layers [Challis et al., 1991] and in pulse-echo fatigue measurements on 0.8 mm thick adhesive bonds [Kline et al., 1986]. Narrow bandwidth transducers, however, cannot generally resolve multiple reflections between interfaces under 0.5 mm apart, requiring evaluation via the total reflection coefficient for a single set of reverberations within the layer [Fraisse et al., 1992] or spectroscopic analysis of the entire joint vibrational modes [Guyott & Cawley, 1988; Bresse, 1988]. Thickness or cohesive property fluctuations have indistinguishable effects on individual vibrational modes but affect each mode differently, allowing extraction of the most likely combination from a sufficiently wide range of modes. Correlating ultrasonic pulse-echo and destructive test results [Dickstein et al., 1988] also needs several features to attain a measure of predictability.

Immersion in water allows a longitudinal wave transducer beam to insonify the sample at arbitrary, non-normal angles to the adherend surface (Figure 3.2.c). Off-axis incident angle adhesion tests rely on the difference in reflection moduli for transverse waves impinging upon either smooth or welded boundaries, which is largest at specific angles determined by the

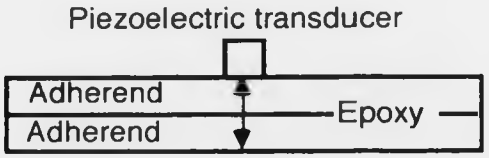

a. Pulse-Echo configuration.

b. Through transmission configuration.

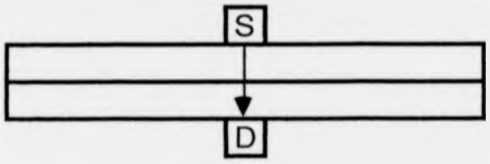

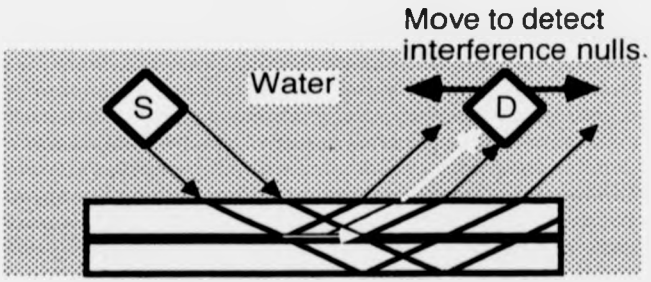

c. Pitch-catch arrangement for Leaky Lamb waves (white arrows), seen in immersion tank interfering with specular reflections (black)

d. Surface-interface-surface travelling (SIST) wave passing under bonded interface (shaded) region to wedge transducer detector D

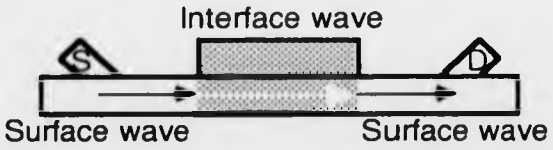

Figure 3.2 Display of various source and detector configurations used in the ultrasonic evaluation of adhesively bonded joints. S = source. D = detector.

material combination [Pilarski et al., 1988; Pilarski & Rose, 1988]. Similar experiments, without immersion, are possible with laser generation but the source directivity must be included. Oblique incidence ultrasound aimed at critical angles to thick composite plate surfaces has been used [Pilarski & Rose, 1989] to initiate subsurface waves, travelling at the longitudinal velocity, which are sensitive to subsurface defects or changes in the material's elastic constants. Critical angles, also located in dry experiments with hemispherical adherends [Hsieh & Rosen, 1993], initiate "leaky Lamb" decaying interface waves, which propagate along the adhesive joint length. Ultrasound leaked into the water interferes with the reflected waves (Figure 3.2.c), giving a characteristic null in the received beam. Changes in the interfacial wave alter the level of interference observed by the receiver with sufficient sensitivity to detect zero-volume disbonds at a steel-epoxy interface [Teller et al., 1988]. Composite plates with total thicknesses less than the relevant ultrasonic surface wavelengths support Lamb-like plate waves, which also radiate acoustic energy into the surrounding water [Chimenti & Martin, 1991]. Such waves have large displacement components parallel to the adhesive interfaces and are thus particularly sensitive to delaminations within composites, which decouple all layers lying below the laminar defect and give plate waves characteristic of a thinner plate. All these leaky Lamb methods use ultrasound propagating short distances along the adhesive layer, making the measurements approximately local.

Leaving the immersion tanks, if the source and detector are moved further apart ultrasound can probe longer joint sections (Figure 3.2.d), a non-local approach which reduces test times at the expense of precise defect location. Horizontally polarized shear and Lamb waves, generated and detected by electromagnetic acoustic transducers (EMATs), have been used to study adhesively bonded joints [He et al., 1988]. On thicker samples, free-surface waves travelling on one adherend mode-convert, upon reaching the adhesive fillet, into interface-parallel layer waves (chapter 2.5), which reconvert to surface waves after exiting the layer at the opposite end, and are then detected [Rokhlin et al., 1980 & 1981]. As interface-parallel layer waves excite particle motion both parallel and normal to adhesive interfaces, the combined surface-interface-surface travelling (SIST) waves are highly sensitive to adhesion changes along bond layers. Velocity variation between samples is easily masked by changes in alloy and epoxy composition, or in surface finish due to previous treatment. On individual samples, however, 0.5 MHz wedge

transducers have detected adhesive property changes during cure [Rokhlin, 1983], which correlate with the bond strength. Unfortunately, though cure monitoring is useful for process control during bonded joint manufacture, measuring in-service degradation remains a problem.

3.3 Producing a Laser-Generated Acoustic Source.

Lasers have attracted serious attention as ultrasonic sources in metals [Scruby et al., 1982] despite the disadvantages of costing more than conventional transducers, tending to cause damage and needing separate, sensitive detectors. One reason is that Q-switched lasers fired at metals produce exceptionally broad bandwidth ultrasonic pulses, with 10 ns rise-times or less. But laser generation's unique feature is its total remoteness from sample surfaces. This drastically reduces variability between observations, and even enables measurements to be made in harsh environments too hazardous for direct contact methods [Dewhurst et al., 1988].

Laser wavelengths used to generate ultrasound in metals most commonly lie in the far red, or near infrared, bands: our 1064 nm Nd:YAG lasers are typical. When a beam of electromagnetic radiation hits a metal surface, photons are absorbed by conduction electrons within distances in the metal of the order of the classical skin depth. Most photons are rapidly reemitted to form a reflected beam and the remaining energy dissipates into the metal via electron collisions. For 1064 nm ($f = 2.82 \times 10^{14}$ Hz) radiation on aluminium, which has conductivity $\sigma \approx 38$ MS m^{-1} and permeability $\mu \approx 4\pi \times 10^{-7}$ H m^{-1}, the classical skin depth $\delta = [\sqrt{\pi \sigma f \mu}]^{-1} = 4.9$ nm. Thus, although aluminium reflects about 90% of 1064 nm radiation, high intensity laser beams still deposit substantial energy into a small region of metal. Early studies of the effect [White, 1963; Ready, 1965] show surface temperature rise-times comparable with those of the laser pulse intensity. Rapid thermal diffusion into the metal is also seen, and depths of several microns reach the surface temperature within the 10 ns timescales of laser pulses. However, compared with liquids or transparent media (see Figure 3.3), laser interaction with metals is very much a surface effect and, as long as the shape of the illuminated area is not significantly altered, energy deposition is insensitive to the laser beam angle of incidence. An alternative mechanism explains the transfer of laser energy into ultrasound in metals with near perfect reflectivity (Figure 3.3.c), such as aluminium at 10 μm CO_2 laser wavelengths [Taylor,

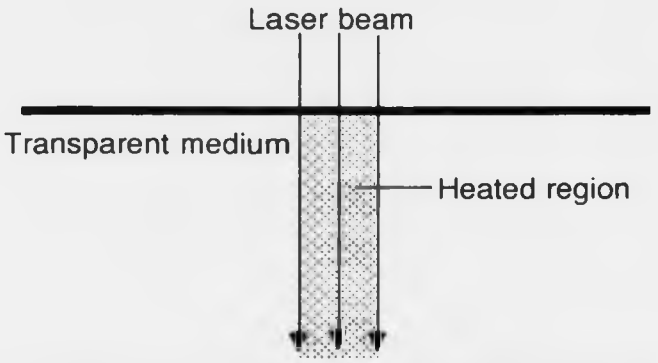

a. Absorption of laser energy in transparent material.

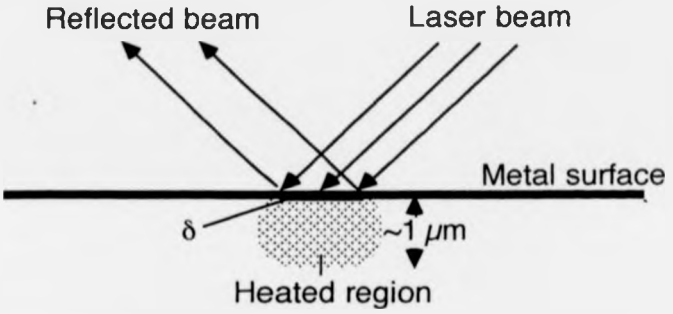

b. Absorption of laser energy by metal.

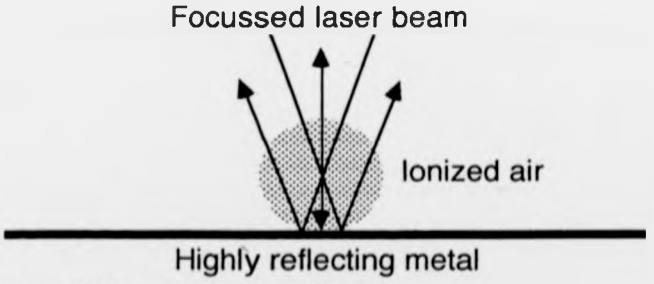

c. Air breakdown at focus of laser beam.

Figure 3.3 Illustration of the effect of laser beams impinging upon different surfaces.

1990]. Radiation, reflected to a focus just above the metal surface, is sufficiently intense to cause impurity-seeded air breakdown, generating a plasma which pushes against the surface to create an ultrasonic pulse. Generation of this kind is not studied here, but foci before the incoming laser beam hits the metal, including accidental back reflections off convex surfaces, can cause local air breakdown and are thus avoided throughout.

Having established the mechanism by which laser energy enters the metal, the next problem is to define the form of the acoustic source. Before this, however, it is worth describing the particular apparatus which I used. Laser pulses at 1064 nm were generated by a Spectron Laser Systems SL401 Nd:YAG laser, operating in Q-switched mode using a type PCA/18/82 Pockels cell positioned within the laser cavity. A multimode configuration was used, producing an unfocussed beam of 3 mm diameter (measured on polaroid burn-paper) with an asymmetric intensity distribution. For single-shot operation, the laser repetition rate is set at 1 Hz, giving a maximum pulse energy of 120 mJ and pulse width of 10 ns. For some of the measurements a Lumonics Hyperyag HY400 Nd:YAG laser was used. This also operated multimode, having a 200 mJ pulse energy and 4 mm diameter beam with annular intensity distribution. Unfocussed, the lasers thus provide fluxes of 170 MW cm $^{-2}$ and 160 MW cm^{-2}, respectively, at the test surfaces and the slight differences in beam shapes are not discernible from the ultrasonic waveforms observed. Considerable changes in the ultrasonic waveforms are seen, however, when optics are used to change the energy, power density or spatial appearance of the laser beam. In a typical arrangement (Figure 3.4), the beam passes through an expanding lens and is then focussed to a line by the cylindrical lens. This configuration is frequently used when generating surface waves, as line sources produce strongly directional radiation [Aindow, 1986]. Such waves would be picked up by a detector placed some distance away on the same surface. A more symmetric source results when using a spherical lens in place of the cylindrical, either enhancing the laser spot power density by settling the point of focus on the sample surface, or reducing it by focussing beneath. Section 3.2 has already mentioned the laser requirement of a clear line of sight to metal surfaces, effectively precluding the pulse-echo arrangements common with piezoelectric transducers. Attempts to avoid this problem, using EMAT detectors with a central hole, still encountered trouble with ringing because of receiver proximity to the laser blast [Hutchins et al., 1991]. Thus, within the bounds of this thesis,

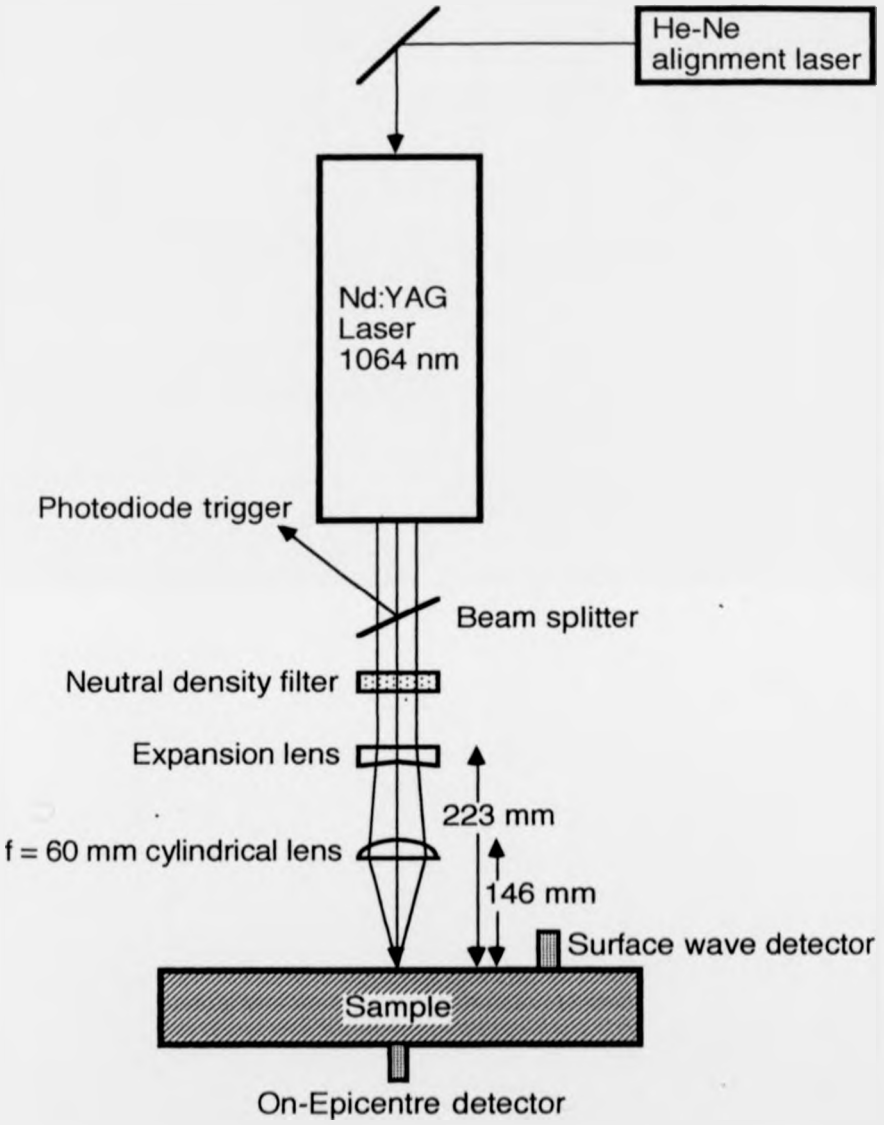

Figure 3.4 Schematic diagram of experimental laser arrangement for generating ultrasound in metals.

"on-epicentre" measurements are always taken, send-receive fashion, on the surface of the sample opposite the laser source.

Neutral density filters reduce the energy at the surface, and hence the amplitude of the generated ultrasound. Varying the surface power density can greatly alter the ultrasonic waveforms, as seen in a series of on-epicentre measurements made with a Michelson interferometer on a 9.90 mm thick block of milled aluminium (Figure 3.5). Work in the 1980s concentrated upon the characterization of acoustic sources and the various mechanisms behind them. Unlike piezoelectric transducers, lasers generate longitudinal, shear and surface-travelling acoustic modes simultaneously [Ledbetter & Moulder, 1979]. Amplitudes of these modes have been shown to depend on the laser pulse energy as well as power densities at the metal surface [Aindow et al., 1980; and 1981]. At absorbed power densities up to about 10 MW cm^{-2} (incident ~100 MW cm^{-2}), the laser energy suffices only to heat up the volume of metal into which it is absorbed, resulting (see Figure 3.6.a) in the thermoelastic source. The metal, to a first approximation, expands freely normal to the surface, at which stresses vanish, but is constrained in the surface plane by cooler surrounding material, leading to a source which acts like a surface dipole [Rose, 1984]. Such models of broadband, on-epicentre waveforms predict the initial negative step (away from the interferometer, towards the source) marking the longitudinal (P) arrival (Figure 3.5.a), followed by a positive step at the shear (S) arrival. In fact a source of finite depth, which appears when thermal expansion is taken into account, can sustain some stress normal to the surface. This is the probable cause for a small positive-going pulse often observed just prior to the P arrival, but not accounted for by theoretical calculations using point surface dipoles alone [Doyle, 1986; McDonald, 1990].

As the incident power density increases above about 150 MW cm^{-2} the metal absorbs enough energy for the surface to vapourize, material boils off steadily throughout the laser pulse duration and a plasma briefly forms above the surface (Figure 3.6.b). The expanding plasma exerts pressure on the metal surface, creating normal stresses which enhance the longitudinal and Rayleigh modes in the acoustic waves, with respect to the shear [Dewhurst et al., 1982]. The positive precursor to the longitudinal arrival thus becomes progressively larger in amplitude until it dominates the waveform (Figure 3.5.b). This weak ablation regime is the

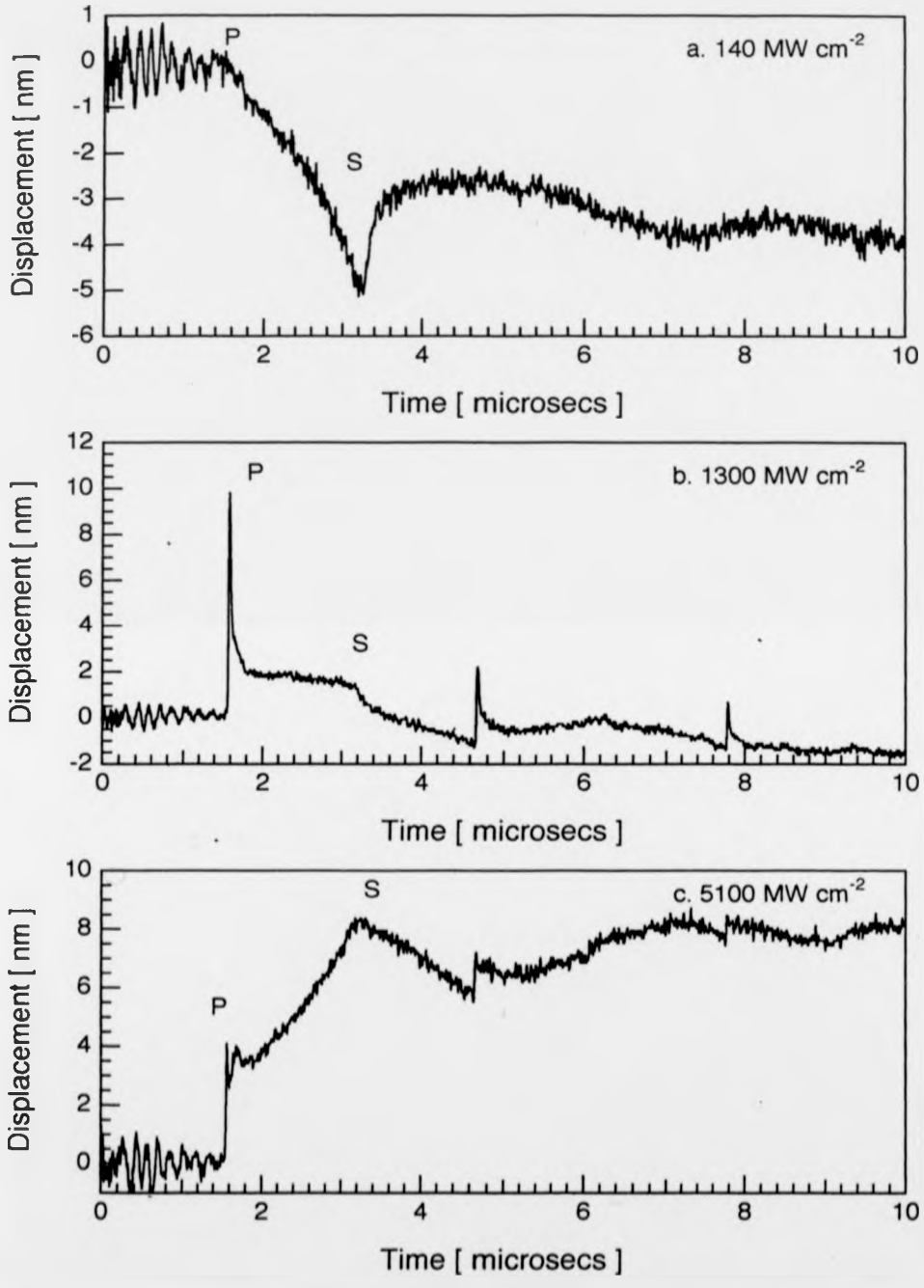

Figure 3.5 On-epicentre through transmission measurements on 9.9 mm thick aluminium with rough milled (±0.2 mm) surface. a). Thermoelastic source, b). weak ablation source, c). strong ablation (dense plasma) source.

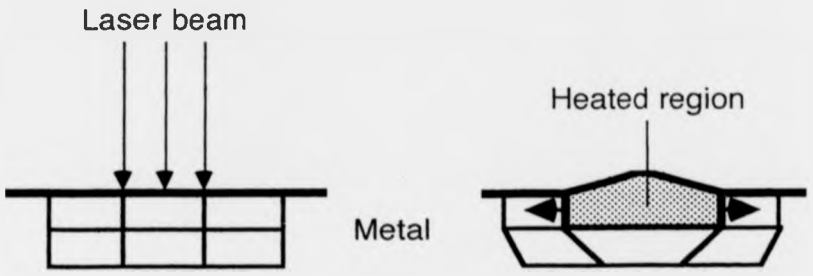

a. Thermoelastic regime. Expansion of heated region in metal causes stresses mainly in the plane of the surface.

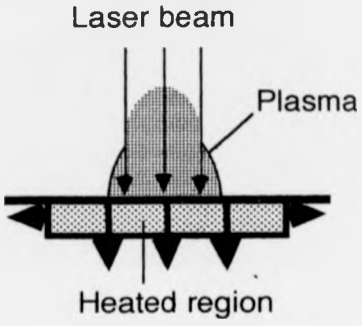

b. Weak plasma regime. Ablated material causes a piston-like recoil, which lasts a similar time to the laser pulse.

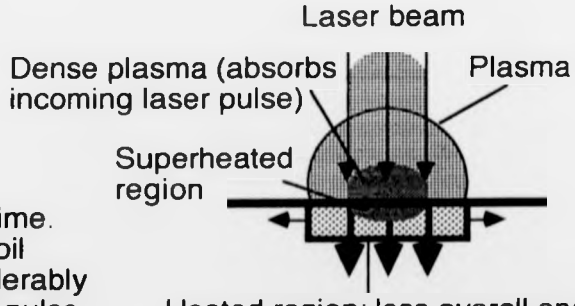

c. Dense plasma regime. Ablation causing recoil stresses lasts considerably longer than the laser pulse.

Figure 3.6 Illustration of the laser-generated ultrasonic sources that are associated with different laser beam power density regimes.

most useful for displacement-based observations as the surface normal source provides a large amplitude single pulse, modifications to which are easily discernible. As the power density increases, so does the depth of metal heated to vapour temperatures, and rapid boiling of the surface creates a much denser plasma, which blocks the laser radiation above the metal surface (Figure 3.6.c). The amount of energy due to thermal expansion at the surface is thus reduced, and the shear and longitudinal wave amplitudes decrease. However, the effect is partly offset in the longitudinal arrival [Aindow et al., 1981] by the increase in pressure on the surface due to the raised plasma energy. At the end of the laser pulse, the dense plasma begins to cool, lowering the vapour pressure above the surface, which thus continues to boil at steadily lower temperatures long after the laser pulse ends. The result is a normal stress source which is more Heaviside step than delta-function [Hutchins et al., 1981a]. Such a source has already been examined in the context of seismology [Knopoff, 1958], and the resultant on-epicentre strong plasma waveforms can be seen to resemble the integrated weak plasma results (Figures 3.5.b.&c).

A comparison of Rayleigh waves generated by line and point sources under thermoelastic and plasma conditions is shown (Figure 3.7), using data taken by Dr. C. Edwards using a Michelson laser interferometer [Edwards et al., 1991]. The low amplitude arrival travelling at approximately twice the Rayleigh velocity is the surface-travelling P-wave: in the thermoelastic traces it becomes lost in the noise. Once again the effects of changing laser power density can be seen in the plasma source enhancement of the first positive peak in the Rayleigh wave [Scala & Doyle, 1989]. The difference in arrival times results from sample repositioning to avoid generation on the ablation-damaged region. For true non-destructive testing, the thermoelastic regime is mandatory. However, damage on thick aluminium is slight: a focussed line might be 40 mm x 47 μm (±1%) in area and about a micron deep, easily removed with Brasso™. The primary problem in this thesis is to identify what exactly can be seen by laser ultrasonic probing of adhesive bonds, and for this the greater amplitude ablation sources have been invaluable in creating broadband ultrasonic pulses with nm amplitudes and rise-times of the order of 10 ns (frequency components from DC to 30 MHz, with most of the energy propagating at frequencies below 5 MHz). Sizeable amplitude surface-travelling waves may also be generated on thin specimens [Hutchins et al., 1989] as described in chapter 5. Generation mechanisms are identical, but the low mass per unit area of foil means that thermoelastic sources give ample

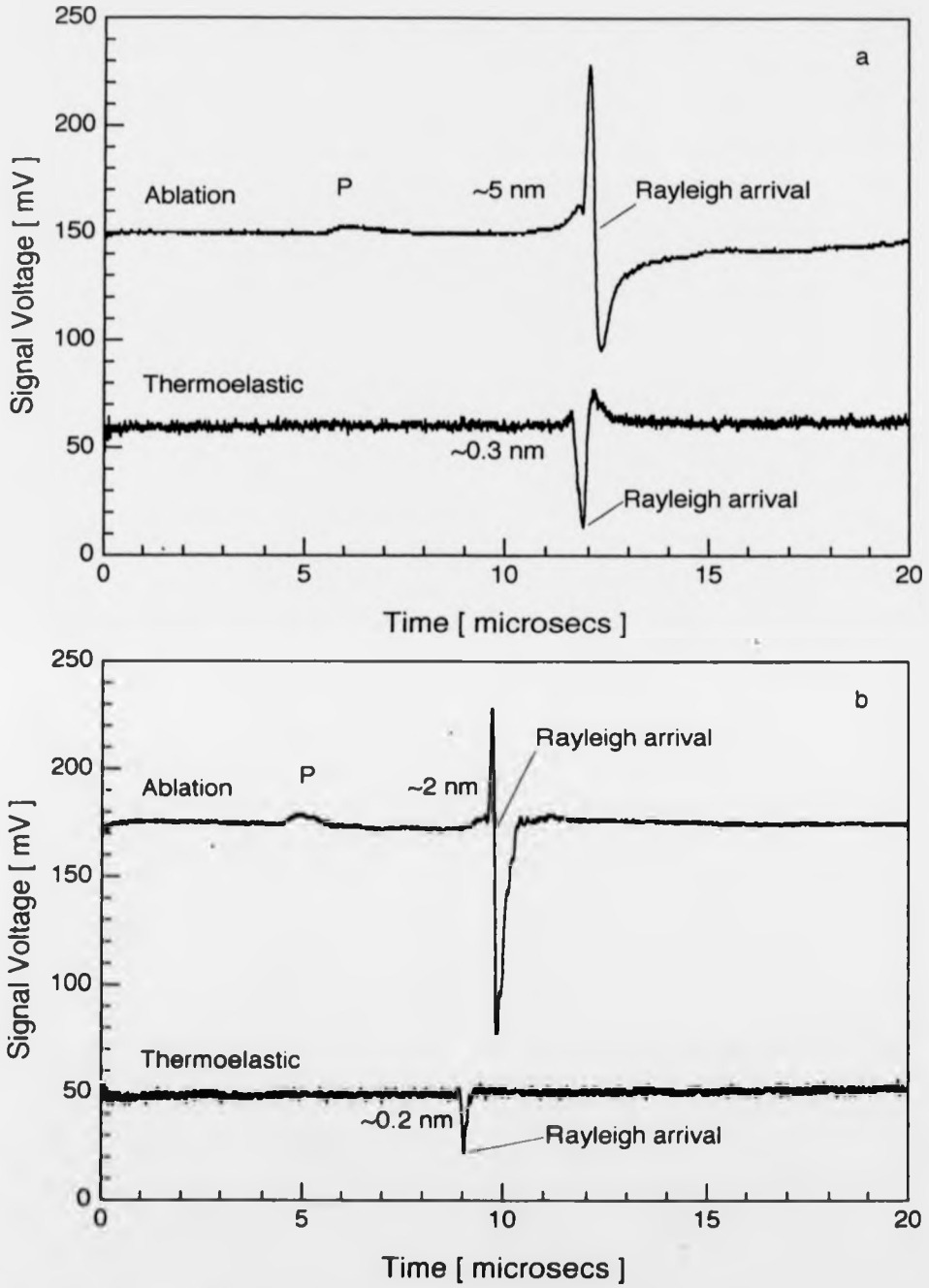

Figure 3.7 Surface-travelling Rayleigh and sub-surface longitudinal (P) arrivals on aluminium, detected by interferometer. a). Laser point source, b). laser line source. From Dr. C. Edwards [Edwards et al., 1991]

ultrasonic signals. Indeed, strongly ablating sources not only produced saturation problems with our detectors, but deposited enough energy to punch holes in the thinnest samples.

In general, however, the thermoelastic source generates low amplitude, and thus extremely noisy, waveforms although features known to exist from ablation measurements may still be identified by averaging or other enhancement procedures. An alternative, when even minor damage to the sample surface is unacceptable, is to try to enhance the source amplitude without plasma creation. One way is to use constraints on the surface, which have been shown to improve signal amplitudes [von Gutfeld & Melcher, 1977; Hutchins et al., 1981b] in one of two basic ways. A transparent, inflexible slide placed on the surface removes the free surface condition and allows the buried source to produce longitudinal waves. Alternatively, a thin liquid or solid coating is applied to the surface, from which it is thrown or ablated by the impacting laser pulse, to feed a weak plasma that contains coating rather than surface material. Surface coatings, such as spit, oil or paint, increase amplitudes without destroying surfaces but they are less useful for standard measurements as successive laser pulses remove the coating and result in shot-to-shot changes in the source. Another way in which surface wave amplitudes have been enhanced is by scanning the source parallel to the surface at the same velocity as the surface wave [Dan'shchikov, 1987]. Such methods may be used to enhance both Rayleigh and Lamb modes [Yamanaka et al., 1991a&b], producing monodirectional waves. Amplification of the surface wave preserves the thermoelastic appearance but is, in practice, limited by the length of surface over which a scan can be maintained. As an added advantage, high power laser pulses are not required (ms durations for a 1J pulse were quoted). Savings on the laser cost, however, are offset by the need for relatively complicated rotating mirror arrangements to produce scanning speeds in the 3000 m/s Rayleigh velocity range, calibrated to accuracies of a few per cent. Such systems offer damage-free, laser generation of relatively high (~1 nm) amplitude surface waves, but need further refinement to be of widespread use in nondestructive testing.

I have generally used ablating sources, to minimize problems with noise and avoided constrained sources to maintain repeatability. Chapters 5 and 7 use focussed line sources for surface wave generation, chapter 4 focussed point sources for through thickness measurements

observed on-epicentre. The most interesting source, described in detail in chapter 6.2, uses optics to create a spatial periodicity in the laser intensity at the surface and impose a periodicity on the acoustic surface wave. For truly non-destructive evaluation, ablation sources cannot be used but signal amplitudes may be maintained by following one of the alternative directions described above.

3.4 Detecting Laser-Generated Ultrasound without Surface Contact.

For a group which has invested in the optical technology required for laser-generated ultrasound, the natural progression is towards a compatible optical detection technique, retaining the remote, non-contacting, broad bandwidth and accurate positioning qualities of the source. Measurements of laser-generated ultrasound have been made with thick piezoelectric ceramic transducers [Dewhurst et al., 1983], gaining broad bandwidth at the expense of sensitivity with respect to the commoner resonant piezoelectric transducers. But such transducers, though relatively unaffected by degradation of a surface, do require acoustic coupling to the sample, with all the problems of contact that this entails. Thus non-contact detectors are preferred, though the current alternatives, even on the most highly polished, optically flat surfaces, still have less than a tenth of the sensitivity of broadband transducers.

There are several non-contact methods of wideband ultrasonic signal detection [Dewhurst et al., 1987]. Capacitative transducers use the changing capacitance of a charged metal plate positioned close to a conducting sample to measure normal surface displacements. These transducers have the advantage of output linear with displacement, offset by a need for conducting samples and, because of the critical signal dependence on micron source-to-detector distances, optically flat surfaces. The situation is improved with small detection area, spherical probes [Cooper, 1985; Cooper et al., 1986] but capacitance transducers, though non-contacting, are certainly not remote. The same is true for electromagnetic acoustic transducers (EMATs), which are described in detail in a later section. EMATs are eddy current devices, and hence need conductors on which to operate, but they do not require polished surfaces as they can tolerate millimeter surface standoffs. This makes them easier to use than capacitance transducers, with the added advantage that EMATs can detect motions both parallel and normal to the surface plane. Although EMATs are simpler in concept than optical detectors, the signals

produced by an EMAT depend upon its magnetic field configuration and the rate of change of sample surface displacements, making them more difficult to predict. I am thus deferring detailed discussion about EMATs until I have dealt with optical detectors, easily the most remote, and often the most point-like, of the non-contact transducers.

For solid, opaque materials the range of optical techniques available has been comprehensively reviewed [Monchalin, 1986; Scruby & Drain, 1990], with the bulk of attention directed towards detection using interferometry. The simplest non-interferometric technique is to use an expanded laser beam incident nearly normal to the surface and observe the resulting diffraction pattern. Continuous wave ultrasonic displacements create a moving surface grating, producing diffraction peaks that are only sharp when the beam diameter overlaps a large number of grating elements. This requires a long ultrasonic wavetrain and makes the technique unsuitable for the single-shot, laser ultrasound pulses used in this work.

The non-interferometric technique most suitable for pulsed work relies on the deflection of a tightly-focussed laser beam reflected off a highly-polished surface. In the simplest variant a cylindrical lens expands the beam, which has a Gaussian intensity distribution, into a line parallel to the path of deflection, and a photodiode placed in the beam wing detects the intensity changes as the beam moves [Sontag & Tam, 1985]. Alternatively, a detector receiving half of the undeflected beam, part-blocked by a knife-edge, will monitor a change in intensity when the beam is deflected by surface deformation [Noui & Dewhurst, 1990]. The effect is enhanced if the knife-edge detector is replaced by a split photodiode, with output from each half fed into a differential amplifier, placed to give a null reading for the flat surface. Beam deflection is particularly useful on a thin, transparent sample, when the output from an interferometer is complicated by components in the sample beam reflected from both the front and back surfaces.The detector is only linear for small angular deflections and thus represents large but slowly varying wave-forms more accurately than it does low amplitude, short rise-time arrivals. In this respect it complements the Michelson interferometer, which is strictly linear only for small displacements, and given the similar sensitivities of the two, is probably the better detector for aluminium foils below 500 μm thick. I opted for an interferometer as my studies of aluminium bonded joints have concentrated on measuring displacements of somewhat thicker samples.

Interferometers exist in a variety of different combinations, designed for in-plane displacements [McKie & Wagner, 1988], holographic filtering [Aharoni et al., 1987] or otherwise enhanced suitability to industrial environments [Monchalin, 1986; Scruby & Drain, 1990]. However, for sample surfaces polished optically flat and examined under low vibration, relatively clean, laser laboratory conditions, quoted sensitivities of the various interferometers are all within an order of magnitude. Under such circumstances, the most obvious choice is the simplest, and modified Michelson interferometers also have the advantage of being portable and, most importantly, of giving easily calibrated output which is linear with the displacements that I wish to observe.

3.5 Modified Michelson Laser Interferometers as Ultrasonic Transducers

Critical to the interferometer performance is the choice of laser, which determines both the operating frequency of the device (many components must be anti-reflection coated) and also the power available. In early experiments, the version of Michelson interferometer [McKie, 1985] which I used contained a 5 mW Hughes He-Ne laser, providing a multimode beam of continuous wave radiation around 632.8 nm, and thus required mirror-quality sample surfaces to return sufficient light amplitudes. Construction within the group of a more sensitive interferometer followed the recent commercial availability of the Adlas 300, a compact, high power, diode-pumped Nd:YAG laser producing 90 mW continuous wave, visible (532 nm) radiation via frequency-doubling optics located in the laser cavity. Aluminium surface displacements have been measured with the 90 mW laser version of the Michelson interferometer, after only rudimentary surface preparation. The waveforms of Figure 3.5 were obtained with this device off an unpolished, milled aluminium surface, which is flat but covered in fine circular grooves, approximately 0.1 mm deep, aligned along the path of the milling tool. Single-shot waveforms generated, using similar laser power densities, on polished and "off the shelf" extruded aluminium blocks are compared (Figure 3.8). A clear signal is detected by the Adlas interferometer on the poor surface, and could easily be enhanced by averaging, but direct comparison with the He-Ne interferometer is not possible, as the latter would not stabilize in the absence of sufficient return signal from the sample surface. The modified Michelson interferometer bears a detailed description, along with a brief outline of the new laser.

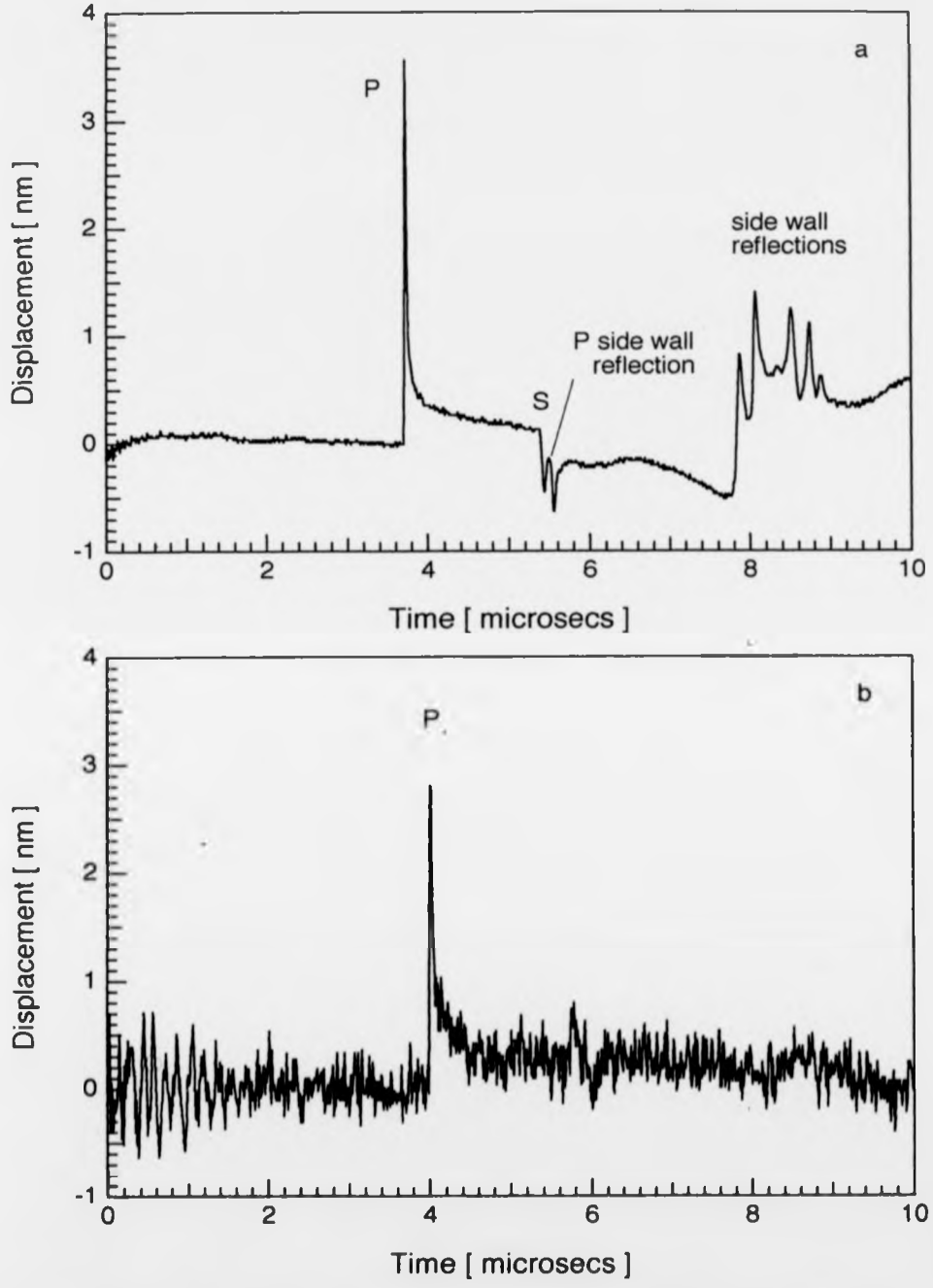

Figure 3.8 Adlas interferometer observations of on-epicentre through transmission weak ablation arrivals on 25 mm thick aluminium. a). Polished sample (25 mm wide). b). Rough unpolished sample (75 mm wide).

The Adlas 300 Nd:YAG laser rod (Figure 3.9) is pumped by a diode laser with an emission wavelength sensitive to changes in temperature, enabling factory tuning of the diode wavelength to one of the Nd ion absorption bands. The highly divergent diode laser beam is focussed onto the laser rod, which emits 1064 nm radiation that builds up in the laser resonating cavity between Mirrors 1 and 2. Above a threshold intensity, the non-linear frequency-doubling process activates and light at 532 nm, which is less highly reflected by the mirrors, can escape through the collimating Lens 2. Any 1064 nm radiation which escapes Mirror 2 will have been diverted by the frequency-doubling optics and can be stopped by the aperture. The emerging beam has a divergence of 1 mrad and, because only the highest energy temporal mode is selected by the non-linear frequency-doubling process, contains linearly-polarized radiation in a single spatial (TEM_{00}), single longitudinal mode.

The interferometer arrangement is much the same for either laser. Optical feedback from the interferometer into the laser cavity is eliminated through the use of polarizing optics [Scruby & Drain, 1990]. A polarizing cube beam-splitter divides the polarized laser beam, which is first rotated by a half-wave plate, adjusting the relative amplitudes of light in the two arms to optimize the signal-to-noise ratio for differing quality sample surfaces. On highly-polished surfaces the interferometer is operated using a neutral density filter, despite a diminution of sensitivity under stabilization, to avoid saturated amplifier circuitry in the unstabilized interferometer. The quarter-wave plates ensure that light, returning back along the two interferometer arms after reflection at the ends, will be polarized orthogonally to the outgoing light, and thus directed onto the photodiodes by the beam-splitter cube.

The interferometer detects displacements, normal to the sample surface, averaged over the area of surface under the light beam. In order to resolve fine spatial detail on the acoustic waveforms, it is thus necessary to focus the laser spot as tightly as possible at the ends of the two arms. This is achieved with two f = 160 mm anti-reflection coated lenses (Lens 3) placed at 160 mm from the sample surface and reference mirror respectively. The spot size achieved in this way is of the order of 25 μm. Oscillations of the sample at frequencies below 700 Hz, resulting from ambient vibrations, are stabilized by a feedback loop from the detector amplifier to a Ling V101 electromagnetic vibrator upon which the reference mirror is mounted. The

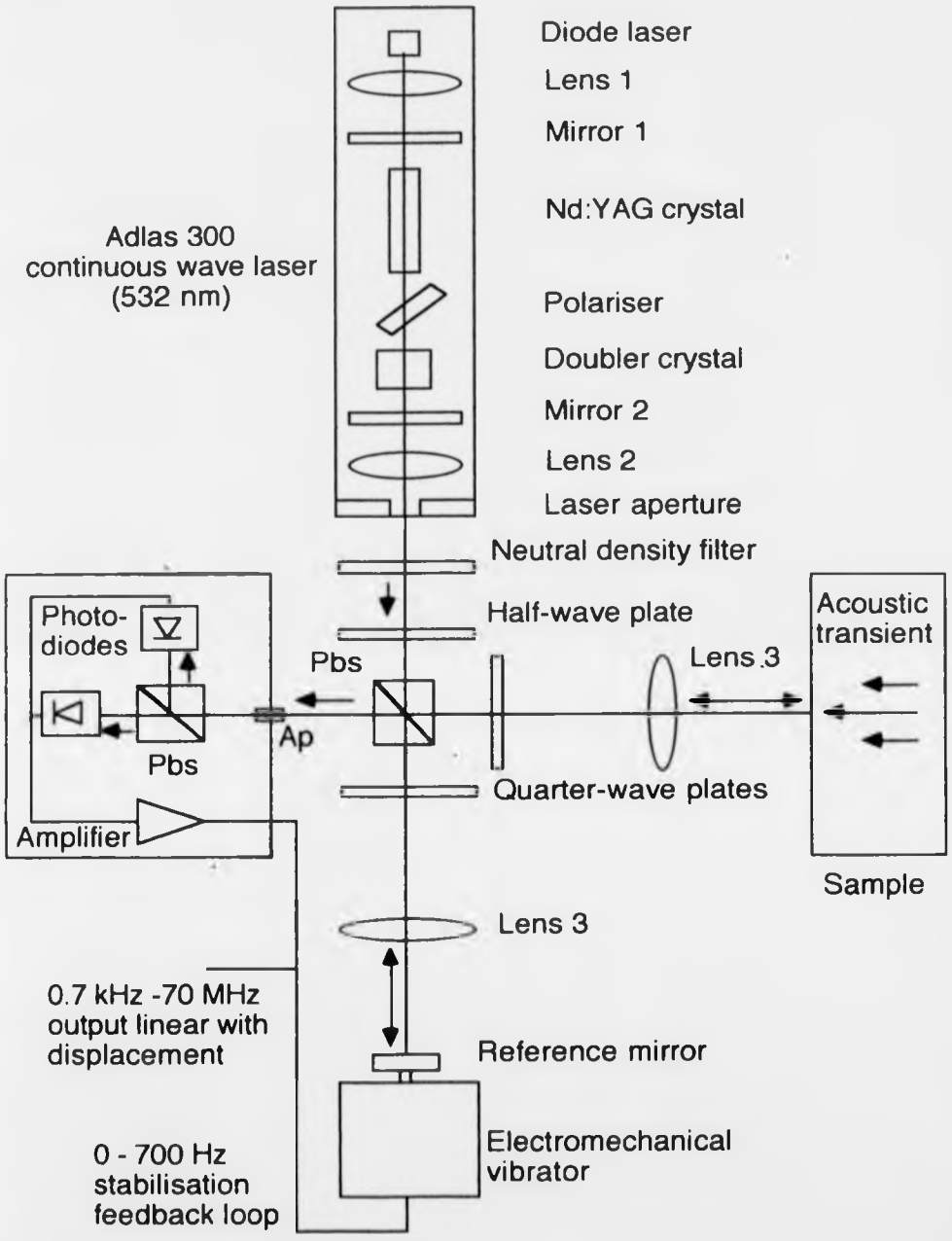

Figure 3.9 Schematic diagram of Michelson interferometer built with ADLAS 300 laser. [Pbs. = polarizing beam-splitter cube, Ap. = aperture].

stabilization point is chosen to maximize the region over which interference intensity is linear with surface displacement, and connections to the vibrator are adjusted to give a positive signal for small movements toward the interferometer.

The bandwidth for the system is limited at low frequencies by the feedback stabilization loop. The 1 ns rise-time of the BPX65 pin-photodiode detectors, combined with a 3 ns rise-time in the Comlinear CLC103AI amplifier circuitry, determine a high frequency limit of the order of 70 MHz, with 4 ns rise-time. The photodiodes are chosen to have as small an area as possible, in order to minimize the rise-time, and operated in a balanced configuration to minimize the effects of intensity modulations on the laser beam. Light arrives through the aperture in a pair of linearly and orthogonally polarized beams and passes through a second cubic polarizing beam-splitter angled at 45° to the polarization planes, which interferes the incoming light and channels the resultant beams onto the two photodiodes. Their subtracted and amplified output is captured on a Lecroy 9400 digital storage oscilloscope.

Assuming that light passing through the aperture contains orthogonal electric field components $E_{R0}\, e^{i(2\pi\nu t + \phi)}$ and $E_{S0}\, e^{i(2\pi\nu t + \psi)}$, reflected from reference mirror and sample, it is possible to calculate the resultant fields, E_+ and E_-, at detectors receiving light from a second cube beam splitter at an angle α to the incoming beams.

$$E_+ = (E_{R0} \cos(\alpha)\, e^{i\phi} + E_{S0} \sin(\alpha)\, e^{i\psi})\, e^{i 2\pi\nu t} \qquad \ldots 3.5.1$$

$$E_- = (E_{R0} \sin(\alpha)\, e^{i\phi} - E_{S0} \cos(\alpha)\, e^{i\psi})\, e^{i 2\pi\nu t} \qquad \ldots 3.5.2$$

$$\therefore \quad |E_+|^2 - |E_-|^2 = E_{R0}^2 \cos(2\alpha) - E_{S0}^2 \cos(2\alpha) + 2\, E_{R0} E_{S0} \sin(2\alpha) \cos(\phi - \psi) \qquad \ldots 3.5.3$$

For the beam-splitter angle $\alpha = 45°$, the two static terms on the right should vanish. In practice the two photodiodes are not identical but their positions can be adjusted to obtain optimum cancellation. Thus, if $E_T^2 = |E_+|^2 - |E_-|^2$ and taking intensity $I \propto E^2$,

$$I_T \approx 2 \sqrt{I_{R0}}\, \sqrt{I_{S0}} \cos(\phi - \psi) \qquad \ldots 3.5.4$$

Maximum sensitivity occurs for small sample displacements x, (giving path difference 2x)

about positions at which $I_T = 0$. Thus for a stabilized system $\psi = \phi - 2\pi\,(1/4 + \text{integer} - 2x/\lambda)$ where λ is the interferometer laser wavelength. For photodiode voltages $v \propto I$, the interferometer output is calculated as

$$v = (V_p / 2) \sin(4\pi x / \lambda) \approx V_p (2\pi x / \lambda) \qquad \ldots 3.5.5$$

where V_p = the peak to peak output voltage of the unstabilized system.

The sensitivity v/x is thus proportional to V_p, the maximum peak to peak voltage variation as the interferometer beams move in and out of phase, and will drop when a lower laser power, or deterioration in surface reflectivity, decreases the intensity of light reaching the photodiodes.

The displacement noise level is the ratio of measured voltage noise to the sensitivity, but it can also be estimated theoretically [Scruby & Drain, 1990], assuming that the minimum detectable signal occurs for a displacement x_{min} such that the voltage v_{min} or current i_{min} equal their corresponding noise values.

$$\Rightarrow \quad x_{min} = \frac{\lambda\, v_{min}}{4\pi v} = \frac{\lambda\, i_{min}}{4\pi\, i} = \frac{\lambda}{4\pi}\,\frac{\sqrt{(2\,h\,\nu\,\Delta f)}}{\sqrt{(\eta\, W_L)}} \qquad \ldots 3.5.6$$

where, a laser of power W_L, wavelength λ and frequency ν hits a detector of efficiency η for a time Δt (having an associated bandwidth $\Delta f = 1/2\Delta t$). h is Planck's constant.

A highly reflecting surface is implicitly assumed, so that the full laser power hits the detectors: rough surfaces scattering radiation into uncorrelated speckles create extra noise. The minimum displacement theoretically detectable due to the effect of laser noise is thus inversely proportional to $\sqrt{W_L}$. By comparison, the rms noise of the stabilised system measured a steady 1.1 (±0.1) mV on the oscilloscope when the interferometer laser power was varied with neutral density filters. Thus the displacement noise varied, inversely with sensitivity, as $1/W_L$ from which I conclude that noise on the system is dominated by the 25 μV input noise voltage on the amplifier (gain = 40) and not by the laser. The theoretical x_{min} calculation for the 532 nm interferometer, assuming $h = 6.626 \times 10^{-34}$ Js, $\Delta f = 70$ MHz, $\eta = 0.75$ and $W_L = 90$ mW, gives $x_{min} = 1.2$ pm (increasing to 2.6 pm when the beam power is filtered down to 18 mW). This can be compared with measured rms noise levels from polished aluminium of 8 pm with

18 mW of laser power, and a decrease to 3 pm at 45 mW (Figure 3.10). At maximum laser power the Adlas interferometer appears to be sensitive to displacements very close to its theoretical minimum. However, the interferometer is only used at full power on rough surfaces, for which the sensitivity is greatly reduced by scatter, and a value of x_{min} = 200 pm as measured on an unprepared extruded aluminium bar (Figure 3.8) is more likely.

Precision measurements of acoustic transients using laser Michelson interferometers commonly encounter mode-beating problems. A He-Ne laser with over 2 mW power is likely to have 3 or more longitudinal modes, each with frequency n/T_c, where n is integral and T_c is the time light takes to make a round trip of the laser cavity. Equation 3.5.5 thus becomes

$$v(n) = (V_p / 2) \sin (4\pi \times n / cT_c) \qquad \ldots 3.5.7$$

When x = 0, all the v(n) are in phase and, since adjacent modes have values of $n >> 1$ which only differ by 1, the phases remain very close even when x exceeds several wavelengths of the light. But when $x = cT_c/4$, half the laser cavity length, the $\sin(\pi n)$ dependence ensures that adjacent modes will produce voltage signals in antiphase, resulting in little or no total signal. As the sample arm is made a whole laser cavity length longer than the reference arm, the voltage signals once again add constructively and the original signal is restored. Satisfactory operation of interferometers built with such lasers normally requires the sample to beam-splitter distance to lie within 1 mm of an optimum value, such that the two arm lengths are equal or differ by integral multiples of the laser cavity length. With a single longitudinal mode laser, mode-beating is eliminated and the interferometer can sit any distance from the sample within the constraint of the coherence length (9 m for the Adlas 300 laser). The interferometer is thus far more flexible and produces substantially lower shot-to-shot variation between laser-generated waveforms. However, maximum interference is still achieved when the two arm lengths are equal, due to the 1 mrad beam divergence. Wavefront curvatures of the two beams are identical only for equal path differences, and interference is reduced as a result of the relative change in curvature arising when the reference and sample beam path lengths differ.

The single mode laser also eliminates a second mode-beating effect which occurs with the multimode He-Ne. At 1.5 GHz for a 10 cm cavity in vacuo, beats between modes are outside the range of ultrasonic frequencies studied, but a frequency dependent refractive index

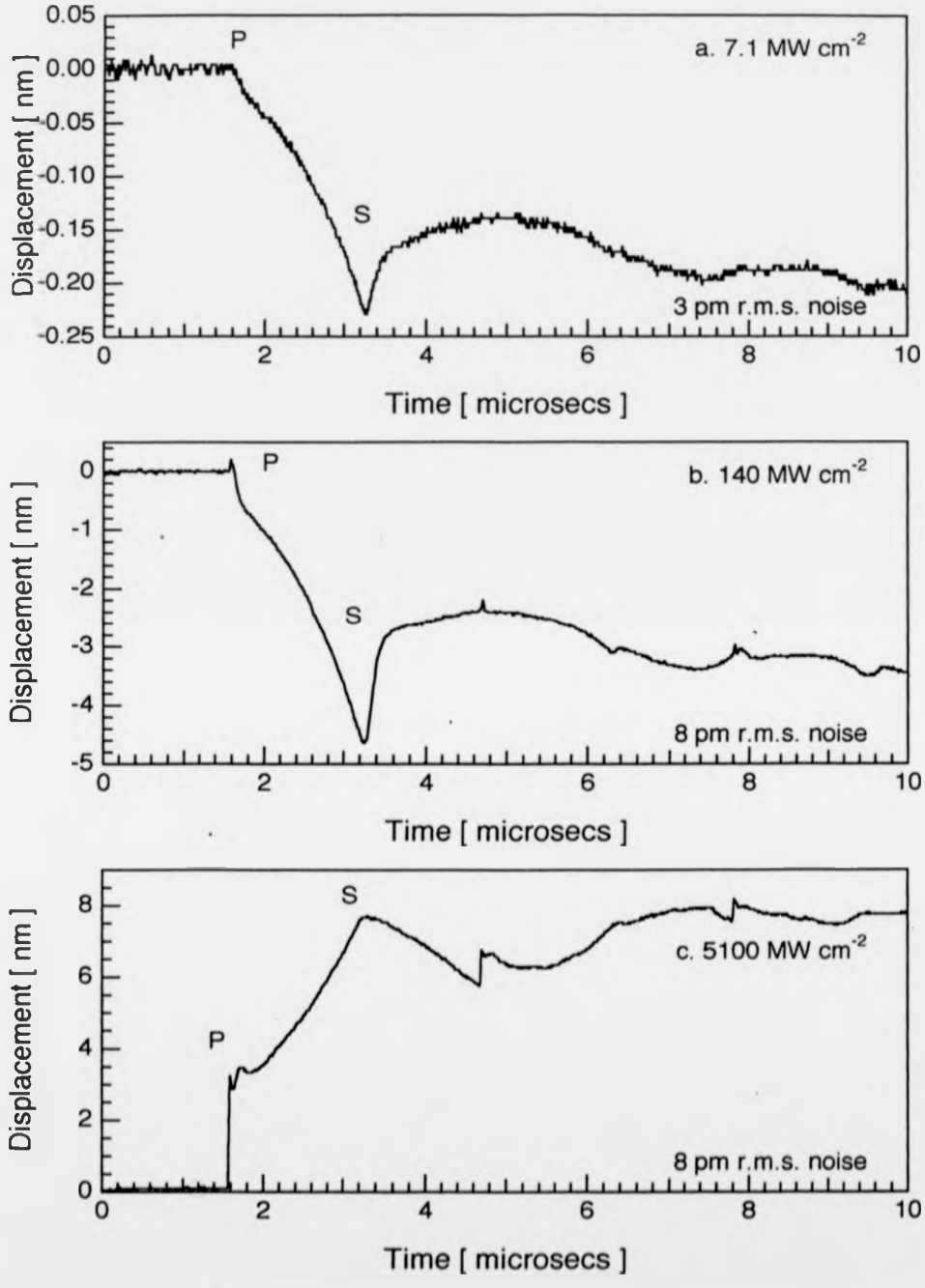

Figure 3.10 On-epicentre through transmission arrivals detected by interferometer on 9.9 mm thick polished aluminium. a). Thermoelastic source, b). intermediate source, note emergent longitudinal peak, c). strong ablation source.

change in the material, associated with the laser emission line, depresses frequencies below the line's centre frequency and raises those above. This has the effect of increasing the beat frequency between the pair of modes which straddle the centre frequency of the emission line with respect to those of beats between remaining modes. Thermal drifting of modes, as the laser cavity length fluctuates with temperature, thus causes extra beat frequencies which vary from a maximum when two modes are equidistant from the centre frequency, to zero for a mode sitting on the centre frequency. These fluctuations, with frequencies lying in the same range as those of laser-generated ultrasonic signals, are absent when the Adlas laser is used.

In summary, the Michelson laser interferometer is a relatively bulky, but nonetheless portable detector, which requires careful alignment to highly polished sample surfaces in surroundings largely free of vibration. In the configuration which I have used, it detects only surface normal displacements, with sensitivity given by equation 3.5.5 and theoretical noise level by 3.5.6. The Michelson interferometer's usefulness as a transducer for laser-generated ultrasound stems from a pointlike detection area, its remoteness from sample surfaces and, most of all, from its ability to produce calibrated output which is linear with displacement.

3.6 Ultrasonic Detection with Electromagnetic Acoustic Transducers

In contrast to interferometers, electromagnetic acoustic transducers (EMATs) provide cheap non-contact detection of ultrasonic waveforms on electrically conducting surfaces. An EMAT detector generates a static magnetic field at the conductor surface, movement of which gives rise to eddy currents: these in turn generate a fluctuating magnetic field, detected as an induced voltage across the EMAT coil. In non-magnetic aluminium alloys, the eddy currents are generated via a Lorentz force interaction [Kawashima, 1976,1984], giving EMAT responses proportional to the rate of change of surface components perpendicular to the static field. A wide variety of EMATs, suitable both for detecting and generating ultrasound, have been described [Frost, 1979], reflecting the many permutations of coil shape with production mode and orientation of the static magnetic field. Generating EMATs are in principle merely EMAT detectors operated in reverse. The practical difference is that the varying current in a generating EMAT coil must supply enough momentum for both electrons and lattice ions near the conductor surface to move, while the current in a detector coil results mainly from conduction electron

eddy currents below an already moving surface. A generator EMAT thus requires high, rapidly varying currents [Latimer & Whaley, 1988] and is generally larger than an equivalent detector, which needs fewer turns of finer grade wire in its coil. The use of EMATs in pulse-echo mode, both generating and receiving, is further restricted by technical problems with the dead time, due to ringing in the coil following discharge of the generation current. Narrowband detectors have been formed from EMATs with meanderline coils but, for laser-generated ultrasound, the most useful designs are those with narrow coils which have a wideband sensitivity to surface motions [Hutchins et al., 1985, 1986]. In the most compact detectors, electromagnets providing the static field are replaced by permanent magnets made of recently developed ceramics capable of retaining large magnetic fields. Several comparative studies of transducers have used EMATs with $SmCo_5$ [Hutchins et al.,1986: Dewhurst et al., 1987], but our group has obtained improved performance with NdFeB magnets [Edwards & Palmer, 1990].

EMAT signal responses to pulsed ultrasound on aluminium are predicted on the basis of an empirical relationship, derived from the exact solution for monochromatic, sinusoidal surface oscillations on a non-magnetic metal in a spatially invariant, static, magnetic field [Kawashima, 1984]. The emf generated when surface waves from a line source, oriented along the $\mathbf{x}_2$ axis in an $\mathbf{x}_1$-$\mathbf{x}_2$ conducting surface, pass under a long, narrow EMAT coil in the $\mathbf{x}_2$-$\mathbf{x}_3$ plane with its lowest edge, of length L, a distance G above the surface, is given by:

$$\text{Emf} \approx N L \left[a_3(G)\, B_{1C}\, \frac{d}{dt} u_3(t) \;-\; a_1(G)\, B_{3C}\, \frac{d}{dt} u_1(t) \right] \qquad \ldots 3.6.1$$

where, N is the number of coil turns, the components of the coil field $\mathbf{B}_C$ are taken, for ease of calculation, to be static and homogeneous, $u_{1,3}$ are displacements, parallel and perpendicular respectively, to the surface under the EMAT, and $a_{1,3}$ are constants for constant G.

Equation 3.6.1 raises several points. The laser line source, used in many experiments to generate directional surface waves, suggests EMAT designs with long, rectangular coils. Increasing the length L improves the EMAT sensitivity and allows the number, N, of wire turns in the coil to be reduced. I have constructed EMATs with very narrow coils (1 mm wide), although the effective detection area, which also depends on the EMAT's static magnetic field profile, is somewhat wider. A narrow sensitive region is important as the device will average

out oscillations with a spatial period lower than its width [Bushell, Edwards & Palmer, 1991]. Due to the Lorentz force origin of the electromagnetic acoustic effect, the emf contains two separable terms, in which the normal surface displacement pairs with the in-plane component of the EMAT's magnet field and vice versa. The simplest EMAT designs are therefore the Normal EMAT, with static magnetic field predominantly parallel to the sample surface, sensing normal surface displacements, or the Shear EMAT, which has a field perpendicular to the surface, measuring in-plane motion. In practice, either EMAT type has fringing fields, and hence some sensitivity to motion in both directions. Equation 3.6.1 assumes spatially homogeneous static magnetic fields, but variations can be accommodated by convolution of theoretically obtained waveforms with appropriate aperture functions [Edwards & Palmer, 1989]. The aperture functions can also include broadening effects, introduced as characteristic rise-times, due to the transit times of different ultrasonic modes under the detector. Rayleigh waves, for example, take 300 ns to cover 1mm of aluminium, but faster bulk waves arriving at sharper angles to the surface will spread across the same distance far more rapidly.

I have constructed two EMAT detectors, one normal (Figure 3.11) and one shear (Figure 3.12), using Magnetics Developments Ltd. NdFeB permanent magnets with dimensions 5 mm x 10 mm x 20 mm. The magnetic flux density parallel to the 5 mm dimension, as used for the shear EMAT, was 0.33 T while the normal EMAT produced a calculated 1.1 T in the gap between the mild steel pole pieces. Both EMATs contain pickup coils made of Maplin BL62 fine gauge lacquered copper wire, wound in 20 loops round the brass formers which hold the magnets in place. EMATs have sensitivities which are generally an order of magnitude lower even than for optical detectors and the signals were therefore amplified, usually with a pre-amplifier having a gain of 200 and bandwidth from 3.5 kHz to 10 MHz. Equation 3.6.1 reveals that EMAT signals are linear not with displacement but with the rate at which the displacement changes. Thus the 3.5 kHz lower amplifier limit scarcely affects the signals, as EMATs are poorly sensitive to low frequency disturbances. A major practical problem with EMATs is that fine copper coils are excellent detectors of local electromagnetic noise. Great care is needed to keep EMAT outer casings earthed and in electrical contact with sample surfaces, to maintain maximum electrical shielding. Noise pick-up from the laser discharge is considerably reduced if the laser casing is securely earthed and earth screening of the BNC lead

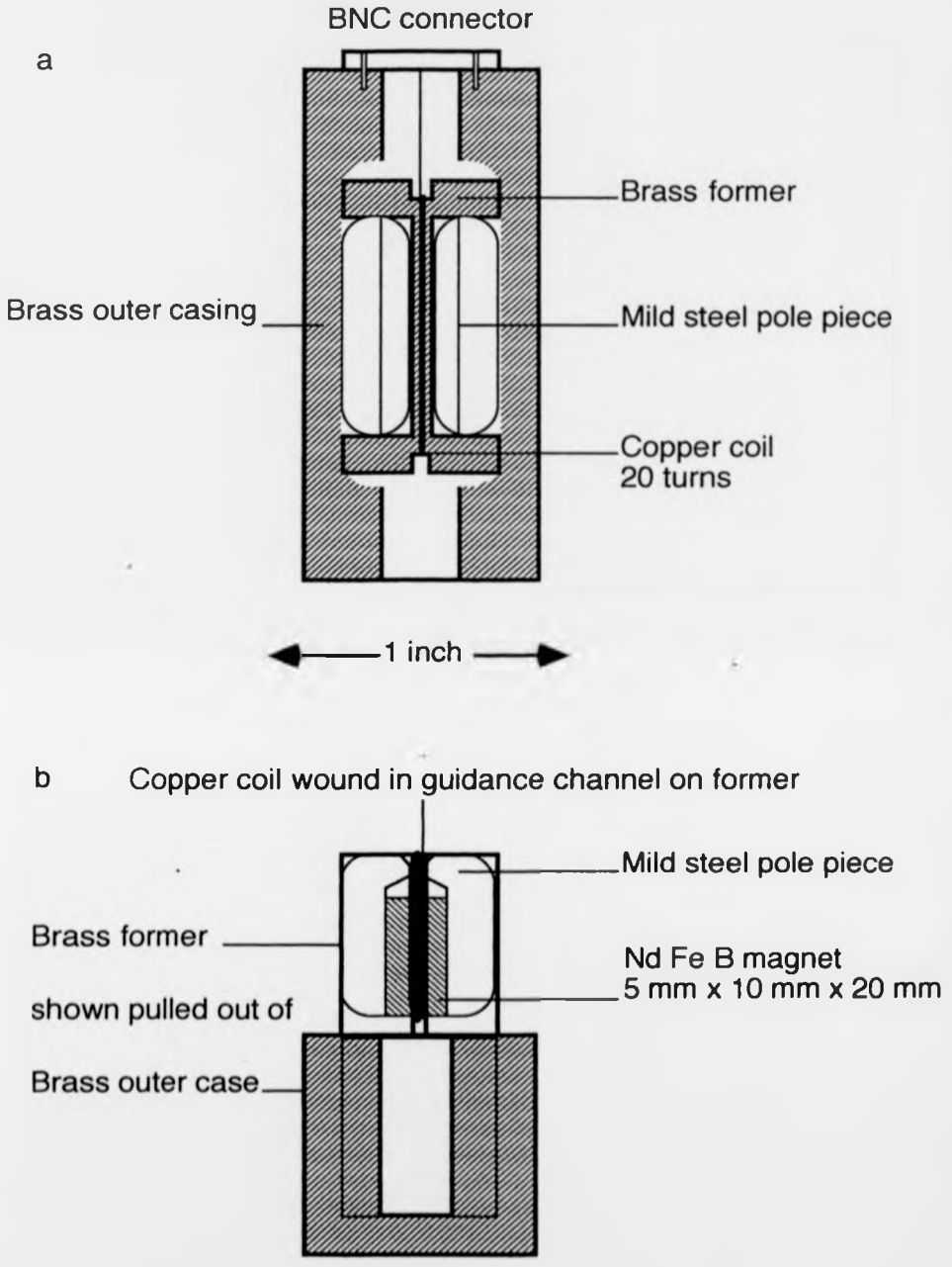

Figure 3.11 Diagram of normal EMAT detector, sensitive to out of plane motion of the sample surface. a). View from the surface. b). Side view with outer casing pulled back.

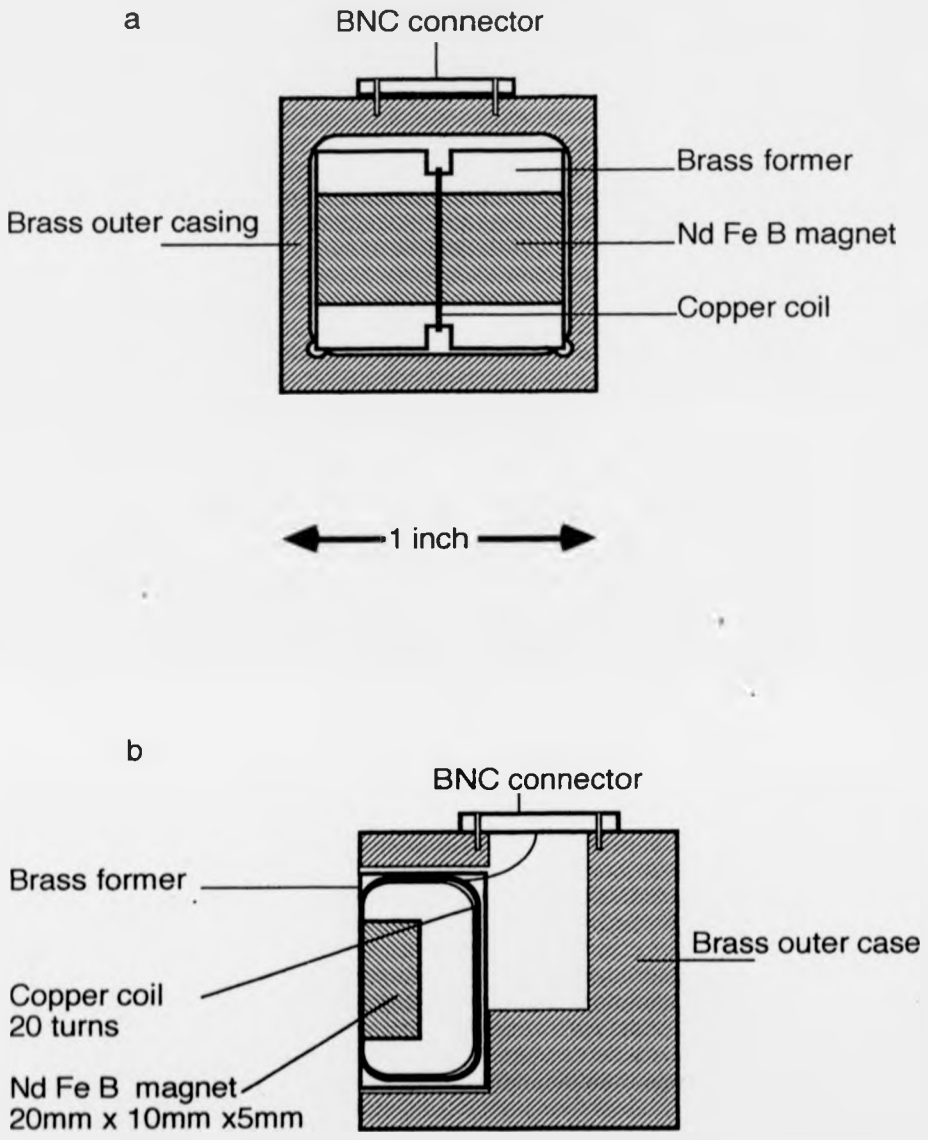

Figure 3.12 Diagram of shear EMAT detector, sensitive to in plane motion of the sample surface. a). View from the surface. b). Cross-section through mid-plane of EMAT.

connecting the EMAT to the pre-amplifier is also recommended. Finally, although EMATs are strictly non-contacting, the emf generated is exponentially dependent upon the distance, G, between coil and sample surface. G thus needs to be both small and carefully controlled. A uniform standoff from many samples was achieved by placing strips of adhesive tape either side of the coil on the EMAT's front face and pushing the device up against the surface. This was not done on thin foils where such contact with the surface led to waveforms which were distorted by mechanical damping.

EMAT signal dependence on the rate of change of surface displacement makes direct sensitivity comparisons with displacement detectors difficult, as small amplitude but rapidly varying signals may generate a strong response, where large amplitude surface movements taking much longer periods of time can pass virtually undetected [Bushell, Edwards & Palmer, 1991]. A detailed comparison between normal EMAT, shear EMAT and the Michelson interferometer is made in chapter 5, where all three detectors are used to observe laser-generated plate waves, from Rayleigh modes through intermediate stages to the zero-order Lamb regime. EMATs are impractical for absolute calibration of displacement as their sensitivities depend critically upon the configuration of field and coil. But, simple to construct and quick to operate, they are highly useful for rapid, exploratory analysis preceding detailed quantitative work. In contrast, the Michelson interferometers (section 3.5) are delicate detectors, readily calibrated to give direct measurement of displacements normal to the sample surface. Both detector types preserve the broad bandwidth and noncontact nature of pulsed laser ultrasonic sources, creating a highly flexible system with which to study the problem of adhesion in epoxy-bonded joints.

CHAPTER FOUR

ACOUSTIC REFLECTIONS BETWEEN EPOXY LAYER INTERFACES

This chapter concentrates upon adhesive property testing with ultrasound propagated perpendicular to the adhesive layer, a standard approach for piezoelectric transducer analyses (chapter 3.2). Though there have been some successful measurements [Hutchins et al., 1991] using annular EMAT detectors straddling a laser source to maintain a line of sight to sample surfaces, I have taken the simpler course of observing laser generated ultrasound in through-transmission, rather than pulse-echo, configuration. But the major difference from resonant piezoelectric transducer tests is the 15 ns half-width of a laser-generated acoustic pulse, sufficiently brief for time domain resolution of longitudinal wave reverberations within adhesive bond layers thicker than just 50 μm. Interface property information may thus be obtained by direct comparison of successive epoxy layer reverberation pulses, without needing a broad time-window Fourier spectrum analysis of adherend and adhesive modes [Guyott & Cawley, 1988a].

Section 4.1 describes the experimental arrangement for sending a strongly pulsed acoustic signal through adhesively bonded layers; beginning with a set of nominally well-adhered bonds (prepared with due care using standard DRA(Aerospace) procedures). In the event of perfect adhesion, the reflection coefficients will be determined solely by the acoustic impedance mismatch between aluminium alloy and epoxy resin. Predictions for observed time-domain waveforms, assuming non-interacting, rigidly connected boundaries between the two materials, set the scene for more detailed analysis using the theory of chapter 2.4. As adhesion changes in good bonds are negligible, the ultrasonic pulses reveal bulk bond layer properties, which are associated with cohesion in the epoxy. Using these ideas in section 4.2, I examine 3 mm thick aerospace alloy plates, forming bonded joints typical of those found in aircraft, with both interferometer and EMAT detectors, the latter being the more suitable for use in on-site testing.

Knowing the adhesive's ultrasonic properties allows the bond layer thickness to be extracted from the time interval between successive reverberation peaks. Changes in joint parameters, such as epoxy or adherend thickness, are examined in section 4.3 as they affect the waveforms and could themselves be mistaken for adhesion losses or, more probably, mask the relatively minor differences due to adhesion variability. Shot-to-shot consistency and the small

(focussed) Michelson interferometer detection area make laser systems ideal for mapping out local variations along bonded samples. For instance, if the adhesive ultrasonic velocity remains constant along a layer, pulse time resolutions allow accurate measurement of relative thicknesses over the bonded area, with obvious implications for quality control.

Lastly, section 4.4 looks at a batch of bonds prepared with a series of defects, intended to set some limits on which defects are most likely to be detected, and thus to suggest defect types which might be amenable to further study. As the adhesion deteriorates, the reflection coefficients are expected to depend increasingly on the interface properties. In the event of a clear air gap developing at the interface, the reflection coefficients lose all dependence upon the adhesive properties, and ultrasonic techniques are well-known for their ability to detect such gross defects as the absence of bonding material. Unfortunately, stress joints may fail prematurely despite being adhered considerably better than this worst case and studies using conventional piezoelectric transducers [Pialucha & Cawley, 1992] suggest that even fatal flaws can produce undetectably subtle effects at the interface. I have concentrated upon gross defects because a systematic application of laser source and interferometric detection to through thickness ultrasonic evaluation of epoxy layer adhesion has not, to my knowledge, been reported. Since pulsed laser ultrasound techniques yield poorer signal-to-noise ratios and more divergent acoustic beams than standard sources, there seems little point in setting up delicate adhesion variation experiments without knowing which major disruptions to the bonded interface will be detected.

4.1 On-Epicentre Experimental Observations of Rigid Bond Reverberations.

Ultrasonic arrivals recorded in this chapter were observed using an on-epicentre through-transmission arrangement (Figure 4.1). Before introducing the sample, careful positioning of the detector under the source's HeNe alignment laser minimizes any deviation from the epicentral axis, as mode-conversion effects alter the reflection and transmission coefficient values for ultrasound incident non-normal to the bonded layer. The Nd:YAG laser has an energy ~100 mJ per multimode pulse, with a 10 ns pulse duration and a beam diameter of 3 (± 0.5) mm. A spherical plano-convex lens with 220 mm focal length converges the beam to a 1.5 (± 0.5) mm spot diameter, giving a 6×10^{12} W m^{-2} (600 MW cm^{-2}) incident power density above the

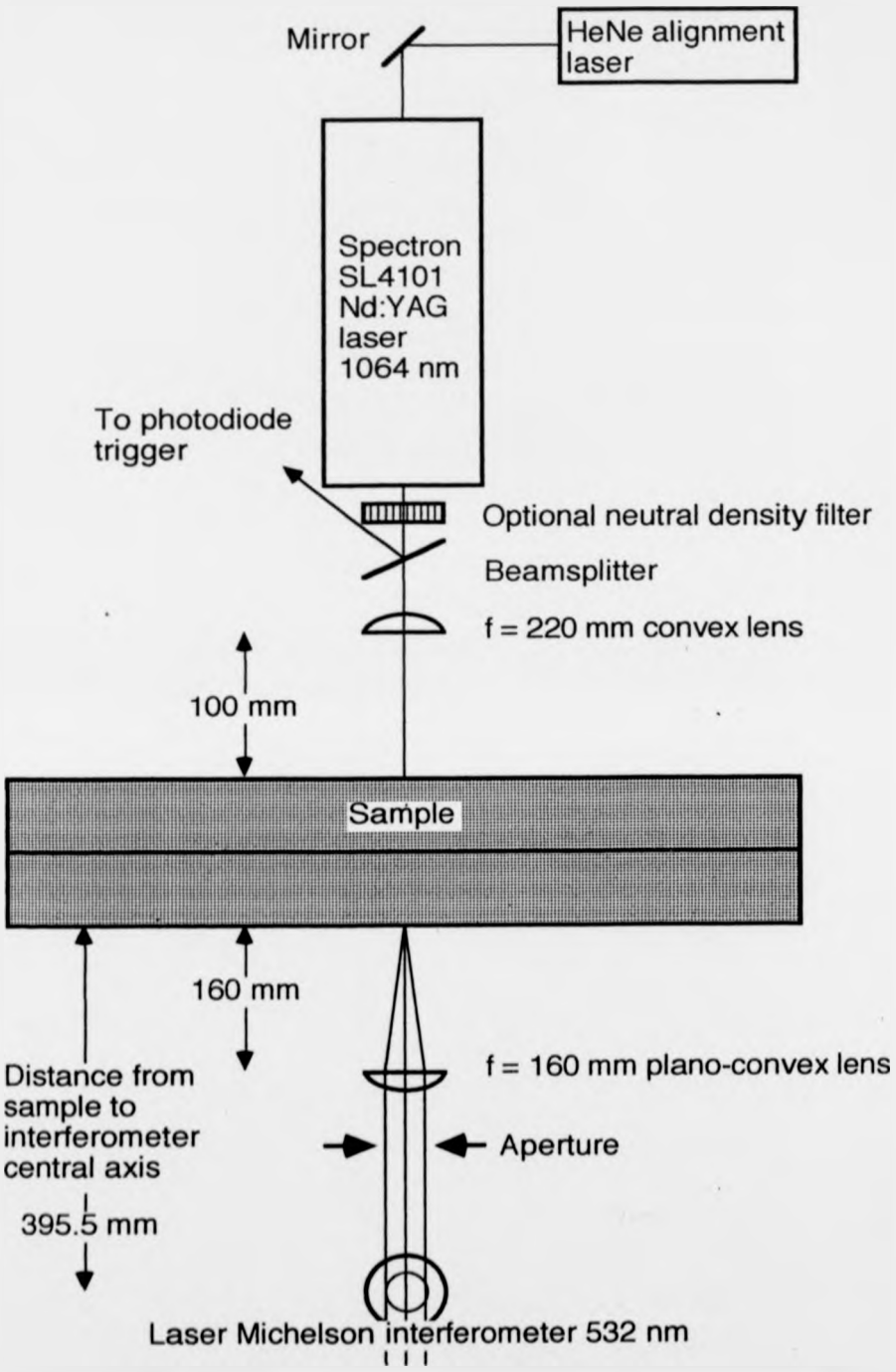

Figure 4.1 Experimental arrangement for the observation in transmission of on-epicentre ultrasonic pulses passing through an epoxy bonded layer.

surface. Fully focussed beams produce much stronger plasmas, which shield the surface (see chapter 3.3), leading to lower amplitude step arrivals and less easily interpreted waveforms. The requisite power density could be obtained by neutral density filtering a fully focussed beam but this reduces the laser energy reaching the surface and hence the ultrasonic pulse amplitude. Following the source shape, ultrasound propagating in isotropic material will be axisymmetric about the epicentre. Detection for the most part is by 532 nm wavelength laser Michelson interferometer (chapter 3.5) although, where stated, EMATs (chapter 3.6) centered on-epicentre only 1 mm above the sample surface, replace the interferometer arrangement (Figure 4.1). Output is digitized by either a Lecroy 9400 digital oscilloscope, giving signals with 10 ns sample period, or a Lecroy 6880A waveform digitizer with 0.742 ns sample period. The 6880A maximum trace length of 7.42 μs is not a severe limitation when detecting individual through transmission pulses and their reverberations, where added time resolution is beneficial, but restricts its usefulness when examining slower-varying surface waves. Directing the semi-focussed source upon a 50.80 mm thick solid aluminium block observed by the 532 nm Michelson interferometer produces typical weak ablation, sharply-pulsed, longitudinal, on-epicentre arrivals (Figure 4.2.a). Note that the 6880A pulse amplitude was held lower by additional defocussing in order to prevent digitizer saturation. Choosing source positions at 12 and 24 mm away from the block edge illustrates the problem of contamination due to ultrasound reflected at the sample edges, which introduces extra noise into a Fourier transform of the arrival (Figure 4.2.b). Unless the reflected arrivals can be reliably removed by signal processing, they define a maximum time window for each given shape of joint, within which signals following the first, directly transmitted pulse may be measured. For instance, a joint with two adherends of square cross section, centred on the source-detector axis has direct and sidewall reflection arrival times in the ratio 2: $\sqrt{5}$. Thin plate ratios are much higher, but cannot be maintained on adherends thick enough to support Rayleigh surface waves without creating unacceptably bulky bonded samples.

Once the experimental configuration is set up, epoxy-bonded joints may replace the solid aluminium block. Pulses initiated at one surface of the aluminium-epoxy-aluminium sandwich split into reflected and transmitted parts at each interface encountered. The result (see Figure 4.3) is an infinite series of diminishing amplitude signals, which reach the opposite

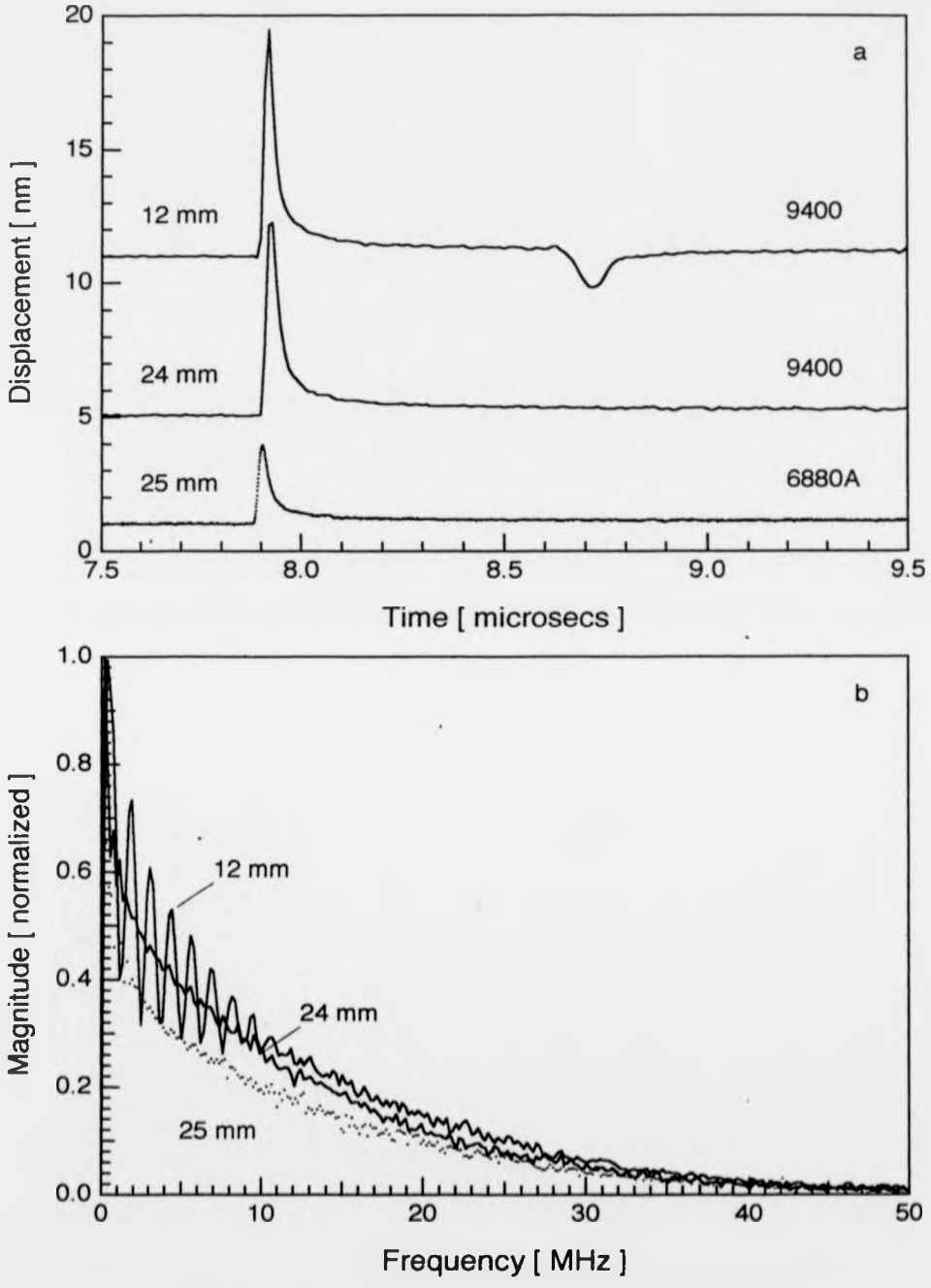

Figure 4.2 Through transmission on-epicentre arrivals on a 50.8 mm thick aluminium sample recorded on Lecroy 9400 oscilloscope or 6880A digitizer at various distances from sample edge. a). Displacements. b). Fast Fourier transform magnitudes, using 512 (8192) points for 9400 (6880A) trace transforms.

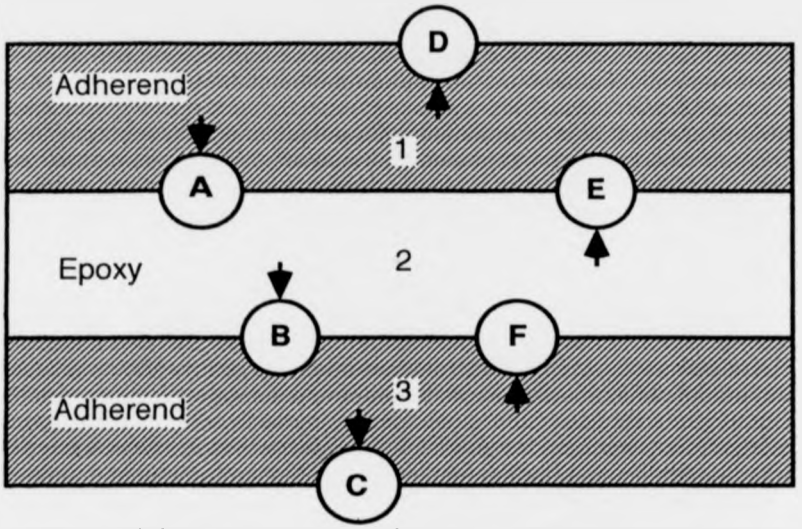

a. Adhesive joint (not to scale), interfaces marked as seen by pulse.

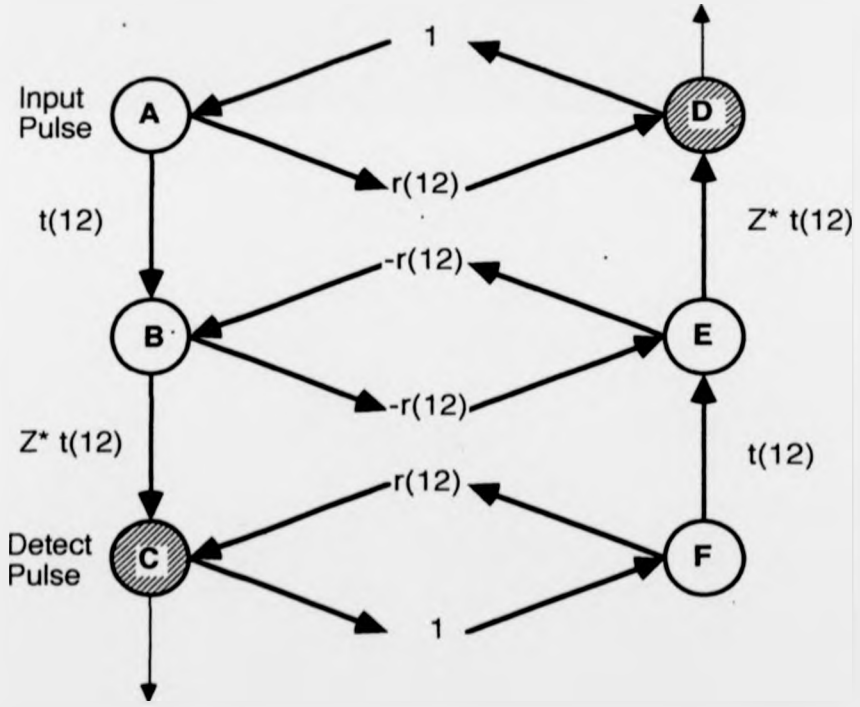

b. Allowed pathways traced by moving from A to C following arrows.

Figure 4.3 Transmission coefficient counting scheme for a pulsed signal reflected within an adhesively bonded sample. a). Interface labels. b). Pulse pathway flow chart.

surface via increasingly complicated routes. A rule of thumb estimate for pulse arrival times and amplitudes [Guyott & Cawley, 1988a] uses a one-dimensional treatment of rigidly bonded interfaces to give reflection and transmission coefficients in terms of the acoustic impedances (Z_i) either side of a material discontinuity. All coefficients are assumed frequency independent. Thus each individual reflected pulse retains the original pulse shape, arriving at a time calculated from the total pathlengths travelled within different velocity media and with an amplitude determined solely by the reflection/transmission coefficients across each interface (Figure 4.3.b). The acoustic impedance in air is neglected at the outer joint surfaces, giving perfect reflection (with non-contacting surface displacement measurements), whilst at epoxy-aluminium interfaces:

$$R_{12} = [\, Z_{Al} - Z_{Ep} \,] / [\, Z_{Al} + Z_{Ep} \,] = [\, 1 - Z^* \,] / [\, 1 + Z^* \,]$$

$$T_{12} = [\, 2\, Z_{Al} \,] / [\, Z_{Al} + Z_{Ep} \,] = 2 / [\, 1 + Z^* \,] \qquad \ldots 4.1.1$$

where $Z^* = (Z_{Ep} / Z_{Al}) < 1$ and hence $R_{12} > 0$.

The shortest path across the joint, running directly from A to B to C, has a pulse amplitude A_D and the next shortest, ABEBC, thus yields a pulse amplitude $R_{12}^2 A_D$. Pulses in the ABn(EB)C pathway with amplitudes $[\, R_{12}^2 \,]^n A_D$ are all in phase with each other, as can be seen when simulating a 210 μm thick Ciba-Geigy (CG) epoxy 312/5 layer (Figure 4.4.a). The direct pulse assumed in the simulation (Figure 4.4.b) is extracted from observed 210 (±15) μm thick CG312/5 bonded layer data (Figure 4.4.a) using an exponential fit to the direct pulse falling edge in regions obscured by later reverberation arrivals. Ignoring possible interference from sidewall echoes, the second simulated train (Figure 4.4.b) follows pulses ADABC and ABCFC reflected off the adherend outer surfaces. These pulses arrive simultaneously when path lengths AD and CF are the same, interfering constructively, while reverberation pulses following paths ABEDABC and ABCFEBC are inverted with respect to direct arrival and ADABEBC or ABEBCFC reverberation pulses and interfere destructively. Pulses reflecting more than once off the adherend surfaces contain multiple arrivals [Freemantle et al., 1993]. A slight thickness difference between adherends thus leads to partially overlapping pulses, which exhibit structure that can obscure, or be mistaken for, true reverberations. The observed 170 μs (±1%) time interval and 0.35 (±10%) amplitude reduction between reverberations were simulated with an epoxy longitudinal velocity = 2470 m/s and $Z^* = 0.254$. Attenuation arising from material and non-planar wavefront characteristics could be included as additional amplitude

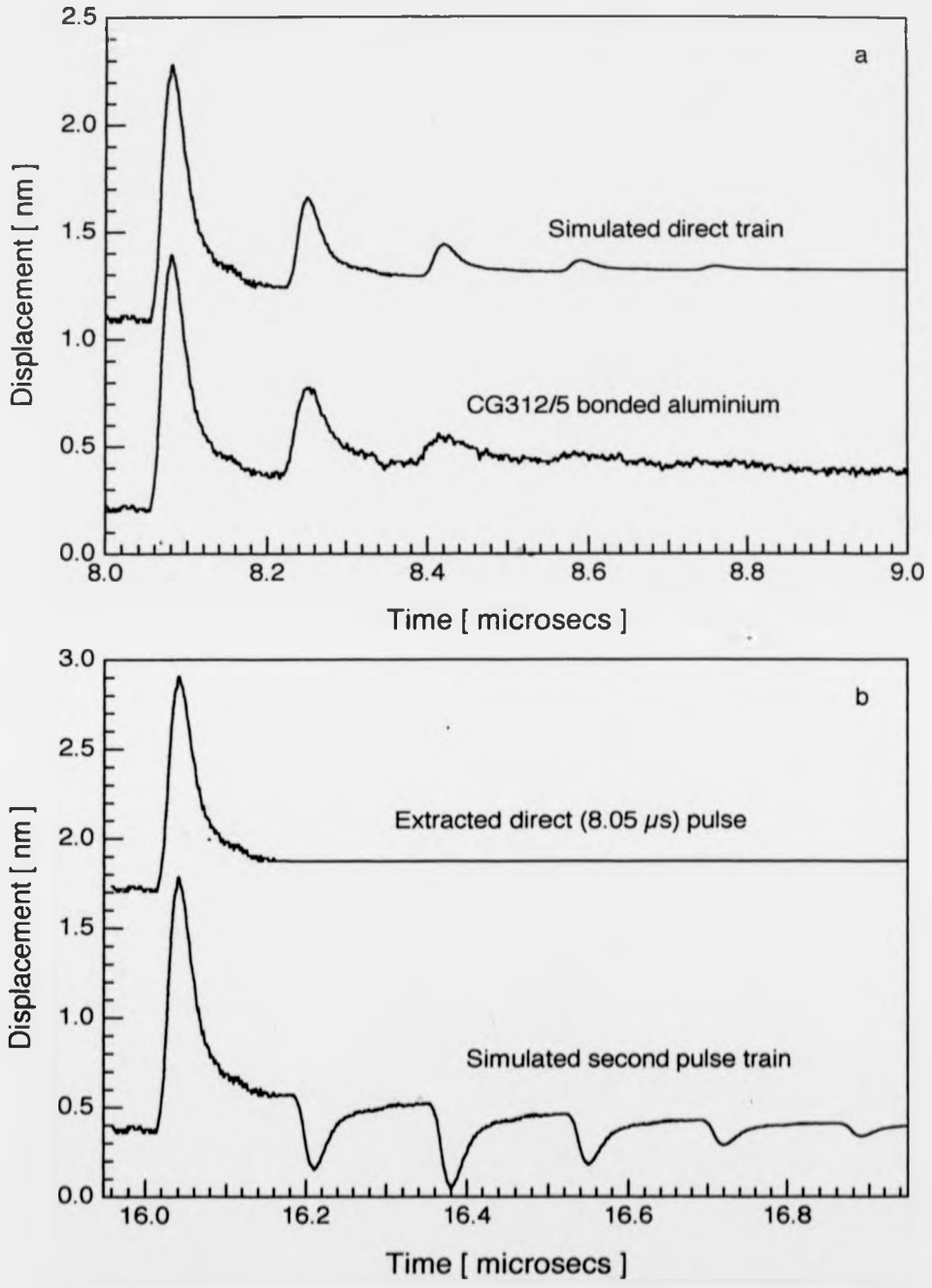

Figure 4.4 Simulation of transmitted on-epicentre reverberating pulse train using frequency independent reflection coefficients. a). Comparing direct pulse trains, simulated and measured. b). Extracted direct pulse, and superposed pulses reflected from the outer adherend surfaces.

factors along each pathway, especially to and from surfaces C and D on thicker adherends. Although the observed direct pulse train arrivals become progressively broader than those simulated, due to dispersion in the epoxy layer, agreement is surprisingly good. To first order, therefore, on-epicentre transmitted ultrasound, detected within a 25 μm detector diameter at 51 mm from the source, does not diverge over the epoxy layer thickness and a reflecting plane pulse approximation holds locally for n(EB) bond reverberations. Quantitative agreement, however, requires a more detailed inspection of individual frequencies: the Z* value quoted above, for instance, implies an unrealistic 1770 kg / m^3 epoxy density.

As only the first direct transmission arrival is single, with a clear train of epoxy reverberations in tow, time domain analysis on all but the direct arrival pulse train must be treated with extreme caution. Concentrating on the first arrival equates to adopting the theory of semi-infinite half space adherends in the chapter 2.4 plane wave calculations. Thus, the results of equations 2.4.14 and 2.4.17 can be used to deduce the epoxy attenuation and phase velocity from Fourier transforms of the extracted direct arrival and first reverberation pulses observed on the 210 μm CG312/5 bonded joint. Lecroy 6880A data allowed a 4096 point transform window for the direct arrival, ending at the *second* reverberation pulse arrival time. Data manipulation was carried out within the Igor 1.24 graphics package (WaveMetrics, 1990). I defined a fall function for the pulses with four parameters, a maximum amplitude and its time of occurrence, which may not be earlier than the pulse's peak arrival time, a non-zero background amplitude and the time taken to reach half the initial amplitude above background. The function was fitted, by Igor's curve-fitting routine, to a portion of the pulse preceding the first reverberation arrival, and used to estimate the direct pulse amplitude between first and second reverberation arrival times. The method's main weakness is a potential for ambiguous fitting which occurs when there are too few points between pulse maximum and the next reverberation arrival. The extracted pulse (Figure 4.4.b) was then subtracted from the original data to uncover the first reverberation, which was observed within a time window shifted by the reverberation period 2T(0) indicated in 2.4.17. The first reverberation falling edge was similarly fitted to remove subsequent reverberations. Finally, after smoothing each trace, the point 0 was matched to non-zero point 4095 - a step causes noise in the fast Fourier transform - which was achieved with a half cosine Hanning taper applied to the leading (~3000) zero level points, before the

peak was centred about time zero. The pulse transform phases and magnitudes are used respectively to calculate the epoxy phase velocity and attenuation (Figure 4.5). Viscoelastic behaviour in the glue, consistent with a single time constant relaxation process (see data analysis linked to Figure 2.2.a & c), accounts for a velocity decrease from 2550 ms^{-1} at 3 MHz to 2180 ms^{-1} at 1 MHz. However, caution is needed for points below 1 MHz, where windowing effects are the most pronounced, or above about 10 MHz when limiting the signal digitization to 8 bits makes phase velocity calculations unreliable. The zero frequency phase velocity, defined in 2.4.17 from the observed T(0), is used to calculate a zero frequency magnitude ratio in 2.4.14, given a 1.72 x 10^7 kg m^{-2} s^{-1} adherend acoustic impedance and epoxy density = 1200 kg m^{-3}. Hence $Z^* = 0.17$ (±10%) at zero frequency, implying a 0.49 magnitude ratio that differs substantially from the plane-wave reflection coefficient seen above.

A countercheck on these results uses the derived velocity and attenuation data to calculate through transmission coefficient magnitudes for a well-bonded epoxy layer (Figure 4.6.a). The same coefficient is estimated by dividing a fast Fourier transform of the entire, interferometer detected, direct arrival train by the isolated direct pulse FFT and multiplying by $Z^* t_{12}^2$ (Figure 4.3). The normalized magnitude spectrum (Figure 4.6.b) shows a series of adhesive bond reverberation peaks, with a 6.1 MHz (± 3%) fundamental bond resonance frequency (164 ns double transit time), which are gradually lost in noise that swamps the low magnitudes encountered at frequencies above 30 MHz. The observed and calculated periodicities agree well, confirming a well-bonded joint, free of defects that would alter the frequency separations (chapter 2.4). The peak amplitudes, however, show very poor agreement. A zero attenuation calculation only marginally underestimates the decay of resonance peak magnitudes with increasing frequency, but inclusion of the very noisy deduced attenuation (Figure 4.5.b) clearly degrades the transmission coefficient simulation (Figure 4.6.a). The observations also include scattering and geometric attenuation, but the discrepancy almost certainly originates from inadequate resolution in the digitizer quantization, as noted while extracting the epoxy absorption data (Figure 2.2.c).

4.2 Extracting Bulk Epoxy Properties from Observations Through Good Bonds.

Having outlined the examination procedures in section 4.1, I will now describe some results from samples which were well-bonded according to the strict preparation procedures

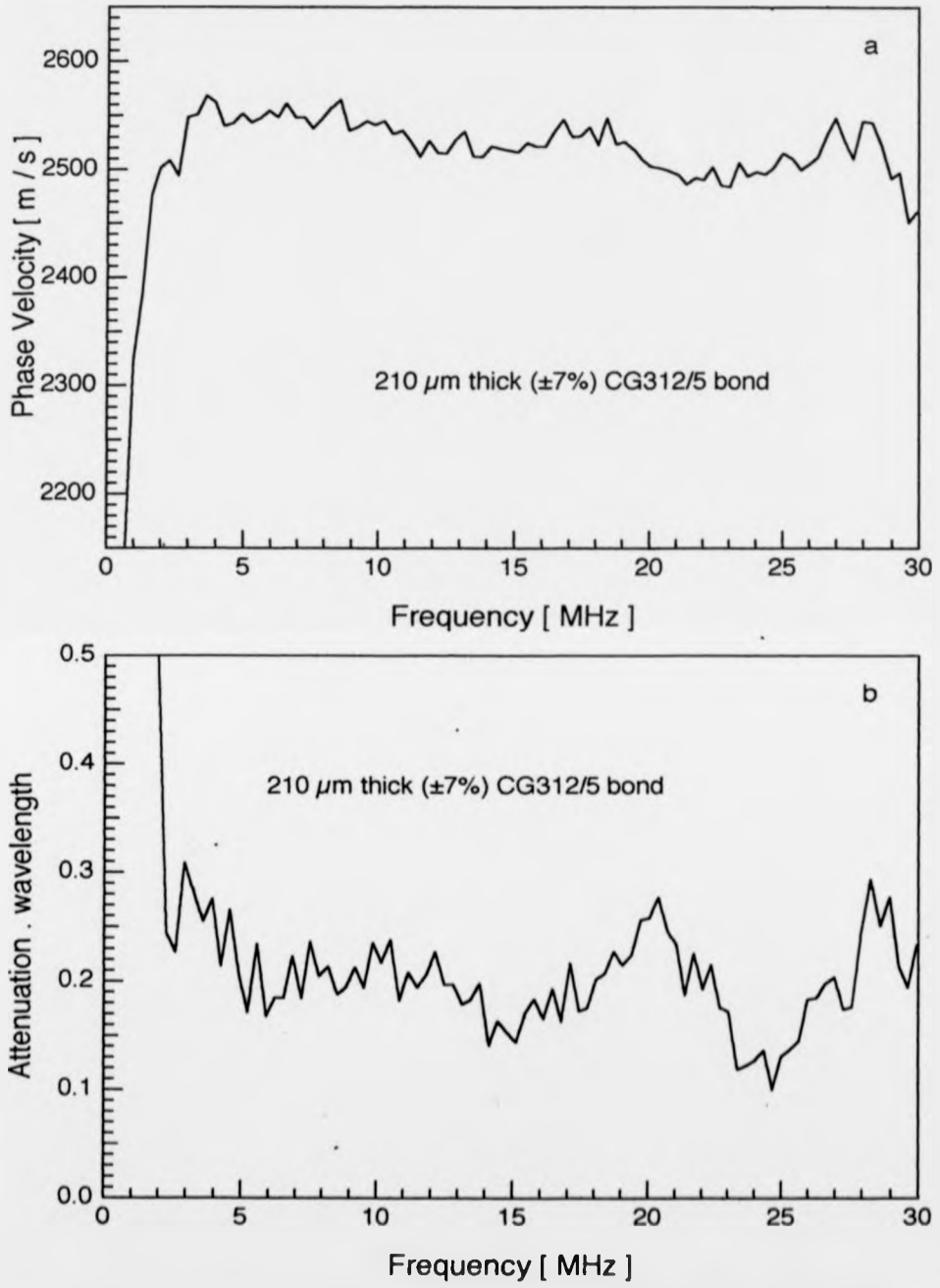

Figure 4.5 a). Phase velocity, b). Attenuation, calculated for an epoxy bond layer 210 μm thick bonding aluminium adherends 25.60 mm and 25.19 mm thick, from consecutive reverberation peaks in the adhesive, arriving on-epicentre after direct transmission across the adherends

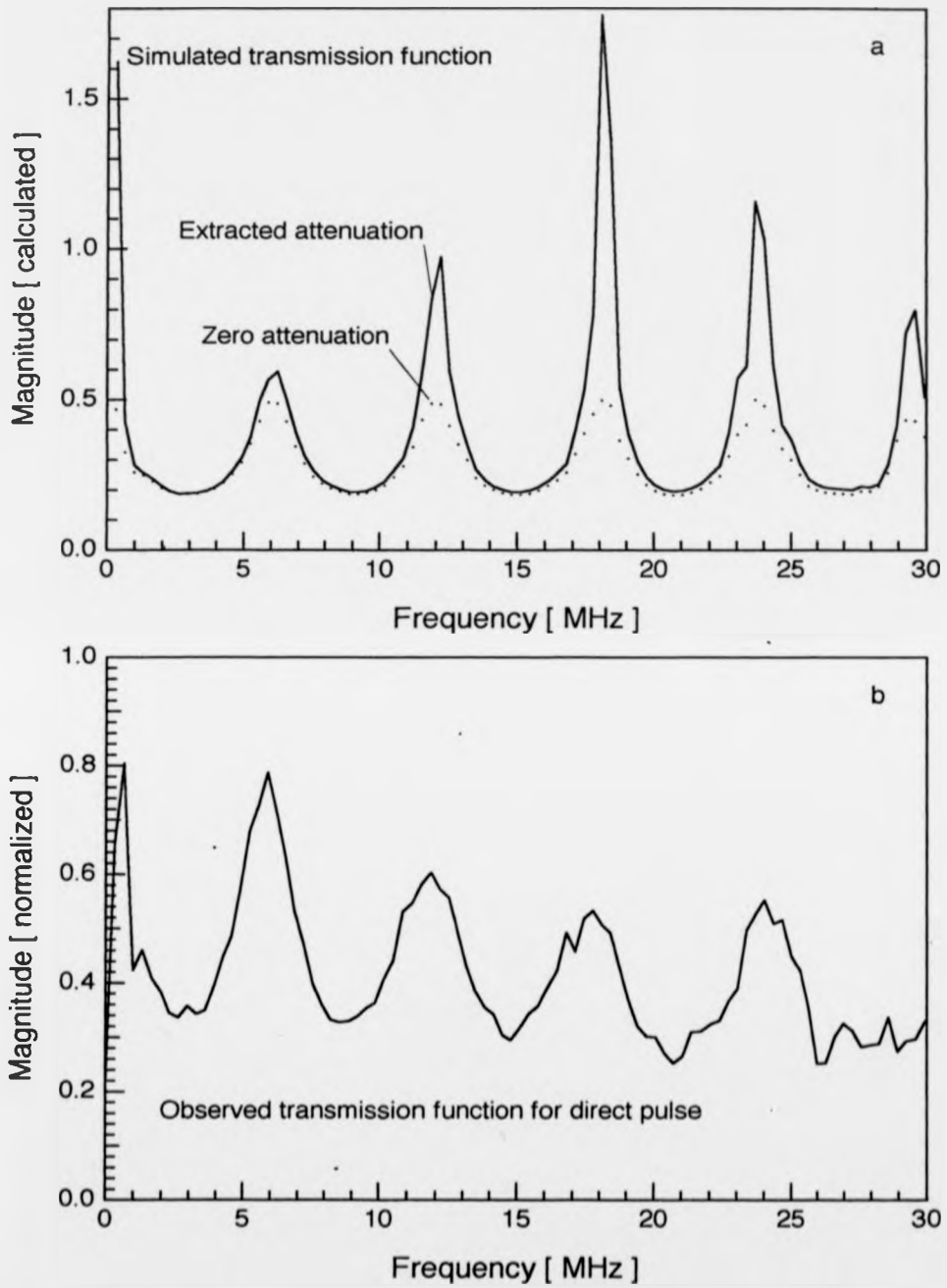

Figure 4.6 Transmission coefficient for direct arrival reverberation wavetrain in 210 μm thick CG312/5 epoxy bond, a). as calculated for halfspace adherends, b). observed, using direct pulse to negate adherend and source effects.

followed in their construction. The first set (Figure 4.7.a) uses standard aluminium aerospace alloy sheet adherends approximately 3 mm thick to form reinforcement joints which might conceivably appear in aircraft. One sample contained adherends which were cleaned, degreased and etched, but underwent no further processing before bonding (see Appendix B.1), another two identical samples were further anodized, in phosphoric and chromic acids respectively to increase the adherend oxide layers. Thus the plain etched adherends have aluminium oxide layers ~0.1 μm thick, the phosphoric acid anodized ~0.5 μm, generally regarded as providing a better key for the adhesive, and the chromic acid anodized a few microns thick, which greatly enhances brittle failure in the oxide layer. A sample (Figure 4.7.b) containing unknown epoxy 460 μm (±7%) thick, bonding 25.4 mm thick aluminium adherends, will be discussed later.

Starting with the plain etched adherend sample bond (Figure 4.7.a), 1 μs transit times across 3 mm aluminium adherends easily exceed the <150 ns transit time in 120 μm (±7%) thick epoxy so that direct arrival reverberations are still captured, on the Lecroy 6880A, after detection by Michelson interferometer (Figure 4.8.a). The 50 mm joint width is so much greater than the 6 mm total thickness that it eliminates any sidewall effects over the timescales of interest. However, longitudinal wave mode-conversion at the bond layer leads to a shear wave arrival around 1.5 μs, which limits the validity range of uncontaminated direct arrivals. A pulse simulation (Figure 4.8.a) shows close behaviour to the observed signal up until 1.5 μs when the change in gradient is consistent with a shear arrival on-epicentre. The simulation predicts qualitatively similar behaviour to the second arrival train but with overly large amplitudes. Tight thickness tolerances on the aluminium alloy plate from which the adherends were cut, and an absence of reflected pulses significantly broadened with respect to the direct arrival, mitigate against thickness mismatching. The most likely culprits are adherend attenuation, especially geometric attenuation arising from the spherical wavefronts, or further interference from shear wave arrivals after 2 μs. Given experimental limitations, the extracted phase velocity (Figure 4.8.b) agrees very well with that found in section 4.1. But the extracted absorption (Figure 4.8.c) is suspect at all frequencies, due to pulse fitting procedure problems in selecting correct background tail amplitudes (compare Figure 4.4.b), and hence half-height decay times, from fits restricted to pulse segments with rapidly falling displacements. No conclusions can be drawn from the mismatch between attenuations observed or predicted from phase velocity data.

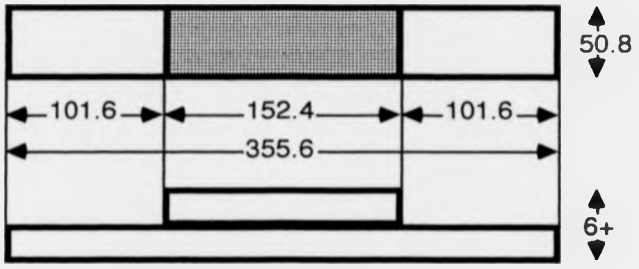

All measurements in mm.

a). Etched aluminium aerospace alloy plates bonded with CG312/5 epoxy approximately 0.1 mm thick.

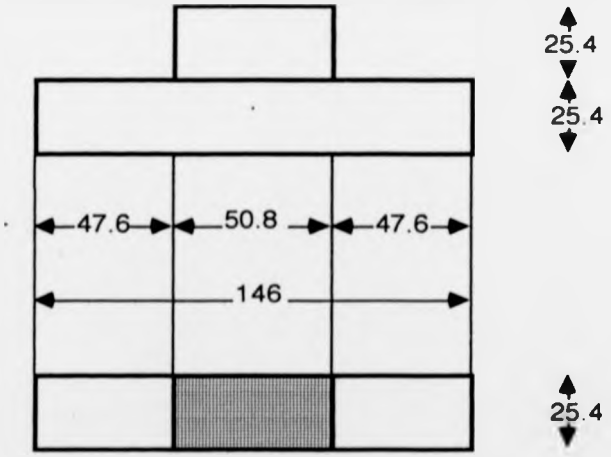

All measurements in mm.

b). Bonded 1 inch thick aluminium alloy adherends attached with approximately 0.5 mm thick epoxy layer.

Figure 4.7 Adhesively well-bonded reinforcement joints.
a). 3 mm adherends, supplied by DRA (Aerospace).
b). 1 inch adherends, supplied by Alcan Ltd..

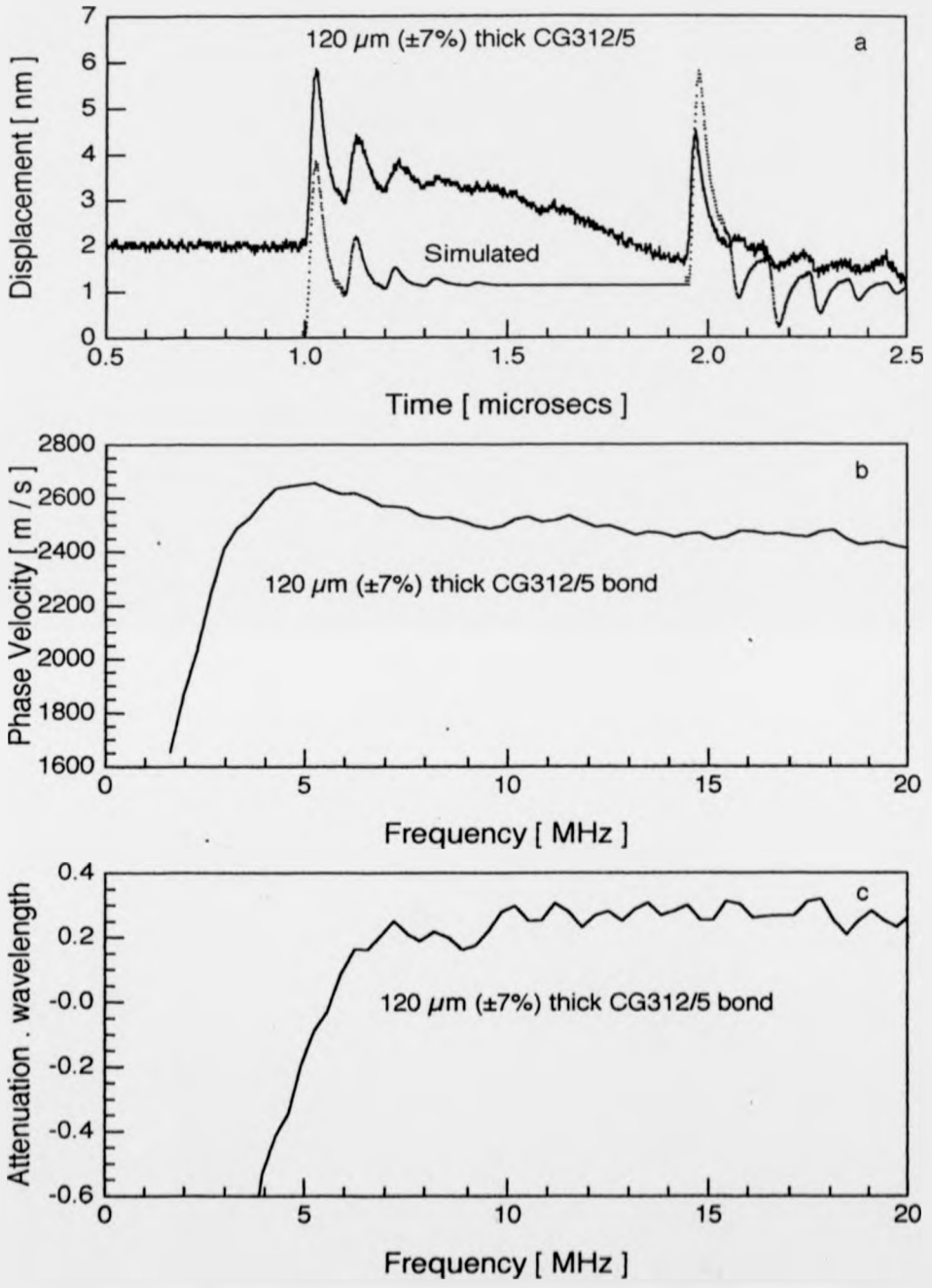

Figure 4.8 Plain etched plates 3 mm thick bonded with 120 μm thick CG312/5 epoxy layer. a). Comparison of simulated longitudinal pulse with observed interferometer signal. b). Extracted phase velocity, c). extracted attenuation.

Michelson interferometry is fine for speculative examination of displacement waveforms, the purview of a research project, but at present is too sensitive for wider use outside laboratories. Substituting the interferometer arrangement by an EMAT designed to measure out-of-plane surface motions (chapter 3.6) retains the non-contact aspect of laser-generated ultrasound, and coupling into a Lecroy 9400 digital storage oscilloscope increases the system flexibility. EMAT output for the plain etched joint (Figure 4.9.a) reproduces reverberations seen by the interferometer (Figure 4.8.a), but the EMAT's sensitivity to motion produces a trace proportional to the displacement differential. Thus, the initial peak of a weak ablation pulse is enhanced with respect to its relatively flat trailing shoulder (Figure 4.2.a). Interferometer output comparisons show that 10 ns Lecroy 9400 resolution, though reduced from 0.742 ns for the 6880A, allows accurate enough pulse shape representation for the dominant resolution effect to be the lower EMAT amplifier bandwidth (chapter 3.5). Phase velocity calculations yield solutions (Figure 4.9.b) within 10% of the interferometer result at frequencies above 2 MHz. Data was taken off unpolished joints, with the 532 nm laser interferometer beam unfiltered to maintain sufficient return signal amplitudes, despite which the phosphoric acid anodized surface scattered too much to permit measurement. Less affected by surface roughness, the EMAT gives results of similar quality to the interferometer between 2 and 16 MHz, above which oscillations in the phase velocity, and more markedly in the absorption (Figure 4.9.c), indicate insufficient signal due to bandwidth limitations. Anodized layer thicknesses are more than an order of magnitude smaller than the 50 μm minimum wavelength predicted for < 30 MHz ultrasound, suggesting that only oxide depths accompanying significant deterioration in bond adhesion will be detected. Observations on the plain etched, phosphoric or chromic acid anodized samples indicate that switching transducers has a larger effect than changing the surface finish, a problem that needs addressing. One reason is that EMAT measurements are less precise due to the poorer resolution on T(0), and further research should show if a mean T(0) based on the integrated area under the pulse [Challis et al., 1991] improves agreement. More research is also needed to improve the definition of appropriate pulse fitting functions and the handling of viscoelastic behaviour below 2 MHz, which the EMAT's relative insensitivity to low frequency motions renders poor.

Another well-bonded joint, with 25 mm (1 inch) thick aluminium adherends sandwiching an unidentified adhesive layer, was donated by Alcan Ltd. (Figure 4.7.b). Interferometric

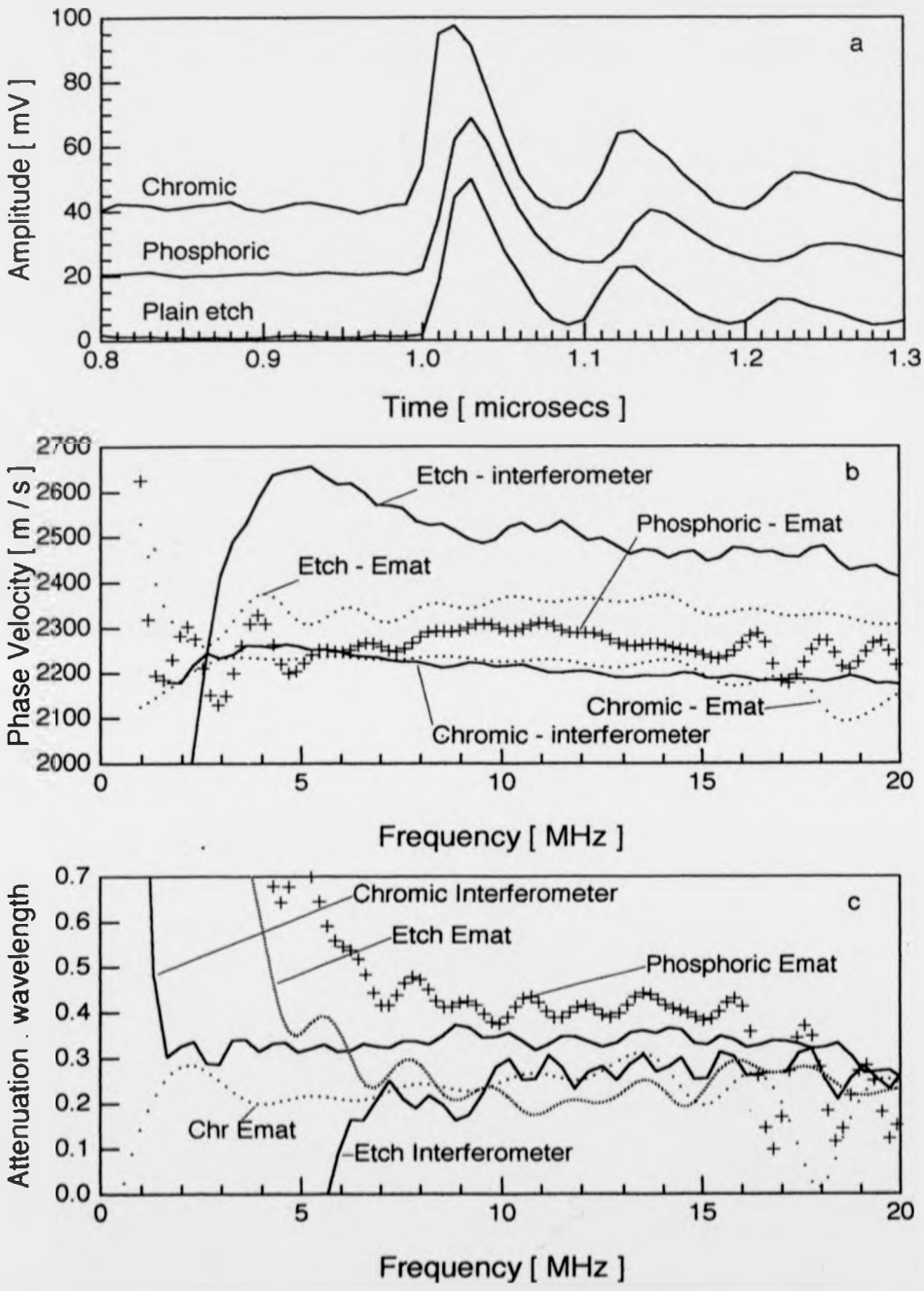

Figure 4.9 CG312/5 bonds with surface finishes [epoxy thicknesses]:- etched [120 μm], phosphoric [121 μm] and chromic [138 μm] acid anodized. a). Normal EMAT detected through transmission direct arrivals, b). extracted phase velocities, and c). extracted attenuations.

detection and the 6880A reveal a displacement over time (Figure 4.10.a) which is similar to the 210 μm CG312/5 case (Figure 4.4.a), except that a 460 μm (±7%) bond layer thickness ensures wider reverberation peak separations. Processing the Alcan bond as per section 4.1 gives a phase velocity (Figure 4.10.b) matching within experimental error that of CG312/5 below 14 MHz, but differing above 14 MHz as higher absorption across the thicker layer forces Alcan bond magnitudes below the noise threshold. Increased pulse dispersion in the longer epoxy pathlength also exacerbates pulse fitting problems encountered earlier, leading to suspect absorption values (Figure 4.10.c), particularly below 3 MHz where negative values are purely artificial. The results are consistent with an epoxy layer of similar material to CG312/5.

4.3 Quality Control of Changing Joint Dimensions Using On-Epicentre Arrivals.

Joints with unknown history are most likely to be encountered in field testing or accident analysis. In quality control, the epoxy composition is generally known and the desire is to monitor the manufacturing process either to detect problems or to regulate the adhesive layer thickness. To investigate varying bond thickness effects, a reinforcement joint (as in Figure 4.7.b) was used, with aerospace alloy adherend base 356 mm long x 25.1 mm thick and top 50.8 mm (2") long x 12.2 mm thick. Original specifications were for CG312/5 adhesive containing a 10 mm wide gap across the centre, but the flow of molten epoxy during cure resulted in a wedge-shaped adhesive layer with no discernable disbond. For rapid examination the source and normal EMAT detector remained fixed and the sample moved on an XY stepping-motor table, halting at 6.35 mm (0.25") intervals (Figure 4.11). In theory an interferometer aligned along the source epicentre would be a better detector, since the displacements it records are unaffected by surface conditions along the scanned sample. However, the problem of keeping a moving sample surface oriented exactly perpendicular to the fixed interferometer beam has yet to be overcome. A lesser problem arises in maintaining a constant 1 mm gap between EMAT and surface; essential if absolute amplitudes on consecutive traces are to be compared. When the XY table only moves between measurements, the detector is easily adjusted, but continuous flow measurements are a lot trickier as any protrusions from moving surfaces have a strong tendency to snatch the EMAT. Passing the generating laser beam through a cylindrical lens creates a focussed, strong ablation source approximately 0.5 mm x

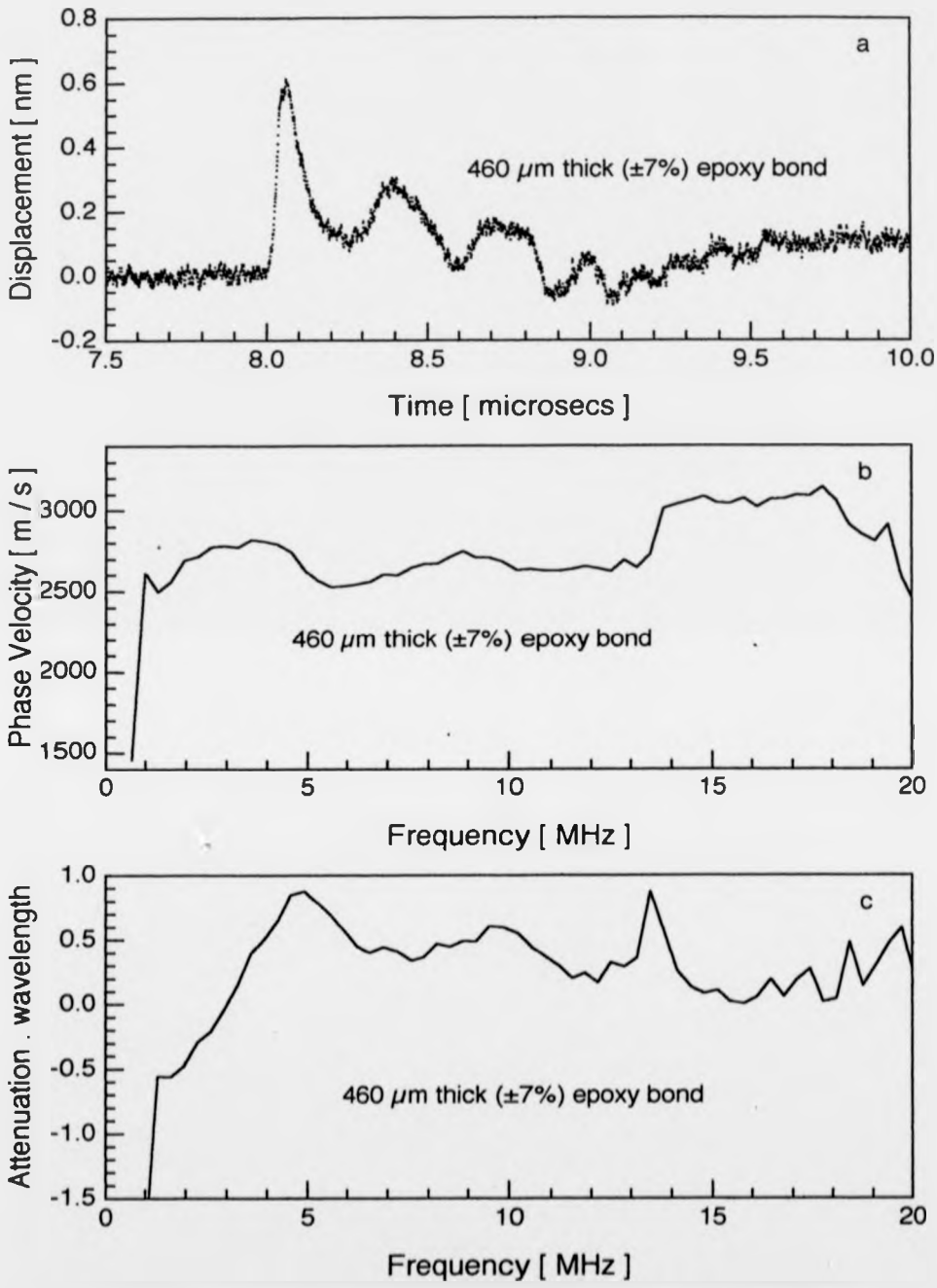

Figure 4.10 0.46 mm thick epoxy layer bonding 25.4 mm thick adherends [donated by Alcan Ltd.]. a). Waveform observed by ADLAS interferometer. b). Extracted phase velocity. c). Extracted attenuation for adhesive layer - values < 0 are artifacts.

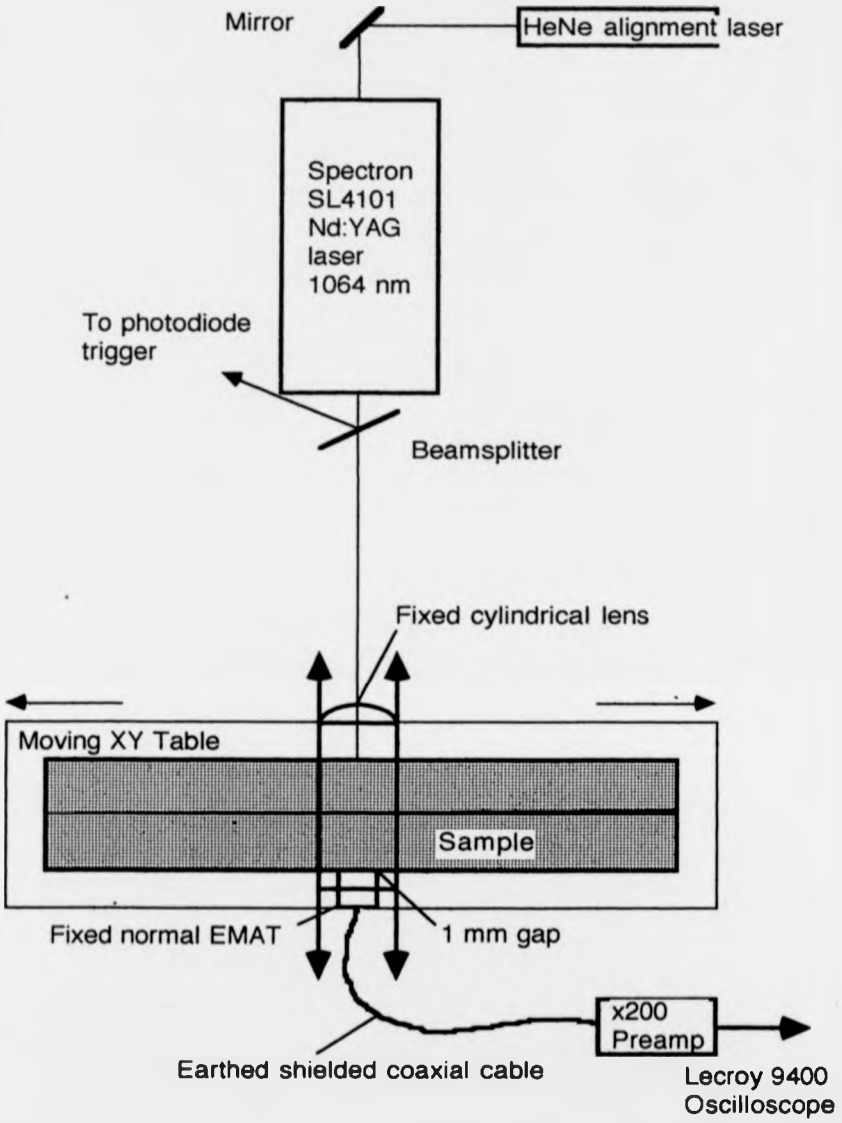

Figure 4.11 Scanning system with on-epicentre detection by normal EMAT of laser-generated longitudinal waves crossing an epoxy bond layer of variable thickness.

3mm in extent, its long axis vertically aligned, parallel with the EMAT coil axis. The EMAT output is fed into a preamplifier with a gain of 200 and nominal bandwidth 3.5 kHz to 10 MHz and sent to the Lecroy 9400 digital storage oscilloscope.

The EMAT scan reveals a series of direct arrival pulses, proportional to the rate of change of displacement resulting from a strong plasma source, followed by increasingly high frequency reverberations in the tapering bonded layer (Figure 4.12.a). The pulses are monopolar and decay to zero in bond layers thick enough to separate reverberations. A combination of source pulse and detector bandwidths sets a 14.6 MHz (± 2%) maximum detectable bond reverberation frequency, implying a 68 ns minimum period. Weak ablation interferometer measurements at one location confirm the EMAT data (Figure 4.12.b), despite slightly faster direct arrival times resulting from material lost in polishing the joint surface. Crosses on the 9440 digitizer trace indicate data points, whereas the 6880A data is plotted as individual dots to illustrate the increased resolution. A reduction in laser surface power density to avoid saturating the 6880A digitizer did not entirely remove the direct ultrasonic pulse extended tail. The EMAT direct arrival reverberation train can be Fast Fourier transformed to obtain magnitude spectra, with peaks at increasing frequencies over the scan (Figure 4.13.a), that graphically illustrate the decreasing wedge thickness. Knowing the frequency associated with a desired mean epoxy thickness, and assuming that the epoxy velocity remains constant throughout, thickness tolerances may be maintained by setting bandwidth limits. I have also analysed individual reverberations to produce phase velocity dispersion curves (Figure 4.13.b). Although these velocity values depend on knowing the thicknesses, identical dispersion characteristics in the 5 to 15MHz range provide strong circumstantial evidence that the velocity really remains constant. The interferometer velocity curve estimates significantly higher values (Figure 4.13.b) because the nearest available thickness, at scan location 12.7 mm, is too large. Comparing EMAT and interferometer estimates shows complete degradation in the EMAT data above 16 MHz due to bandwidth limitations and, hence, the effect of system noise. Phase velocities taken at scan positions 19.1 and 25.4 mm, where the epoxy prepreg was originally absent, do not appear significantly different from velocities at the remaining sites.

If a reference phase velocity dispersion curve is inserted into the phase formula 2.4.17,

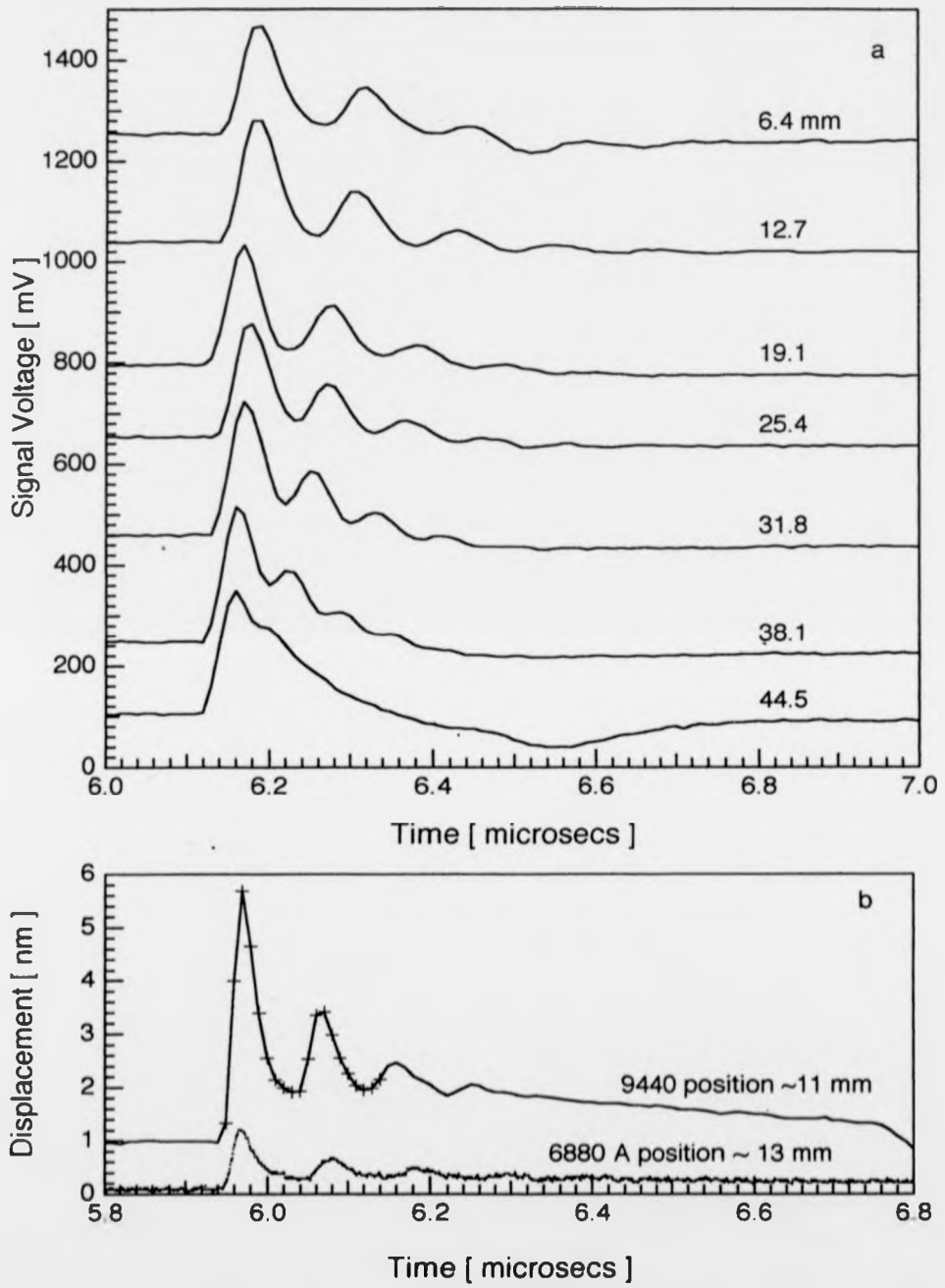

Figure 4.12 On-epicentre through transmission arrivals scanned in 1/4" steps along a wedged CG312/5 layer joint.
a). Detected by normal EMAT and Lecroy 9440, or
b). by 532 nm laser interferometer and 9440 or 6880A.

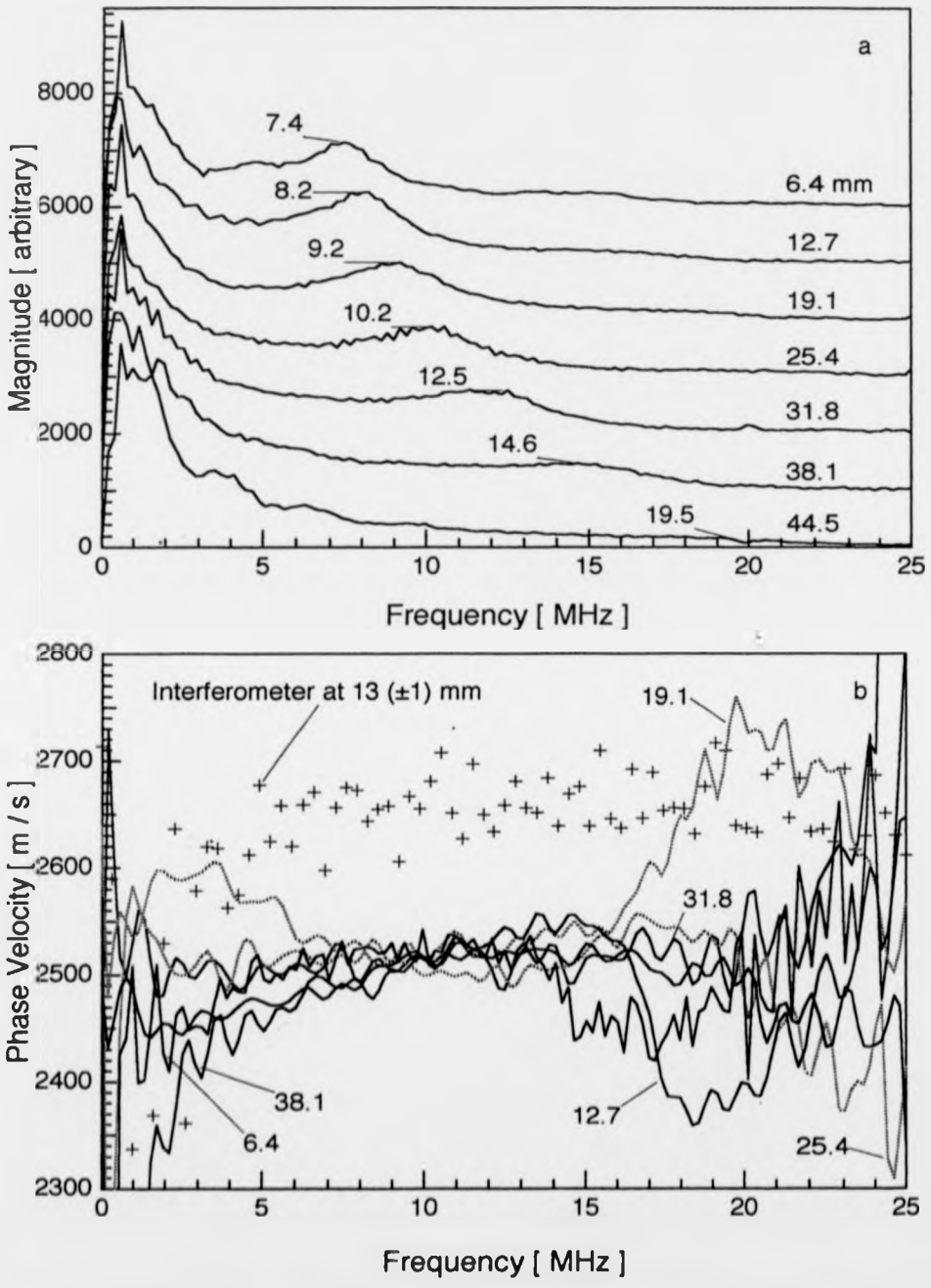

Figure 4.13 Wedged layer joint analysis. a). Fourier transform magnitude peaks [MHz] indicate thickness decrease with each 1/4" scan step. b). Phase velocities extracted from EMAT data and from interferometer observations at about the 13 mm position.

reverberation pulse analysis may be used to extract thickness estimates, which should be frequency independent unless the actual velocity deviates from the reference. Thickness curves obtained from the EMAT pulses (Figure 4.14.a) do in fact indicate frequency independence between 2 and 16 MHz, low frequency deviations stemming from windowing effects. Measured thicknesses plotted against the reverberation frequencies and 5 to 15 MHz mean thicknesses (Figure 4.14.b) provide an estimate of the relative accuracies of each approach. Disagreement between extracted and measured thicknesses appears to result from a systematic 20 μm underestimate in the measurements, as both the gradients are the same, ruling out an overestimated phase velocity as the cause. The thicknesses measured directly used a microscope focussed on the bond's exposed side, after milling to remove the first 2 mm where rounded adherend edges make the layer appear too wide. Milling tools, however, splay the outer metal edges, leaving a burr which has to be filed smooth, and the same effect occurring where the aluminium abutts softer epoxy would explain a 20 μm narrowing of the bond edge with respect to the centre. The transform magnitude peak frequency, inverted to give a nominal reverberation transit time (Figure 4.14.b), is only a single datum and therefore not as accurate a thickness predictor as measures based on a spectral range. However, the inverted frequency detects the trend in thickness, though not the slight bulge between 20 and 30 mm, which appears genuine and not the result of degraded adhesion (chapter 2.4). In adhesion testing, epoxy thickness variation is an inconvenient mask of more subtle boundary effects, but laser acoustic sensitivity to thin layer thickness changes lends the technique to semi-automated quality control of layer thicknesses, with all the advantages that a remote method can bring.

4.4 Examining Ultrasound Transmitted Through Defective Bonds.

DRA(Aerospace) prepared a set of reinforcement joints with 25 mm thick aerospace alloy adherends (Figure 4.15), which contained deliberately specified defects. Given an alloy longitudinal velocity of 6389 (± 0.08%) m s^{-1}, the chosen dimensions ensure a wide time window between the first longitudinal arrival at about 7.9 μs and any possible shear wave arrivals, although the first sidewall reflections arrive at about 8.8 μs, a factor $\sqrt{5}$ / 2 later. Observations up to 0.9 μs after the direct pulse thus consist entirely of signals originating from the bond-disbond region and the time window could be extended by widening joints, were it

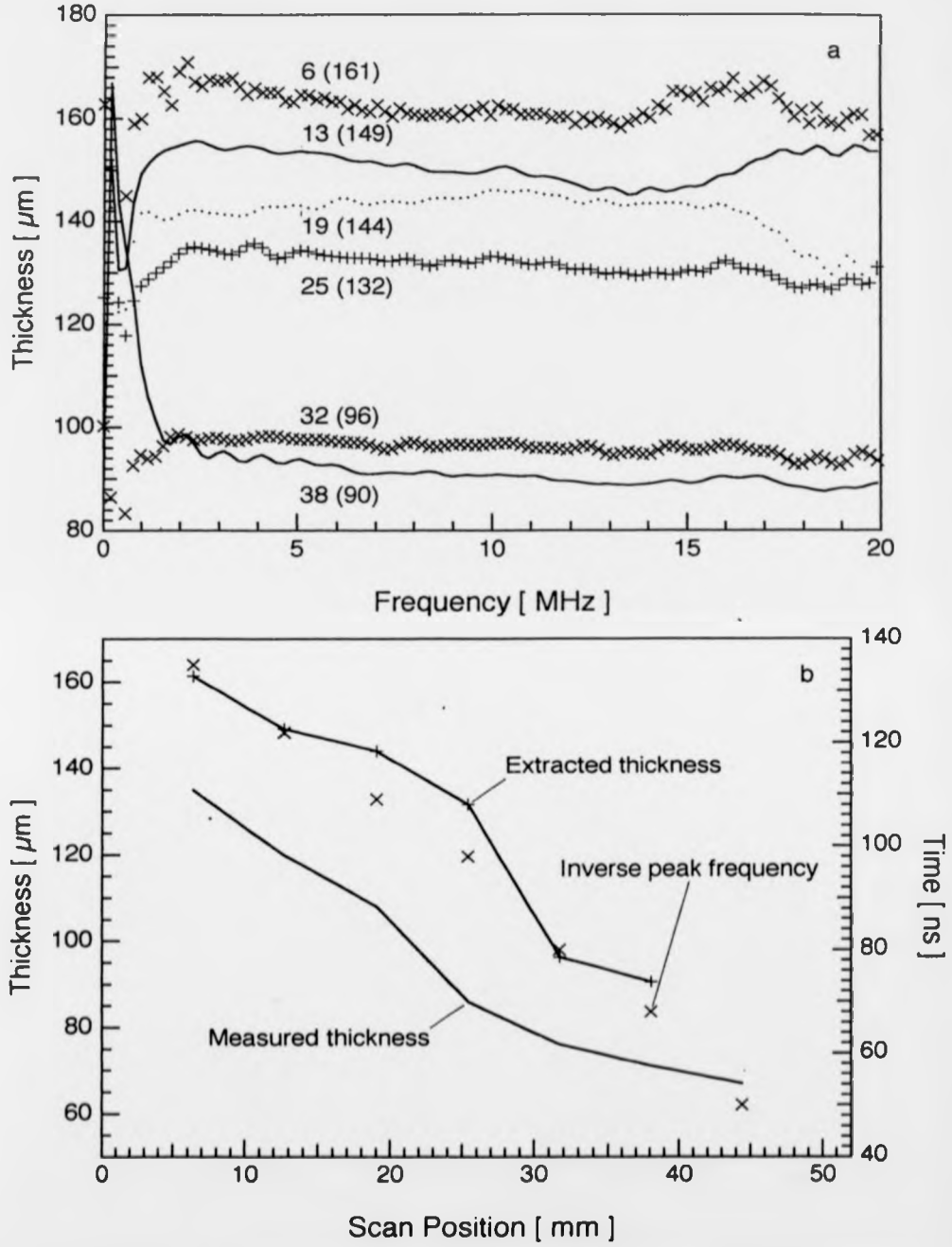

Figure 4.14 Scanning along a decreasing thickness epoxy layer. a). Thickness estimates from EMAT reverberation pulse phase data. b). Intercomparison of thicknesses measured and estimated by different methods.

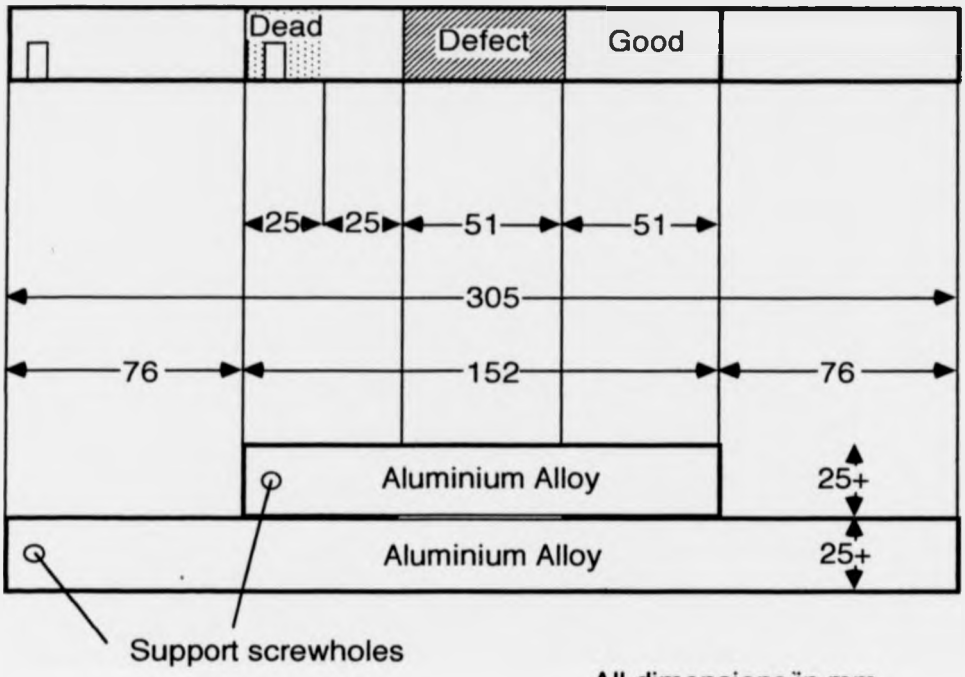

DEFECT TYPES

1. GQ - No adhesive (kept out by wire shims)
2. MQ - Folded Mylar air pocket
3. AQ - Aluminium spacer shim in place of adhesive
4. BQ - Backing plastic left on bottom interface
5. WQ - Wax painted on bottom adherend surface

Figure 4.15 Scale diagram of defective joints, supplied by DRA (Aerospace) using aerospace alloy adherends and CG312/5 epoxy adhesive.

not impractical for these thick samples. While anodizing, the samples are attached at screwholes, which establish unwanted artificial defects that scatter ultrasonic signals heavily in the adherends, causing local dead zones (Figure 4.15). The chosen defects represent possible manufacturing errors and loosely catagorize into those which include an air layer and those, more difficult to spot, in which the defect merely weakens the interface. On-epicentre, through transmission signals were observed at the centre of the good area (defined by the absence of deliberately introduced defect), the transition edge between good and defect and over the defect area centre. However, the cure cycle allows molten epoxy movement which in turn encourages spread or diffusion of defect materials (such as wax) beyond the strict confines of the defect region. I stipulated good and defective areas 51 mm (2") long in order that measurements through the respective centres should provide clear differences in adhesion conditions.

The first defect was created by removing prepreg from the defect area (Figure 4.15) when assembling the joint, and preventing adhesive inflow from good areas during cure with parallel wires bordering the defect edges. As expected, the difference is particularly acute between well-bonded and air gap defect regions, where the reflection coefficient is ~1 (4.1.1) and no ultrasound is transmitted through to a detector (Figure 4.16.a). Bond strength deterioration due to missing adhesive is thus as easy to detect as its effects are severe. The air gap joint's 135 (±4%) ns peak to peak reverberation time is noticeably smaller than for the other bonds as, without solid support, the adherends are squeezed somewhat closer together and thinner adhesive layers result. The same information appears in a fast Fourier transform of the reverberation signals, normalized to the transformed signal from a 50 mm thick solid aluminium block (Figure 4.16.b). A slight frequency decrease at the bond edge location probably results from the boundary wire, which resists compression during cure, thereby enhancing the local thickness.

Volatile gases accumulating in the bond layer can also create large adhesive voids. These cavities are represented by the Mylar air pocket defect (Figure 4.16.c), in which Mylar film is folded over to trap a bubble of air in the adhesive but still allow epoxy to remain round the edges. Once again, amplitude reduction of the direct arrival pulse and reverberations is total in the defect neighbourhood. However, despite a noticeable absence of any arrival through the air gap defect, sufficient adhesive remains round the air pocket edges to guide a small sidewall

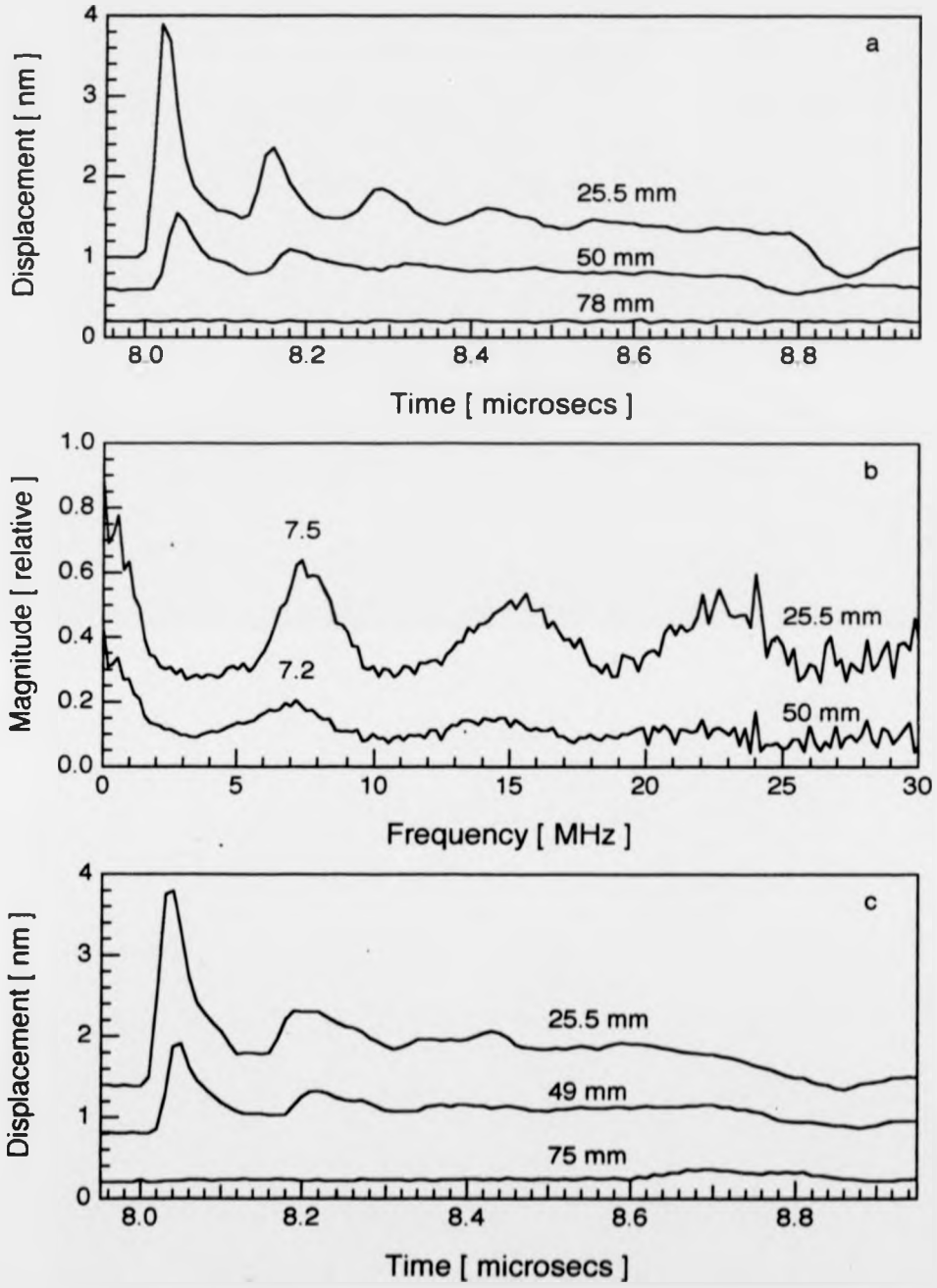

Figure 4.16 On-epicentre arrivals transmitted through bonds with prepared defects: 26 - good, 49 - edge, 75 - defect regions. a). Missing epoxy. b). Fast Fourier transformed missing epoxy data. c). Mylar enclosed air pocket.

echo into the second adherend, where it reaches a detector shortly after 8.6 μs. As the percentage of observed joint area covered by epoxy increases, when scanning across the defect edge say, signal amplitudes rise towards well-bonded levels. There is thus a minimum length scale for void detection, below which the resulting defect amplitude differences are smaller than the usual shot-to-shot variability, but further work is needed to define the relevant limits.

Defects can also result from the presence of solid inclusions, such as the aluminium foil shims used to set joint thicknesses under compression. Three 50 μm thick strips stacked to form a ~150 μm thick foil-filled defect, intermediate between void and weakened interface cases (Figure 4.17.a). The acoustic impedance mismatch between aluminium shim and alloy adherend is small, implying that sufficient pressure applied to the joint will allow monopolar ultrasonic arrivals without reverberations, as for transmission through solid aluminium (Figure 4.2.a). At normal pressures, however, the free foil surfaces merely kiss, trapping thin pockets of air between points of good acoustic contact, and ultrasonic signals in the debond region are erratic (Figure 4.17.a). At 64 mm the defect resembles the air gap disbonds, but at 76 mm a low amplitude signal is detected which appears to contain reverberations. A fast Fourier transform of the signal was divided by the transformed direct pulse, extracted from the 26 mm signal, to obtain a frequency dependent transmission coefficient for the defect (Figure 4.17.b). The transmission coefficient computed, assuming a solid 140 μm thick aluminium layer between aluminium adherends with non-rigid interfaces, agrees reasonably well with observation and predicts reverberations resulting solely from the interface discontinuities. Differences between the two curves arise because the aluminium insert consists of three separate foil layers, allowing additional resonances or even loading by epoxy forced into the defect area when molten.

The remaining two defective bonds rely on interface disruption. The first was created by leaving attached a two inch strip of the backing plastic, which protects the adhesive prepreg prior to use. Unlike intruded aluminium, backing plastic does not produce a disbond, as it softens during the cure cycle and may even dissolve in epoxy, leaving a weakly adhered interface. The backing film is detected in time signals transmitted through the defect (Figure 4.17.c), as good bond measurements on the backing film joint coincide within error to those on the aluminium foil joint, but bond reverberation times increase from 151 ns (±3%) to 190 ns on

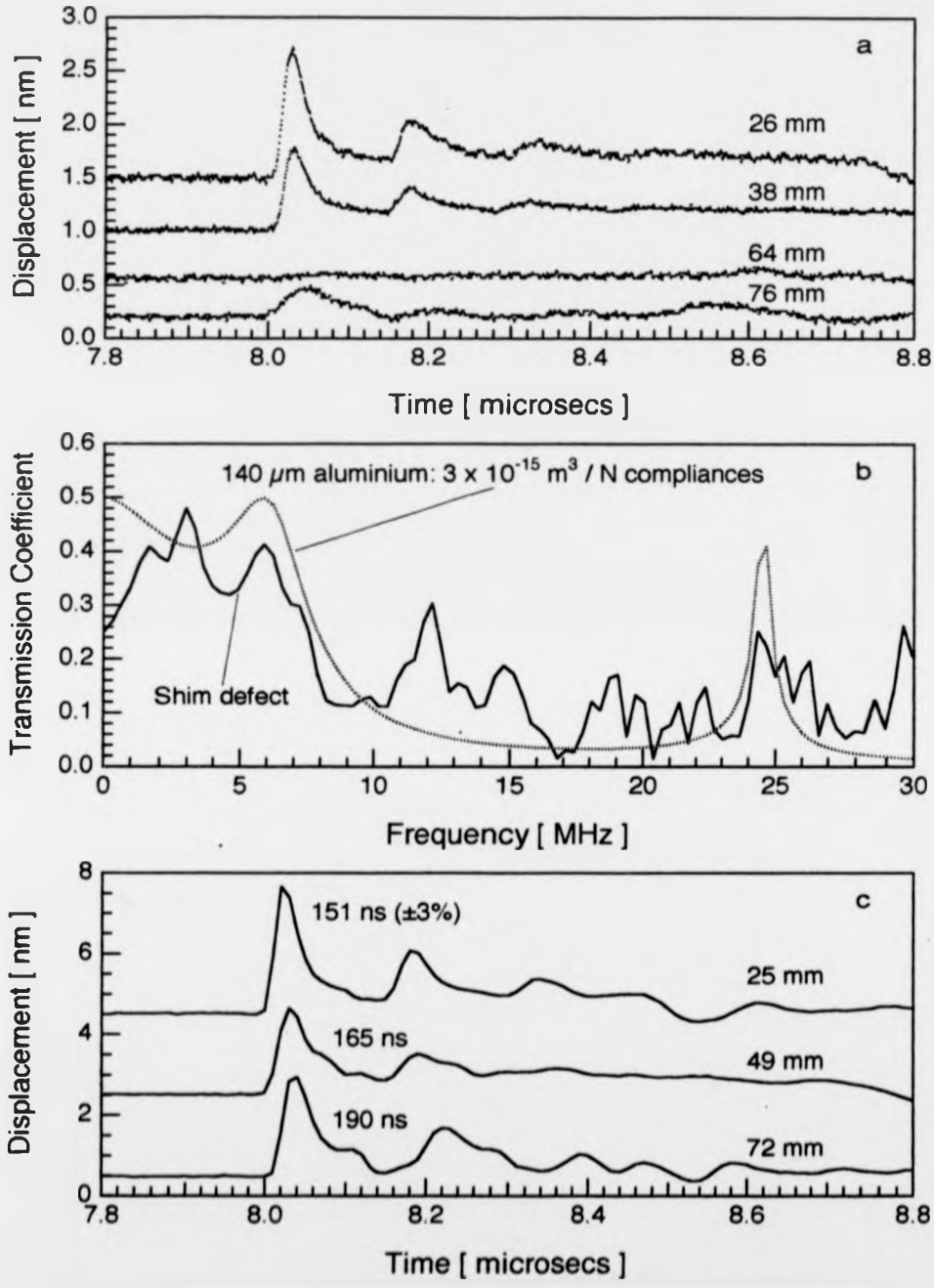

Figure 4.17 Transmission through bond defects: 25 - good, 49 - edge, 75 - defect. a). Aluminium foil shims inserted, b). comparing observed and computed transmission coefficients. c). Backing film left on adhesive surface.

moving into the defect area. Although ultrasound is slowed by passage across a weakened interface, or where the epoxy composition is disrupted, the 25% change is more likely to originate from bond layer expansion, by about 50 μm, due to the extra plastic film thickness.

Time signals detected along the final joint at 12 mm (1/2") intervals, from the well-bonded area to the defect centre, show no such thickness changes (Figure 4.18.a). A 51 mm (2") wide waxed stripe, painted on the lower adherend surface, represents surface contamination, the most insidious class of adhesion defects. Once again, the disruption mechanism is uncertain, as wax melts at the adhesive cure temperature and is expected to diffuse into molten epoxy. Thus, poor adhesion may result from weakened epoxy above the surface or the presence of a wax monolayer remaining at the interface. The waxed stripe behaviour becomes interesting when phase velocity data is extracted from the direct and first reverberation pulses of the (26 mm) good bond and (76 mm) defect signals. Under rigid bonding assumptions, the epoxy longitudinal phase velocity in the defect region drops about 9% from its uncontaminated value over the 5 to 30 MHz frequency range (Figure 4.18.b). By implication, wax uptake into the adhesive is extensive, causing significant behavioural modification in the wax-impregnated epoxy. However, chapter 2.4 suggested that disruption at the interface, requiring neither wax layer mixing nor epoxy velocity changes, could produce the same effect in the ultrasonic transmission. To test this I calculated transmission coefficients using phase velocity and attenuation data extracted under rigid bonding assumptions for the good bond and defect cases (Figure 4.18.c). The good bond transmission was recalculated after introducing a 1.5×10^{-15} m^3 / N compliance at one interface, degrading the rigid bond condition and producing a curve (crosses) in remarkable agreement with that calculated for the defect. Thus, laser ultrasound appears able to distinguish the defect, however caused, although no specific attempt was made to test detection limits by minimizing the amount of wax used [Pialucha & Cawley, 1992].

These defective bonds offer initial evidence that pulsed laser generated ultrasound systems are extremely sensitive to acoustic transmission property changes along bonded samples. Ready distinction, on all five joints, between areas disbonded or believed to be well adhered, encourages progress from A-scans to more usable C-scans. However, further research is needed to calibrate results against destructive tests and set detection limits for each defect type.

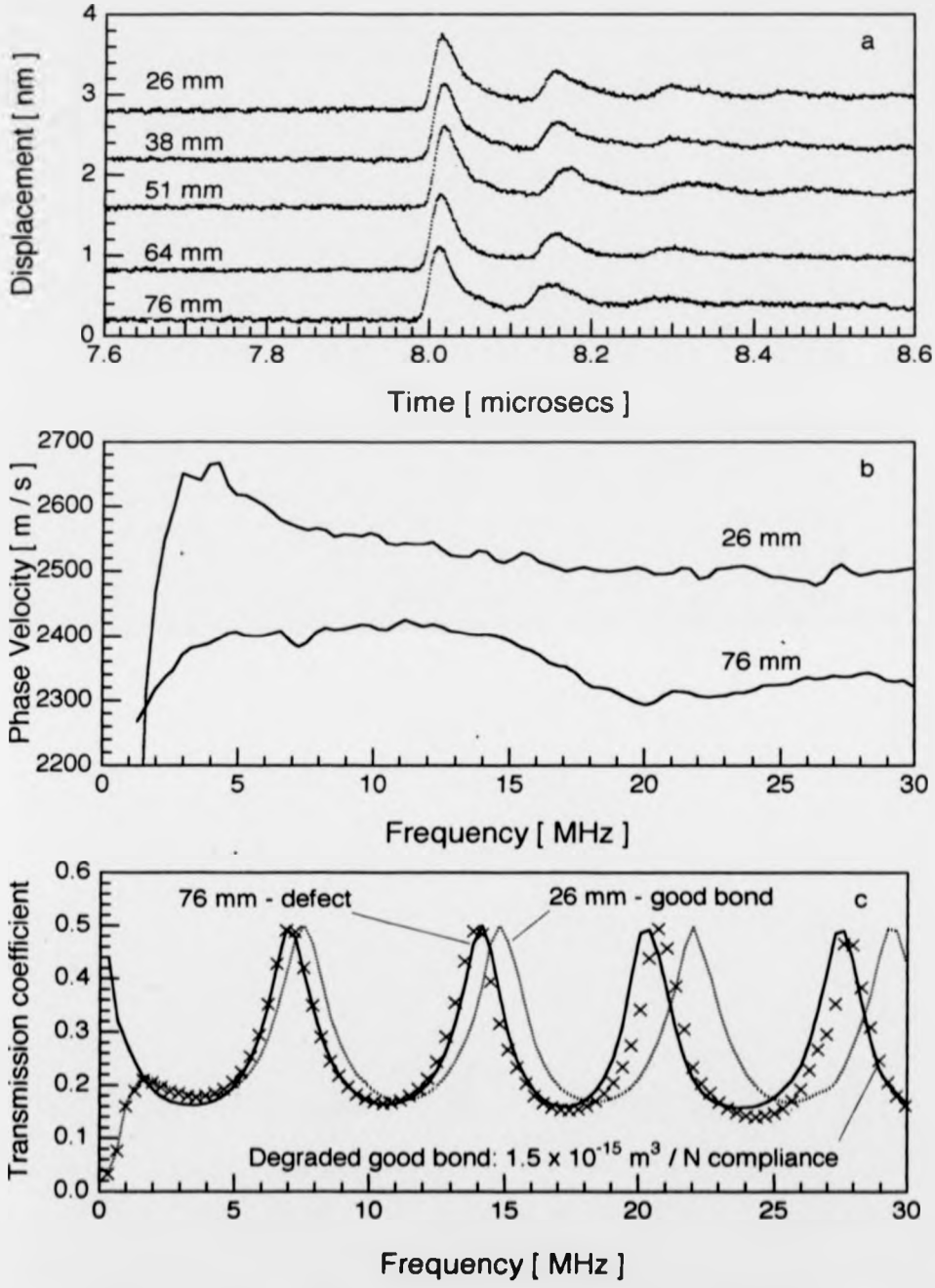

Figure 4.18 Transmission through 170 μm thick epoxy with wax coated surface: 26 - good, 51 - edge, 76 - defect. a). Time signal. b). Extracted phase velocity at 26 and 76 mm. c). Coefficients computed from extracted data.

CHAPTER FIVE

ULTRASONIC SURFACE WAVES OBSERVED ON UNBONDED PLATES

One motive for examining ultrasonic propagation in aluminium alloy plates is to aid the analysis of adhesively bonded joints, presented in Chapters 6 and 7, using interface waves initiated as surface-travelling waves. The surface-interface-surface (SIST) wave approach (chapter 3.2), requires knowledge of the unbonded adherend behaviour as a background against which effects due to changes in the bond can be measured. Radiation of laser-generated ultrasound into the material bulk, for instance, as well as along the surface (see section 3.3) makes it important to identify bulk-travelling arrivals, which reach the detector after reflection at the adherends' outer surfaces and therefore contain no information about the bonded interface. Upon adherends that are thick, with respect to the ultrasonic wavelengths used, low amplitude bulk reflections arrive at widely spaced intervals. Taking progressively thinner samples, bulk and surface components become increasingly difficult to separate, until distinction between the two loses meaning and thin plate waves are observed. Sections 5.1 and 5.2 investigate the behaviour of ultrasonic pulses generated on various thickness aluminium and aluminium alloy plates, in order to establish the range over which pulsed laser generated ultrasound excites the non-dispersive plate wave modes most suitable for probing bonds. According to strict definition, plates should possess thicknesses far smaller than lengths in the remaining two dimensions. However, the line sources invariably used for surface wave generation radiate negligibly parallel to the source axis, unlike the point sources in Chapter 4, so that sidewall reflections are not seen from surfaces perpendicular to the source. I thus treat the thicker samples as plates, even when they are roughly square in cross-section and more rod-like or block-like in appearance.

The surface-travelling wave transition from thick plate Rayleigh regime to that of the thin plate zero order Lamb modes anyway merits observation, as laser work has tended to focus on these two extreme cases, using ultrasonic pulses with wavelengths all either above or below the plate thickness. Narrowband transducers detect much sharper transitions for individual frequencies (Jarosz, 1991) and the extended transition waveforms, observed when wavelengths in a broad bandwidth pulse straddle the plate thickness, are poorly documented. Looking at both in-plane and out-of-plane motions has also produced a useful comparison between the two

EMAT detectors (chapter 3.6) and the He-Ne laser Michelson interferometer (chapter 3.5). Traces presented in section 5.2 indicate clearly the relative usefulness of these different detectors on aluminium samples with a wide range of thicknesses.

For optimum results, section 5.2 observations suggest interferometric detection on thick aluminium samples, to guarantee dispersion effects due solely to interaction with the adhesive bond. However, close examination of unbonded control samples revealed a second source of surface-travelling wave dispersion on thick plates, due to a thin, hardened surface layer probably arising from the extrusion methods used to produce them. Although the preparation of joints for bonding does, unfortunately, damage the surface as a result of the etching and anodizing processes, it is unlikely that these alone are responsible for the effects observed. As surfaces which have been milled do not exhibit such dispersion, section 5.3 examines the hardening effect. On test samples the presence of small amplitude variations due to dispersion can be partly offset by keeping the source to detector distance fixed and concentrating on differences which emerge as a result of changing the bond. This requires that all the samples are assembled from roughly identical bars and is impractical for industrial process monitoring.

5.1 The Propagation of Ultrasound in Aluminium Plates.

The propagation of ultrasonic waves along a plate, parallel with its surfaces, is governed by the Rayleigh-Lamb frequency equation [Lamb, 1917]. For single-frequency plate excitations, this equation gives a numerical relationship between the frequency and wavelengths of various plate oscillation modes. For symmetric and antisymmetric motions of the plate respectively:

$$\tanh(\beta h) / \tanh(\alpha h) = 4\alpha\beta k^2 / (k^2 + \beta^2)^2 \qquad \ldots 5.1.1\ s$$

$$\tanh(\beta h) / \tanh(\alpha h) = (k^2 + \beta^2)^2 / 4\alpha\beta k^2 \qquad \ldots 5.1.1\ a$$

where, $\alpha^2 = k^2 (1 - (\omega / kC_L)^2)$, $\beta^2 = k^2 (1 - (\omega / kC_T)^2)$,

ω and k are the frequency and wavenumber of the propagating wave, 2h is the plate thickness, C_L is the longitudinal velocity and C_T is the shear velocity of ultrasound in the plate material.

The solutions to equation 5.1.1 simplify in two limiting cases, where the acoustic

wavelengths are much longer or, conversely, much shorter than the plate thickness. When all wavelengths in a broadband ultrasonic pulse are much shorter, the case approximates that of ultrasound propagating along the surface of a semi-infinite medium [Rayleigh, 1885]. Rayleigh's formulation of the elasticity equations is obtained from equation 5.1.1 by letting hk $\rightarrow \infty$. For both symmetric and antisymmetric waves:

$$C^3 - 8C^2 + 8(3 - 2C_T^2 / C_L^2)C - 16(1 - C_T^2 / C_L^2) = 0 \qquad \ldots 5.1.2$$

where $C = \omega^2 / k^2 C_T^2 = C_R^2 / C_T^2$.

The cubic's lowest positive root, lying between 0 and 1, yields the phase velocity of a non-dispersive, Rayleigh wave (Figure 5.1.a) travelling parallel to the surface. Despite ultrasonic wavelengths in aluminium lying around 3 mm at 1 MHz, surface displacements (depicted out of scale) are ~1 nm with particles moving in retrograde elliptical orbits. The Rayleigh wave is distinct from other waves that radiate into the bulk of a semi-infinite medium, in that its amplitude decays exponentially with depth [Viktorov, 1967], only disturbing material less than a few wavelengths below the surface. In plates thicker than a few Rayleigh wavelengths, surface-travelling waves are unaware of a second surface, encountered at depths where they excite negligible displacements, and closely resemble Rayleigh waves. Thus a broadband surface-travelling ultrasonic pulse generated on a thick metal plate will be non-dispersive and have an appearance independent of plate thickness. The principal effect of the second surface is to redirect radiated energy back towards the first, so that surface and bulk waves are no longer completely decoupled. However, pulses with energy confined near the surface lose amplitude more slowly with increasing source distance than isotropically radiating bulk waves, making thick plate surface and bulk components readily separable.

As the plate is made thinner, reflected bulk waves traverse less material, resulting in greater amplitudes and shorter time interval separations when they reappear at the surface. At the same time, an increasing proportion of the component wavelengths exceed the plate thickness, causing the sharply-pulsed surface wave observed on thick plates to disappear. This is associated with a progressive loss of the lowest frequency (long wavelength) contributions to the Rayleigh pulse as the depth of plate material becomes small enough to affect their dispersion characteristics.

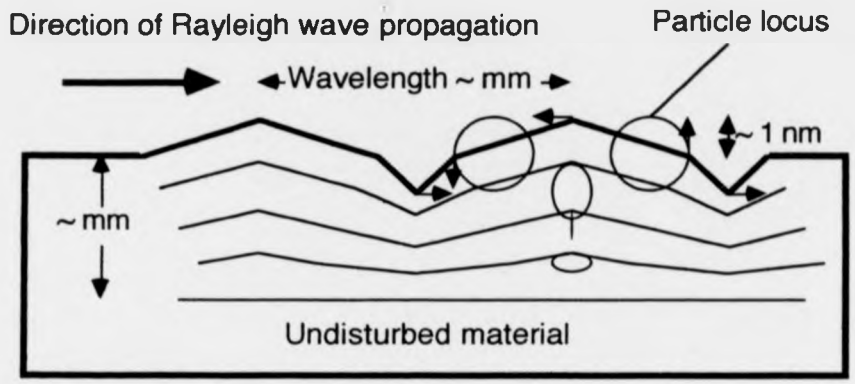

a. Surface wave propagation on thick plates: elliptical surface motion

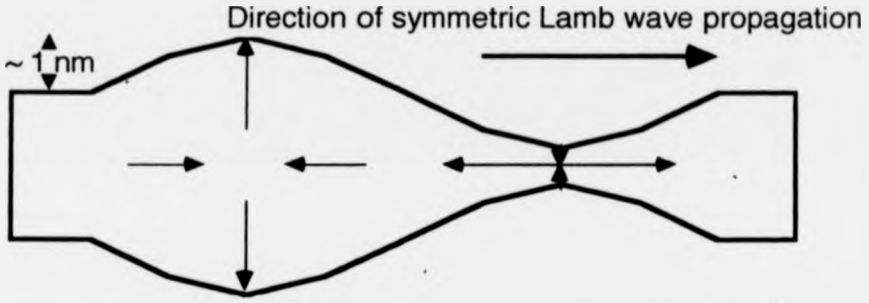

b. Thin plate zero-order Lamb mode: in-plane & out-of-plane motion

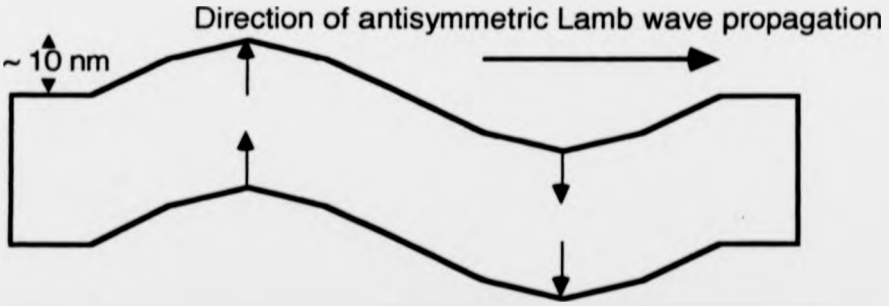

c. Thin plate zero-order Lamb mode: mainly out-of-plane motion

Figure 5.1 Illustration of ultrasonic plate modes. a). Rayleigh wave on thick plate. b). Symmetric zero-order Lamb wave. c). Antisymmetric zero-order Lamb wave.

Examination of calculated dispersion curves [Viktorov, 1967] suggests an approximate frequency $f_{min} \approx 8C_T / 2h\pi$ below which, for given plate thickness 2h, Rayleigh waves cannot propagate. Taking $C_T = 3140$ m/s in aluminium, a 12.8 mm plate thickness gives $f_{min} = 620$ kHz, while a 1.72 mm thickness raises f_{min} to 4.6 MHz. Fourier transforms of the Rayleigh pulses show low magnitudes for frequencies above 5 MHz, and it thus comes as no surprise in section 5.2 to see that 1.72 mm is the thinnest plate upon which arrivals at the Rayleigh velocity are discerned.

Setting $hk \rightarrow \infty$ as one limit in the Rayleigh-Lamb equation, suggests an opposite limit where the plate thickness is small compared with all wavelengths in an ultrasonic pulse. Rayleigh waves no longer exist because disturbances on one surface have insufficient depth to decay completely and therefore create disturbances at the opposite surface too. At the same time, reflected bulk waves arriving at a detector sited many plate thicknesses away from the source are packed so closely together in time that they cannot be detected individually. Instead, the separable surface and bulk waves are replaced by Lamb modes, which affect both surfaces simultaneously but travel along the plate parallel with the surfaces (Figure 5.1.b &.c). This behaviour can be approximated by letting $hk \rightarrow 0$ in equations 5.1.1s & a, which on expanding small terms leads to expressions for the zero-order Lamb mode phase velocities:

$$V_S^2 = \omega^2/k_S^2 = 4C_T^2 (1 - C_T^2 / C_L^2) \quad \ldots 5.1.3$$

$$V_A^2 = \omega^2/k_A^2 = (1/3) h^2 k_A^2 V_S^2 \quad \ldots 5.1.4$$

where V_S, V_A are the phase velocities of the S_0 symmetric wave and A_0 antisymmetric wave.

The symmetric wave thus behaves non-dispersively on infinitessimally thin sheets and travels at the finite, sheet wave velocity. Calculations show that the symmetric wave displaces particles primarily in the plane of the sheet [Hutchins et al., 1989]. The antisymmetric wave on the other hand is dispersive, moves progressively more slowly as the plate thickness reduces and is accompanied by mainly out of plane displacements. Equations 5.1.3 and 5.1.4 apply to a homogeneous, isotropic, thin sheet, allowing a single ultrasonic pulse measurement of the A_0 and S_0 velocities [Dewhurst et al., 1987] to determine both thickness and, for known Poisson's ratio, the material elastic constants. Expressed through C_L and C_T, the elastic constants can be estimated without the Poisson ratio if the A_0 mode series expansion contains the next higher

order term ($\omega \approx ak^2 + bk^4$) [Hutchins et al., 1989]. These methods rely on velocity measurements, which are more readily repeatable than amplitude readings, but of course break down if dispersion effects make it impossible to identify an individual feature to which a velocity can be assigned. In principle though, elastic constants of plates which are thick, compared with the shortest pulse wavelengths, can be deduced by matching theoretical and experimental waveforms [Spicer et al., 1990]. Such numerical procedures would be heavy on computer time and, for optimum results, require accurate guessing of the temporal and spatial acoustic source distributions, which can vary with each laser shot. But in circumstances where the velocity is unmeasurable, or not visibly altered by changes in properties of the materials under test, such analysis of waveform amplitude as a function of time is necessary. An early experimental priority, therefore, is to assess which adherend thicknesses will support surface-travelling waves with the clearly-defined features desired for simple analyses.

5.2 Acoustic Waves in Plates of Varying Thickness.

This section presents a series of experiments on aluminium samples with thicknesses ranged from 63 mm down to 28 μm, using broadband ultrasound generated by a laser line source (Figure 5.2). The pulses were generated by ablation (see chapter 3.3) on the thicker plates –thermoelastic sources produced sufficient amplitudes on thin plates– and contained frequency components from below 1 MHz to 30 MHz (wavelengths greater than 5 mm down to 100 μm). The ultrasonic signal was detected on the same surface 20.0 mm (±2%) from the source with electromagnetic acoustic transducers (EMATs), sensitive either to the normal or tangential surface velocity (chapter 3.6), and a stabilized homodyne laser interferometer operating at the 632.8 nm HeNe wavelength (chapter 3.5). The sample was positioned normal to the Nd:YAG beam for EMAT measurements, but had to be tilted to let the larger interferometer observe at 20 mm without blocking the generator beam. Light from the reflected Nd:YAG pulse, or the ablated plasma, was blocked from entering the interferometer by aperturing the He-Ne beam and positioning a blast guard near the surface. The blast guard damped larger amplitude disturbances on thin foils, which forced alternative positioning of the interferometer on the back surface 20 mm off-epicentre (Figure 5.2) on samples under 0.5 mm thick. Signals due to symmetric and antisymmetric waves are respectively unaltered and inverted upon

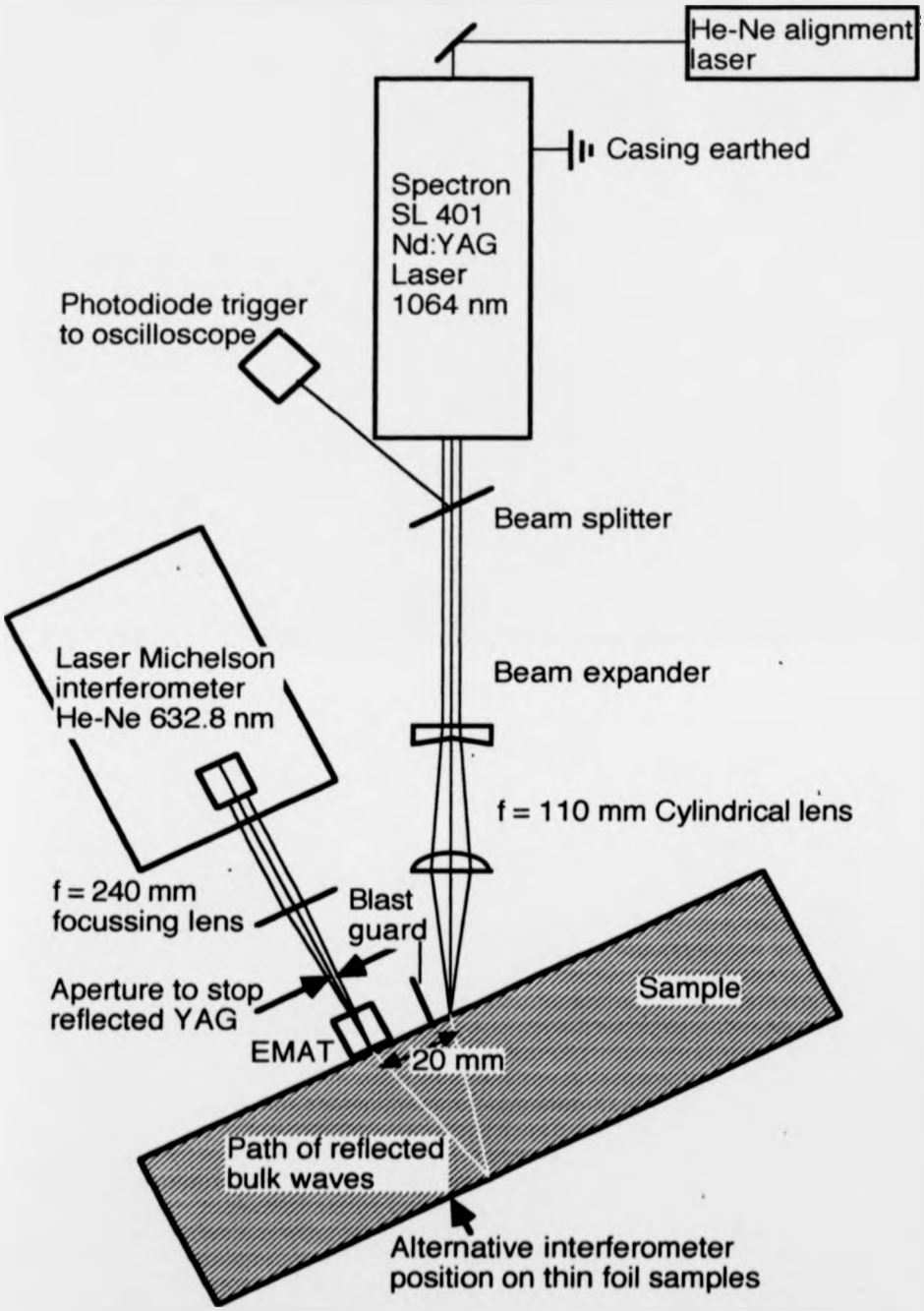

Figure 5.2 Schematic diagram showing arrangement for laser generation of plate waves, with detection by either EMAT or laser Michelson interferometer (both illustrated).

repositioning, so that no information is lost by the manoeuvre. The interferometer bandwidth is 1 kHz to 75 MHz, compared with a 3.5 kHz to 10 MHz bandwidth on the preamp (gain of 200) used to amplify EMAT output. Traces from both detectors were captured on a Lecroy 9400 digital storage oscilloscope.

The first set of waveforms (Figure 5.3) depict surface arrivals on 63.16 (±0.02) mm and 25.20 (±0.02) mm thick aluminium blocks, originating from an ablating line source (compare Figure 3.7). The ultrasonic signal onset is marked by the arrival of a surface-skimming longitudinal head wave (P): noise on the EMAT traces before this point is due to electromagnetic interference from the pulsed laser. Surface waves (R) travelling at the Rayleigh velocity (roughly half that of the surface P wave) are clearly seen, with components normal (Figure 5.3 a & b) and parallel (Figure 5.3 c) to the surface as predicted by theory. There is also no major difference in surface-wave shape for the two plates, although decreasing thickness decreases (from infinity for true Rayleigh waves) the time taken by waves radiated into the bulk to reemerge at the surface after reflection or mode-conversion off the sample back wall.

Bulk arrivals are identified (Figure 5.3) by the number of transits made as longitudinal (p) or shear (s) waves. The reflected pulses have greater amplitudes as the thickness diminishes but, in these thick plates, are still well-separated in time and easily distinguished from the larger Rayleigh signal. Another feature which characterizes most bulk waves is their arrival at angles nearly normal to the surface, disturbing almost simultaneously the entire area under a detector. Comparing 2p (bulk) and p (head) arrivals highlights the detected pulse broadening in surface-travelling waves, for which transit times beneath a detector are maximized. Both EMATs have 1 mm wide coils and consequently detect a Rayleigh wave which appears broadened relative to that observed by the interferometer [Edwards & Palmer, 1989], where the detector size was limited by focussing the laser spot. Displacement sensitive interferometer traces also confirm the relative enhancement of low amplitude bulk arrivals by the EMATs, a result of their sensitivity to velocity. Differentiating the 25 mm interferometer displacement waveform (Figure 5.3.a) with respect to time allows a direct comparison with EMAT data for the same plate (Figure 5.4). Apart from the increased widths of the EMAT arrivals, interferometer and normal EMAT waveforms (Figure 5.4.a &.b) are very similar. Normal EMAT arrivals not detected by

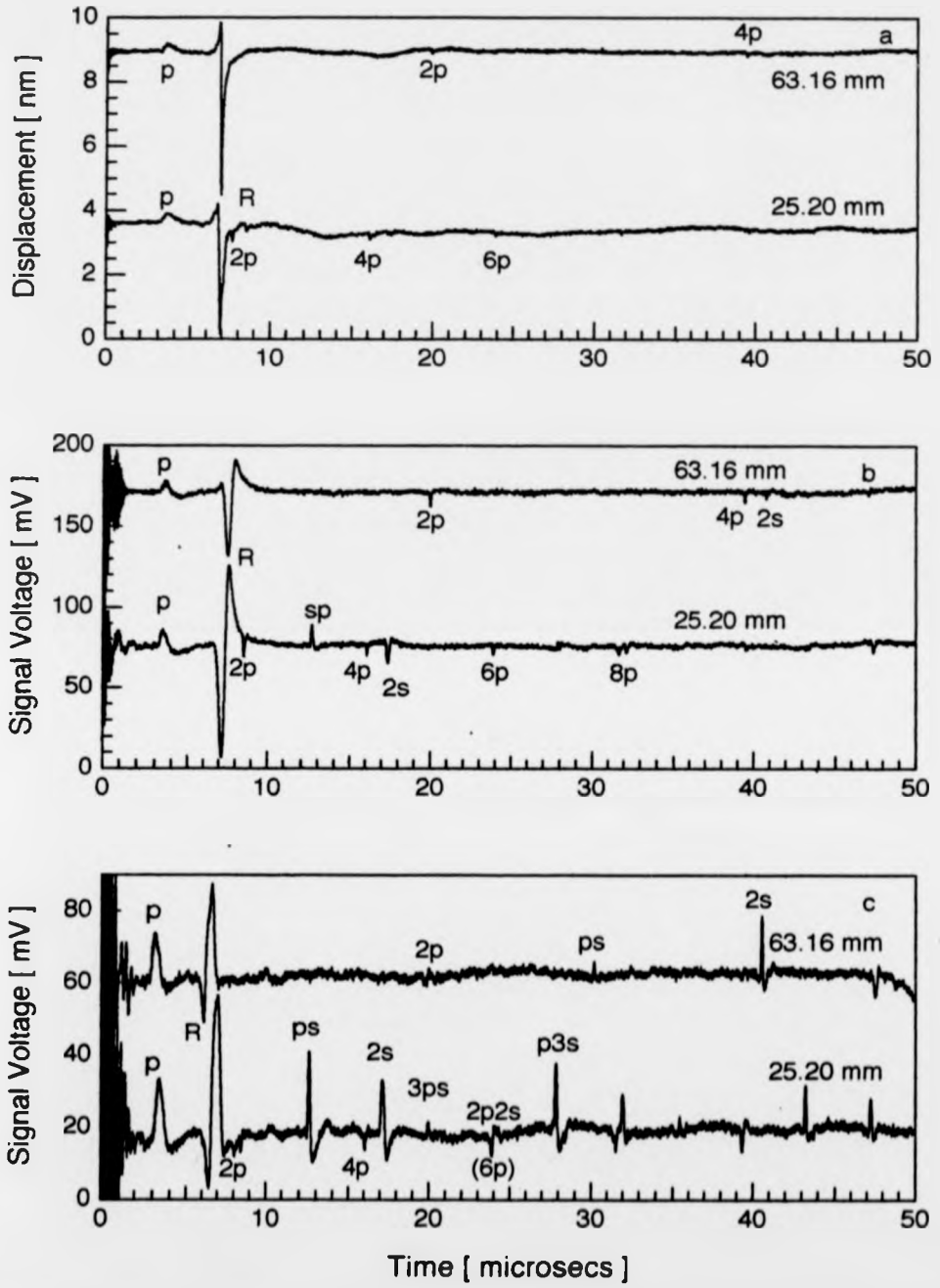

Figure 5.3 Ultrasonic pulse arrivals detected on thick aluminium samples by a). 632.8 nm laser Michelson interferometer b). normal EMAT (detects mainly out-of-plane motion), c). shear EMAT (detects mainly in-plane motion).

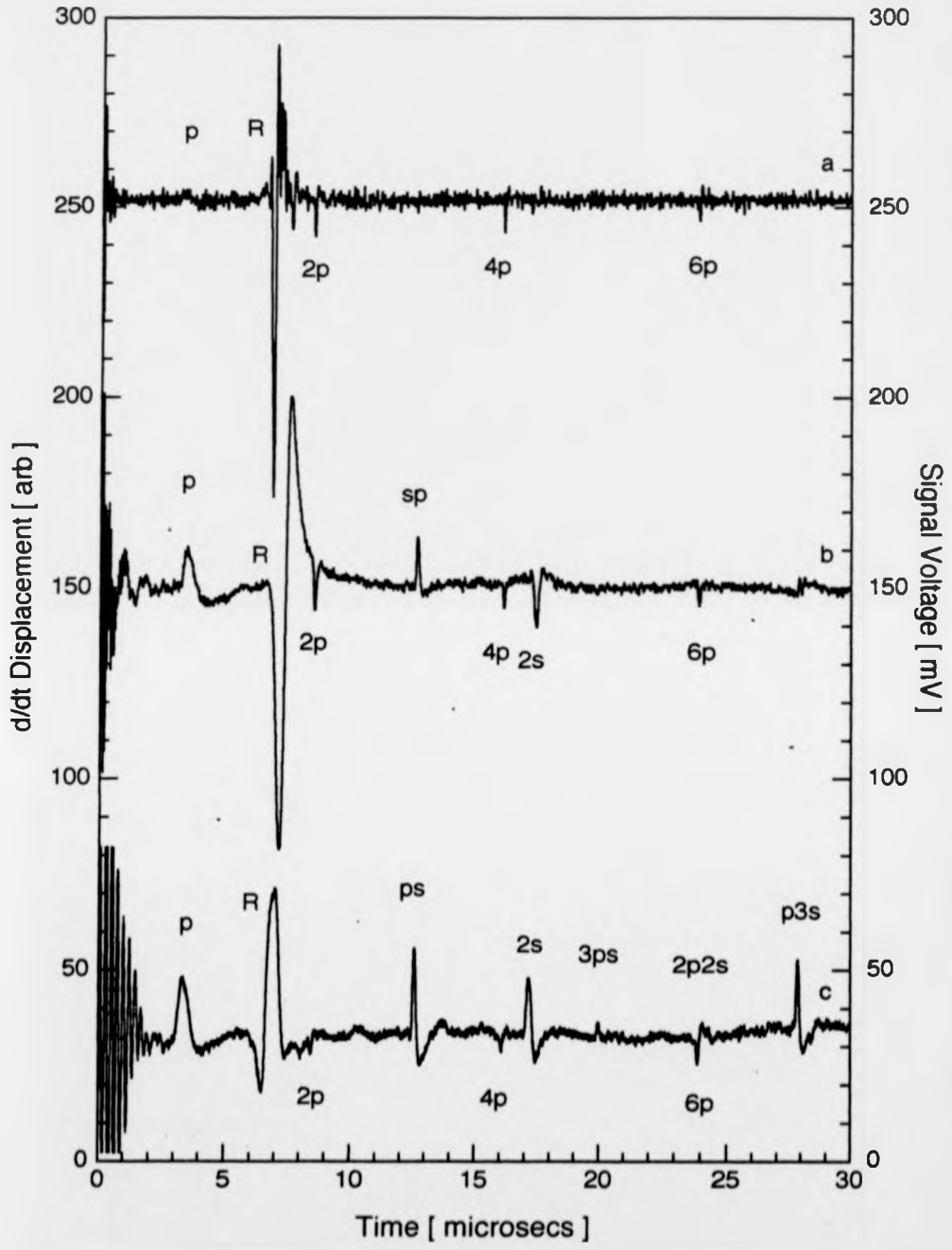

Figure 5.4 Comparison of surface displacement rates on 25 mm thick aluminium sample. a). Smoothed interferometer trace, time differentiated and normalized to Rayleigh peak of b). normal EMAT signal. c). Shear EMAT signal.

the interferometer are attributed to EMAT magnetic field fringing effects, which occasion a degree of sensitivity to the in-plane surface motion detected by the shear EMAT (Figure 5.4.c).

Moving on to the other plate thickness extreme, interferometer waveforms detected on 28 μm (±4%) and 53 μm (±4%) aluminium foils (Figure 5.5.a) show the very large amplitude zero order antisymmetric Lamb mode (A_0) arrival. EMAT velocity sensitivity is again apparent from the enhancement of the symmetric sheet wave (S_0), which arrives at the same time in both foils, exciting out-of-plane and a greater amplitude in-plane motion. The interferometer detects a small out-of-plane displacement at the S_0 arrival (Figure 5.6), which is lost on traces scaled to A_0 arrival amplitudes at frequencies below 1 MHz (Figure 5.5.a). As plate thicknesses increase from 108 μm to 441 μm, the S_0 arrival is encroached and finally submerged by the front-running, high frequency, A_0 mode components (Figure 5.6.b) which, in accordance with dispersion relation 5.1.4, have the highest phase velocities. The shear EMAT detects little in-plane motion associated with the A_0 mode, which corresponds to flexural plate motion virtually free of shear (Figure 5.5.c). However, the normal EMAT should sense A_0 arrivals detected by the interferometer (Figure 5.5.a) and an apparent absence of antisymmetric motion in the 28 μm foil (Figure 5.5.b) is probably due to mechanical damping of large amplitude displacements, given the EMAT's proximity to the surface. Unlike the interferometer, where the detector spot is point-like, EMAT detector areas are spatially broad, integrating contributions received at each point across the active detector width [Edwards & Palmer,1989]. Thus on the 53 μm A_0 wavetrain, the signal seen by the interferometer (Figure 5.5.a) is seen by the EMAT as a superposition of waves, which interfere destructively at around 23 μs (Figure 5.5.b).

Variations in displacement waveforms on plates from 12.80 mm down to 108 μm thick were also observed by the interferometer, still placed at 20 mm (±2%) from a generating laser line source. Referring to the large and small thickness plate displacements (Figures 5.3.a & 5.5.a) indicates an order of magnitude signal amplitude increase as the plate thickness drops from 12.8 mm to 108 μm. The interferometer waveforms (Figure 5.7) are therefore presented in their unscaled digitized format, in which integer values between 0 and 255 represent the amplitude range across the storage oscilloscope screen. Each trace is directly proportional to displacement. The Rayleigh wave amplitude is seen to fall with respect to those of other Lamb

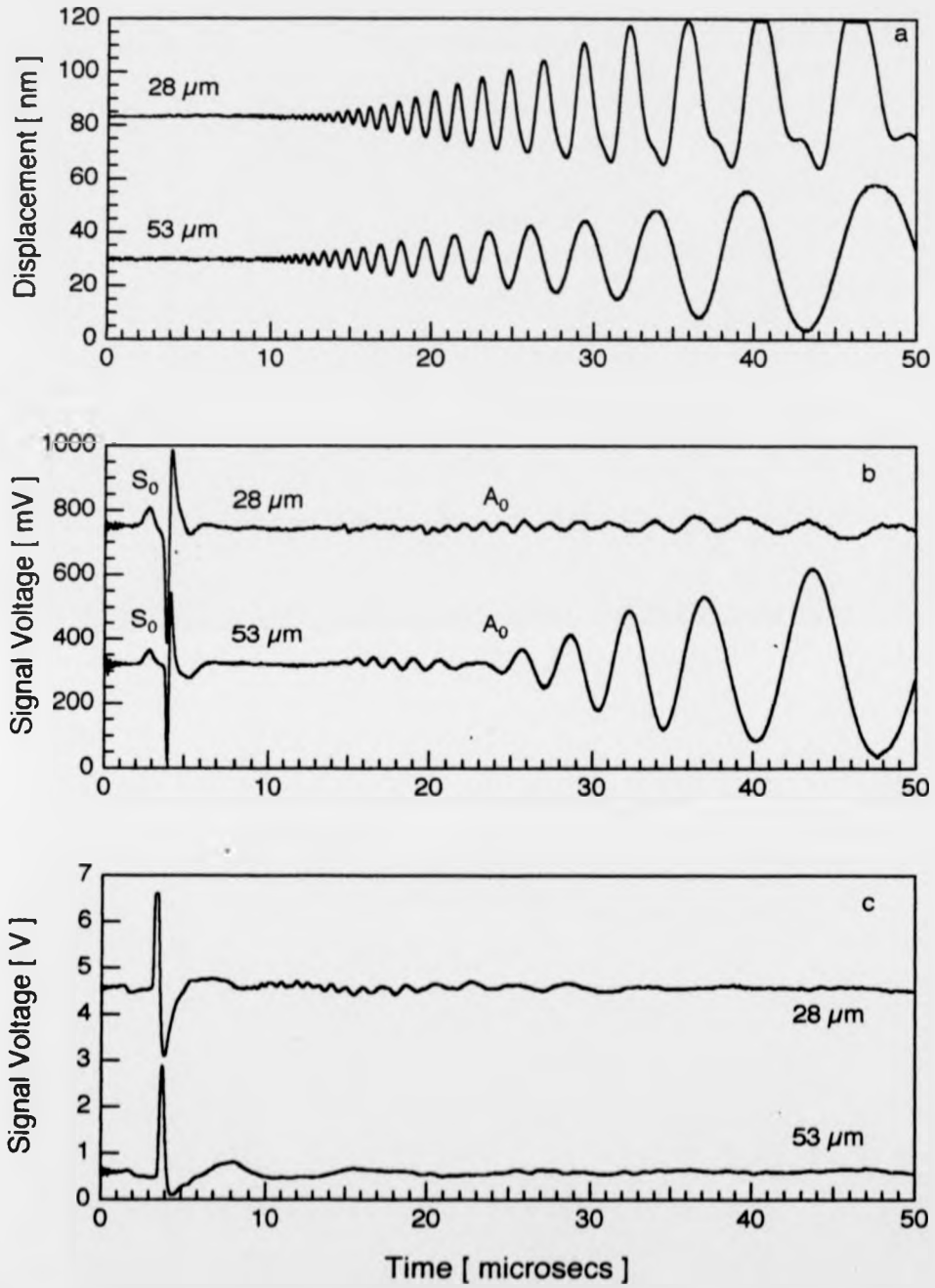

Figure 5.5 Ultrasonic plate waves detected on thin aluminium foils. a). A_0 mode predominates in 632 nm laser Michelson interferometer traces. b). Normal EMAT senses both zero order modes. c). Shear EMAT senses S_0 only.

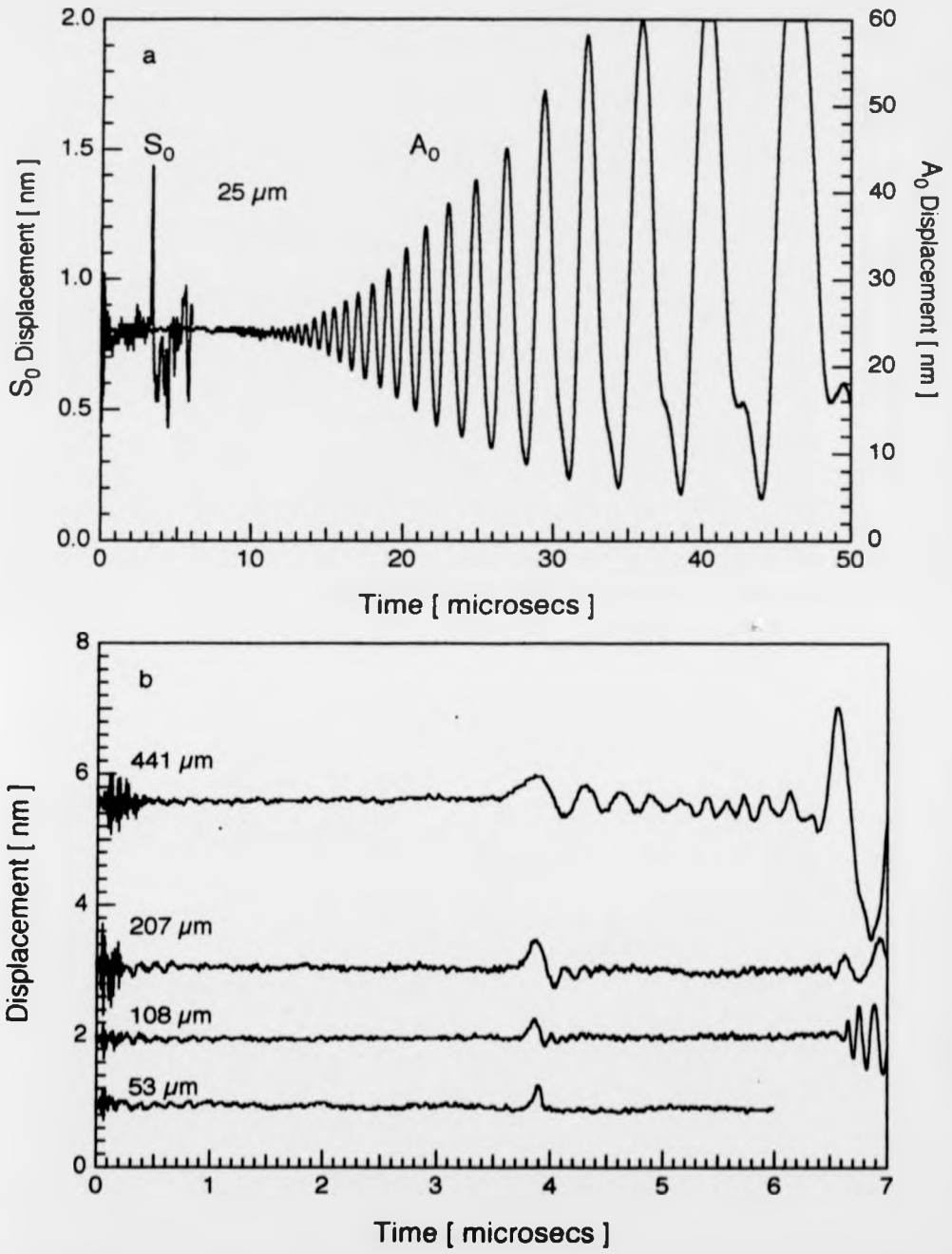

Figure 5.6 Thin plate waves detected by 633 nm laser Michelson interferometer on aluminium. a). Comparing symmetric and antisymmetric arrivals on 25 μm thick plate. b). Symmetric arrivals on different thickness samples.

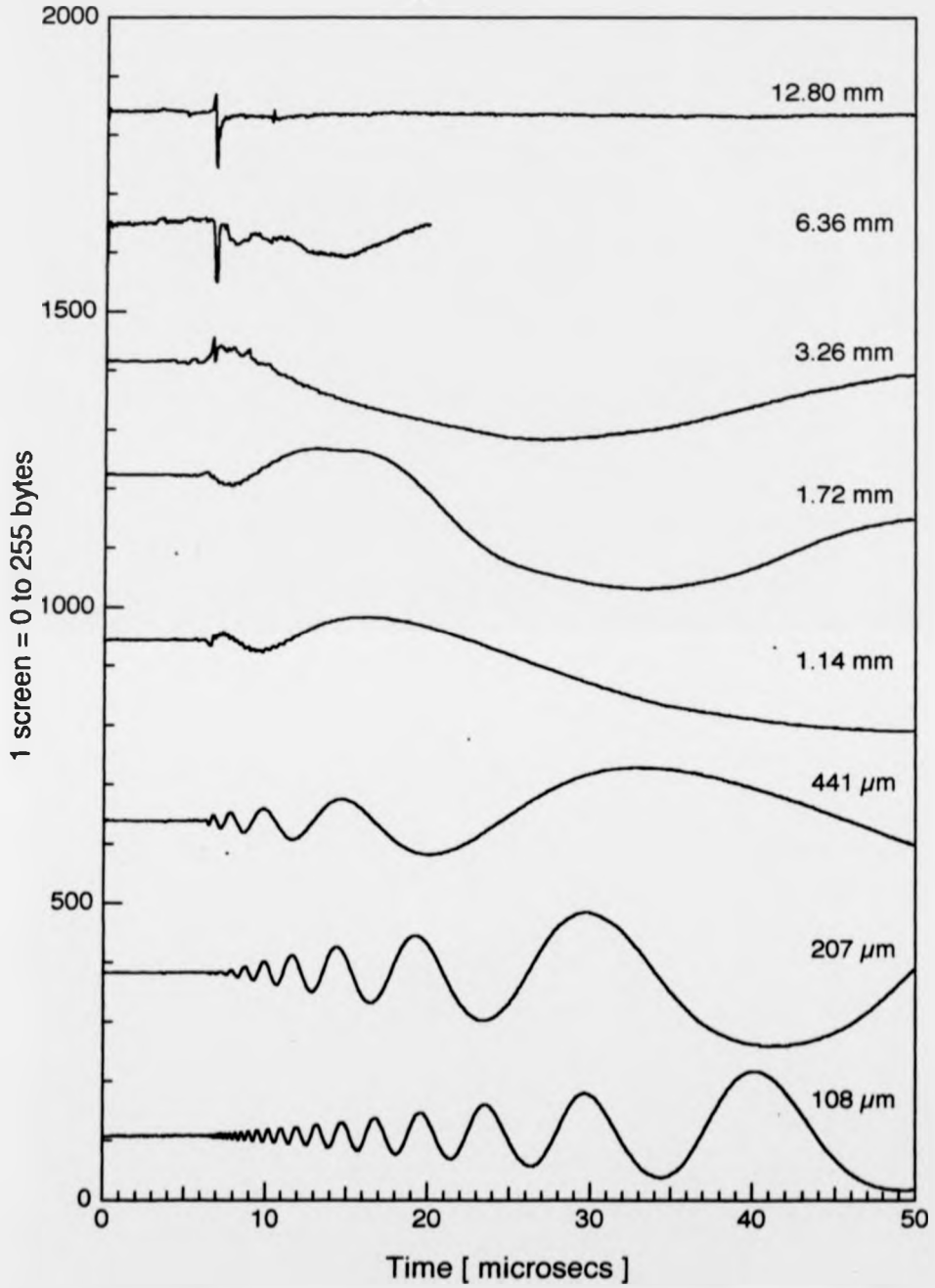

Figure 5.7 Ultrasonic signals detected by 632.8 nm laser Michelson interferometer on intermediate thickness aluminium plates. Traces proportional to displacement viewed as on digital storage oscilloscope screen.

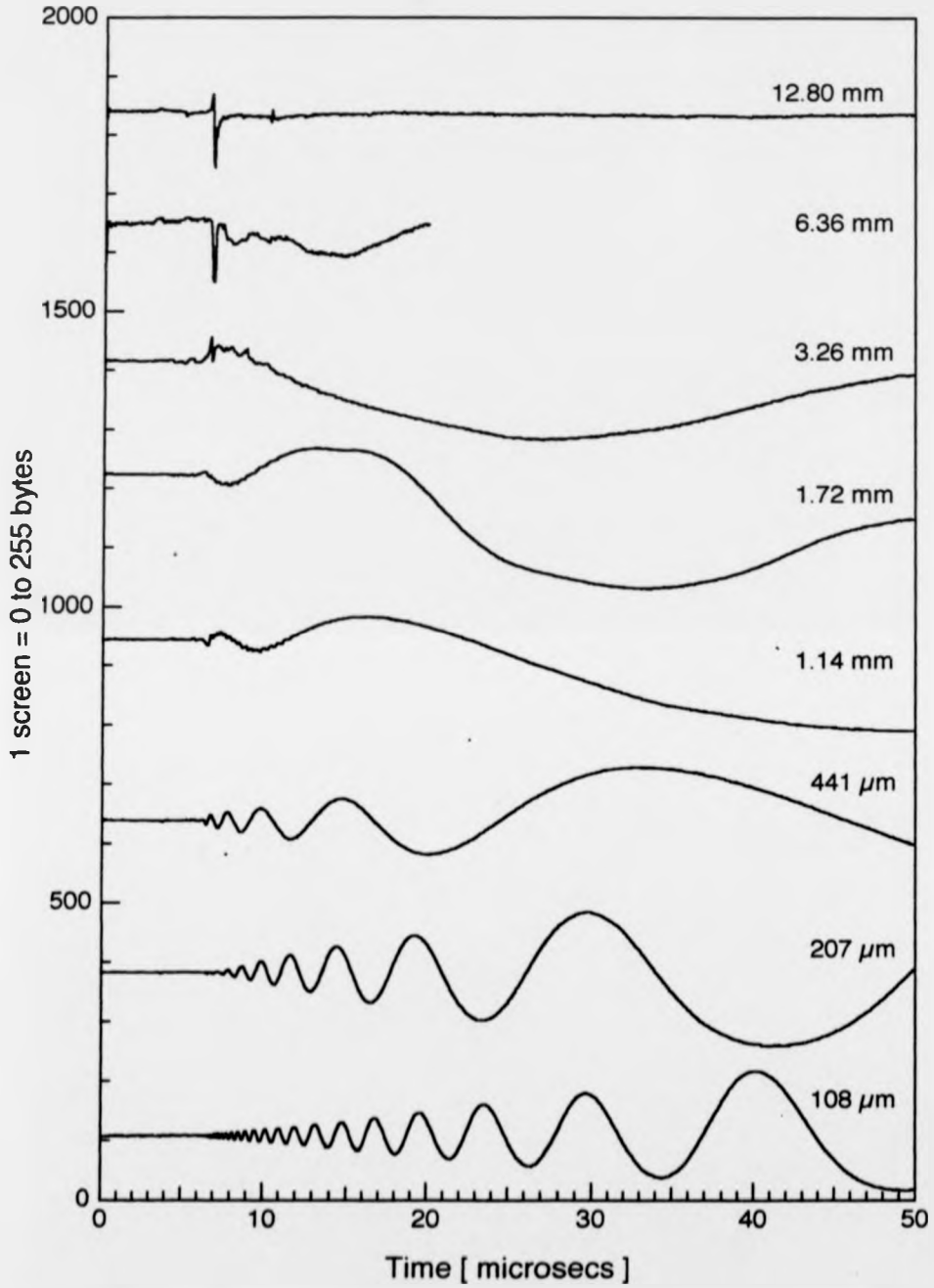

Figure 5.7 Ultrasonic signals detected by 632.8 nm laser Michelson interferometer on intermediate thickness aluminium plates. Traces proportional to displacement viewed as on digital storage oscilloscope screen.

modes, amongst which it is finally lost, as the plate thickness decreases. Normal EMAT and shear EMAT traces (Figures 5.8 & 5.9) for the same plates, show the amplitude increases more explicitly. They also illustrate the bulk wave arrivals on intermediate thickness plates piling up behind the vanishing Rayleigh arrival into characteristic "dragon-spine" curves, before merging totally on thin plates into the smooth low frequency envelopes of the zero order Lamb modes.

The search was for plate thickness and wave mode combinations that let sharply-pulsed surface-travelling waves in aluminium propagate undispersed. One candidate is the non-dispersive Rayleigh wave. The 12.80 mm (±0.5%) plate is the thinnest examined (Figure 5.7) for which the interferometer detects a sharp Rayleigh pulse that is not followed by a significant amplitude dispersive wavetrain, and it is dubious if the EMATs are useful even on 12.80 mm plate. A fast Fourier transform of the Rayleigh pulse observed by the interferometer on 63.16 (±0.02) mm thick aluminium (Figure 5.10.a) suggests detected pulse frequencies up to 14 MHz, when low magnitudes and random phases indicate a signal submerged by noise. Laser generated, through transmission pulses exhibit frequency ranges 3 times wider (Figure 4.2.b), due partly to a switch from point to line source for surface waves, but mainly to the longer transit times of slow moving surface pulses across the detector spot. The normal EMAT, limited by poor sensitivity to low frequency motions and a wider detection area, detects the same pulse with a bandwidth between 250 kHz and 2.5 MHz (Figure 5.10.b). Rising phase above 2.5 MHz is an artifact of the phase unwrapping routine under random phase conditions. Thus, unless ruled out by operational considerations, the Michelson interferometer is far better for SIST wave detection on plates above 12 mm thick. For pulses generated by the laser arrangement described above (Figure 5.2), a 12 mm to 440 μm transition thickness range exists, over which there is no sharp arrival at the Rayleigh velocity but zero order Lamb modes have yet to dominate. Subtle dispersion effects, due to varying adhesion, in SIST waveforms on plates with thicknesses in this range will be extremely difficult to detect. However, the limits should only be taken as approximate because thickness ratios to wavelength and to source-to-detector distance both affect the onset of dominant A_0 and S_0 modes. On the 207 μm (±1%) thick plate the EMATs, especially the shear EMAT, are very sensitive to sharply-pulsed, non-dispersive sheet waves, suggesting S_0 initiation of SIST wave bond probes on plates under 210 μm thick. An S_0 pulse detected by the shear EMAT on 53 μm (±4%) thick aluminium shows a 200 kHz to 3 MHz

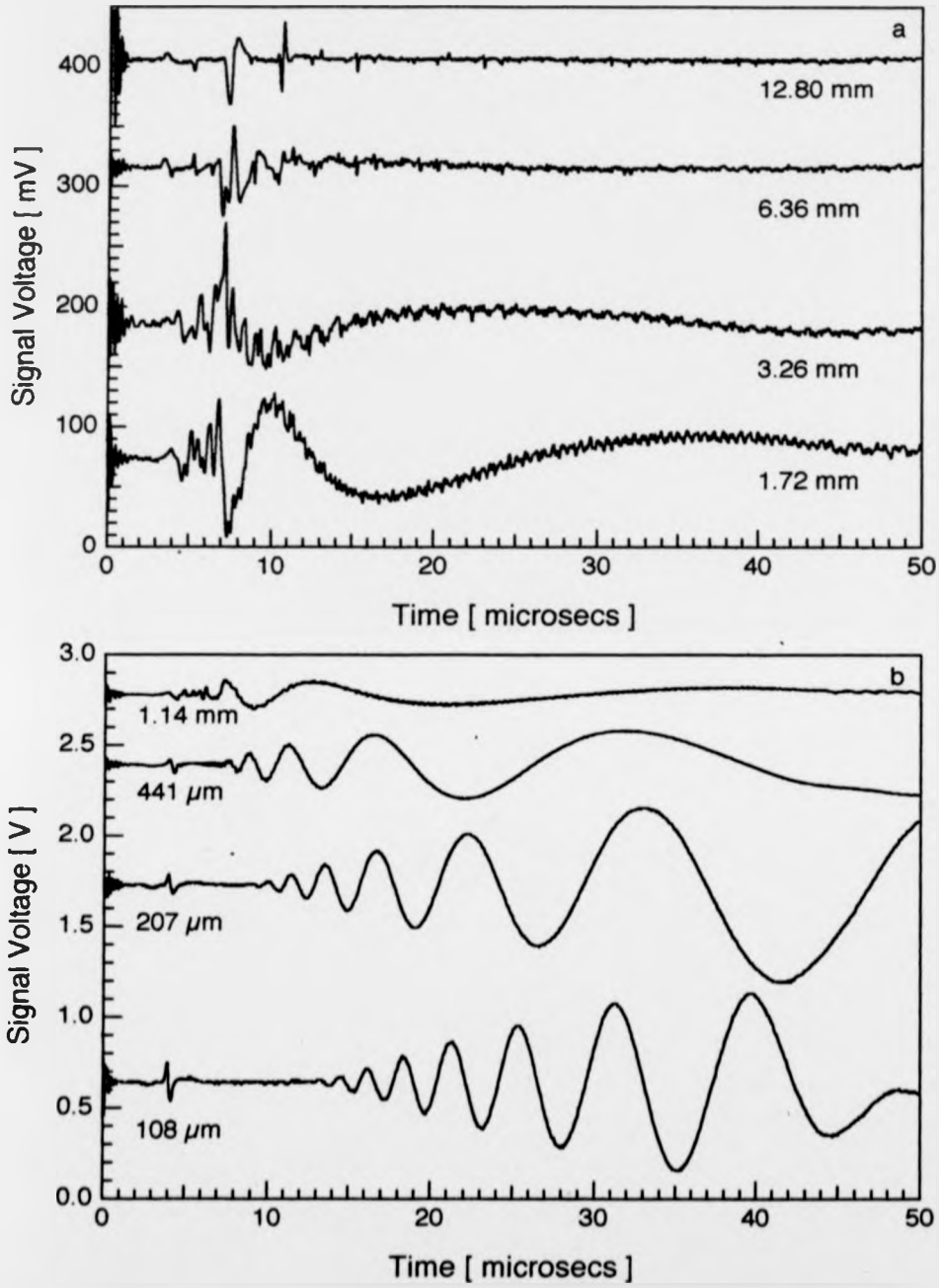

Figure 5.8 Plate waves on intermediate thickness aluminium samples detected by normal EMAT, sensing out of plane motion. Amplitudes for a). thicknesses 12.8 to 1.72 mm are lower than for b). 1.14 mm to 108 μm.

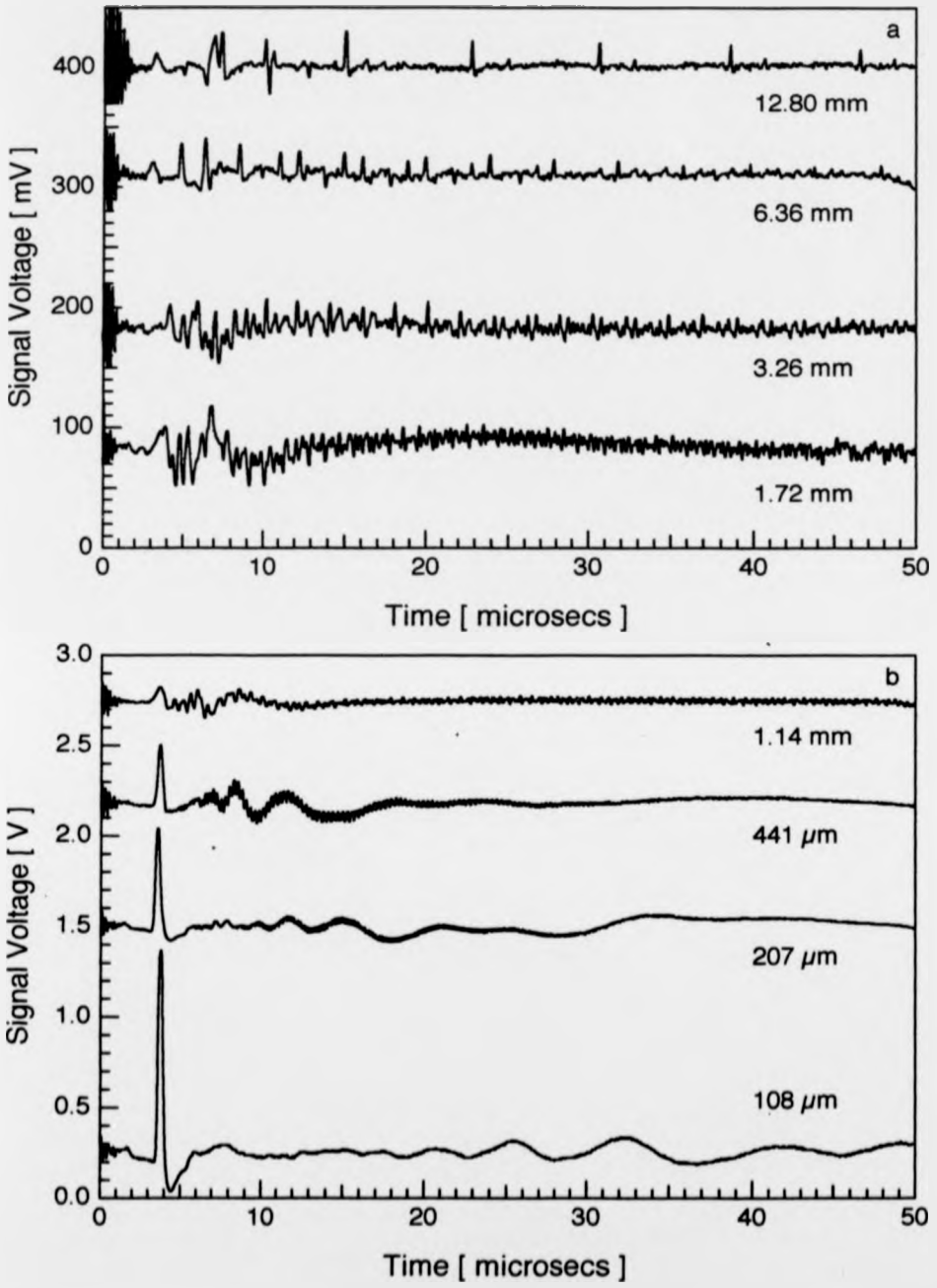

Figure 5.9 Plate waves on intermediate thickness aluminium samples detected by shear EMAT, sensing in-plane surface motions. Again note the signal amplitude variation between a). and b). thickness ranges.

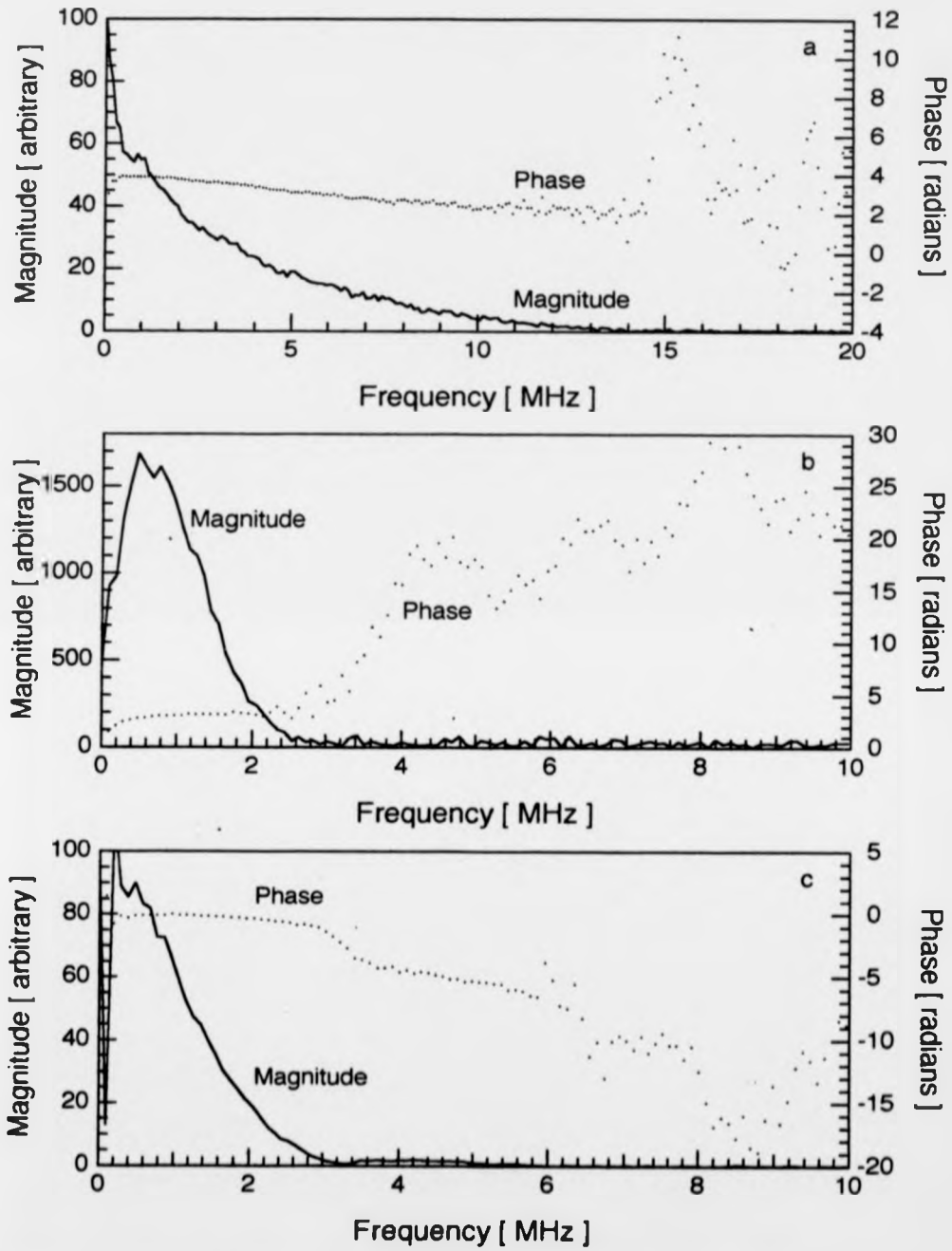

Figure 5.10 Comparing FFT phase and magnitude data for a). Rayleigh arrival detected by 632.8 nm laser Michelson interferometer, or b). by normal EMAT, c). S_0 Lamb mode arrival detected by shear EMAT.

frequency range similar to that observed when the normal EMAT detects a Rayleigh pulse. Low sensitivity relative to the antisymmetric zero order Lamb mode makes Michelson interferometers less suitable than the shear EMAT for sheet wave measurements, although heterodyne interferometry has been used to detect the larger in-plane S_0 wave component [Yu et al., 1989] and could provide an alternative.

5.3 Observations of Surface Layer Effects on Unbonded Aluminium Plates.

Although section 5.2 measurements chart behaviour on plates of varying thickness, they are only detected at one position 20 mm from the source. A series of measurements made on an individual sample at different source-to-detector distances allows comparison between waveforms, from which more accurate estimates both of dispersive effects and the surface wave velocity may be obtained. The laser and interferometer were rearranged from the static source configuration (Figure 5.2) to one in which the source position could be varied (Figure 5.11) by sliding a plate, upon which a 45° mirror - coated for Nd:YAG radiation - and line focussing optics were mounted. An ablating line source generated a series of waveforms on a 64 (±0.5) mm thick aluminium sample with source-to-detector distances between 40 mm and 110 mm (Figure 5.12). Surface-travelling waveforms are aligned to their minimum points, each of which denotes the Rayleigh velocity arrival, and a straight line fit through all eight arrival times plotted versus position gives a precise Rayleigh velocity, $C_R = 2957$ (±0.3%) m/s, from the gradient. Interference with any reflected bulk waves which happen to arrive at similar times modifies individual surface-travelling wave shapes. But, in general, bulk wave arrival times have nonlinear time dependences on source-to-detector distance and an algorithm to overlay selected surface components and then sum the traces produces a compound waveform in which the surface wave is enhanced with respect to bulk components. Manipulations carried out upon the waveforms above result in a far cleaner trace (Figure 5.13.a) aligned to the 40 mm position arrival. The technique is useful only with non-dispersive waves, however, and requires a clearly defined feature on each trace against which the waves can be aligned. At this point it is worth reporting an attempt to use the method to pull surface components out of the bulk wave "noise" on thinner plates and thereby extend the range of plate thicknesses on which sharply pulsed laser-generated surface waves are observed. It failed, because thicknesses at which bulk

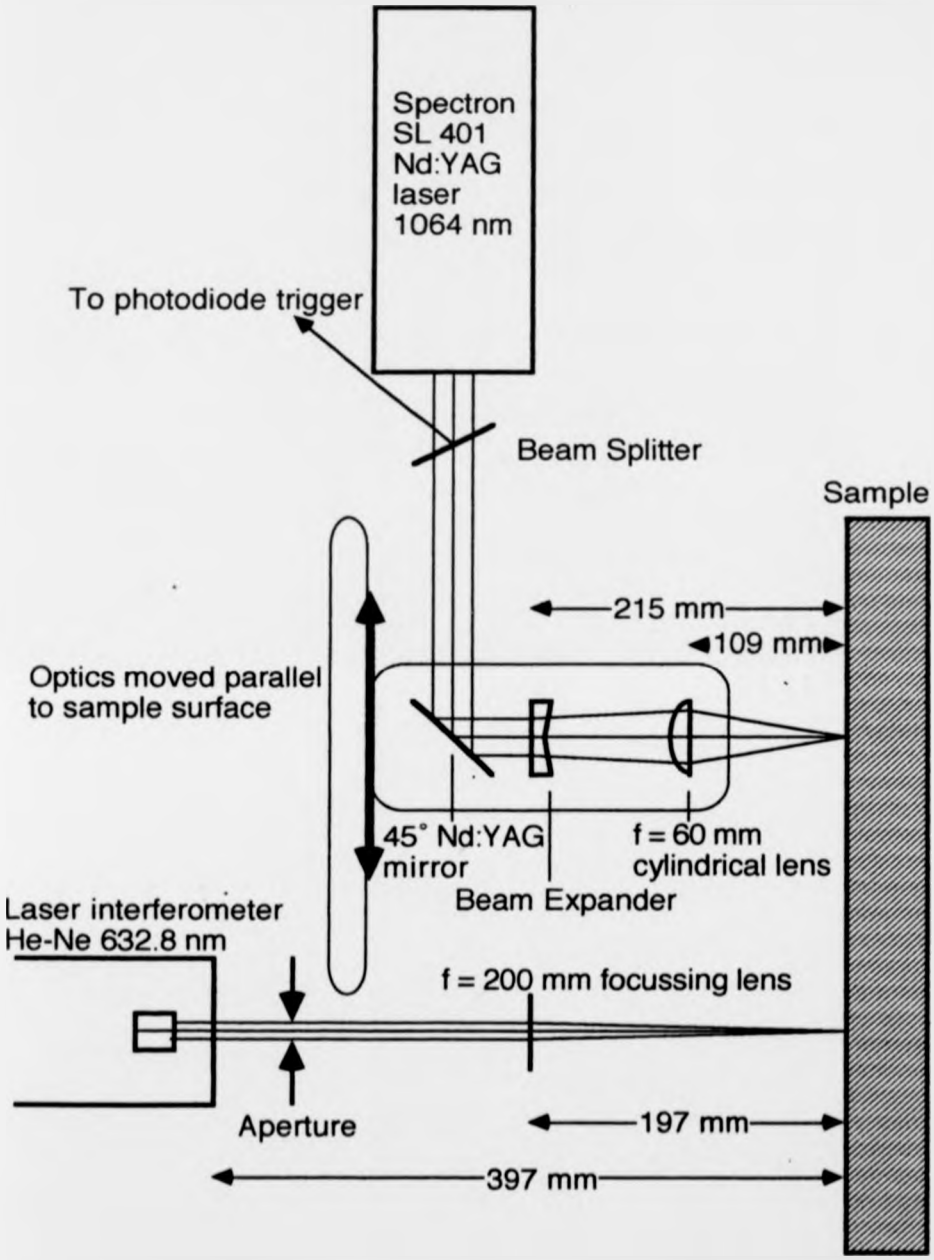

Figure 5.11 Illustration of layout for laser generation, and Michelson interferometer detection, of plate waves at variable source to detector distances.

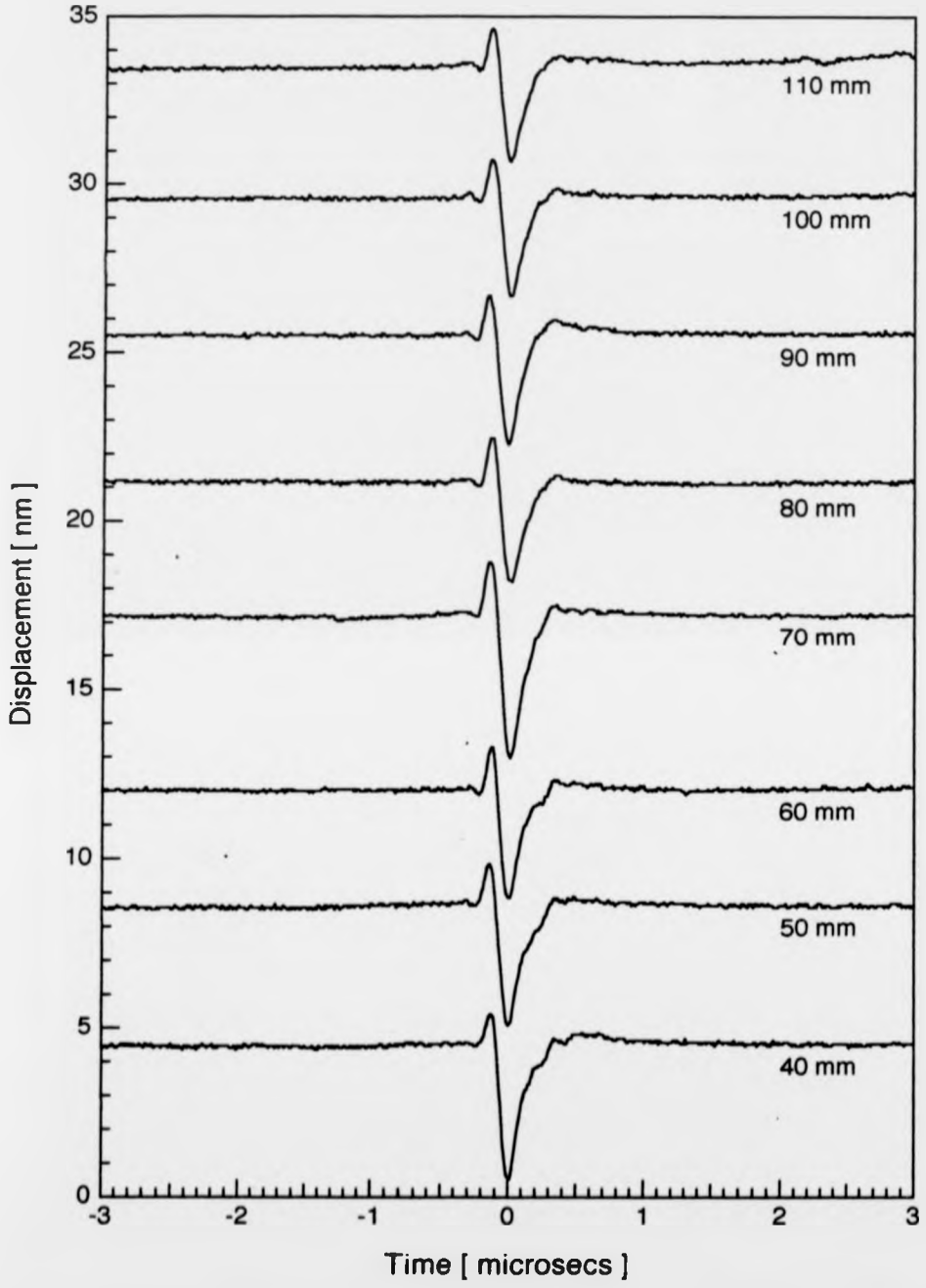

Figure 5.12 Weak ablation line source pulse arrivals on 64 mm thick aluminium aligned to the Rayleigh arrival times at source to detector distances marked. Detection by 632.8 nm laser Michelson interferometer.

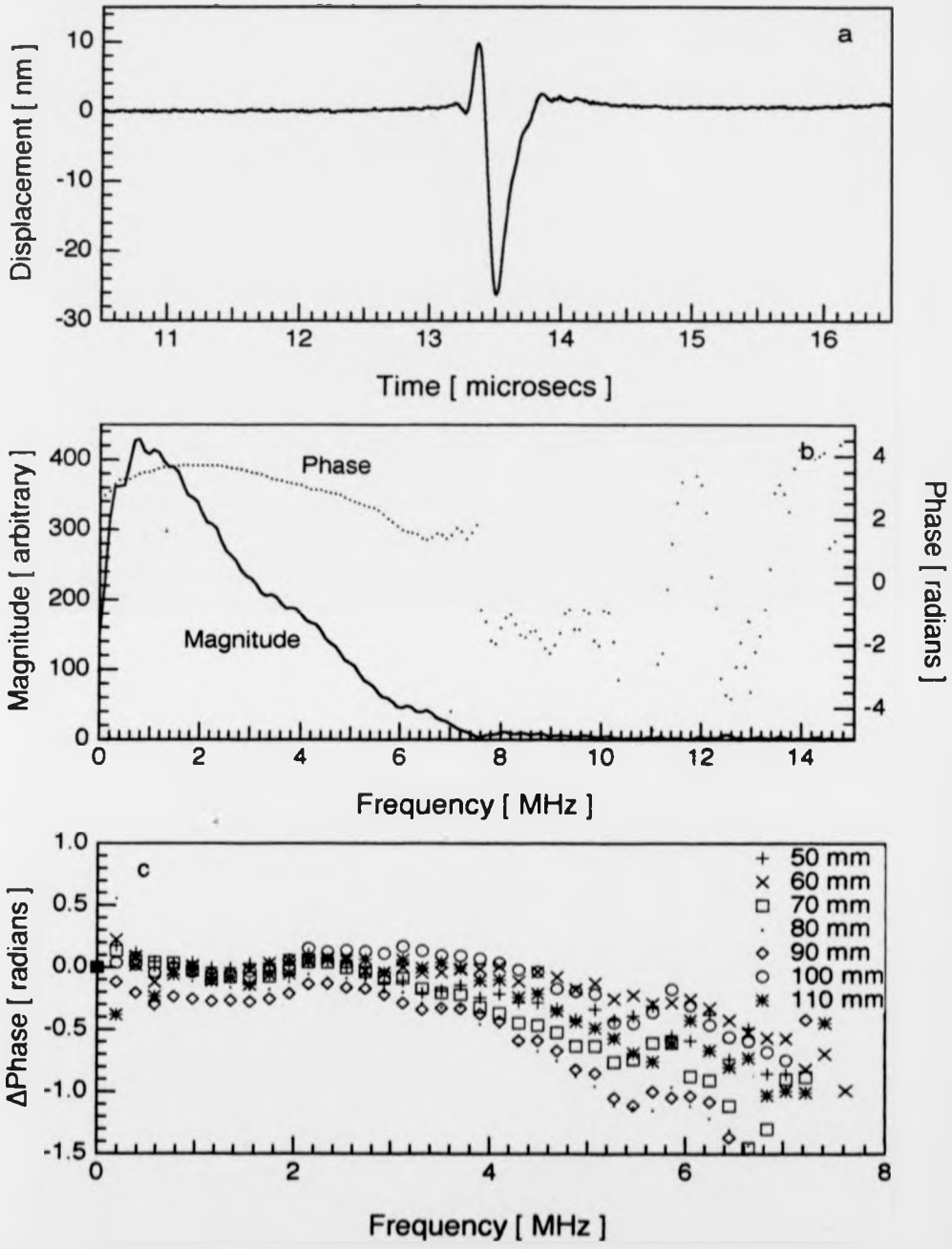

Figure 5.13 Non-dispersive surface wave observations on a 64 mm thick aluminium sample. a). Sum of traces as aligned in Figure 5.12. b). Non-dispersive phase relation from FFT of summed trace. c). Phases vary little with position.

wave arrivals become frequent enough to interfere badly with the surface wave are also those for which surface waves become dispersive, so that distinguishing a consistent alignment point becomes impossible and the compound trace simply smears out. Thus the surface wave enhancement (Figure 5.13.a) seen when individual, digitized traces (Figure 5.12) are shifted and summed, is computational verification of the observation that traces appear non-dispersive.

Further confirmation comes from Fourier transforming the surface-travelling waves and examining their phase dependence upon frequency [Sachse & Pao, 1978; Hutchins et al., 1989]. In dispersive media the wavenumber k is complex,

$$k = \beta(\omega) + i\,\alpha \qquad \ldots 5.3.1$$

where $\beta(\omega) = \omega / [v(\omega)]$ and ω is real in the absence of dissipative effects (chapter 2.5). The displacement u (L, t) thus has a Fourier transform

$$u(L, \omega) = | F(\omega)\, e^{-\alpha L} |\; e^{i[\beta L + \omega \xi]} \qquad \ldots 5.3.2$$

where $F(\omega)\, e^{-i\omega\xi}$ is the Fourier transform of the source disturbance, F (t) = u (0,t). The summed pulse (Figure 5.13.a), detected at a nominal distance L from the source, was zeroed to the Rayleigh arrival minimum, corresponding to a $-t_L$ time shift, and fast Fourier transformed (Figure 5.13.b). This gives a displacement phase spectrum:

$$\phi(\omega) = \beta(\omega) L + \omega \xi = \omega [(L / v(\omega)) - t_L] + \phi_0(\omega) \qquad \ldots 5.3.3$$

Since v is frequency independent for non-dispersive waves, choosing t_L correctly sets the square bracket term in 5.3.3 to zero, leaving the measured phase equal to the source phase, which is invariant with detector position. The observed phase spectrum (Figure 5.13.b) shows less than π variation between 0 and 7.5 MHz when the pulse magnitude vanishes and the phase goes random, some or all of which is due to the source phase frequency dependence. Taking the difference between phase spectra at locations L_1 and L_2 removes the unknown source phase from the expression for phase velocity, v:

$$\delta\phi(\omega, \Delta L) = \omega [(\Delta L / v(\omega)) - \delta\tau] \qquad \ldots 5.3.4$$

where $\Delta L = L_2 - L_1$, $\delta\tau = t_{L2} - t_{L1}$ and $\delta\phi = \phi(\omega, L_2) - \phi(\omega, L_1)$.

Near zero differences between phase spectra for the 40 mm position pulse and remaining

Rayleigh arrivals (Figure 5.13.c) confirm the absence of dispersion.

The 25.2 mm thick plate waveforms (Figure 5.3) suggested that surface waves travelling along 25.2 mm thick aerospace alloy bar, from which a majority of the bonded joint samples are made, would also be non-dispersive. Modifications to non-dispersive surface-travelling pulses resulting from interactions along an adhesive bond interface should thus be readily identifiable. However, observations on 25.20 (±0.02) mm thick aluminium alloy, using an ablating line source at distances 40 mm to 110 mm away from the detector, show clear evidence of surface wave dispersive broadening with increasing travel path (Figure 5.14). Manifestation of dispersive effects on the unbonded aluminium aerospace alloy was unexpected and highly undesirable, since the choice of thicker adherends was intended to remove the severe dispersion observed in samples under 10 mm thick. Slight reflectivity differences between the 64 mm thick aluminium and 25 mm aerospace alloy reduce the ablation source strength on the latter closer to the thermoelastic regime (Figure 3.7), changing the waveform shapes from those observed earlier (Figure 5.12) without greatly affecting the surface acoustic wave frequency content. However, comparing phase spectra on the 25 mm thick sample shows a progressive increase in the more distant waves' high frequency phases (Figure 5.15.a), from which 5.3.4 implies a phase velocity that decreases with frequency. Behaviour of this kind is observed on substrates capped at the surface by a thin layer of lower ultrasonic velocity material, the so-called loading case [Lorenz et al., 1989 & 1990]. Where two discrete layers are present, dispersion is usually highly pronounced, as for a surface-travelling wave detected 49 mm from an ablating source on a 24.82 (±0.02) mm thick aluminium electrode coated with 60 (±5) μm thick Nickel (Figure 5.15.b). C_R = 2749 m/s for Nickel and $C_R \approx$ 2910 m/s for aluminium ensure that the electrode represents a loading combination and the phase below 4 MHz shows a strong increase with frequency (Figure 5.15.c). The decrease above 4 MHz may be an artifact of the phase unwrap routine when the increase between consecutive points exceeds π. Compared with the boundary encountered between two dissimilar materials, the aerospace alloy surface layer properties differ only marginally from those of the subsurface into which it graduates. It thus seems likely that the layer was formed, by either aligning grains along the direction of motion or work hardening, during the rolling and extruding processes used in the manufacture of the material into bars.

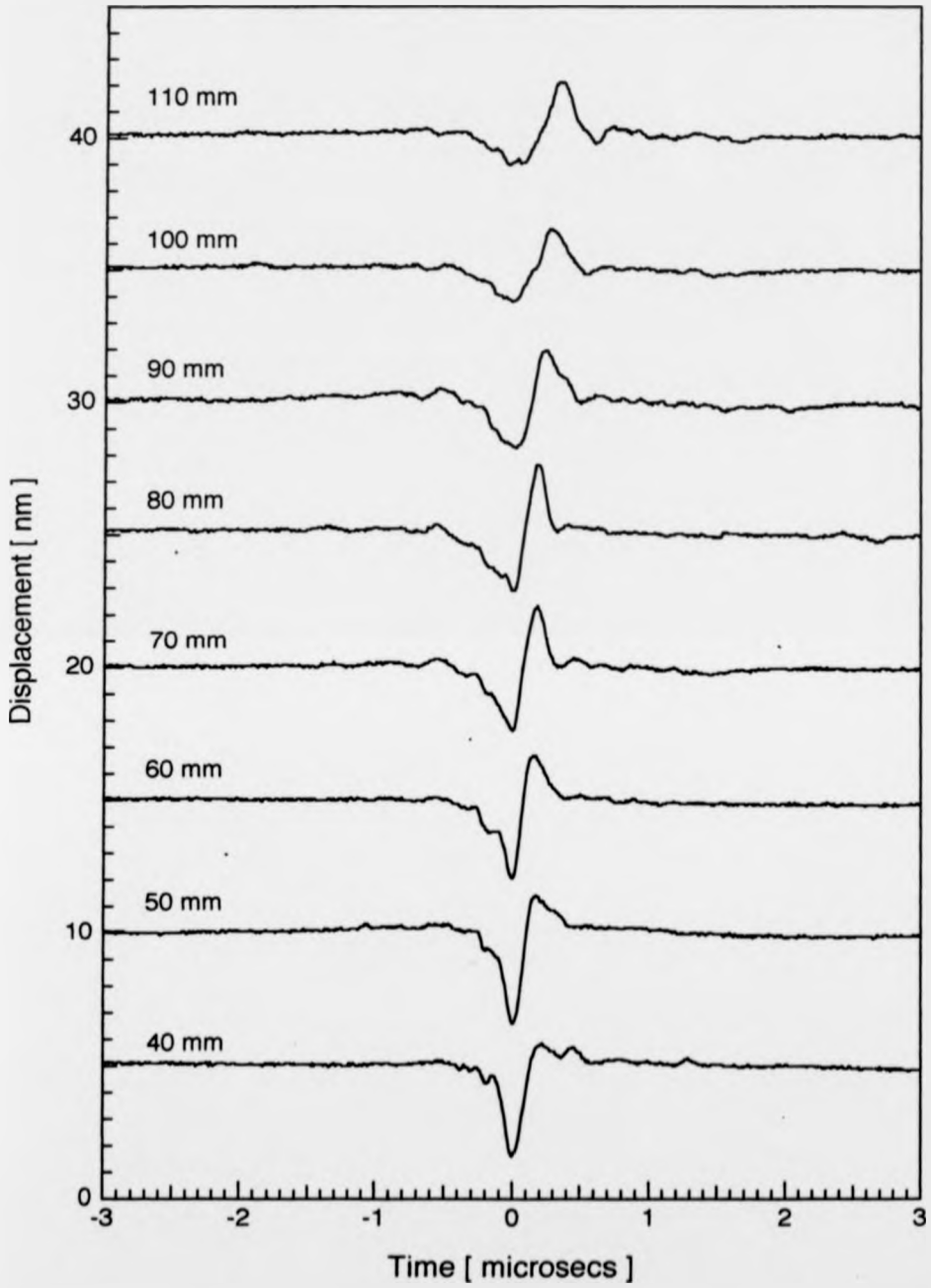

Figure 5.14 Line source pulse arrivals on 25.2 mm thick aluminium aligned to the Rayleigh arrival times at source to detector distances marked. Progressive broadening of pulses with distance observed by interferometer.

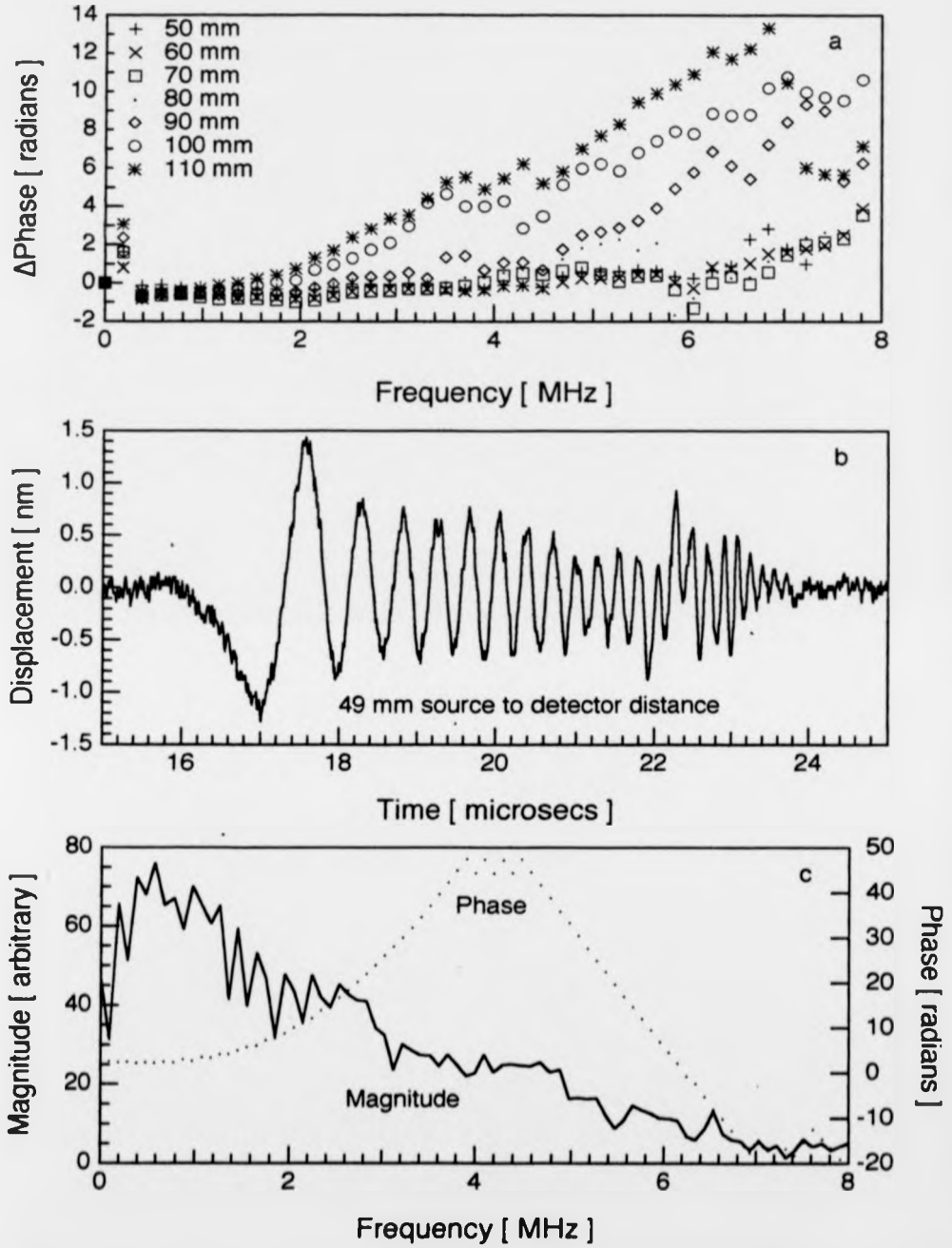

Figure 5.15 a). Phase difference from 40 mm spectrum of line source pulses on 25.2 mm thick aluminium, showing dispersion. b). Surface wave on 24.8 mm aluminium with 60 μm thick nickel coating gives c). highly dispersive phase relation.

As final proof that surface effects were responsible, I milled 1.5 mm off the alloy bar's top surface, and repeated waveform observations at distances of 40 mm, 70 mm, 100 mm on the unmilled (Figure 5.16.a) and milled faces (Figure 5.16.b). Removing the surface layer considerably reduces dispersive effects, with under 3 radians variation in the summed, milled trace, phase spectrum (Figure 5.16.c) up to 8 MHz, when random noise fluctuations begin to drive the phase unwrap program. Evidently the top layer properties differed from the material beneath and were responsible for the problem. Tests on the surface with a Knoop hardness tester, an elongated diamond indenter tapping the surface under 20 g impulse, gave Knoop hardness figures of 342 for the milled surface whether or not the diamond and bar long axes were aligned. The bar's unmilled rear surface gave a 284 reading when the indenter's long axis lay along the bar length but only 240 when it was aligned perpendicular. The milled surface thus appears both harder and more isotropic than the unmilled surface, which supports the idea of a reduced velocity outer layer. Arrival time measurements give an effective zero frequency velocity of 2936 (± 0.3 %) m/s for the unmilled surface, which matches 2938 (± 0.3 %) m/s for the milled surface Rayleigh velocity, as predicted for the loading combination.

Pulsed ultrasonic techniques for the examination of plate or layered structures are becoming increasingly sophisticated in their ability to interpret modifications to surface-skimming ultrasonic features. However, reliable identification of such modifications, and hence the applicability of these techniques, is limited to situations where the original features are themselves relatively simple in structure. The Michelson laser interferometer's excellent spatial resolution has enabled the detection of much more subtle dispersion effects, due to surface hardened layers on extruded bars. Such effects, which are easy to confuse with surface modifications due to the presence of an adhesive bond, can be removed by milling off the pre-bonded surface layer. In practice, plates used in aerospace bonded joints are not milled, and it is thus necessary to limit the effects of substrate dispersion in other ways. One such is to fix the source-to-detector distance at which measurements are made, while varying parameters of interest, like the length of bonded region between source and detector. In this way any bulk or surface-travelling arrivals remaining unchanged, as the conditions vary, are more easily identified.

Sections 5.1 and 5.2 have shown that both the Rayleigh wave on thick plates, and the

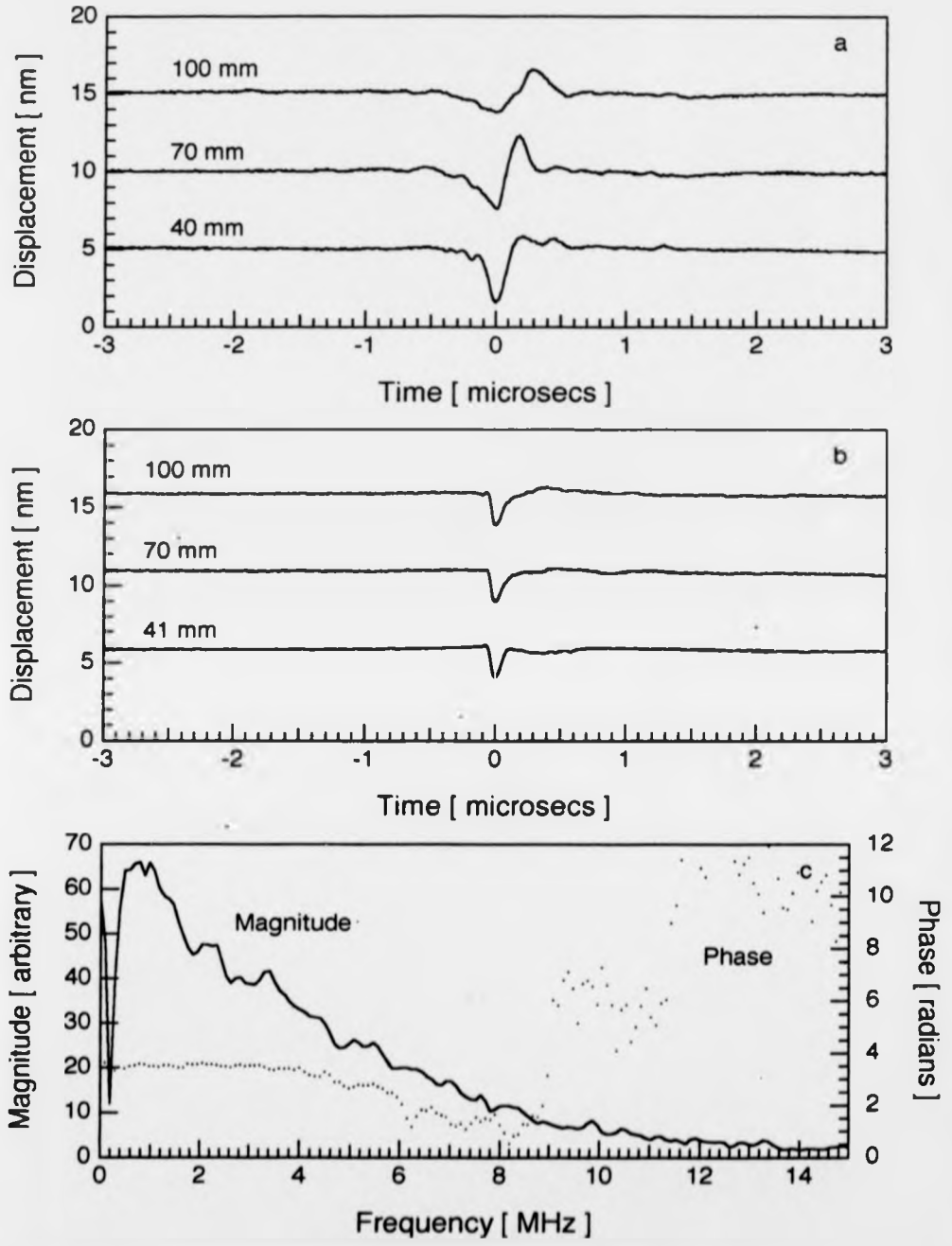

Figure 5.16 Comparing arrivals on 23.7 mm thick plate milled and unmilled surfaces. a). Dispersive pulse on unmilled side. b). Dispersion greatly reduced on milled surface. c). FFT of aligned and summed milled surface traces.

symmetric sheet wave (S_0) on thin plates are suitable for SIST wave bond defect detection (chapter 3.2), due to their sharply pulsed, non-dispersive character and insensitivity to changes in sample thickness. EMATs are cheap and portable detectors of such waves, retaining the advantage over other transducers of broad bandwidth and contact-independence. More accurate time measurements are possible with the Michelson interferometer, only sensitive to out-of-plane surface displacements, which is used in chapters 6 and 7 to observe effects due to varying conditions in the bonded regions of adhesive joints. Section 5.2 experiments have shown that the choice of adherend thickness can make a very large difference to the ease with which surface-travelling waves detect such changes. There is a pessimum aerospace alloy plate thickness range for our standard laser-generated acoustic pulses between 0.44 mm and 12 mm. This range unfortunately covers all the plate thicknesses most commonly encountered in aircraft, suggesting either that a means of producing different ultrasonic frequencies should be sought, or that the use of surface wave probes should be avoided. For test purposes, however, thicker samples are acceptable and 25 mm thick adherends have been chosen as standard.

CHAPTER SIX

SURFACE ACOUSTIC WAVE EXCHANGES WITH EPOXY INTERFACES

The greatest adhesive interface area in an aerospace structure generally resides in joints between the outer skin and main framework, which are most readily accessible from the outside. Ultrasonic research on adhesive layers is thus biassed markedly towards pulse-echo studies (chapter 3.2), using the reflected components of waves which can also be detected in transmission through an epoxy layer (Chapter 4). Normal or oblique incidence pulses with ultrasonic frequencies below 10 MHz will not resolve under 100 μm thick adhesive layers, even by spectral analysis. Pulses generated by the Spectron SL401 (chapter 3.3) just resolve reverberations in layers 60 μm thick, but picosecond pulse lasers are needed on aeroplane bonds with thicknesses down to 1 μm, suggesting that a different approach should be tried. Alternative adhesion quality test methods are also desirable because interface perpendicular displacements are continuous across surfaces in close contact, adhered or otherwise, reducing sensitivity to adhesion properties in longitudinal, laser generated, epicentral waves detected by Michelson interferometer. Substituting a shear EMAT sensor improves detection of in-plane epicentral motions generated by thermoelastic laser sources, an advantage as bulk waves with large displacement components along the interface plane are more adhesion-sensitive [Pilarski et al., 1988 & 1989; Pialucha & Cawley, 1991]. There are still problems, however, with the out-of-plane components that contaminate shear EMAT signals and with thermoelastic source amplitudes, which are low. To retain the Michelson interferometer, a probe wave must be chosen with displacement components in-plane, maximizing susceptibility to variations in epoxy adhesion strength, and out-of-plane, enabling detection. Surface-travelling waves create elliptical displacements which have precisely the properties required, as damping of motions parallel with the surface reduces the wave energy and hence the out-of-plane amplitudes observed.

Few engineering materials are as conveniently transparent as a perspex-glass interface, along which non-dispersive travelling Stoneley waves have been observed directly using dual beam interferometry [Claus & Palmer, 1980]. Interface waves are generally initiated as surface-travelling waves on an exposed portion of one adhered surface and convert into interfacial waves upon reaching the bonded region. Since the waves are only detected upon reemerging as

surface-travelling waves on another exposed portion, I refer to them in general as surface-interface-surface-travelling (SIST) waves. The two simplest configurations for an adhesive bond are the lap-shear, or lapped, joint and the reinforcement joint (Figure 6.1.a &.b). On reinforcement joints, surface waves leaving the bonded region travel along the same surface as the incident waves (Figure 6.1.c), whereas for lapped joints (chapter 7.3) SIST waves are detected travelling along the surface facing that on which they began. Wave behaviour prior to interaction with the adhesive (Chapter 5) led to the choice of mostly 25 mm thick adherends, ensuring laser generation of broad bandwidth, Rayleigh-like, surface-travelling pulses. It is thus easier to identify subtle modifications to detected surface-travelling waves, which are observed when a bonded joint substitutes the free surface alloy adherend.

A representative 0.2 mm thick CG312/5 epoxy layer, bonding aluminium adherends, sustains travelling interface wave modes (Figure 2.4 and related text), all except one of which have low frequency cutoffs and are highly dispersive. Section 6.1 describes experimental results from a series of increasing length bonds, incrementing the distance over which SIST pulses are dispersive. Frequency analysis of SIST signals, which are still detectable after traversing 102 mm (4") long bonded regions, is complicated by the presence of bulk-travelling waves detected simultaneously with the surface arrivals. Imposing a periodic spatial modulation upon the laser acoustic source creates surface waves modulated at a single frequency, while on-epicentre bulk waves remain sharply-pulsed, making them easier to separate from SIST signals. I have therefore extended an optical interference technique, previously used on lasers generating narrowband ultrasonic surface waves above 10 MHz, to produce waves in the 0.1 to 10 MHz frequency range within which most SIST pulse frequencies appear to lie. Section 6.2 describes the optical patterns formed on planar surfaces by a pair of overlapping, coherent laser beams, while section 6.3 outlines an experimental layout to generate periodic sources for modulating surface waves at variable, single frequencies. Section 6.4 reports monotonic acoustic wave experiments to determine the effects of differing bondlengths on individual period modulations and to compare various frequency waveforms observed on a single joint with the Fourier analysed broadband pulses. Finally, 6.5 presents the results of measurements upon a set of bonded samples containing deliberate flaws (see chapter 4.4), to assess SIST wave performances as interface adhesion probes.

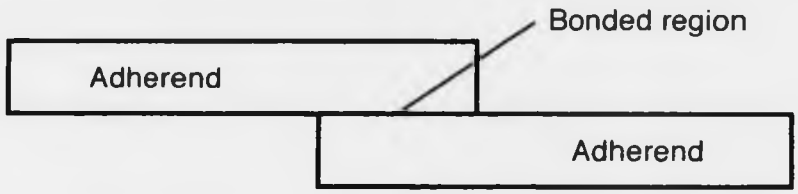

a. Lap-Shear Joint

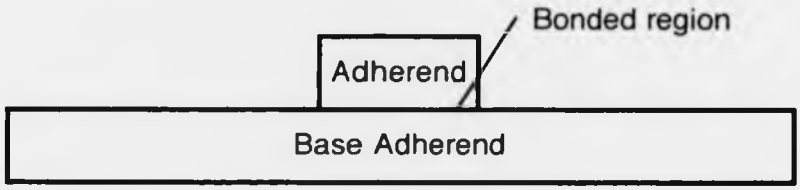

b. Reinforcement Joint

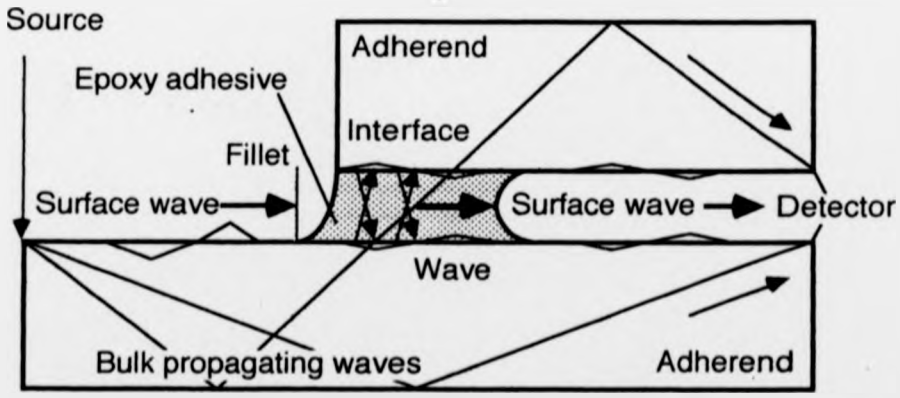

c. Surface-interface-surface travelling (SIST) and bulk-propagating ultrasonic waves in adhesively bonded joints.

Figure 6.1 Standard configurations for adhesively bonded joints. a). Lapped joint. b). Reinforcement joint. c). Acoustic wave pathways illustrated on a hybrid adhesive joint.

6.1 Modifications to Pulsed Surface Waves by Bonds of Varying Length.

In this section, surface-travelling ultrasonic waves probe epoxy-bonded aluminium samples previously examined by ultrasound transmitted through the joint (chapter 4.1 & 4.2). The joints, of varying bond length, were assembled at DRA(Aerospace) under strict conditions to guarantee good quality adhesion. Unlike similar work using narrowband piezoelectric transducers [Rokhlin et al., 1980 & 1981], the laser-generated ultrasonic pulses have broad frequency bandwidths, which in principle enable information about SIST wave dispersion to be extracted. In practice, both bulk-propagating waves (also generated by the laser and reflected onto the receiver) and detector bandwidth broadening by surface-travelling arrivals degrade the data. Finally there is always uncertainty as to the exact laser generated acoustic source distribution, which is generally deduced from the waveforms produced but needs to be known before a single waveform can yield dispersion data. However, by fixing the source-to-detector distances, it is possible to observe progressive differences in frequency content between broad bandwidth pulses travelling under differing lengths of adhesive bond.

A schematic diagram of the apparatus (Figure 6.2) shows a 1064 nm wavelength Nd:YAG laser beam focussed by a cylindrical lens. The resulting ablation line sources are restricted to 50 μm wide as pulse broadening, due to the acoustic signal propagation time across the source width, limits Rayleigh wave bandwidths. Line sources generate broadband, directional surface waves that initiate the SIST waves of interest, as well as inevitable bulk waves, both of which are observed by a detector on the surface. For thick adherends, the generated and detected surface-travelling waves are non-dispersive and travel at the Rayleigh velocity. Waves propagate along the adhesive-aluminium interface in a weakly-dispersive mode, with phase velocity between the aluminium Rayleigh and epoxy longitudinal velocities, or in strongly dispersive modes, which vanish completely below minimum cut-off frequencies and never exceed the epoxy longitudinal velocity (chapter 2.5). For thin adherends (or very low frequencies) the situation is more complicated as the bond acts like a compound plate, and adhesion data has to be extracted from plate frequency resonances [Lowe & Cawley, 1991].

In a preliminary probe, a normal EMAT fixed 127 mm away from a laser-generated line source detects SIST waves on a set of nominally identical quality adhesively bonded reinforcement

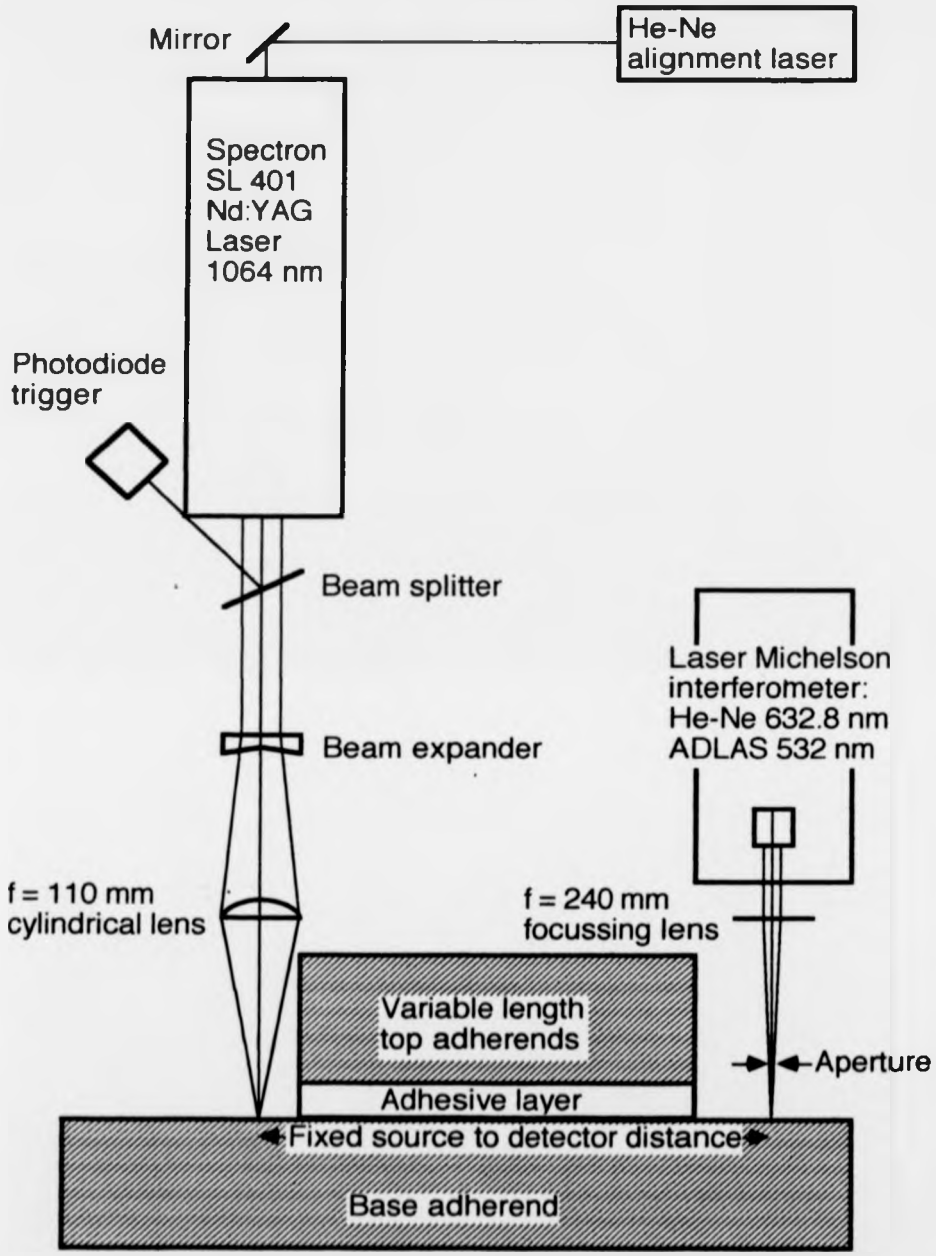

Figure 6.2 Laser generation of SIST waves on reinforcement joints bonded with CG312(/5) epoxy. Source to interferometer detector distance is fixed while bond lengths vary.

joints with 25 mm thick adherends. The source and detector straddle each smaller joint adherend (as in Figure 6.2), which increase in length from joint to joint producing bonds between 12.7 and 102 mm long. The EMAT signals, amplified 200-fold by a 3.5 kHz to 10 MHz bandwidth preamp, show that imposing even the shortest length bond upon the free surface has a dramatic effect on the observed waveform (Figure 6.3.a), attenuating the SIST wave and possibly dispersing it, since the detected pulse appears both to broaden and change shape. Note that SIST and free surface Rayleigh arrival times hardly differ, supporting the notion that the low frequency motions reaching the EMAT are carried by the 0 MHz weakly-dispersive interface wave mode. Thus, though progressively increasing the bond lengths reduces the signal amplitude, waves are still observed after passage under 102 mm of bond. As the EMAT width averages out rapid spatial variations in surface-travelling waves which pass beneath its coils, observing detailed structure on dispersive waveforms is difficult. For comparison, therefore, several measurements were repeated with the He-Ne (632.8 nm) laser interferometer (Figure 6.3.b), using a 200 mm focal length lens to produce a tightly-focussed detection spot. Better resolution of the SIST arrival by the interferometer reveals a problem with bulk wave arrivals (compare Figure 5.3), which are too closely spaced in time, at 127 mm source-to-detector distances, to separate easily from the surface-travelling wave. These bulk waves have undergone multiple reflections along the adherend and are therefore damped heavily on the 101.6 (±0.1) mm long bond by transmission into the top adherend through attenuating epoxy. The EMAT arrivals at 41.9 and 45.8 μs do not correlate with interferometer out-of-plane displacements and result from sensitivity to in-plane surface wave motion at the divergent edges of the EMAT static magnetic field.

Bulk waves are a lesser problem in a second series of results taken, at a position 69 mm from the source (Figure 6.4.a), by the frequency-doubled Nd:YAG (532 nm) laser interferometer, with its spot focussed to 25 μm diameter by a 50 mm focal length lens. However, bonds over 55 mm long cannot be studied at this distance. For comparison, signals detected 64 mm from the source by normal and shear EMATs are also included (Figure 6.4.b &.c). Fast Fourier transforms of free surface waveforms (Figure 6.5.a), where the normal EMAT clearly gives no significant amplitude response to frequencies over 2.5 MHz, demonstrate the bandwidth reduction when an EMAT replaces the interferometer. The interferometer detected phase remains constant,

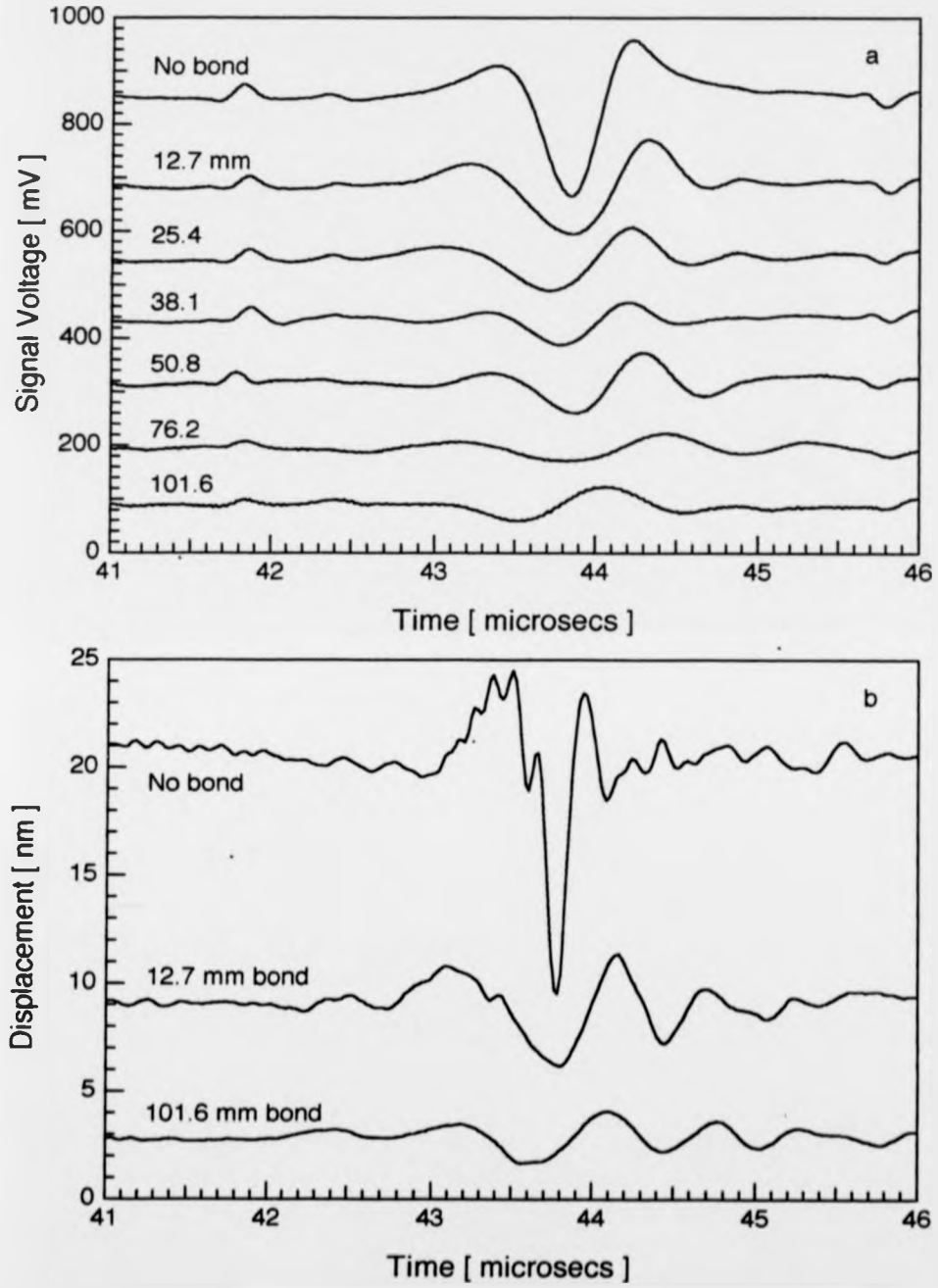

Figure 6.3 Ultrasonic SIST waves detected on reinforcement joints, with varying bond lengths, at 127 (±0.5) mm from a laser line source by a). normal EMAT and b). 632.8 nm laser Michelson interferometer.

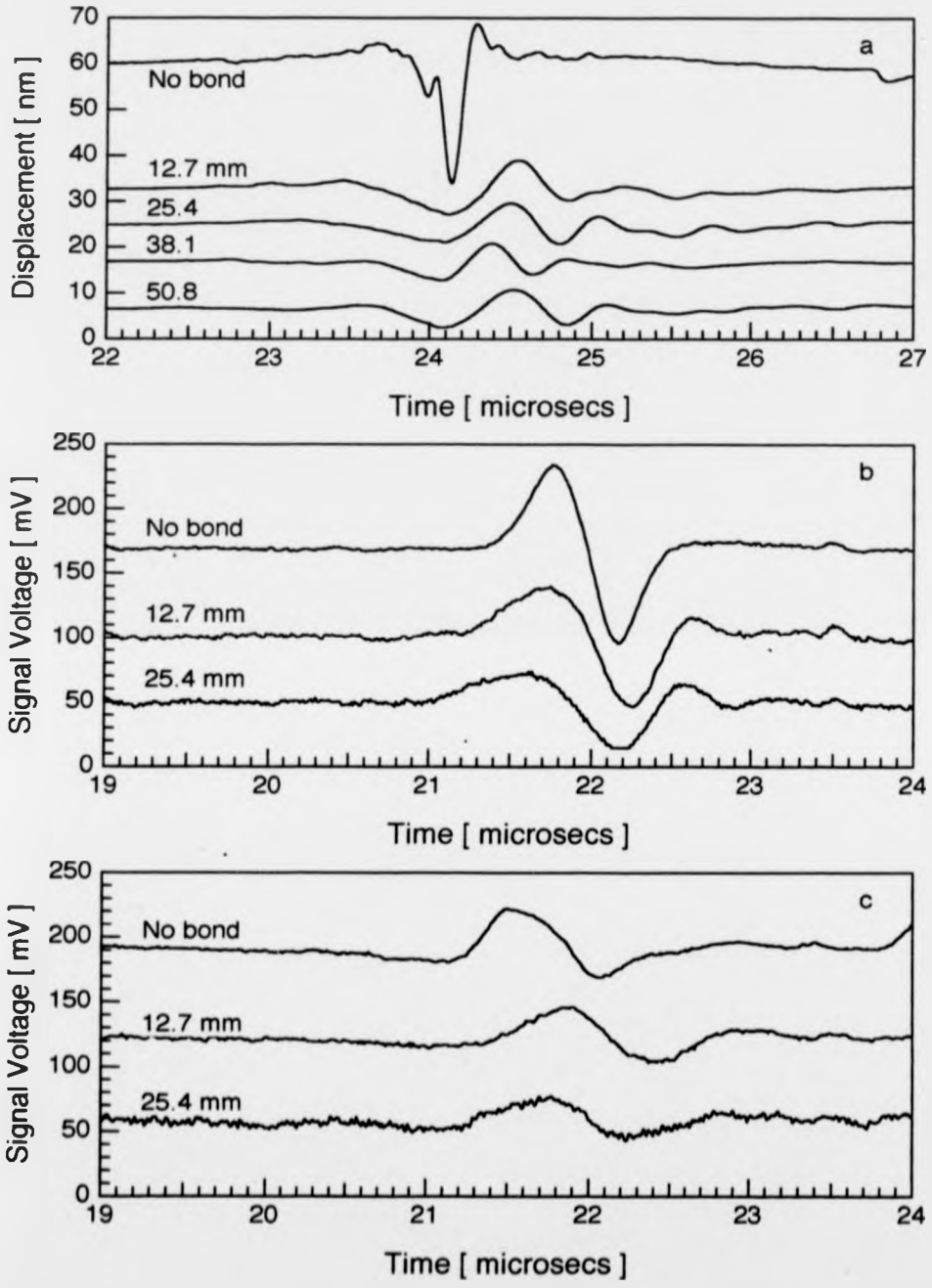

Figure 6.4 Ultrasonic SIST waves on reinforcement joints with 25 mm thick adherends. a). Detected by 532 nm laser Michelson interferometer at 69 mm from line source, and at 64 mm by b). normal EMAT or c). shear EMAT.

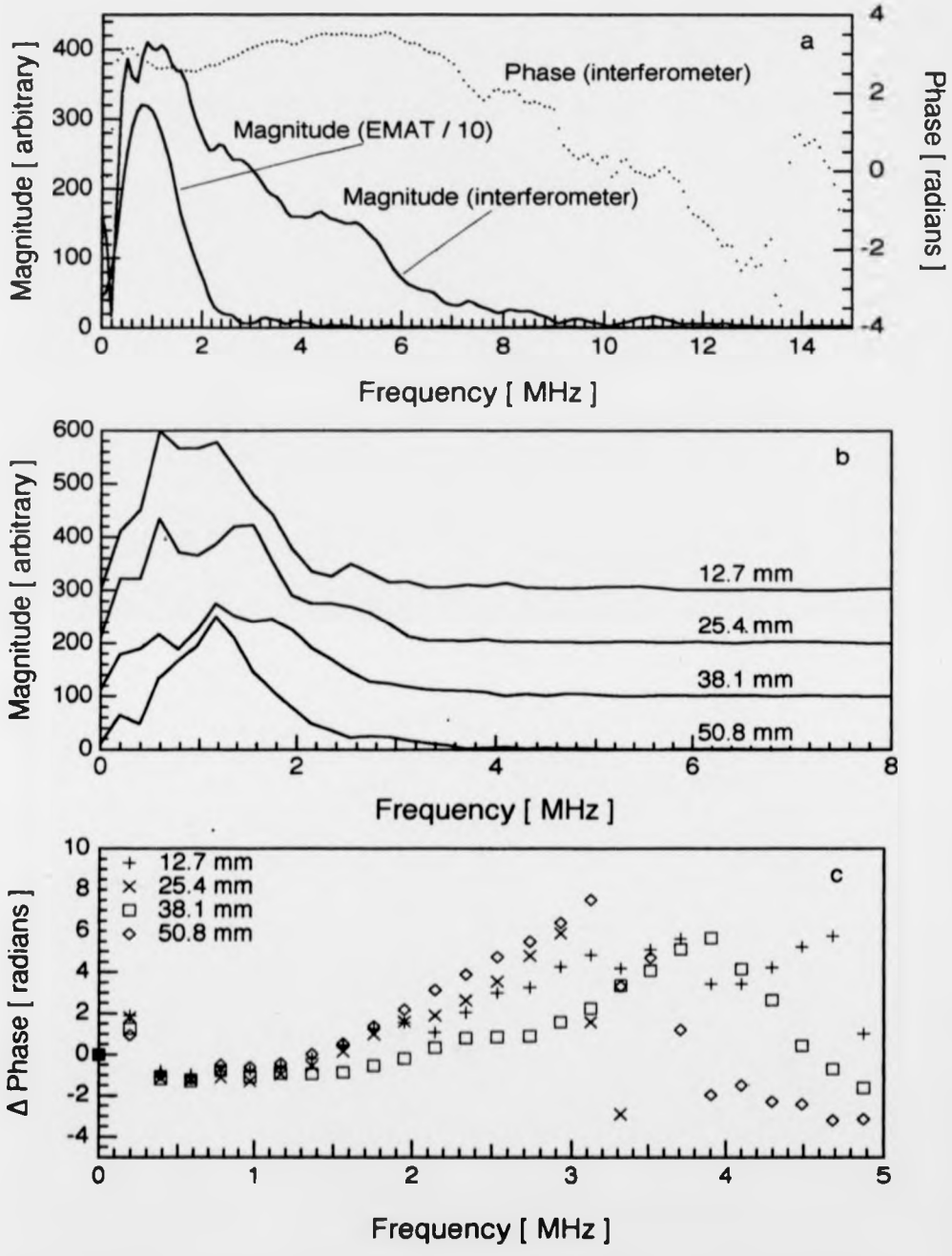

Figure 6.5 Fast Fourier transformed SIST waveforms. a). Free surface observations by 532 nm laser interferometer & normal EMAT. Bond length effects on b). magnitude and c). phase spectra detected by interferometer.

to the nearest radian, until 7 MHz, above which signal amplitudes are suspect. Fourier transformed interferometer data on 12.7 to 51 mm long bonds (Figure 6.5.b) shows even the 12.7 (±1) mm bondlength suppressing almost completely any frequencies above about 3MHz, a move which affects interferometer data more than the EMATs where such frequencies are anyway undetected. Somewhat surprisingly, given the result of imposing the initial 12.7 mm, interferometer signals vary less systematically as bond lengths range from 12.7 to 51 mm, although there is a decrease in magnitudes, implying stronger attenuation, between 2 and 3 MHz. Phase data for the bonds (Figure 6.5.c) presents a similar picture, with all lengths appearing dispersive above 1.4 MHz but no clear trend between them. Lack of systematic variation could derive from property differences between bonds of nominally identical quality, but is more probably a sign that mode conversion from surface to interface waves at the bond fillet closest to the source, and back again at the edge nearest the detector, accounts for most of the observed attenuation.

On reinforcement joints, the SIST wave approach to defect detection differs markedly from through transmission in that a complete absence of adhesion maximizes signal amplitudes at the detector. A defect located anywhere in the path of a SIST wave running along a joint should therefore increase the detected signal with respect to perfect bond levels, although frequencies above 3 MHz are damped so rapidly -a piece of sticky tape will do- that they are useless for bonds more than ~1 mm long. The very narrow frequency range within which bond length dependent changes are apparent (Figure 6.5.b) poses a problem, as frequencies not significantly affected when a portion of the free surface is subjected to well-bonded boundary conditions are unlikely to be sensitive to changes in adhesion quality. This suggests that it would be helpful to look at the behaviour of monotonic surface waves passing under similar length bonds. By varying the generating frequency it should be possible to give a direct picture of how the presence of adhesive affects different frequencies and, hence, tune SIST waves to give maximum sensitivity to changes in the bonded region.

6.2 Periodic Spatial Modulation of a Laser Source for Acoustic Wave Generation.

In the majority of cases where laser-generated ultrasound is used, the intention is to exploit the laser's fast rise-time to produce a broad bandwidth, sharply-pulsed acoustic source. However, periodicity in the acoustic source may be introduced by either spatial or temporal

periodicities present in laser pulses hitting the sample surface. Temporal modulation of long-cavity mode-locked lasers with pulse repetition frequencies between 2.5 and 13 MHz has been used to produce narrowband ultrasound [Deaton et al., 1991]. Q-switched lasers used to generate periodic acoustic waves require an imposed spatial periodicity, first demonstrated with optical masking of the laser beam [Lee and White, 1968]. Less optical power was discarded when two interfering beams, from a prism-split, Q-switched laser beam, generated 30 MHz surface waves on quartz [Cachier, 1970], a frequency which was increased to 800 MHz by using a modulated laser. Since then interfered beams have been used to generate GHz frequency acoustic waves, both in liquids [Nelson et al., 1982] and on metal surfaces [Faran et al., 1990; Harata et al., 1990], and to produce Lamb wave frequencies between 2.5 MHz and 23 MHz [Nakano & Nagai, 1991]. The system described in section 6.3 generates still lower frequencies, between 880 kHz and 20 MHz [Bushell et al., 1991].

Describing the system theoretically is straightforward. Two overlapping coherent radiation beams, of wavelength λ, separated by angle $\delta\theta$, and lying in a horizontal (X-Z) plane produce vertical planes of constructive interference aligned with the axis bisecting the beams (Z axis in Figure 6.6). The interference region is directed onto a sample surface such that the two beams are incident at angles θ and ϕ either side of the surface normal and $\theta + \phi = \delta\theta << 1$, which is possible when both beams are the same side of the normal and one angle is thus negative. Assuming circular cross-section beams, the pattern observed on a vertical sample surface (Figure 6.6.a) has an elliptical envelope and sinusoidally modulated intensity with spacing, d:

$$d = \lambda / (\sin\theta + \sin\phi) \qquad \ldots 6.2.1$$

If the sample surface lies in the X-Y plane, its normal coincides with the Z axis and

$$d_{min} = \lambda / 2 \sin(\delta\theta / 2) \approx \lambda / \delta\theta \qquad \ldots 6.2.2$$

In laser-generated ultrasound, a spatially modulated radiation intensity at the sample surface creates a periodic acoustic source, and hence surface-travelling waves, also with wavelength d. Thus for small angular beam separations, the approximate acoustic wavelength (from 6.2.1) is:

$$C_R / f = d \approx \lambda / (\delta\theta \cdot \cos\phi) \qquad \ldots 6.2.3$$

where C_R, f are, respectively, the surface acoustic wave phase velocity and frequency.

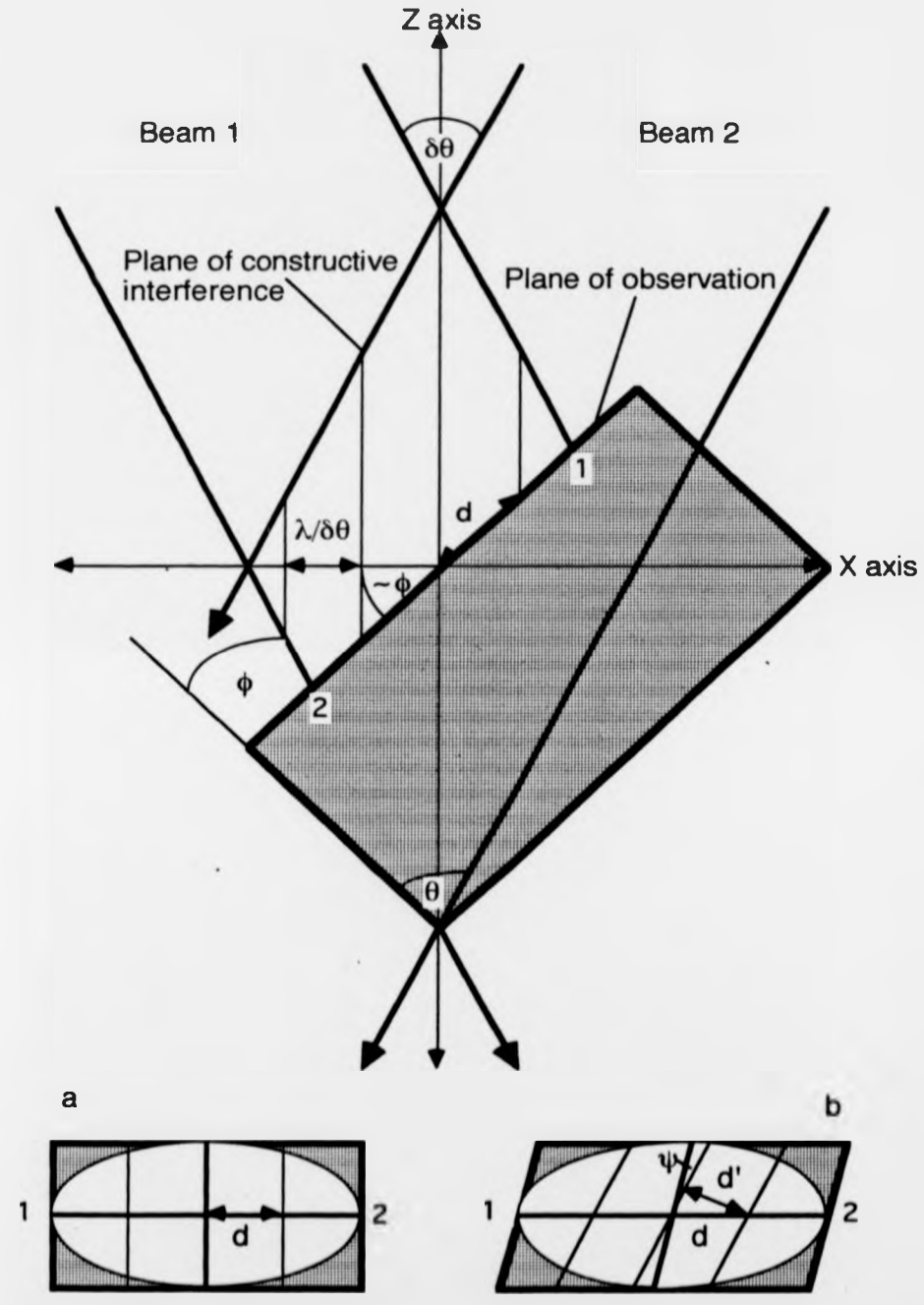

Figure 6.6 Plan view illustrating interference fringes observed on intersecting laser beams. Inserts show patterns seen on a). vertically upright, b). tilted sample surfaces.

The beam angular separation is in practice much smaller than illustrated (Figure 6.6) and the two beams are both incident, to first approximation, along the Z axis. This in turn implies a sample surface oriented $\sim\phi$ to the X axis or $\sim (\pi / 2) - \phi$ to the Z axis. A final complication, which is worth avoiding, occurs when the surface is tilted out of the vertical about the line 1-2, by an angle η. The fringe pattern tilts an additional angle ψ in the rotated surface plane, away from the rotated vertical, which remains perpendicular to the invariant 1-2 axis (Figure 6.6.b). Using vector notation and a rotation matrix transformation on the observation plane, which intersects fixed planes of constructive interference, gives a tilt angle

$$\psi = \cos^{-1}(\cos^2 \eta + (\sin^2 \eta / \cos^2 \phi))^{-1/2} \quad \ldots 6.2.4$$

and hence a distance between tilted fringes d' where,

$$d' = \cos \psi (\lambda / \delta\theta \cos \phi) = \lambda / (\delta\theta (\cos^2 \phi \cos^2 \eta + \sin^2 \eta)^{1/2}) \quad \ldots 6.2.5$$

The angle ψ vanishes and 6.2.5 reduces to 6.2.3, as required, when $\eta = 0$, and when $\phi = 0$. Thus tilt has a negligible effect on beams incident approximately normal to the surface but becomes increasingly important as the surface rotates in the X-Z plane, making oblique angles, $\sim\phi$, with the X axis. Tilting the sample also increases the beam area projected onto the surface, reducing tbe laser power density. It is thus desirable to adjust the surface tilt (or equivalently the incident beam plane) until the fringes are aligned perpendicular to the envelope ellipse's long axis (Figure 6.6.a) and directional waves moving parallel to the long axis are produced.

6.3 An Experimental Arrangement for Laser Generation of Periodic Acoustic Sources.

The interference system (Figure 6.7) set up in consultation with Dr. H. Nakano uses a Lumonics HY400 pulsed Nd:YAG laser beam, passing through a beam splitter coated to divide 1064 nm radiation incident at 45° into two equal intensity beams. The two beams then bounce off 45° Nd:YAG coated mirrors (angled slightly off 45°, Figure 6.7) to bring them together again at the sample surface a distance, D, typically in the region of 2.5 m, away. Now

$$\delta\theta \approx a / D \quad \ldots 6.3.1$$

where a, the beams' separation as they leave the optics, has a lower limit (~ 4 mm) to avoid

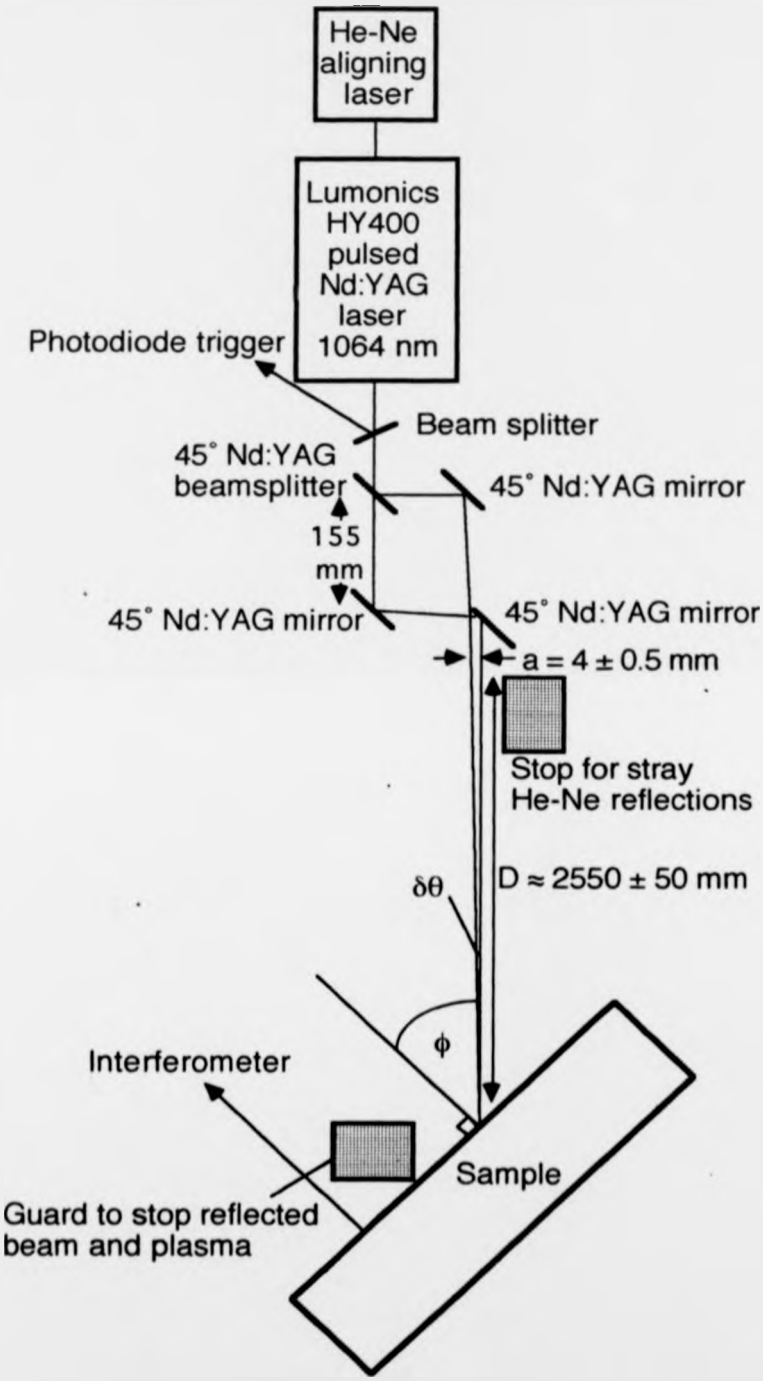

Figure 6.7 Experimental arrangement for the optical generation of a periodic acoustic source.

distortion near the mirror edges. So the angle between beams ≈ 1.6 mrad (320 arcsecs). When generating low MHz Rayleigh waves in practice, a is minimized and D, a length limited by the laboratory space available, is altered to vary $\delta\theta$ as per 6.3.1. Decreasing $\delta\theta$ lowers the frequencies observed but reduces, eventually to one, the number of fringes in the source, for which the interference area remains roughly constant while d increases. However, the fringe period may equally be varied, from 6.2.3, by rotating the sample in the X-Z plane to adjust ϕ (Figure 6.6). Increasing ϕ leaves the fringe number unaltered but progressively distorts the source shape from a series of line fringes into a row of spots, with subsequent reduction in energy density at the surface. Maintaining sufficient energy density appears to be the overriding factor in determining the lowest acoustic frequencies this method can achieve. I needed to vary both angles to obtain the broadest range of frequencies. Perhaps a simpler way to achieve the longest wavelengths required is to expand the optical pattern [Edwards et al., 1991] with a short focal length concave lens placed near the sample surface (so that both beams traverse very similar paths through the lens). This preserves source shapes but cuts down the energy density, both as a result of expansion and from transmission losses through the extra optics, making the method more suitable for thin sample Lamb wave measurements where lower source strengths are acceptable.

The He-Ne alignment laser beams, with differing wavelengths from the YAG beams, are not reflected in the same manner by the coated optics, and care was taken to stop spurious reflections, which cause confusion when adjustments have to be made. When the laser beams arrive at non-zero angles to the sample normal, it is also necessary to block specularly reflected Nd:YAG radiation, which is still powerful enough to cause damage, particularly to the detector. Michelson interferometers were used for this run of experiments, as EMAT detection widths are larger than the wavelengths created by optical interference and simply average any modulations on the ultrasonic signal. Even with the 25 μm spot size of a focussed interferometer, surface wave modulations much above 20 MHz are blurred. Acoustic source broadening, due to the outward propagation of surface waves during the source lifetime, also limits the attainment of high frequencies. Periodic waveforms are seen only when the fringe spacing is large compared

with the ~30 μm distance covered by a Rayleigh wave over the ~10 ns source duration. The ultrasonic wavelengths generated can be calculated (using 6.2.5) from a knowledge of the experimental arrangement, or measured directly from burn patterns on the sample surface. A more accurate method is to calculate the wavelength from the measured frequency of arrivals on a thick plate of known Rayleigh velocity material, used to calibrate the system. Once the acoustic wavelength is known, new materials are inserted into the system and the observed frequencies used to calculate phase velocities [Nakano & Nagai, 1991].

Using 6.2.3, with ϕ = 31.9° (±0.4°), D = 2560 (±20) mm, a = 4 (±0.5) mm and Nd:YAG wavelength 1064 nm, a 63.16 (±0.02) mm thick aluminium sample calibrating my system gives a calculated 3.7 (±10 %) MHz frequency for 2944 (±0.1%) m/s Rayleigh velocity. Blocking one of the split Nd:YAG beams leaves the sample surface exposed to a single beam, arriving after reflection off either one or two mirrors (Figure 6.7). The HeNe (632.8 nm wavelength) laser Michelson interferometer placed 68 (±0.5) mm from the source centre detects relatively broad, low amplitude acoustic pulses (Figure 6.8.a), as the laser beam is unfocussed and has lost at least half its energy in the beam-splitting optics. Overlapping both optical beams imposes a sinusoidally varying radiation intensity on the source, though surface acoustic wave amplitudes only vary proportionally if the sample is isotropic and laser power densities remain in the thermoelastic regime. The interfered wave amplitude is more than double either individual beam acoustic amplitude due to a fourfold increase in peak-to-peak radiation intensity upon interference. However, as inhomogeneity in the laser beam cross-section also contributes to spatial variation at the source, the observed waveform results from a convolution of the interference pattern with the individual source pulse distribution. Fast Fourier transforms of the surface-travelling wave before (Figure 6.8.b) and after interference (Figure 6.8.c) show clear imposition of an interference frequency upon the underlying pulse magnitude spectrum, with which it is approximately out of phase. The interfered wave to single beam magnitude ratio reveals a sharply-peaked superposition spectrum with 3.4 (±0.1) MHz centre frequency (Figure 6.8.c), confirming calculations. Rising phases above 4 MHz again indicate unwrapped noise.

A series of measurements on 63.16 mm thick aluminium (Figure 6.9), by Michelson interferometers situated around 69 mm from the mean source position, demonstrate interference

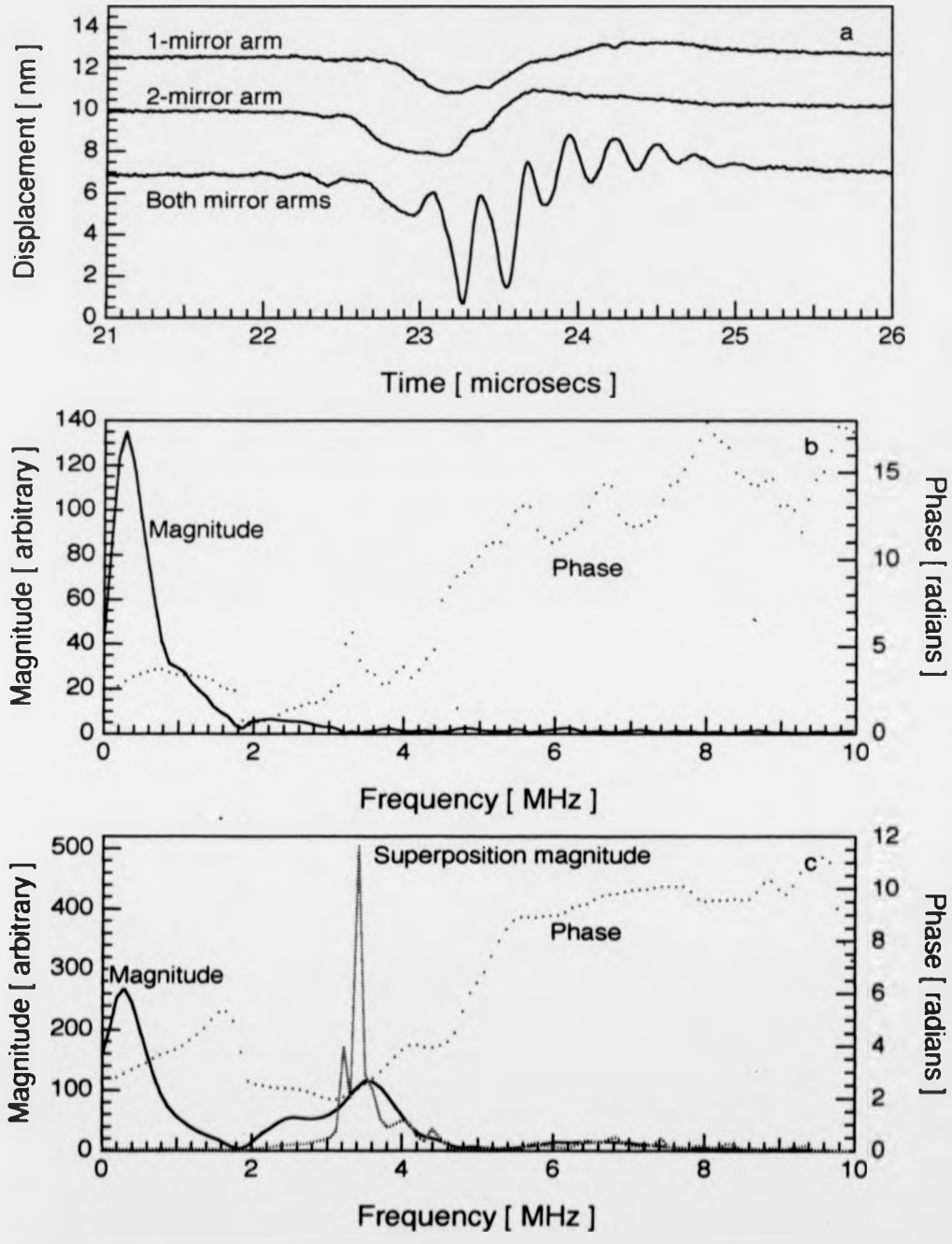

Figure 6.8 HeNe laser interferometer waveforms detected 68 mm from source on 63 mm thick aluminium. a). Interfered & individual beam acoustic signals. b). 1-mirror arm pulse FFT. c). Two beam interference source waveform FFT.

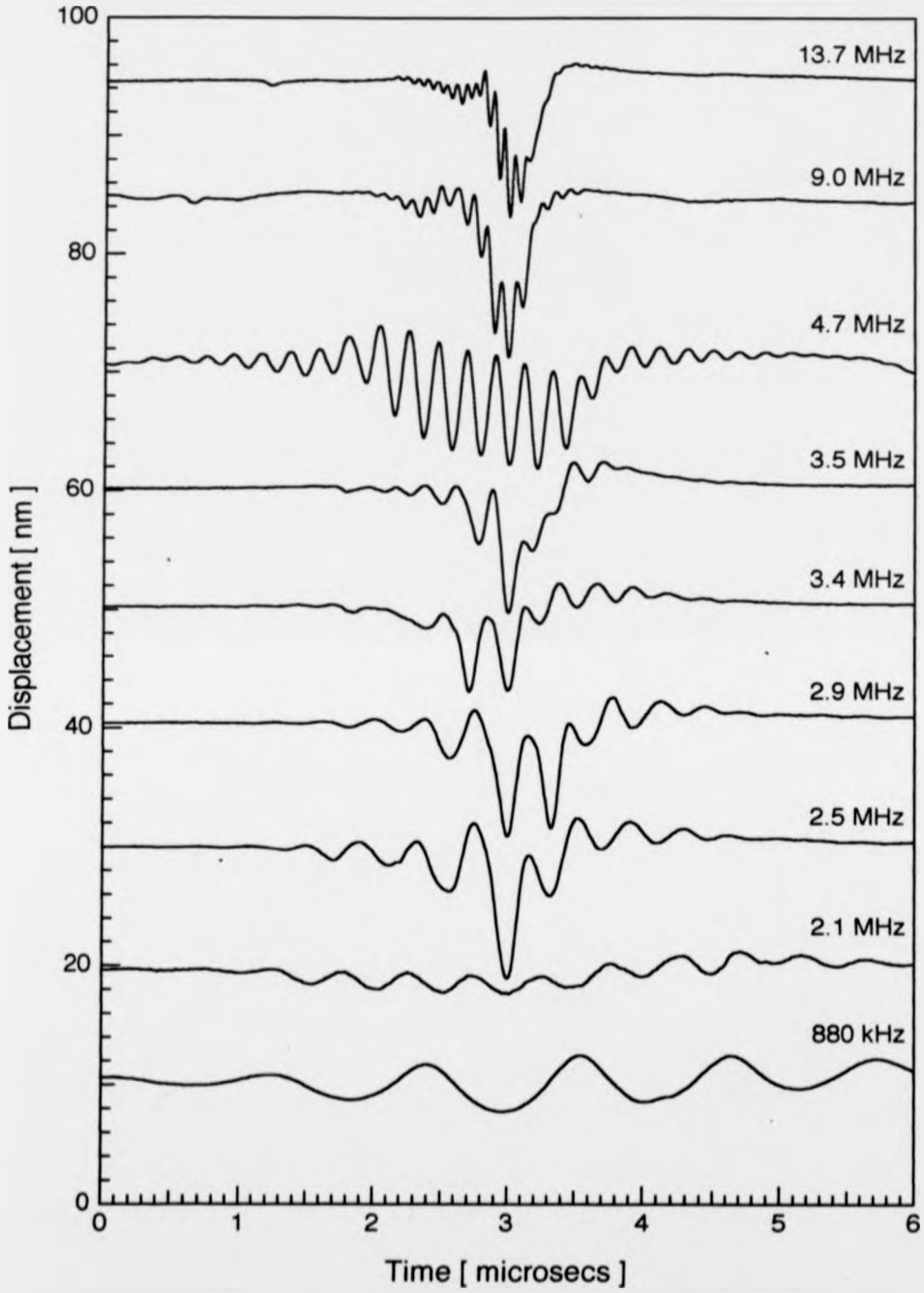

Figure 6.9 Interfering source Rayleigh waveforms on 63.16 (±0.02) mm thick aluminium ~69 mm from source centre. 9.0, 3.4 & 2.1 MHz superpositions detected by 632.8 nm (otherwise 532 nm) laser interferometer.

source production of frequencies between 13.7 (±0.2) MHz and 880 (±90) kHz. Beams incident normal to the sample surface generated the 13.7, 9.0 and 3.5 MHz source periodicities, which superimpose upon clearly discernable underlying carrier pulses, 3.5 MHz being the lowest frequency obtainable at $\phi = 0$ (Figure 6.7). When ϕ increases, reducing the superposition frequencies, until sample surfaces approach glancing angles with the beams, the pulse envelopes become more extended and lower in amplitude, as the source increasingly spreads across the surface. Pulse timings around the 23 μs mean Rayleigh arrival time are similarly scattered, as broad sources are hard to align accurately, and the compared waveforms (Figure 6.9) are therefore arbitrarily centred within a 6 μs time window. At the lowest frequencies, sources look more like strings of points than of lines, which further decreases signal amplitudes at the detector as more ultrasound radiates perpendicular to the superposition direction. Thus Fast Fourier transformed high frequency interference waves have broad, low magnitude peaks well separated from the broad, low frequency carrier pulse waveband, the amplitude of which is normalized to 100 (Figure 6.10). Source broadening reduces surface wave bandwidths, causing almost complete disappearance of the underlying pulse component in an 880 kHz spectrum dominated by the interference peak. Superposition frequency first harmonics visible in the 4.7, 3.4, 2.9, 2.5 and 0.88 MHz spectra probably result from Fourier transform aliasing, given the strong waveform periodicity, though the source may contribute indirectly by supressing waves with wavelengths that are non-integral factors of the interference spacing. A 23.68 (±0.02) mm thick sample of the aerospace alloy used in adhesively bonded joints gave similar waveforms (Figure 6.11). Despite holding the interfering source apparatus fixed at each frequency while substituting various samples, as described in sections 6.3 to 6.5, source conditions rarely reproduce exactly and centre frequencies found from FFT data (Figure 6.12) vary slightly from the 63 mm thick aluminium values. Note that the 13.7 MHz superposed waveform is not repeated and a 1.9 MHz wave replaces the first run's 3.5 MHz observation. These results show that the interfering beam technique provides calibrated, tuneable, single superposition frequency ultrasonic pulses, in a waveband useful for nondestructive evaluation, while still retaining laser generation's remote, noncontacting characteristics. Sections 6.4 and 6.5 use single frequency surface-travelling waves to probe adhesive bonds with varying lengths and adhesion properties for defects.

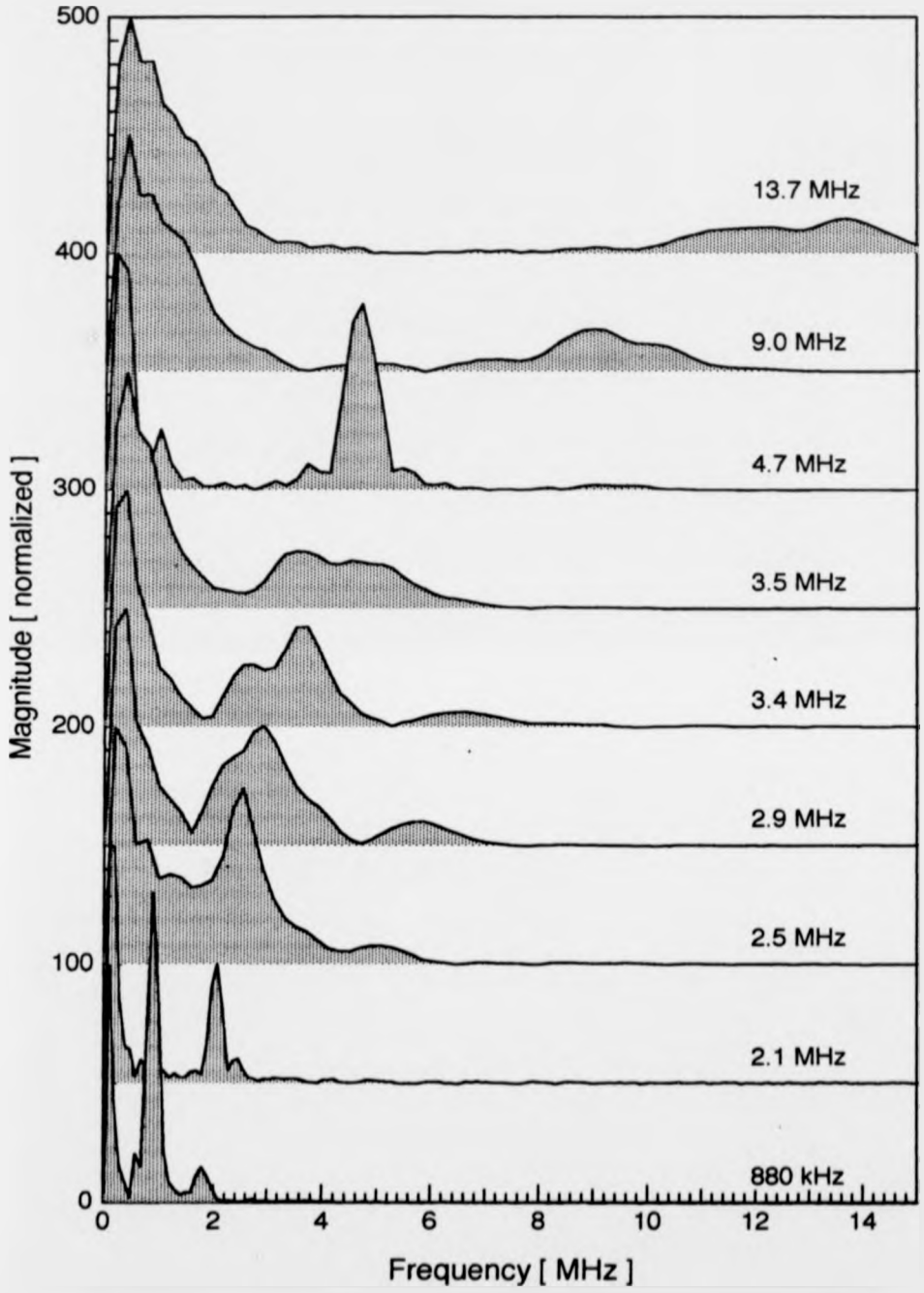

Figure 6.10 Fast Fourier transform magnitude spectra for interfering source Rayleigh waveforms on 63 mm thick aluminium. Normalized to the amplitude peak of the low frequency carrier pulse component in each waveform.

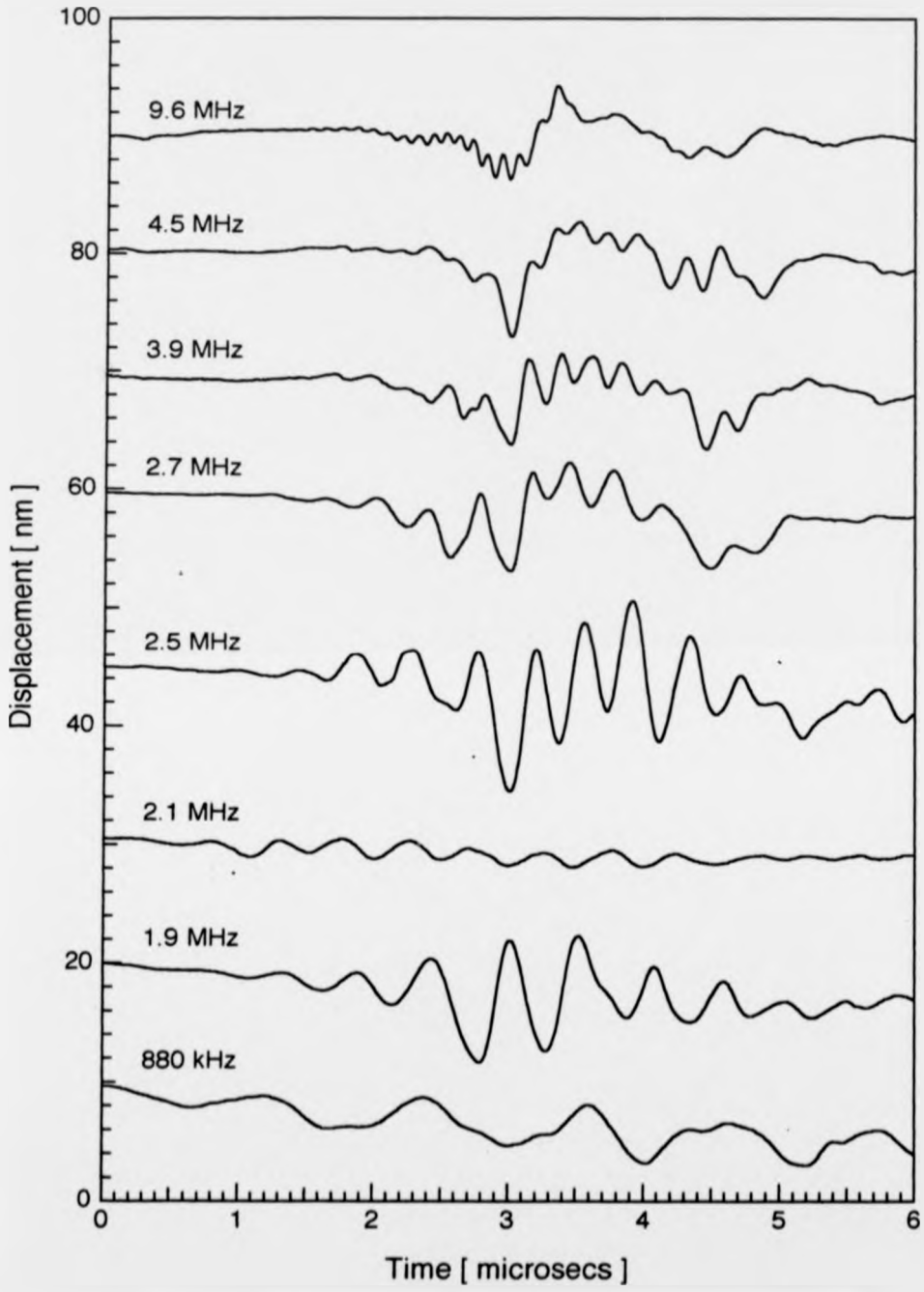

Figure 6.11 Interfering source surface-travelling waveforms on 23.68 (±0.02) mm thick aluminium alloy ~69 mm from source centre. Again 9.6, 3.9 and 2.1 MHz waves are detected on HeNe, not ADLAS, laser interferometer.

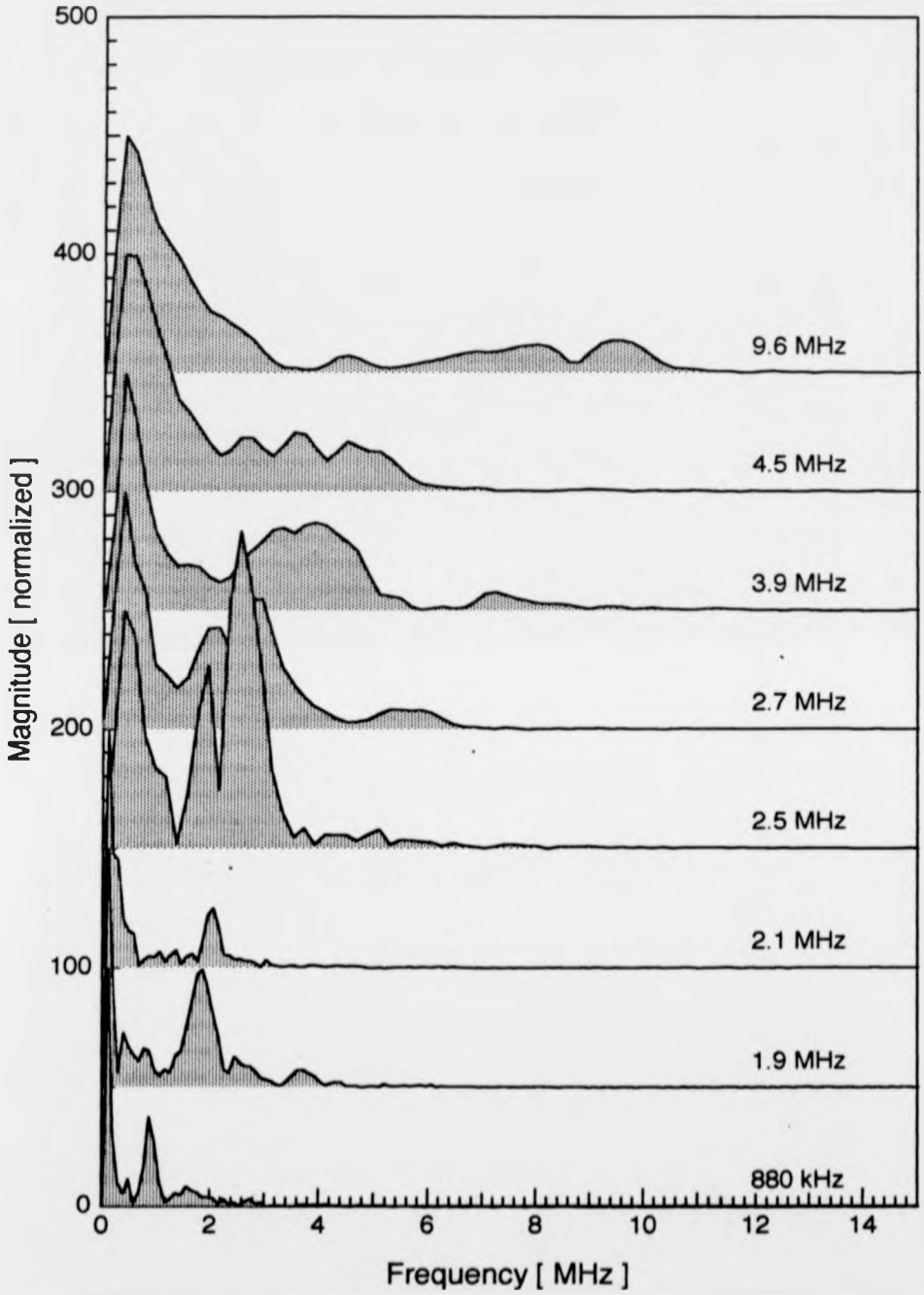

Figure 6.12 Fast Fourier transform magnitude spectra for interfering source surface waveforms on 24 mm thick aluminium. Each waveform is percent normalized to the amplitude peak of its own low frequency carrier pulse component.

6.4 Frequency Analysis of Surface Acoustic Waves Propagated Under Bonds.

This section presents the results of passing SIST waves generated by periodic sources along reinforcement joints, described in section 6.1, in which aluminium alloy adherends between 12 and 51 mm long are bonded to 356 mm long bases, all 25 mm square in cross-section. The source and detector, positioned a mean distance of 69 mm apart (Figure 6.2), observe SIST waves propagating along the base adherend surface at the free surface velocity (within experimental error). As graphically illustrated by interferometer detected, normal displacement waveforms (Figure 6.13), a 12.7 mm long interface layer, the shortest available in this experimental series, completely strips surface acoustic waves of 9.6 MHz, 4.5 MHz and 3.9 MHz interference source frequency components. Fast Fourier transforms confirm the obvious absence of high frequency components in the time signals, also remarked in broadband pulse data (Figure 6.5). 2.7 MHz is the highest superposition frequency observed after transiting a 12.7 mm long bond (Figure 6.14.a). FFT magnitudes from 2.7 MHz interference sources (Figure 6.15.a), normalized to a maximum of 100 to compare frequency distributions, show the free surface superposition peak (†) considerably reduced by a 12.7 mm bonded pathlength, and damped out altogether by bonds over 25.4 mm long. Thus, free surface wave magnitude attenuation at 2.7 MHz provides a crude measure of bond length, separating bonds over 38.1 mm or under 25.4 mm long. However, wave arrival times (Figure 6.14.a), though difficult to measure accurately, indicate SIST group velocities which are similar, within variations encountered due to fluctuations in material compositions, and not therefore reliable guides to adhesion properties. This at first appears to contradict earlier analyses [Rokhlin et al., 1980; 1981] based upon phase velocity variations. In that instance though, adhesive resin cure behaviour versus temperature and time was monitored on individual systems with carefully fixed geometry. This chapter compares different bonded joints and small velocity changes may be present, but not discerned above the grosser effects of slightly altered geometry or material property variations between samples.

At still lower frequencies, where the source is extended, free surface pulses have progressively narrower bandwidths and attenuate less quickly when they encounter bonds. For instance, a 50.8 mm long bond is needed to damp out 1.9 MHz periodicities (Figure 6.15.b) and the time waveform retains a low amplitude modulation even at that length (Figure 6.14.b).

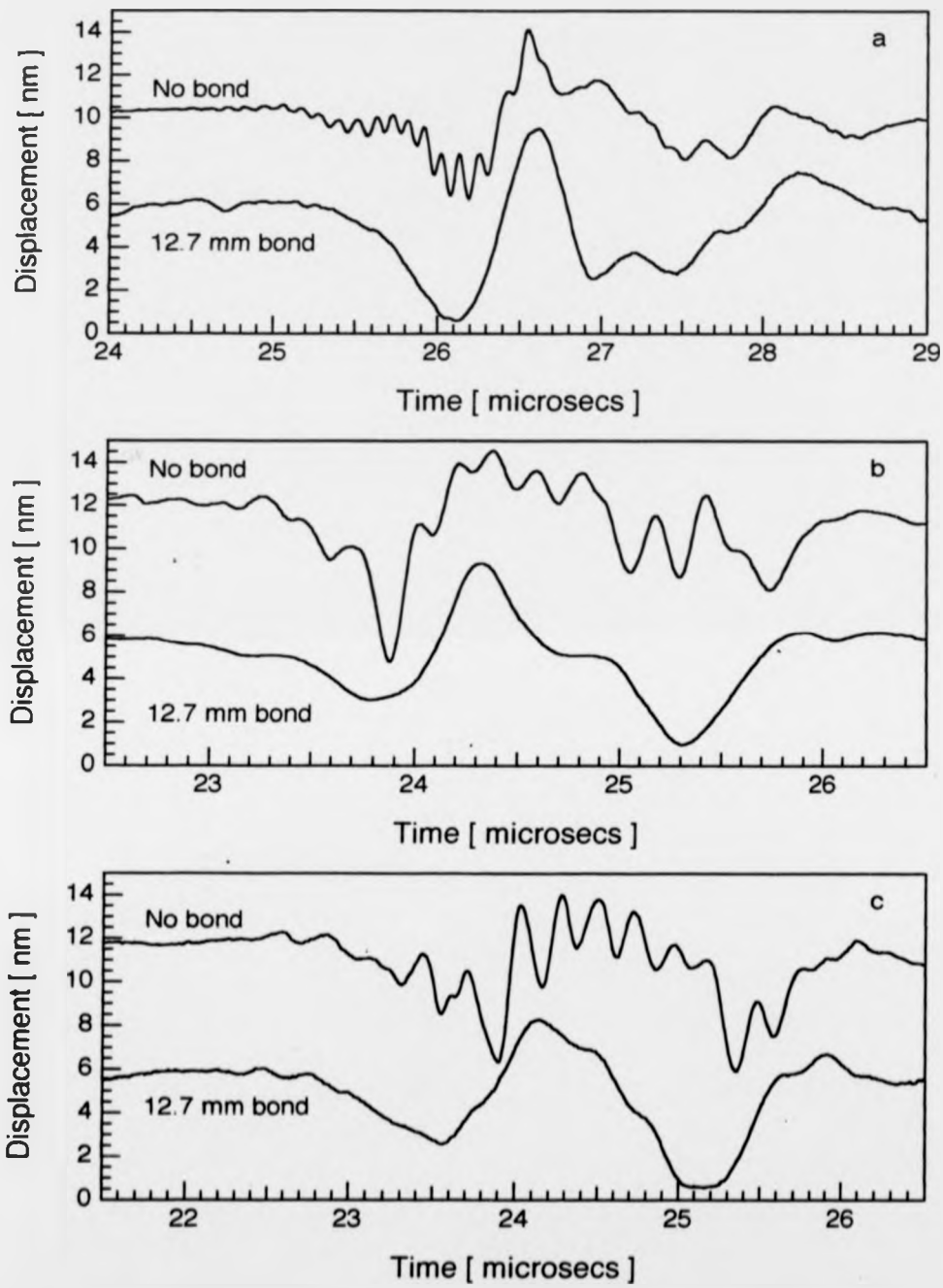

Figure 6.13 Interferometer detected surface-travelling waveforms on 23.68 mm thick aluminium and 12.7 mm long epoxy reinforcement joint having 25 mm thick adherends, with a). 9.6 MHz, b). 4.5 MHz, c). 3.9 MHz periodic sources.

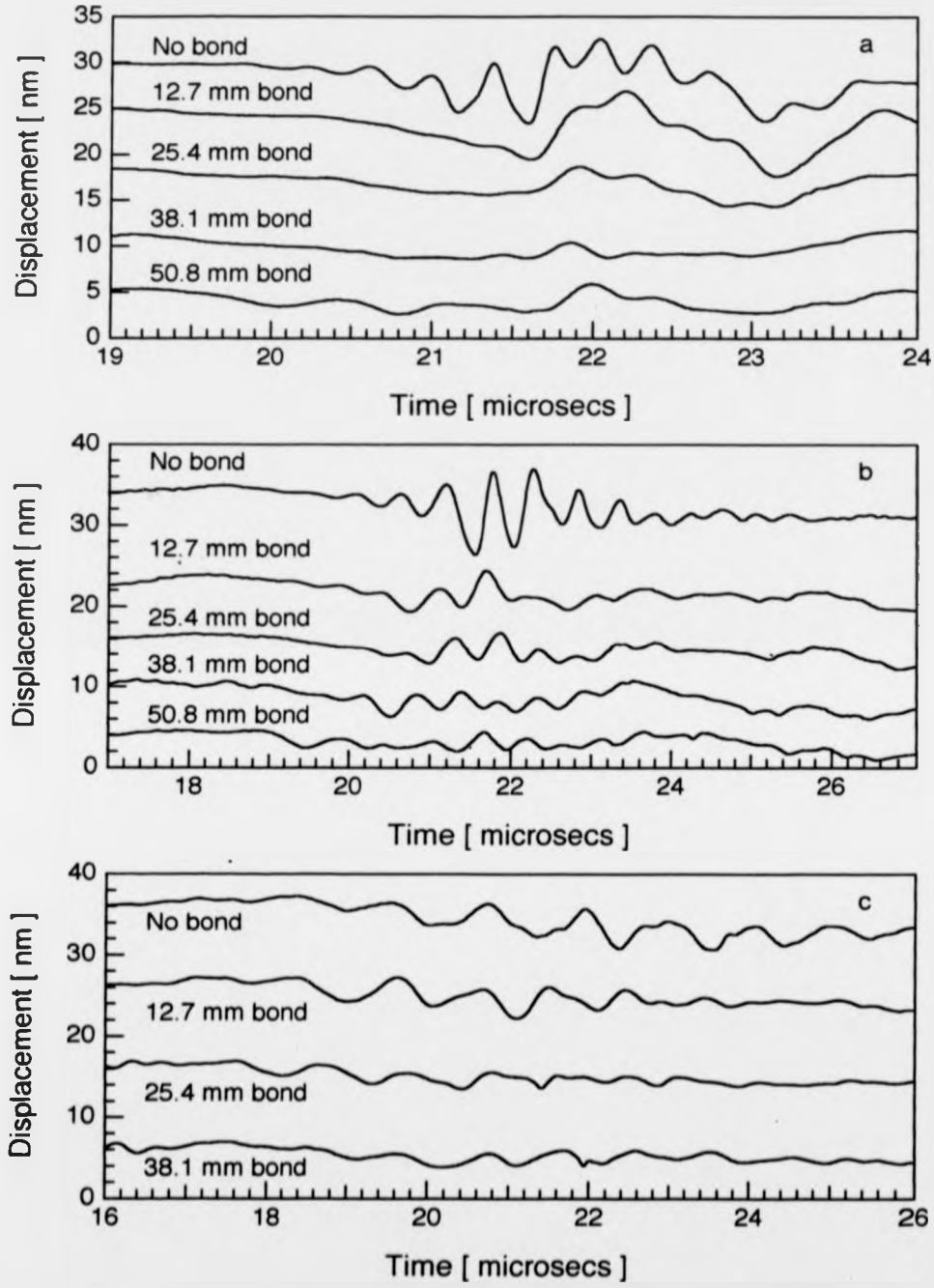

Figure 6.14 Interferometer detected surface-travelling waveforms on 23.68 mm thick aluminium or on reinforcement joints with variable length CG312/5 epoxy bonds. Superposed source frequencies a). 2.7 MHz, b). 1.9 MHz, c). 880 kHz.

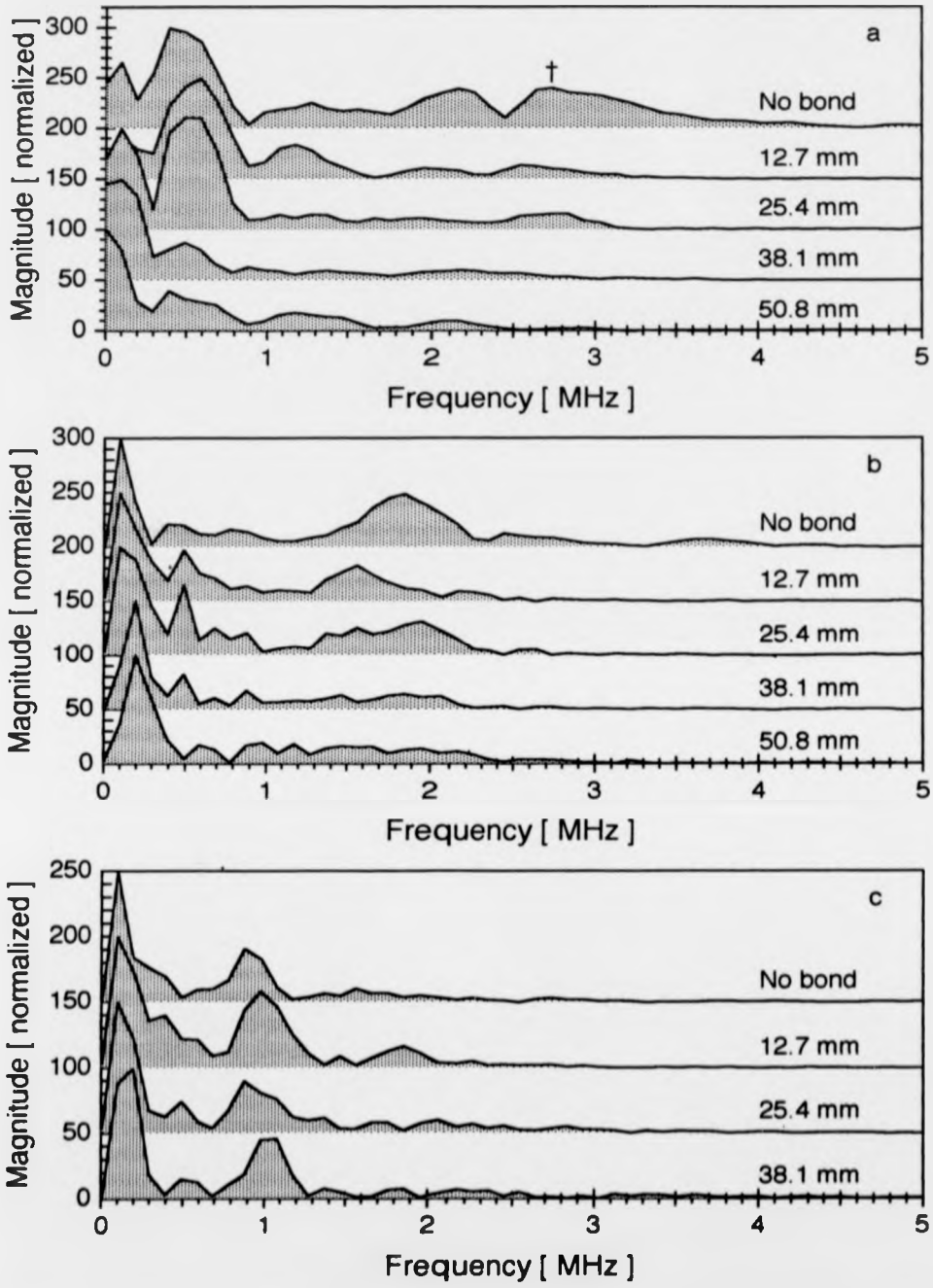

Figure 6.15 Fast Fourier transform magnitude spectra for interfering source surface waveforms on 24 mm thick aluminium & variable length CG312/5 epoxy reinforcement joints, with a). 2.7 MHz, b). 1.9 MHz and c). 880 kHz periodic sources.

880 kHz oscillations are virtually unaffected by bondlengths up to 38.1 mm (Figures 6.14.c & 6.15.c), above which the bonded region is too long to fit between the detector and a 20 mm wide source. These observations support interface wave calculations in chapter 2.5 for 0.2 mm thick CG312 epoxy layers bonding aluminium adherends. At 1 MHz only the 0 MHz interface mode exists (Figure 2.4) with 2930 (± 1%) m/s phase velocity, equal to the aluminium alloy Rayleigh velocity, and 2900 m/s group velocity. As the 0 MHz mode is weakly dispersive at frequencies below 8 MHz, low frequency SIST wave components can appear after bond lengths greater than 100 mm (Figure 6.3). At 2.5 MHz, a second, 1.6 MHz cutoff frequency mode is predicted with 1500 (± 2%) m/s phase velocity. This mode is highly dispersive and has a 2900 (± 1%) m/s group velocity at 2.5 MHz, which rises to a peak 3300 (± 1%) m/s at around 3.1 MHz before levelling out at about 2750 m/s at 8 MHz. A rapid onset of damping in the SIST wave interference term is observed, with frequencies above 3 MHz damped too heavily by bonded regions to be detectable, at 70 mm mean source to detector distances, and frequencies below 2 MHz barely perturbed by bonds less than 50.8 mm long. This suggests that higher frequency interface waves switch into the higher group velocity 1.6 MHz mode and are thus dispersed much more severely. Frequencies above 3 MHz are vetoed for SIST wave defect detection in bonds over 10 mm long. 2.7 MHz (Figure 6.15.a) or 2.5 MHz (Figure 6.16) interference source waves however, show useful sensitivity over the 0 to 100 mm length range encountered in this chapter. If the test system (Figure 6.7) is calibrated with well-bonded joints, bond lengths deduced from ultrasonic SIST wave data should agree with direct measurements of the external joint dimensions. Disagreement implies a variation in the joint properties which may originate from defects in the epoxy bond layer. This link is examined in section 6.5.

6.5 Testing the Quality of Adhesively Bonded Joints.

Several defective reinforcement joints (also constructed at DRA Aerospace) were examined using the broadband pulse system of section 6.1, from which frequency information is obtained via Fast Fourier transforms of the signals received. Defect, and equivalent well-bonded joint, results are compared with 2.7 MHz and 2.5 MHz narrowband interference source observations. The reinforcement bonds' external dimensions were kept fixed, with a 25.4 mm long upper

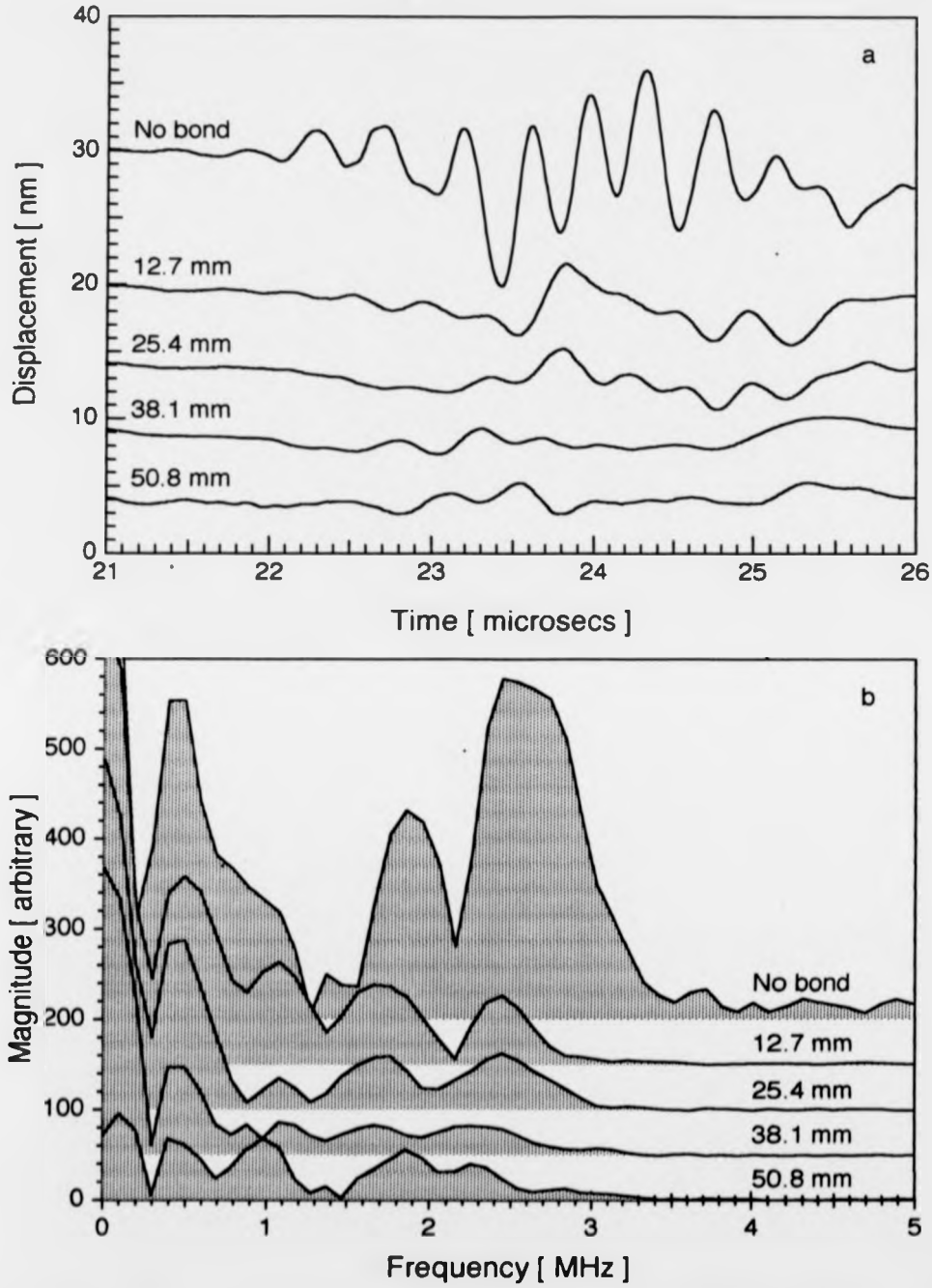

Figure 6.16 Surface-travelling waveforms detected by 532 nm laser Michelson interferometer on reinforcement joints with variable length CG312/5 epoxy bonds. a). Waves from 2.5 MHz interference source. b). FFT magnitude spectra.

adherend, but adhesion at the bond centres was impaired by defects deliberately incorporated prior to the joint curing cycle. The first defect joint contained an air gap due to a 10 mm long missing piece of the CG312/5 prepreg (chapter 3.1). Carrier embedded in CG312/5 impedes the return flow of molten epoxy, leaving a gap, albeit less than the original 10 mm in length, through which daylight is visible. The second joint was assembled identically, using epoxy CG312, which contains no carrier. Ultrasound appears incapable of detecting presence or absence of carrier directly, but epoxy flows more easily during cure, resulting in a closed gap and thinner bond layer. Both defects decrease the bonded interface area lying between source and detector, while increasing the free surface area, nominally equivalent to reducing the external bond length. In another case, a 10 mm long strip of liquid Frekote release agent, painted on the aluminium surface, provides a poorly-adhered area.

Broadband SIST pulses reveal differences in signals from the defective bonds and a 25.4 mm long control well-bonded joint (Figure 6.17.a), although variation between defects is slight. However, the changes observed are counterintuitive, as removing part of the bonded region decreases SIST wave amplitudes, despite decreasing the path length over which they disperse. Fast Fourier transform magnitude spectra of the SIST pulses (Figure 6.18.a) show amplitude reduction on defect samples at frequencies between 0.4 and 3 MHz. One reason might be that gaps introduce an extra finish and start to the bonded region (creating SISIST waves!), with mode conversion at those points significantly affecting the final SIST waveform. Alternatively, by impeding motion at the interfaces, defects may simply suppress the 0 MHz interface mode, without specifically stimulating mode conversion to free surface waves. In this context, it would be useful to carry out further experiments, maybe comparing a 50 mm long bond with a single joint containing two separate 12 mm long bonds, aligned with outer edges also 50 mm apart. Interference source waves at 2.7 MHz superposition frequency show only minor variations between well-bonded and defective joints (Figures 6.17.b & 6.18.b), but again defects produce components above 3 MHz which are not detected on the good bond. Signal variations below 1 MHz have to be treated with caution due to possible bulk wave contamination. 2.5 MHz superposition data (Figures 6.17.c and 6.18.c) presents similar results.

The broadband pulse data is best compared through FFT phase spectra (Figure 6.19.a),

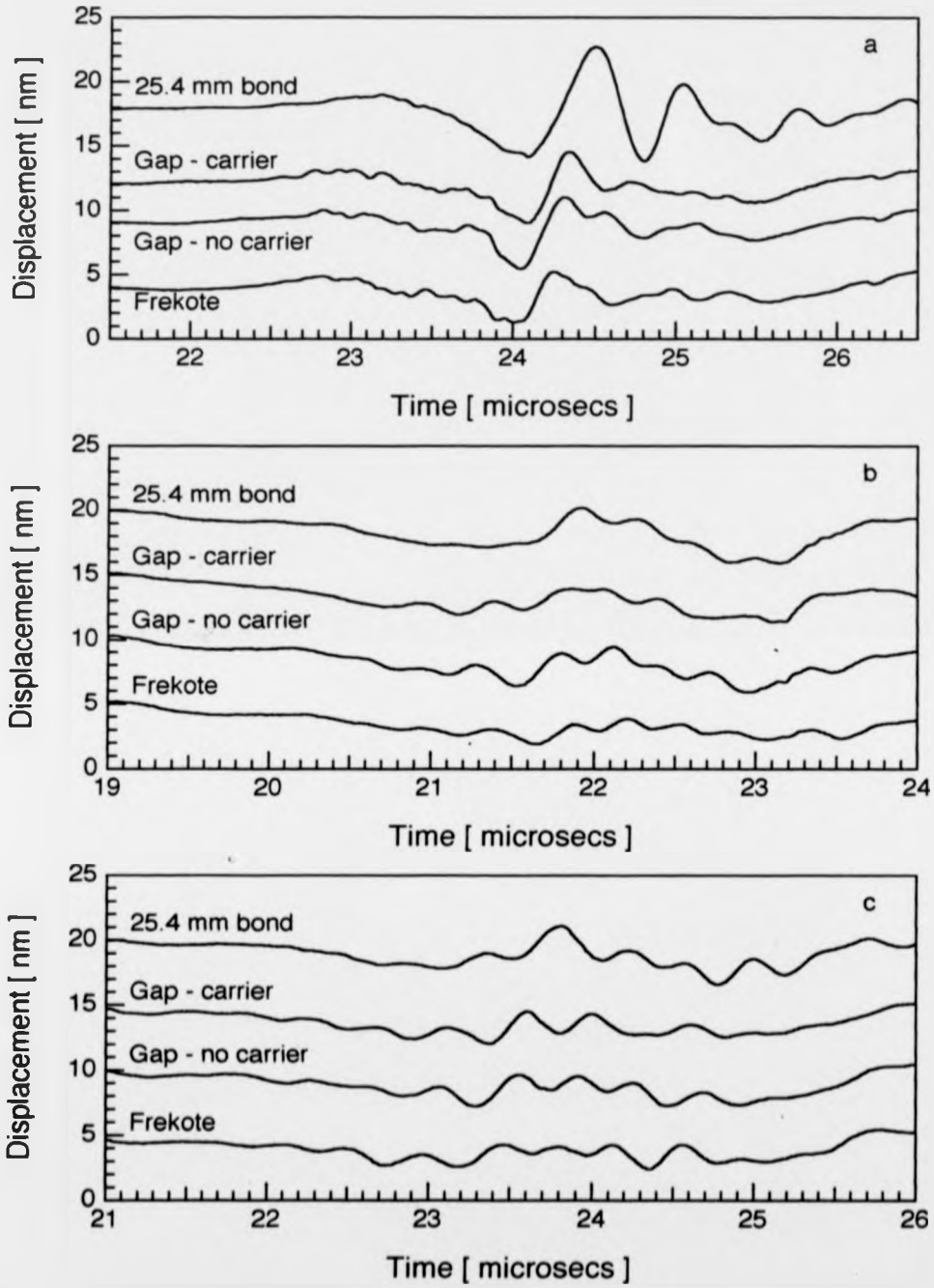

Figure 6.17 SIST waveforms detected by 532 nm laser interferometer on 25.4 mm long epoxy joints both well-bonded and with defects ~10 mm wide at bond centre. Source a). pulsed, or with b). 2.7 MHz, c). 2.5 MHz superposition frequency.

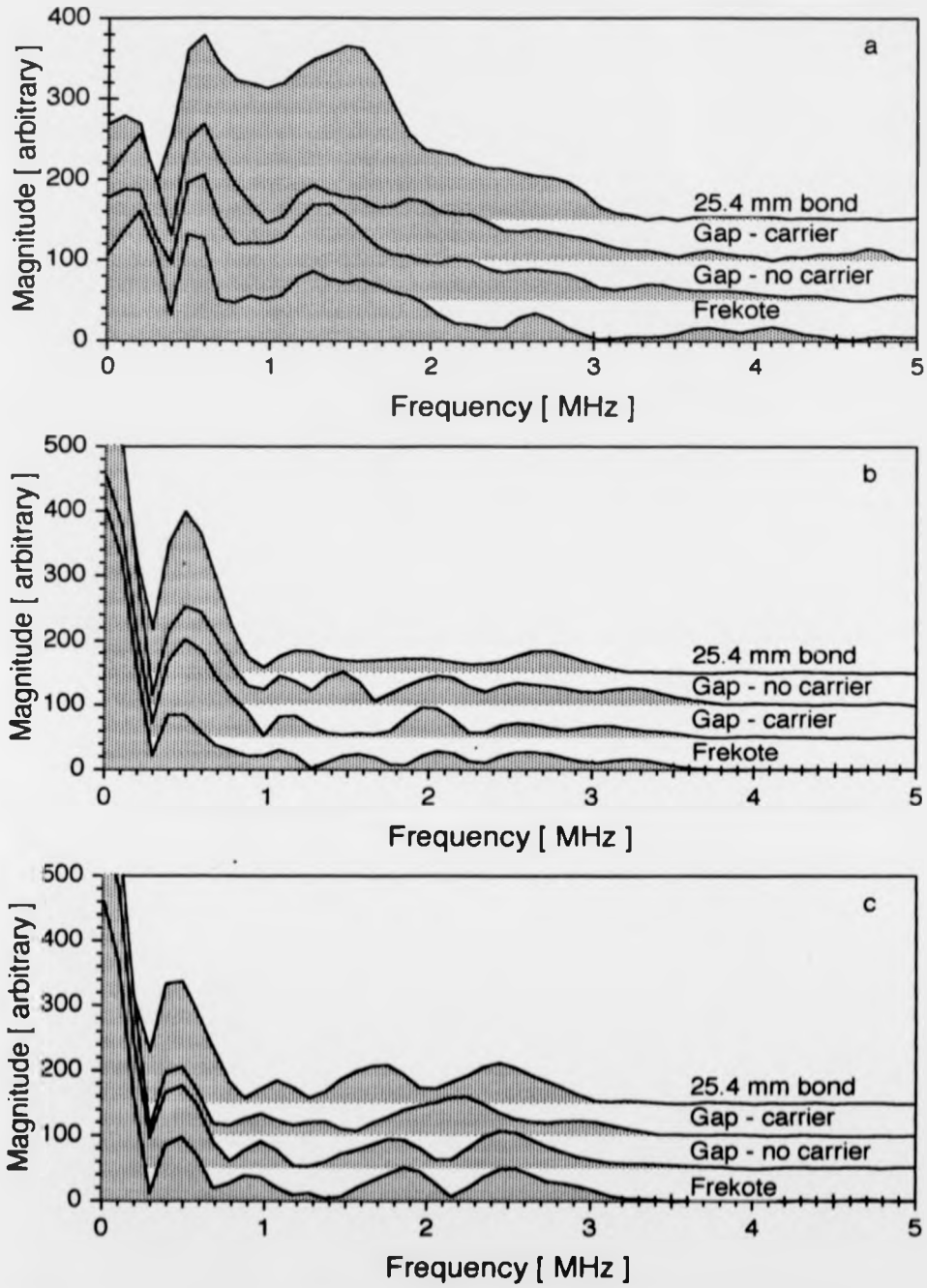

Figure 6.18 Fast Fourier transform SIST wave magnitude spectra from 25.4 mm long epoxy joints both well-bonded and with defects ~10 mm long at bond centre. a). Pulsed or b). 2.7 MHz, c). 2.5 MHz interfered laser acoustic source.

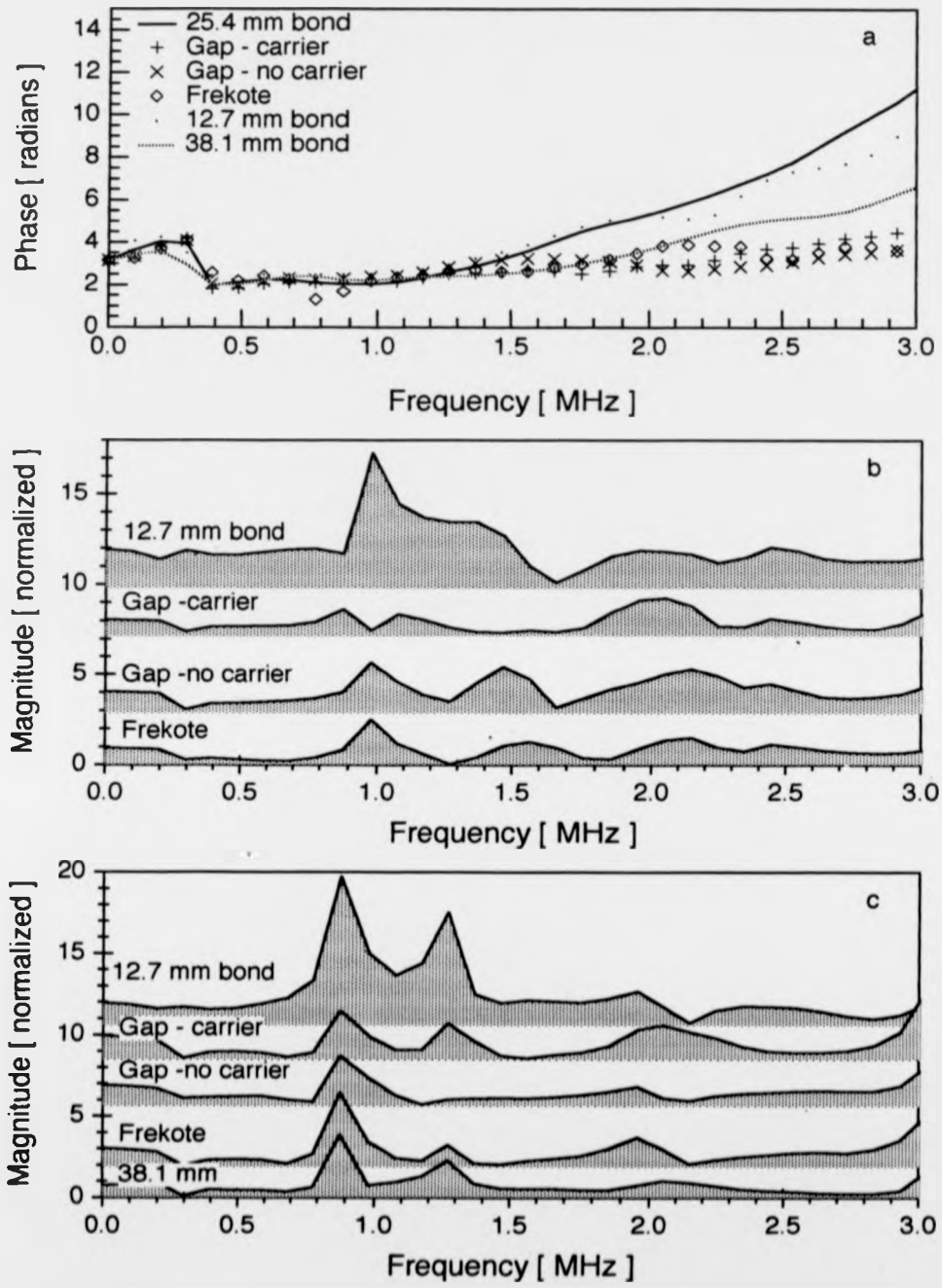

Figure 6.19 Defect detection on 25.4 mm long reinforcement joints. a). SIST pulse phase spectra of defect and varied length bonds. b). 2.7 MHz & c). 2.5 MHz superposed SIST wave magnitude spectra, normalized to 25.4 mm good bond.

which readily distinguish well-bonded and defective samples at frequencies above 1.5 MHz, again without appearing to distinguish between the types of defect involved. This is encouraging because a through thickness adhesion probe would find it harder to pick out the Frekote-released defect than a simple gap in the adhesive. For comparison, I have included phases taken from the 12.7 (±0.2) mm and 38.1 (±0.2) mm long well-bonded joints. The shorter bond phase closely resembles that of the 25.4 mm good bond, which appears dispersive above 1.5 MHz. None of the defect joints appears dispersive between 1.5 and 3 MHz, therefore appearing more like the longer bond length, suggesting heavier SIST wave attenuation than in the 25.4 mm good bond. Whilst SIST waves are clearly capable of separating defects in 25.4 mm bonds, phase comparison becomes much more difficult on longer bonds, for which contaminating bulk waves arrive closer together in time and SIST waves are dispersed to a degree where the pulses no longer have obvious zero points. The latter problem is also encountered in 2.5 MHz and 2.7 MHz superposition runs, suggesting that comparisons between magnitude spectra are more useful. By normalizing the defect magnitudes to the 25.4 mm long good bond magnitude, changes are observed due to the different bonds at frequencies between 0 and 3 MHz, above which well-bonded sample magnitudes are vanishingly small. For the 2.7 MHz source (Figure 6.19.b), the Frekote and CG312 gap defect spectra appear more similar than the CG312/5 gap spectrum. All three defects show markedly different behaviour from the 12.7 mm good bond at frequencies below 1.7 MHz and markedly similar behaviour between 1.7 and 2.3 MHz. However, at the frequency of interest, 2.7 MHz, the defect magnitudes lie close to 1, confirming little deviation from the original 25.4 mm well-bonded joint. A similar comparison for the 2.5 MHz interfered source (Figure 6.19.c) includes the normalized 38 mm long bond magnitude spectrum, which resembles the Frekote defect, in particular, extremely closely. However, despite a correlation between magnitude attenuation and bond length (section 6.4), which is most sensitive for 2 to 3 MHz frequencies, observations at 2.5 and 2.7 MHz show barely significant responses to epoxy bond defects.

This chapter has thus presented a strictly non-contacting method for producing narrowband surface-travelling ultrasonic signals with frequencies continuously variable between 880 kHz and 20 MHz. The method can produce narrowband waves in circumstances where broadband pulses obtained from a standard laser source are undesirable, and yet conditions are too harsh

to admit narrowband piezoelectric transducers. The ability to select individual frequencies has great potential for dispersive wave analysis and dispersion curve mapping, as the system is relatively easily switched between frequencies. Narrowband signals probing adhesively bonded regions of varying length and bond quality provide evidence which corroborates tests carried out, on the same samples, by broadband ultrasonic pulses. For technical reasons, the shortest available bonded reinforcement joints were 12.7 mm long and such joints entirely damp out superposition frequencies over 2.7 MHz. Although frequencies from 2.7 MHz down to 2 MHz give signals, passed under bonds, with amplitudes which are highly sensitive to the bond length, such waves appear relatively insensitive to interface quality. Studies indicate that overly high interference frequencies were chosen and that waves under 2 MHz will make more suitable interface adhesion probes. In addition, the experimental system geometry was too flexible to be held sufficiently constant between consecutive samples to detect changes in ultrasonic interface wave velocities, which are expected from variations in bond adhesion. Using a fixed optical superposition wavelength allows the optical arrangement to be bolted down or even simplified, for example by replacing the 45° mirror arrangement by a Fresnel biprism. And if the samples inspected are sufficiently manoeuvrable to be clamped into a set position relative to the optical arrangement, test repeatability would be greatly improved. For general work, phase spectra from broadband laser generated SIST pulses are capable of picking out bond defects, and further work is needed to map out the technique's limits. For experimental purposes laser Michelson interferometers were used to produce out-of-plane displacement waveforms, but the concentration on frequencies below 2 MHz indicates that EMAT detectors offer a suitable, less expensive alternative. To end on a note of caution, however, the results described in this chapter were all obtained on bonds with adherend thicknesses deliberately chosen to sustain Rayleigh free surface waves at the acoustic frequencies generated by the laser source. The waveforms observed are therefore considerably simpler than those detected on plate thicknesses more commonly encountered in aircraft manufacture.

CHAPTER SEVEN

FURTHER SURFACE ACOUSTIC WAVE EXPERIMENTS

Chapter 6 detected ultrasonic signals propagating as surface-interface-surface travelling (SIST) waves under reinforcement joints, where one adherend extends either side of a shorter adherend bonded to it. This chapter examines laser-generated ultrasound arriving at detectors via various paths across adhesively bonded joints, after initiation as surface-travelling pulses. Section 7.1 begins with surface-travelling waves reflected back by the adhesive region to detectors on the same surface as the source (Figure 7.1.a). Such waves are interesting for three reasons. Firstly, the reflection mode provides information which complements transmitted SIST wave data, since ultrasound which is not reflected must either scatter or pass along the bond. Secondly, the reflection mode has the advantage that detectors also observe the initial surface Rayleigh wave, whichever side of the source they lie, as symmetry ensures that a laser line source sends out equal amplitude surface pulses in both directions. Measuring the incoming wave on the same detector as the reflected wave allows accurate comparison of fast Fourier transform data, removing the effects of shot-to-shot source variability. Finally, since reflected waves only appear when a bonded region is present, they must therefore have interacted with at least part of the bond. Observed signals retain their sharply pulsed appearance after leaving the bond, the absence of spread indicating that reflection occurs in a well-defined region under the fillet, close to the second adherend edge (Figure 7.1.a). Ultrasonic probes sensitive to changes in this region could considerably aid bond strength predictions, as a weak adhesive fillet substantially reduces the entire bonded joint's strength.

Section 7.2 describes detection on the second adherend top surface (Figure 7.1.b) of surface-travelling waves initiated on the first adherend and coupled externally to the second via the adhesive fillet. Once again, the main interaction between ultrasound and epoxy occurs over the fillet region, making these waves of potential interest to bond strength studies. Externally coupled surface waves also need to be studied to determine how significant a part they play in removing energy from the incoming surface acoustic wave.

Section 7.3 monitors the emergence of SIST waves on the second adherend surface,

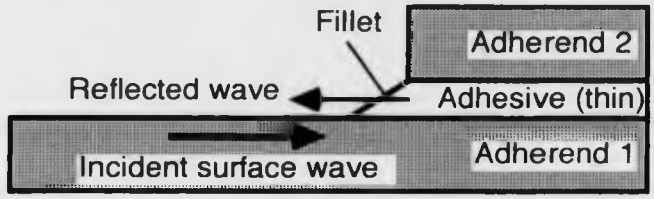

a. Wave reflected at edge of adhesive layer.

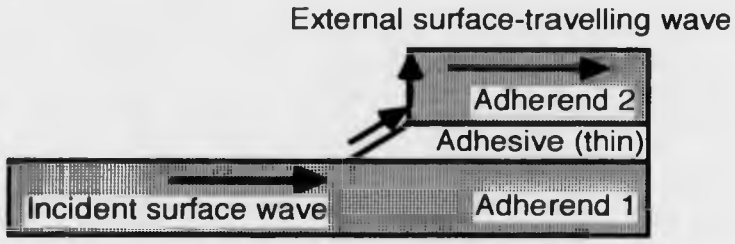

b. Wave diverted by edge of adhesive layer.

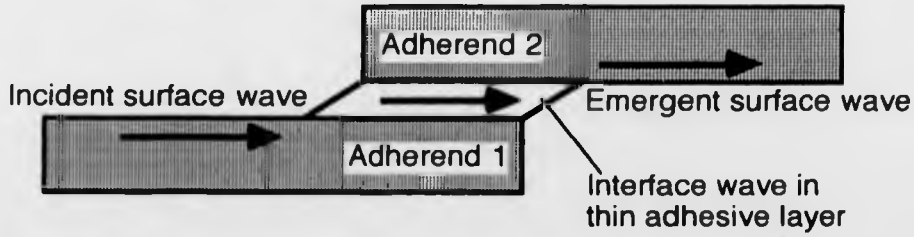

c. Wave transmitted across adhesive layer.

Figure 7.1 Different interactions observed between surface-travelling waves and epoxy bonded interface regions.

opposite the first surface along which they enter the bonded region (Figure 7.1.c), after coupling between surfaces over the interface portion of the wave. This is only possible in the lapped bond configuration as illustrated, unlike the previous top surface and reflected wave cases which apply equally to lap-shear and reinforcement joints. The experimental configuration for lap SIST waves requires source and detector lying either side of the bonded joint, which might not always be convenient, but at least provides a means of studying what is probably the more useful type of joint. Information gained from lap SIST waves differs from reflected and diverted wave data in that the entire bonded region is traversed and not just an area around the fillet. However, as remarked for reflected and diverted surface waves, lap SIST waves must interact with the bonded region at least once on their way to the detector, compared with direct reinforcement joint SIST waves (Chapter 6) which travel along the first adherend even if the second adherend is absent. The lap arrangement also screens many of the reflected bulk waves (see chapter 5.2) which arrive at incorrect angles to pass directly through the adhesive bond "window" and reflect onto a detector. The SIST waveforms obtained are treated in similar fashion to those observed in Chapter 6 and are generally less contaminated by bulk waves.

7.1 Examining Surface Waves Reflected at the Adhesive Fillet.

Reflected surface acoustic waves have been used in several surface defect studies [Cooper et al., 1986]. Theoretical treatments break such problems down into reflection from 90° (down) steps or 270° (up) steps. Reflection from a bonded joint edge (Figure 7.1.a) corresponds most closely to the latter case, which is known to cause extensive incident wave mode conversion. My experimental arrangement for detecting reflected surface-travelling waves (Figure 7.2) uses an expanded pulsed laser beam focussed by a cylindrical lens to form an ablating line source on the sample surface. Out-of-plane surface-travelling wave displacements are detected at the focussed spot of a Michelson laser interferometer (chapter 3.5), positioned between the source and the bonded region edge, at a fixed distance D from the source. In this way, the incident surface wave is detected at a fixed time, followed at a later time by the reflected wave. Samples are moved to alter the distance, d, between bond edge and detector, enabling relatively weak reflected signals to be distinguished from bulk wave arrivals, which are unaltered by such manoeuvres.

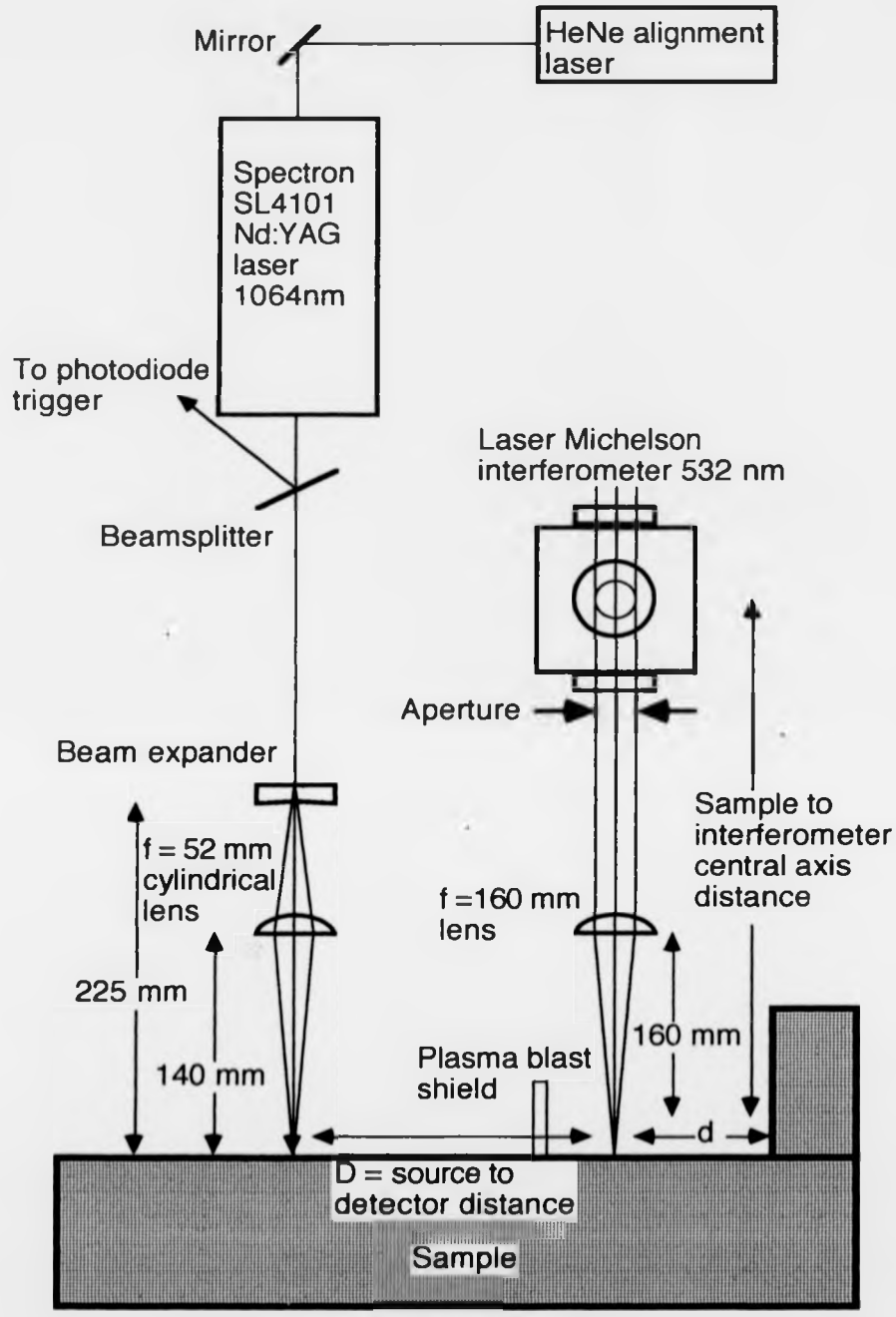

Figure 7.2 Experimental configuration used to investigate surface waves reflected by an adhesively bonded region.

A series of measurements made at source to detector distance D = 45.5 (±0.5) mm start with a solid aluminium block 47.5 mm thick, out of which a 270° step 17.5 mm deep is milled. Waveforms detected at d = 5.0 (±0.5) and 15 (±0.5) mm from the bond (Figure 7.3.a) register incoming arrivals (R) at the 2910 (±1%) ms^{-1} Rayleigh velocity, and bulk wave arrivals (sp and 2s), but no obvious reflected wave. The reflection from the sample end on the source side opposite the step which arrives at 25 μs on the d = 15 mm trace, illustrates the need for measurement at more than one d as, without knowing that its arrival time decreases with increasing d, it could be mistaken for a step reflected wave.

Comparing waveforms detected in the same geometry on a 102 mm long reinforcement joint bond with 25.4 (± 0.2) mm thick adherends, reveals clearly visible (†) reflected waves (Figure 7.3.b). Incident surface wave (R) arrival times give a 2930 (±1%) ms^{-1} Rayleigh velocity, from which the distance d travelled by the reflected pulses is estimated. Interestingly, calculated distances correspond to the detector to sample edge separation, which is approximately 2 mm more than the detector to fillet edge distance. This indicates reflection at the geometrical corner of the joint, rather than at the point where surface waves first encounter epoxy resin. An absence of reflected signals in the solid 270° corner case, however, shows that reflection at a bond is not accounted for solely by the increased total adherend thickness in the bond region. Reflection coefficients for surface waveforms at the boundary between a free surface and a layered structure are calculable from chapter 2.5 theory once current uncertainties in the interface wave solution are finally settled. Surface waves on a 25.4 mm thick adherend are Rayleigh-like, giving non-dispersive reflected waveforms which are enhanced, with respect to background noise and bulk-travelling arrivals, when traces detected at different d distances from the bond are overlapped and added (Figure 7.3.c). The reflected pulse has an order of magnitude lower amplitude than the incident surface wave (Figure 7.3.b) and flanking disturbances which appear to result from dispersion rather than bulk wave interference. Examining fast Fourier transform magnitude spectra of the three summed 102 mm long bond incident and reflected waveforms, indicates a frequency-dependent attenuation which gives the largest reflected wave amplitude reductions below 1.5 MHz (Figure 7.4.a). This accords with Chapter 6 observations that frequencies below 2 MHz are transmitted more strongly than higher frequencies.

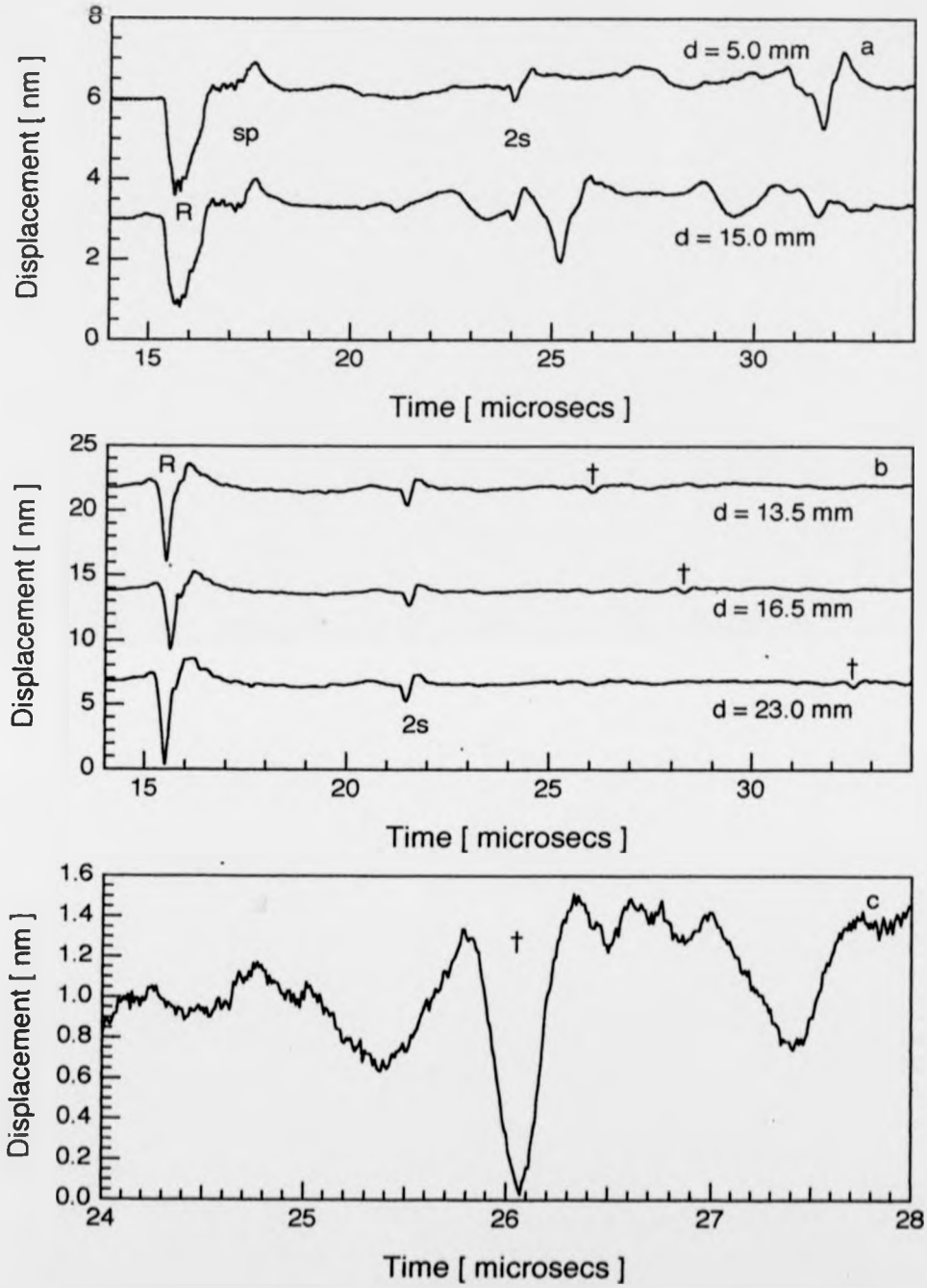

Figure 7.3 Incident and reflected surface waves detected by laser interferometer, at D = 45.5 mm, off a). milled step in solid aluminium sample and b). 102 mm long epoxy bonded joint. c). Sum of three reflected waveforms in b).

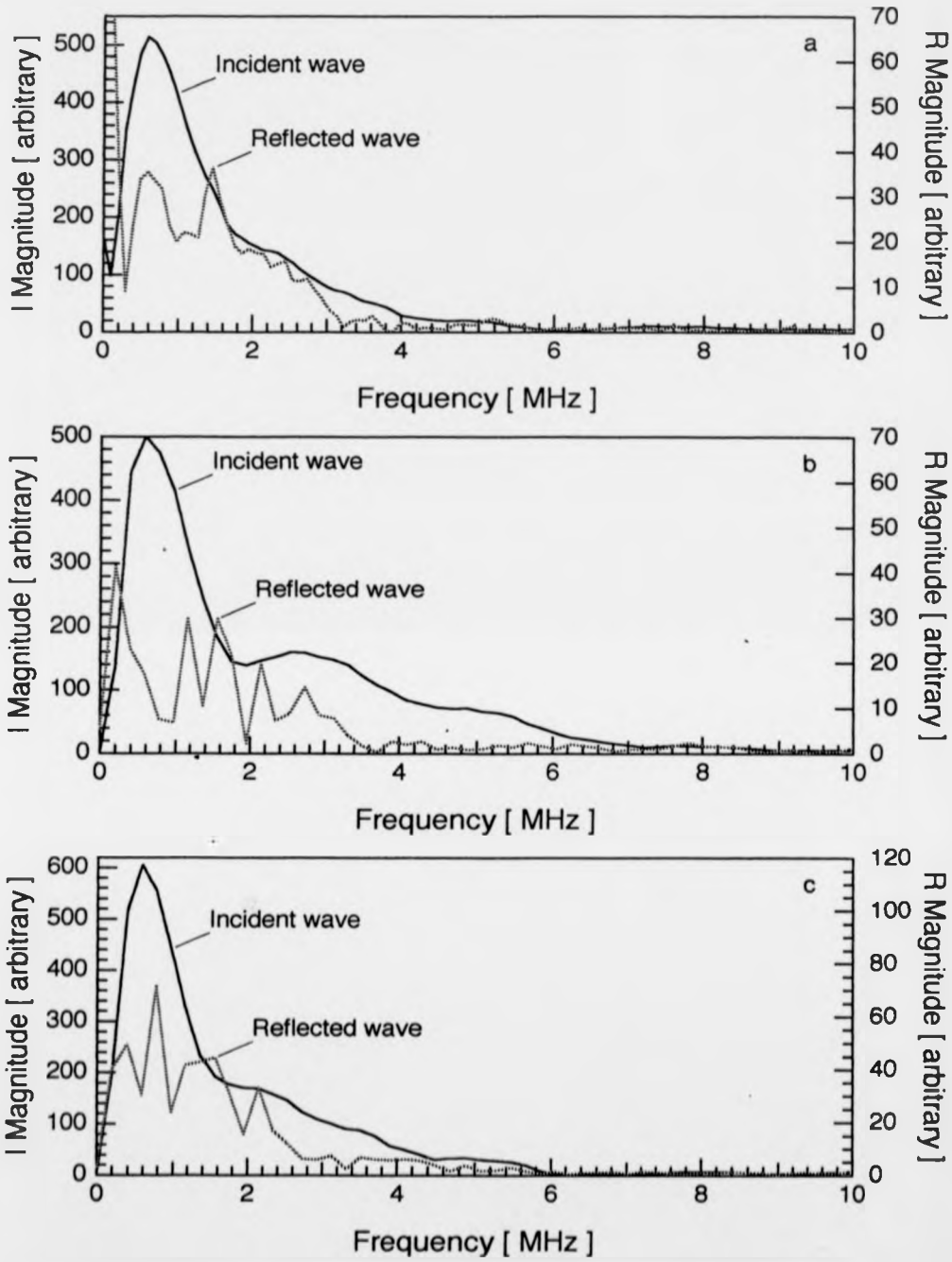

Figure 7.4 Fast Fourier transform magnitude spectra for summed surface waves at D = 46 mm, incident and reflected by front edge of bonds a). 102 mm long, and 12.7 mm long with b). 25.4 mm and c). 0.57 mm thick top adherends.

Very similar behaviour is observed (Figure 7.4.b) on a reinforcement joint with top adherend still 25.4 mm thick but only 12.7 mm long, as expected from the near identical aspect that each joint presents to oncoming surface-travelling waves. The 2 MHz knee in the incident wave FFT magnitude spectrum (Figure 7.4.b), which is more prominent than in the longer bond case, is associated with sp bulk wave (15.513 μs calculated arrival time) contamination of the 15.51 μs surface arrival. Some interaction is unavoidable, given the constraints of geometry, but the magnitude knee reduces if the ablation source power density increases, and with it the incident surface wave amplitude relative to the bulk (Figure 7.4.c). Despite applying this slightly stronger source to a joint with a 12.7 (±0.2) mm long top adherend only 0.57 mm, instead of 25.4 mm, thick the reflected wave FFT magnitude spectrum (Figure 7.4.c) differs little from before, with modest magnitude increases at frequencies below 1.5 MHz.

A 12.7·mm long lap-shear joint with 25.4 mm thick adherends presents to incoming surface waves a geometry identical with the 12.7 and 102 mm long reinforcement joints. S3p arrivals just before 21.9 μs and 2p2s arrivals after 26.3 μs are bulk waves, while obelisks mark points around which the reflected surface waves are expected from the 2870 (± 1%) ms^{-1} aluminium alloy Rayleigh velocity. However, there are no clear reflections from the front joint edge (Figure 7.5.a) implying that altering the geometry on the outgoing side of the bond has a surprisingly large effect. Features marked ¡ observed some 9 μs after the expected † arrivals correspond to reflection approximately 12.9 mm beyond the bond region's leading edge, that is to say at the 90° down step where the first adherend ends (Figure 7.1.c). Once again reflected surface waves are enhanced with respect to bulk arrivals by alignment and summation (Figure 7.5.b). Rear edge reflected wave attenuations are not expected to share the same frequency dependencies as for arrivals reflected off the bonded region front edge, and fast Fourier transforming the observed surface waveforms confirms this (Figure 7.5.c). In particular frequencies below 1.5 MHz are once again apparent, indicating that their absence from reflected signals on reinforcement joints is due to transmission mainly within the aluminium substrate. Note however that the rear edge reflection pulse amplitudes are only slightly larger than front edge reflection amplitudes detected on the reinforcement joint (Figure 7.3.c). This is important for two reasons. Firstly, since free surface waves on aluminium lose relatively little amplitude on reflection at the sample edge (Figure 7.3.a and related remarks), low amplitude rear edge

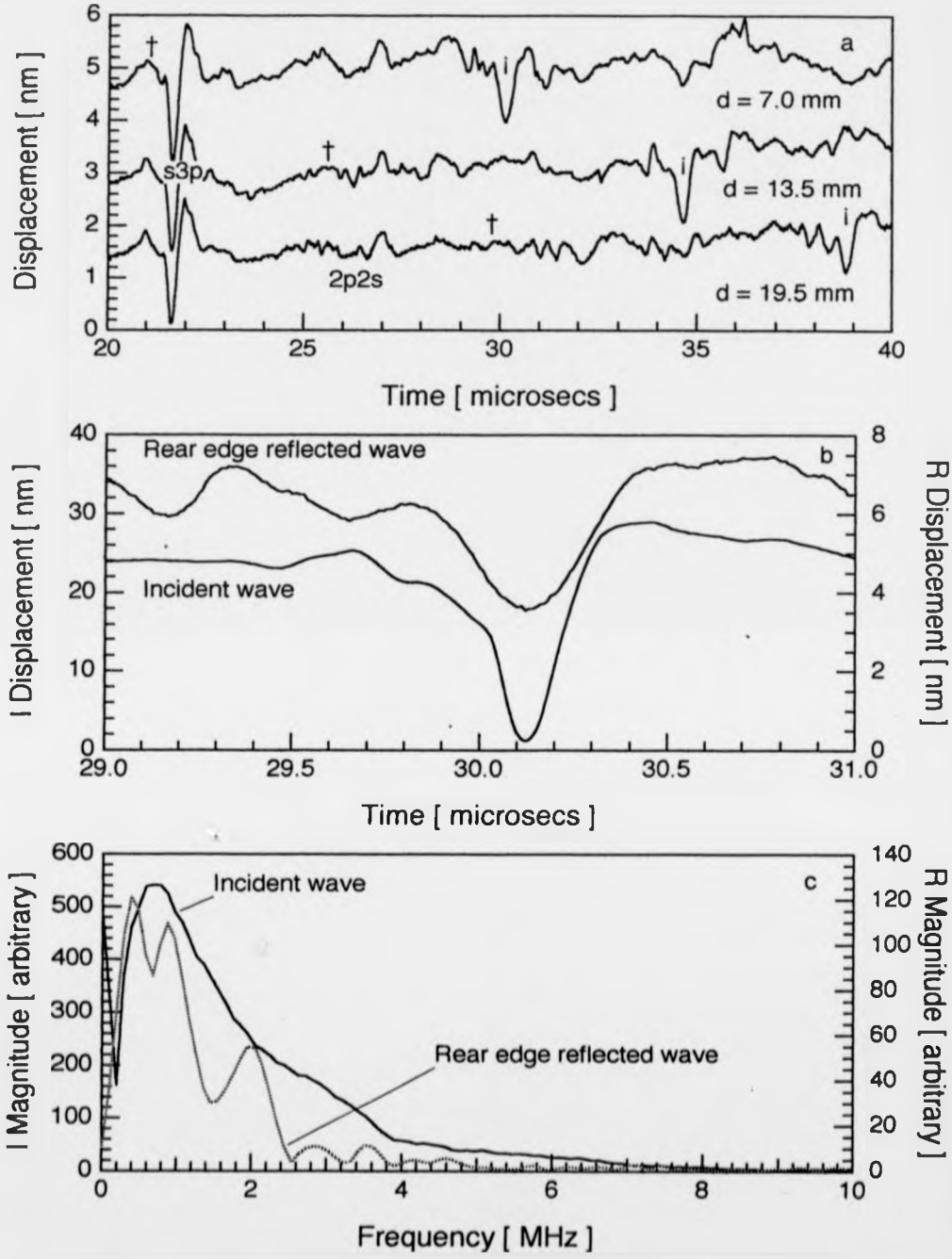

Figure 7.5 Incident and reflected surface waves from lap joint bond edge, detected by laser interferometer at D = 46.5 mm. a). rear edge reflected ¡ waves larger than front reflected † waves. b). Summed waves. c). FFT magnitude spectra.

reflected waves point in favour of the chapter 2.5 theory that ultrasound interacts strongly across the bond layer, rather than staying mainly within the first adherend. Secondly, low reflected wave amplitudes make distinguishing surface wave dispersion from background bulk wave contamination a major problem. As a result it is hard to see reflected surface waves being useful for preliminary diagnosis of defects even on these 25 mm thick bonds. In terms of monitoring incoming surface waves, however, the pre-bond interferometer position is extremely valuable. I would therefore recommend that at least some of any future, transmitted SIST wave, defect sensitivity experiments (Chapter 6) are supported with simultaneous ultrasound detection by interferometers positioned either side of the joint.

7.2 Preliminary Observations of Surface Waves Bridging Adherends Via the Fillet.

Wave components which are not reflected may either travel under the bonded region, or divert at the fillet to travel up the side of the second adherend and onto its topmost surface (Figure 7.1.b). The experimental arrangement for observing waves travelling along the upper surface of the second adherend differs from that in section 7.1 only by setting source and detection surfaces in different planes (Figure 7.6). The top adherend surface was chosen for observation rather than the end face (also indicated) for the practical reason that the adherend ends were deeply-grooved by saw marks and polishing to the standard required for Michelson interferometry would almost certainly damage the fillet. The configuration has the disadvantage that surface waves encounter an additional corner round which they have to pass on their way from fillet to detector. However, even on highly polished, reflecting end faces, there can be problems if the Nd:YAG generating laser beam crosses the Adlas laser interferometer beam, as expanding plasma disrupts the air through which the interferometer beam passes and Nd:YAG radiation can scatter into the detector. One alternative is to dispense with the interferometer and use EMAT detection, although close proximity to a laser blast causes undesirably large initial (electromagnetic) noise on the signals received. If there is room, a 45° mirror could be used to bend an interferometer beam incident normal to the top onto the end face, although it is subsequently more difficult to adjust the beam focus. Finally, an interesting research experiment would be to use a hemicylindrical top adherend, on which surface-travelling wavelengths much smaller than the radius are only slightly dispersive, allowing waves to reach a detector on the

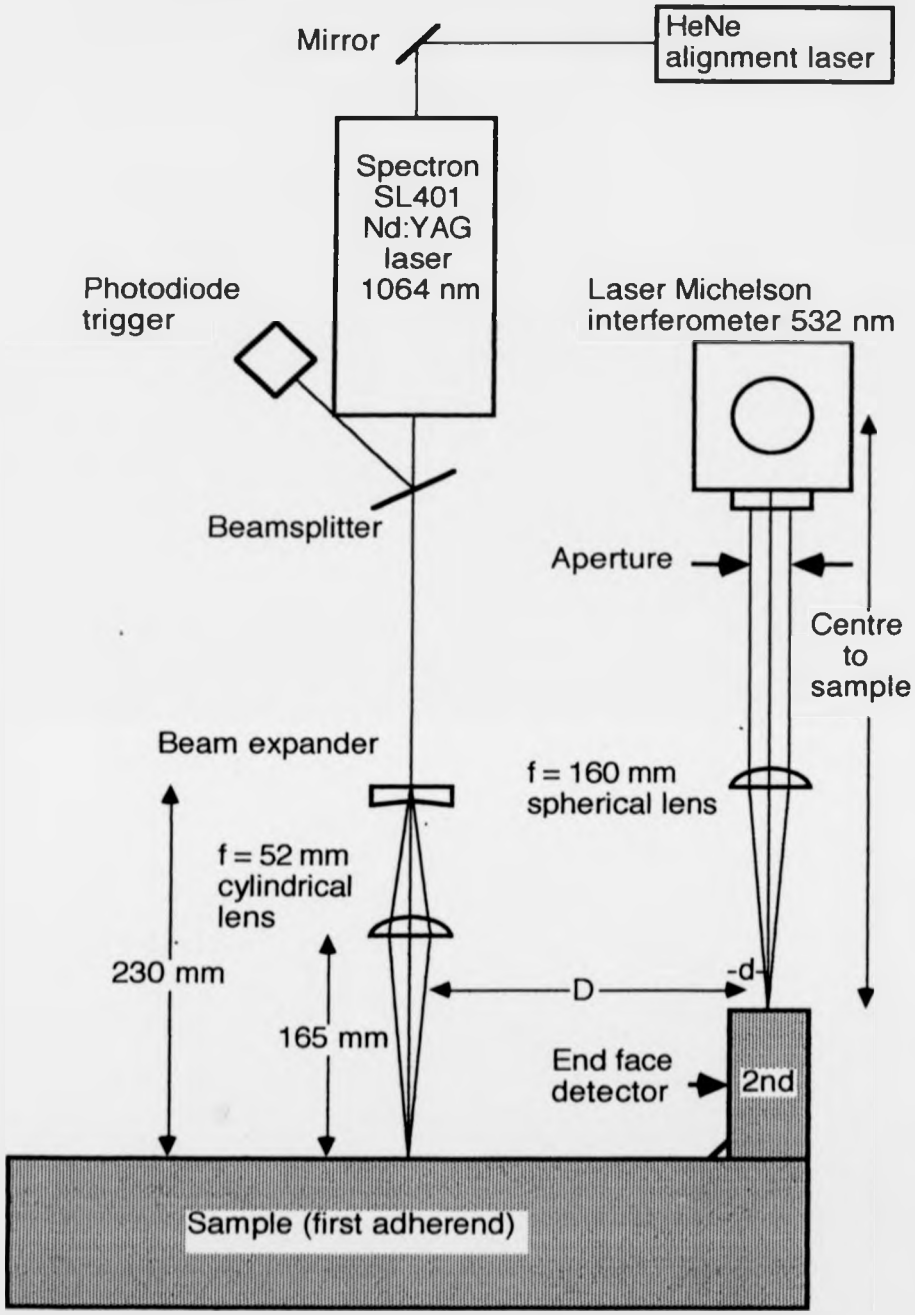

Figure 7.6 Experimental configuration for observing surface waves which cross the adhesive fillet at the bond edge and travel along the second adherend's external surfaces.

curved adherend surface without meeting a corner at all.

For detection on the top adherend surface, a focussed line ablation source is generated at a fixed distance D, chosen to be 38.5 mm, from the detector (Figure 7.6). The separation between the second adherend surface and interferometer centre axis also remains constant, and lenses focussing the Nd:YAG source are moved along the beam to maintain a constant distance from the first adherend surface. Surface waves travel a distance t + D to the detector, where t is the second adherend thickness, unlike bulk-travelling waves, which are either created at the source and reflected via the back surface or arise from surface wave mode-conversion at the 270° corner of the step. On a given sample the surface wave arrival time is therefore fixed, while bulk waves arrive at times that can alter with the detector distance d from the top edge. This is illustrated first on the 17.5 mm deep solid aluminium step (Figure 7.7.a), where a surface-travelling wave is indeed readily detected, independent of d, at 19.21 (±0.01) μs. On a 17.5 mm step, surface waves travel 56 mm from source to detector, implying 2920 (±1%) ms^{-1} for the adherend Rayleigh velocity, which section 7.1 observations confirm. FFT magnitude spectra (Figure 7.7.b) for the d = 4 mm diverted wave and earlier observed incident wave (Figure 7.3.a) coincide within experimental error at wave frequencies lying above 1 MHz, while diversion heavily attenuates frequencies below 1 MHz. Thus, ultrasonic wavelengths shorter than 3 mm are diverted, suggesting that they are small compared with the local radius of curvature at the step base and follow a relatively rounded surface. Longer wavelengths meet a relatively sharp corner where they mode-convert into bulk-penetrating waves.

Diverted surface-travelling waves observed on reinforcement bonds, 102 mm (Figure 7.8.a) and 12.7 mm (Figure 7.8.b) long, arrive later than on the step because the adherends in these cases are 25.2 mm thick. As in section 7.1, substituting a solid step with an epoxy bonded joint has a marked effect on the detected waveforms. Diverted signals observed on the joints have low amplitudes compared with the incident pulses, closer to those of the reflected surface waves. Fast Fourier transform magnitude spectra of reflected and diverted components for the 102 mm long bond (Figure 7.9.a) are broadly similar, implying a similar ultrasonic scattering mechanism in each case. Since the diverted waves show marked attenuation at frequencies over 2 MHz, they are not simply following the fillet's curved outer surface, as they

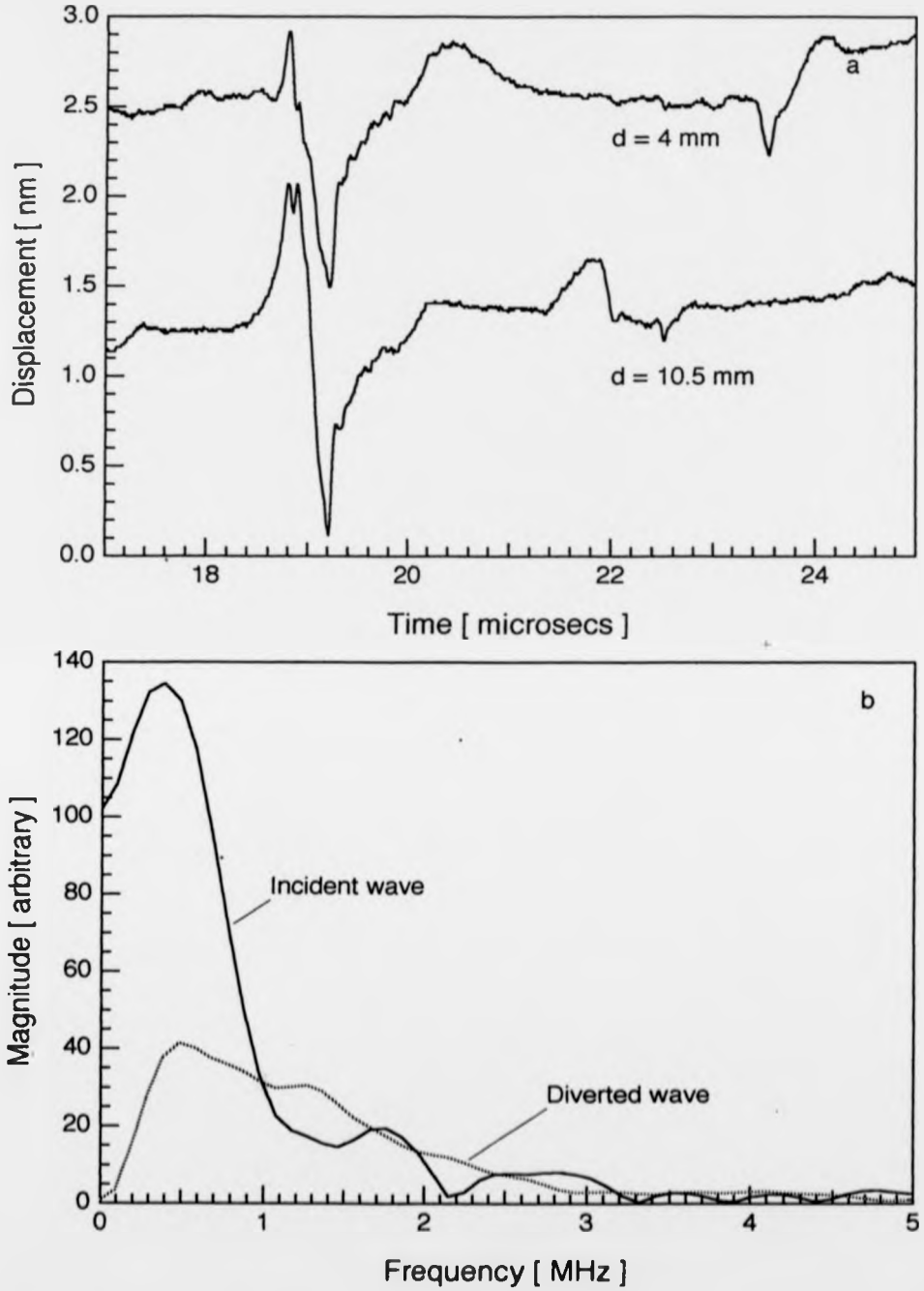

Figure 7.7 a).Acoustic waves travelling along the top surface of a 17.5 mm deep step in solid aluminium sample, between line source and interferometer detector 38.5 mm apart. b). Diverted & incident wave FFT magnitudes compared.

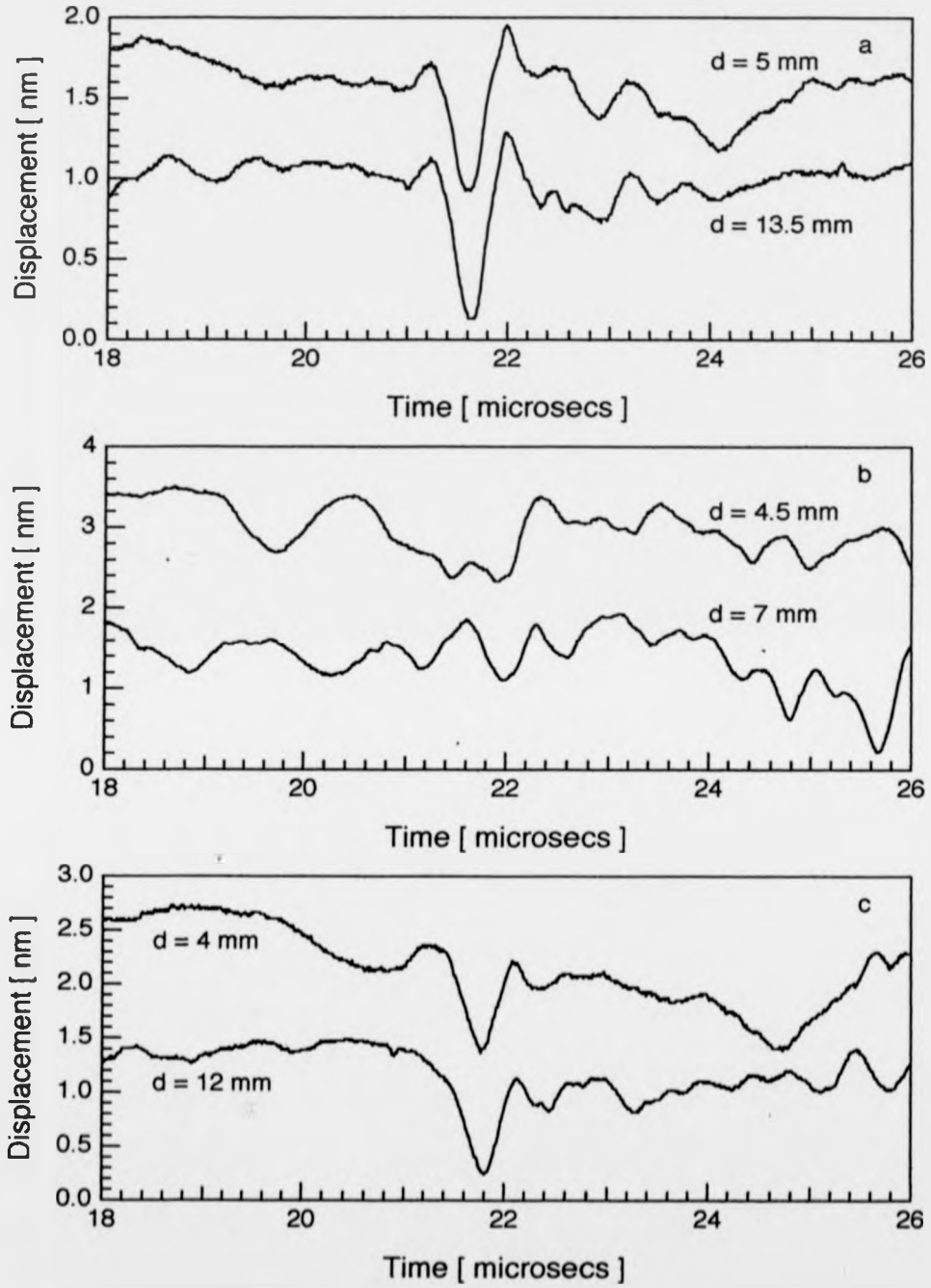

Figure 7.8 Surface waves detected on top of second adherend by laser Michelson interferometer at D = 38.5 mm from line source on reinforcement joints a). 102 mm & b). 12.7 mm long , or on c). lap-shear joint with 12.7 mm overlap bond.

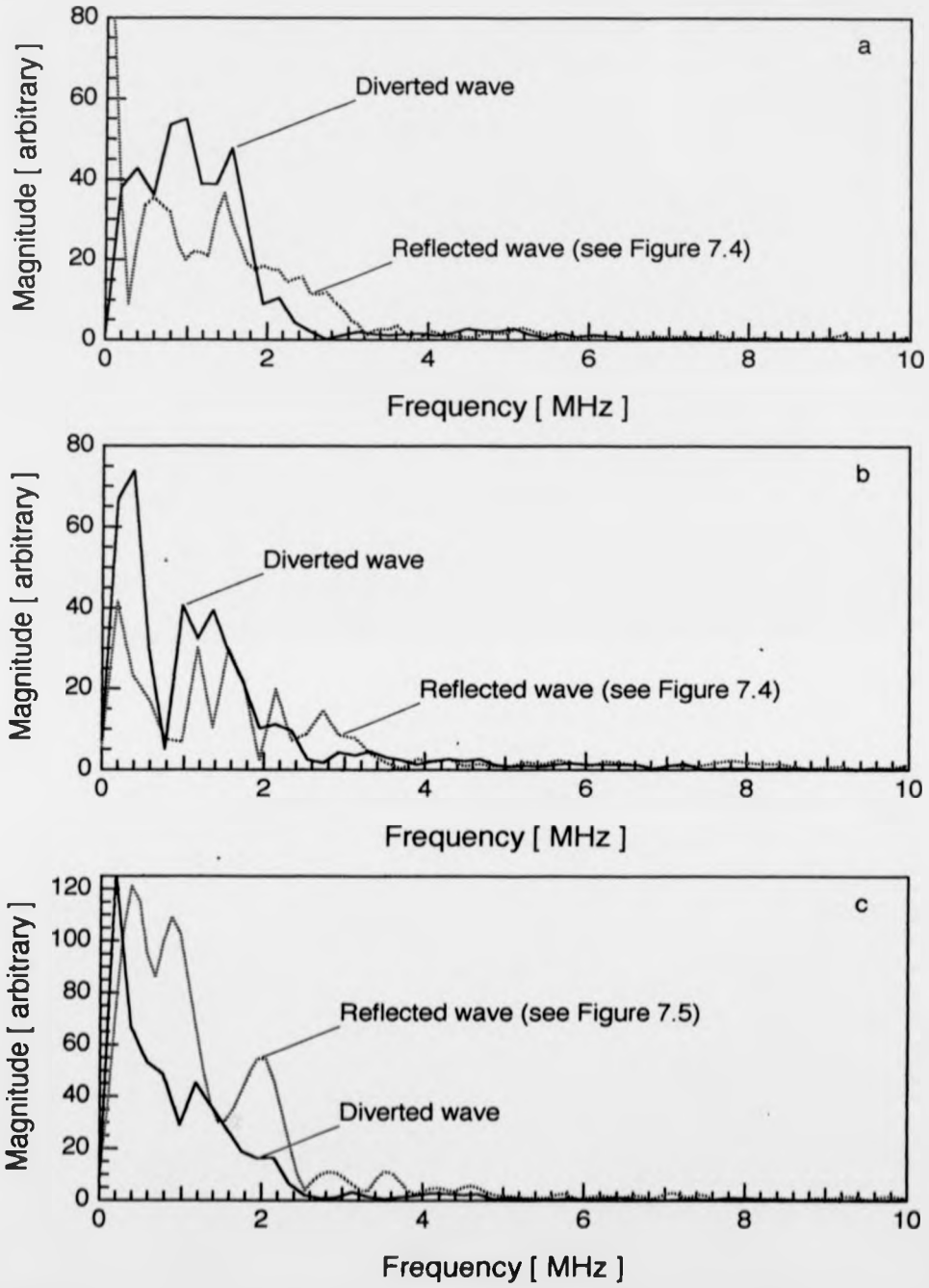

Figure 7.9 Comparing FFT magnitude spectra for reflected and diverted ultrasonic surface waves from line source on a). 102 mm long reinforcement joint, b). 12.7 mm long reinforcement joint, c). 12.7 mm long lapped joint.

did on the solid step. An alternative explanation is that forward-moving SIST waves in the adhesive layer require backward-moving free surface waves on both adherends, in order to maintain boundary conditions at the second adherend edge. Full confirmation, however, must wait until the SIST wave theory is better developed.

Decreasing the reinforcement bond length allows bulk waves which enter the second adherend and hit the end faces to deflect back to the detector more rapidly and with lower attenuation, leading to a high level of background disturbance in the 12.7 mm long joint (Figure 7.8.b). Even so, the FFT magnitude spectra for reflected and diverted waves agree well (Figure 7.9.b), although the frequency spike at 0.4 MHz on the diverted spectrum is probably an artifact resulting from bulk wave interference. In contrast, on the 12.7 mm overlap lap-shear joint, ultrasonic bulk waves transmitted into the 200 mm long second adherend have a long distance to travel before hitting the farther end face and the signal is correspondingly less noisy (Figure 7.8.c). However, agreement between reflected and diverted wave FFT magnitudes is poorer than for reinforcement joints (Figure 7.9.c), because the reflected wave originated from the first adherend end face rather than the front fillet. These results are preliminary, but they suggest the need for further experiments along the lines suggested at the beginning of this section, which should be simpler to analyse. Diverted waves have small amplitudes and are therefore probably not suitable for detecting fillet defects, although well-bonded joints with deliberately damaged fillets have yet to be constructed to confirm this assumption.

So far the second adherends have all been thick enough to support Rayleigh-like surface waves, and keep bulk arrivals well-separated in time. Observations on a reinforcement bond with a 12.7 mm long and 0.57 mm thick second adherend, which no longer appears deep in comparison to the pulse wavelengths, show markedly different waveforms (Figure 7.10). Ultrasound enters the second adherend either as SIST wave leakage from the adhesive (CG312/5 epoxy with carrier), originating from the sharp Rayleigh-like pulse initiated on the first adherend surface, or as transmitted bulk-travelling waves. Reverberations in the thin second adherend produce dispersive waveforms (A*) which resemble free plate zero order antisymmetric Lamb waves with amplitudes that build up as d, the distance from the bond edge, increases (Figure 7.10). The sharply-pulsed, non-dispersive (S*) arrivals must originate from surface-travelling,

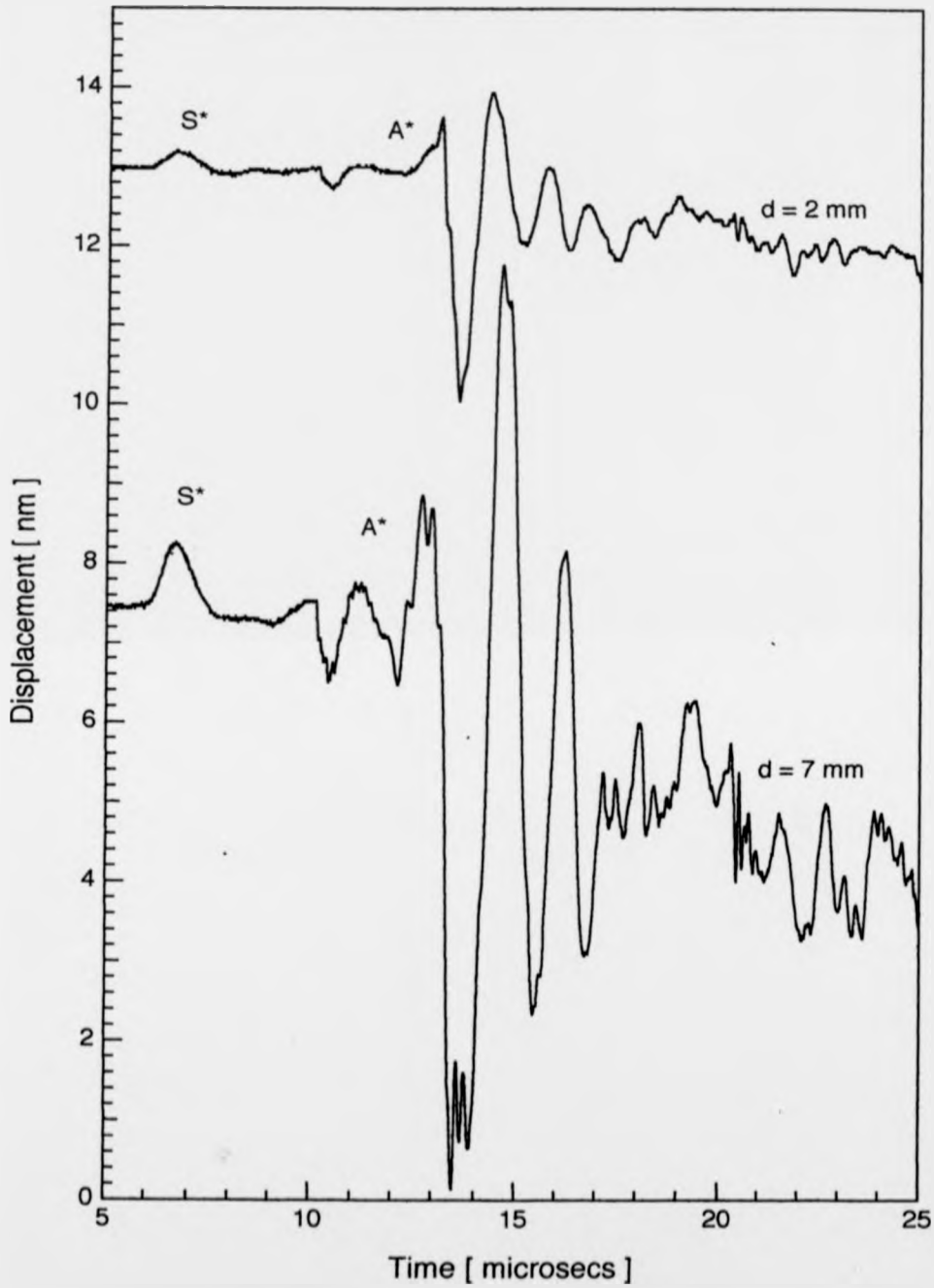

Figure 7.10 Build-up of plate-like acoustic waves detected 38.5 mm from source by 532 nm laser interferometer on surface of 0.57 mm thick x 12.7 mm long adherend, reinforcing (CG312/5 epoxy bond) a 25 mm thick alloy adherend.

6390 ms^{-1} longitudinal velocity, head waves, which cover the 39.1 mm total surface distance from source to detector in 6.12 μs (±1%), the earliest 2p bulk reflections arriving after 10 μs. In this geometry, there is thus a 4 μs time window for the head pulse within which modifications due to fillet defects are not obscured by bulk wave arrivals and could be detected, even though signal amplitudes are low. The large amplitude A* arrivals, however, due to their dispersive nature, are interesting less for fillet defect detection than for implying significant interface wave transfer into the second adherend, though ultrasonic waves which disturb both second adherend surfaces are not strictly speaking localized to the interface. Since the time separation between SIST and diverted waves is proportional to the second adherend thickness, on thin adherends the two are anyway impossible to distinguish, and it is better to concentrate on extracting adhesion data along the entire bond length from observed waveform resonances.

7.3 SIST Wave Transfer between Adhesively Bonded Lapped Joint Adherends.

Aside from scattering, ultrasound which neither reflects nor diverts away from the bonded region progresses as a SIST wave along the adhesively bonded layer to reach a free surface on the far side. Chapter 6 shows that low ultrasonic frequencies interact relatively weakly with the adhesive interface, especially in bonded samples with short (12.7 mm) overlap lengths, and propagate mainly within the aluminium adherend. When the transmitted SIST wave emerges on the second adherend free surface (Figure 7.1.c), however, the emitted wave is guaranteed to have interacted with the adhesive layer and the system thus filters out ultrasonic surface wave components which are of least interest to bonded interface studies.

The experimental arrangement for observing lap-shear transmission waveforms is somewhat different from that used in sections 7.1 and 7.2 as the source laser and interferometer detector beams are directed in opposition to each other (Figure 7.11). However, the source is still an ablating line, produced by focussing the pulsed Nd:YAG laser with a cylindrical lens. The source and detector geometry can in principle be fixed because adhesive layer thickness variations below ~1 mm are negligible in this context. The interferometer beams are focussed by 160 mm focal length, spherical, plano-convex lenses, with 532 nm wavelength anti-reflection coating, placed 160 mm away from the ends of both reference and sample arms to maintain the same extra path length. Even when the separation D stays constant, translating a sample allows

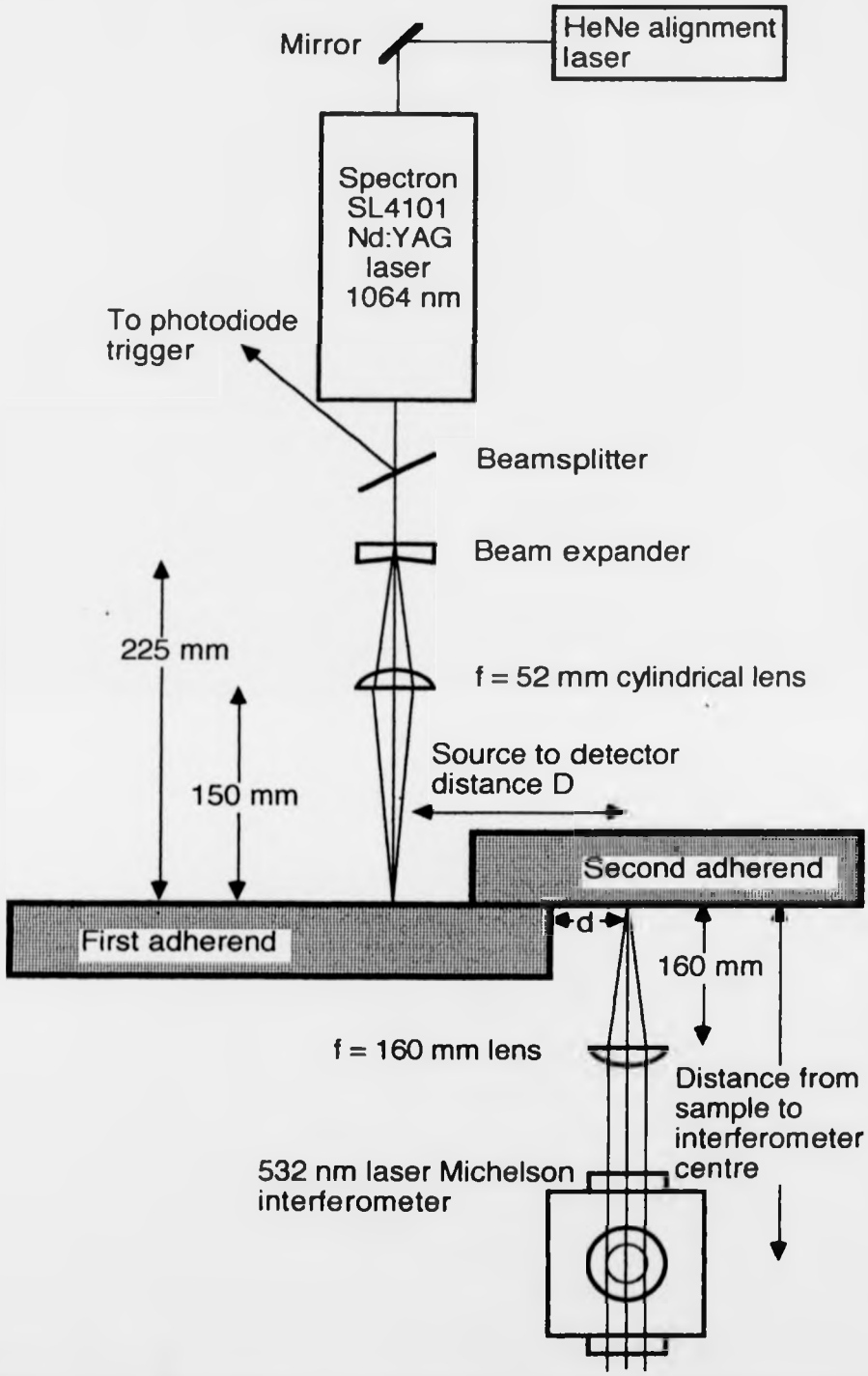

Figure 7.11 Experimental configuration used to investigate SIST waves transmitted across the adhesive layer from the first adherend in a bonded lap joint to the second.

surface displacements to be detected at different distances d from the bond region.

Initial doubts concerning the existence of SIST wave transmission between adherends were dispelled by observations on a sample with a 12.7 mm overlap bond joining 25 mm thick adherends (Figure 7.12.a). This preliminary experiment used a normal (out-of-plane sensitive) EMAT positioned ~30 mm from the source, with d kept as small as possible, given the fillet and detector widths. The main arrival at 10 μs is the transmitted SIST wave, which originates from a pulse travelling along the first adherend surface at the Rayleigh velocity. Interestingly, however, there is also a much earlier (p_{SIST}) arrival which appears to have been generated by the surface-travelling longitudinal wave precursor to the free-surface ultrasonic signal [Pilarski & Rose,1989]. Since the resulting SIST wave needs close to the 6390 ms^{-1} aluminium longitudinal velocity to produce the observed arrival time, it raises the possibility of a velocity solution to the layer wave problem which actually lies above the aluminium shear velocity, a case not covered in Chapter 2. Note also the first reflected bulk arrival (4p), which has to rebound off the first adherend rear face, pass through the bond and reflect off the second adherend rear face before reaching the detector.

The same sample was inspected again (Figure 7.12.b) using a laser Michelson interferometer, positioned 50 mm from the source as the surface close to the bond edge is too scratched to reflect light cleanly. The interferometer detects a SIST wave arrival, with a 5 nm displacement amplitude comparable to that of the incident Rayleigh velocity pulses (see Figure 7.3.b). This is clear confirmation of the role played by SIST wave interactions across an adhesive layer, since ultrasound travelling mainly beneath the first adherend surface and interacting only weakly with the epoxy will reflect at the first adherend end face in preference to transmitting along the second adherend surface. Fast Fourier transform magnitudes for the transmitted waves show good agreement below 2MHz but the EMAT, which has a narrower bandwidth, is proportionately less sensitive to frequencies above 2 MHz than the interferometer. A magnitude mean spectrum for the incident, Rayleigh velocity pulse (see Figure 7.5.c) is compared with the interferometer trace and confirms that most of the motion is transmitted. The largest discrepancies, below 1 MHz and around 2 MHz coincide with maxima in the reflected wave spectrum (Figure 7.5.c), while losses above 3.5 MHz are probably due to epoxy attenuation.

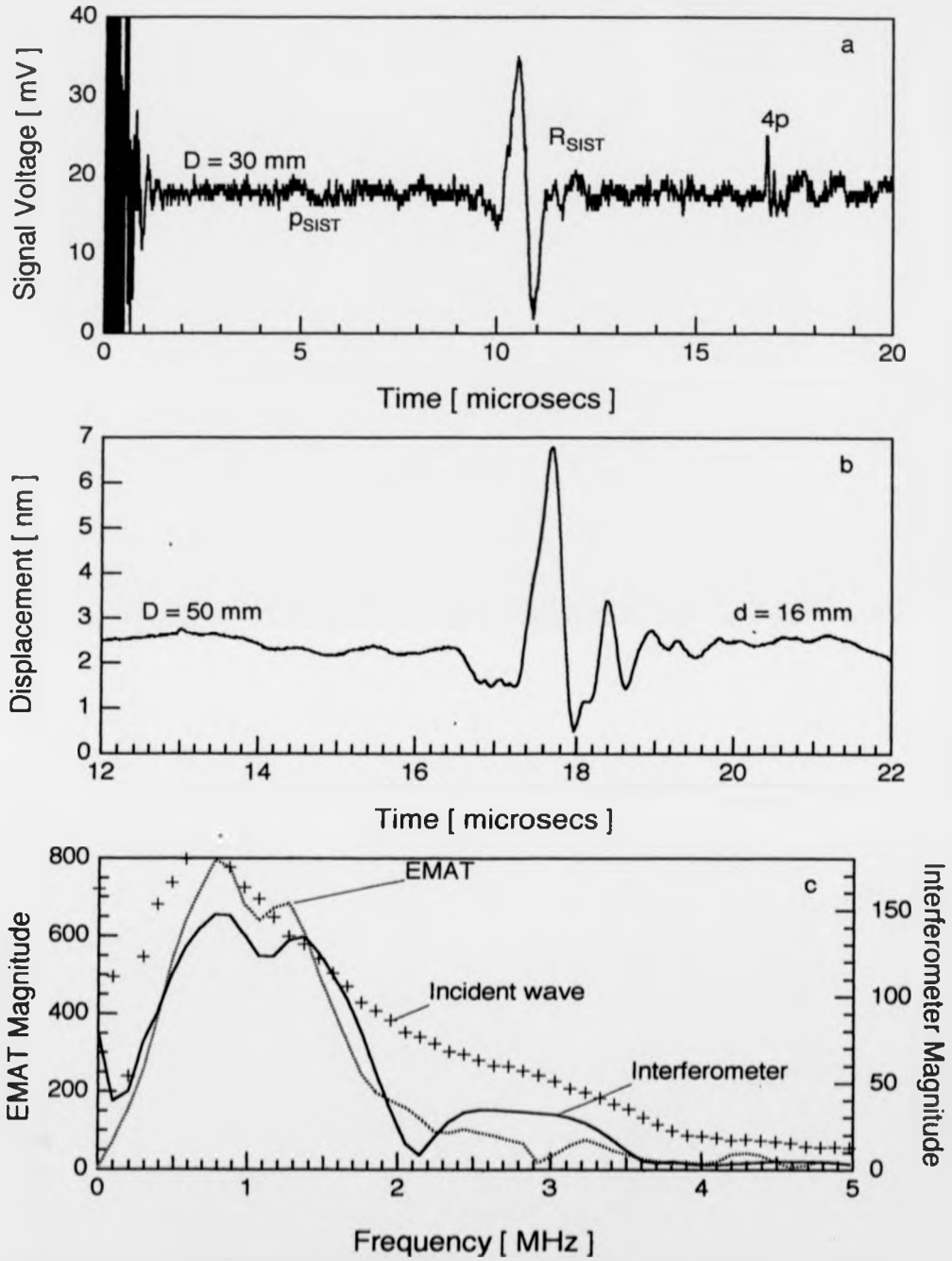

Figure 7.12 SIST waveforms transferring between adherends in a lap-shear epoxy-bonded joint detected by, a). normal EMAT and b). laser Michelson interferometer. c). FFT magnitude spectra comparing transferred waves.

A second experiment was carried out with the interferometer again positioned 50 mm from the source, but using two lapped joints differing only in that the epoxy used (Ciba Geigy CG312) contained woven polythene carrier in one sample (denoted CG312/5) but not the other. The samples were constructed with 12.7 mm overlaps and adherends 25.2 (±0.2) mm and 6.45 (±0.04) mm thick. Comparing ultrasonic waveforms generated on the thinner adherend and detected on the thicker (Figure 7.13.a) shows no significant difference between the two joints, emphasizing that ultrasound only detects epoxy inhomogeneities which create a large acoustic impedance mismatch. However, inverting the CG312/5 sample, to allow generation on the 25 mm thick adherend and detection on the 6.45 mm thick adherend, does alter the waveform observed (Figure 7.13.b) because, though d remains roughly constant, the new geometry decreases SIST path lengths along the thinner adherend where surface travelling acoustic waves are more strongly dispersed. Fast Fourier transform magnitude spectra (Figure 7.13.c) show reasonable agreement between data from all three waveforms, the two detected on the 25 mm thick adherend in particular being nearly identical. The main difference between the switched geometry CG312/5 observations is the appearance of a low frequency peak, centred on 450 kHz, in the longer dispersive pathway waveform. This accords with dispersive plate wave tendencies to concentrate energy into the lowest frequencies, and the time waveforms show the original sharply dipolar pulse (Figure 7.13.b) eroding through dispersion into a monopolar pulse with pronounced side lobes (Figure 7.13.a).

Even more seriously dispersed waveforms are observed after generation on standard 3.0 mm (±5%) thick aerospace alloy adherends. A lapped joint, with 12.7 mm long bond, in which the second adherend is only 0.57 mm thick, shows the onset of a low frequency, zero order antisymmetric Lamb mode in the thin adherend at 50 mm source-to-detector distance (Figure 7.14.a). Chapter 5.2 implies a still more complicated picture for lapped bonds in which both adherends are 3 mm thick, and waveforms detected at D = 50 mm on a 12.7 mm long overlap bond between two 3 mm adherends are highly dispersed with a vestigial arrival close to the Rayleigh velocity (Figure 7.14.b). Moving the detector out to 150 mm from the source, on the same sample, allows a much more pronounced antisymmetric wave to build up, although the noisy appearance suggests that the zero order mode is accompanied by higher orders (Figure 7.14.c). These dispersive waves are unsuitable for simple analyses of bond defects

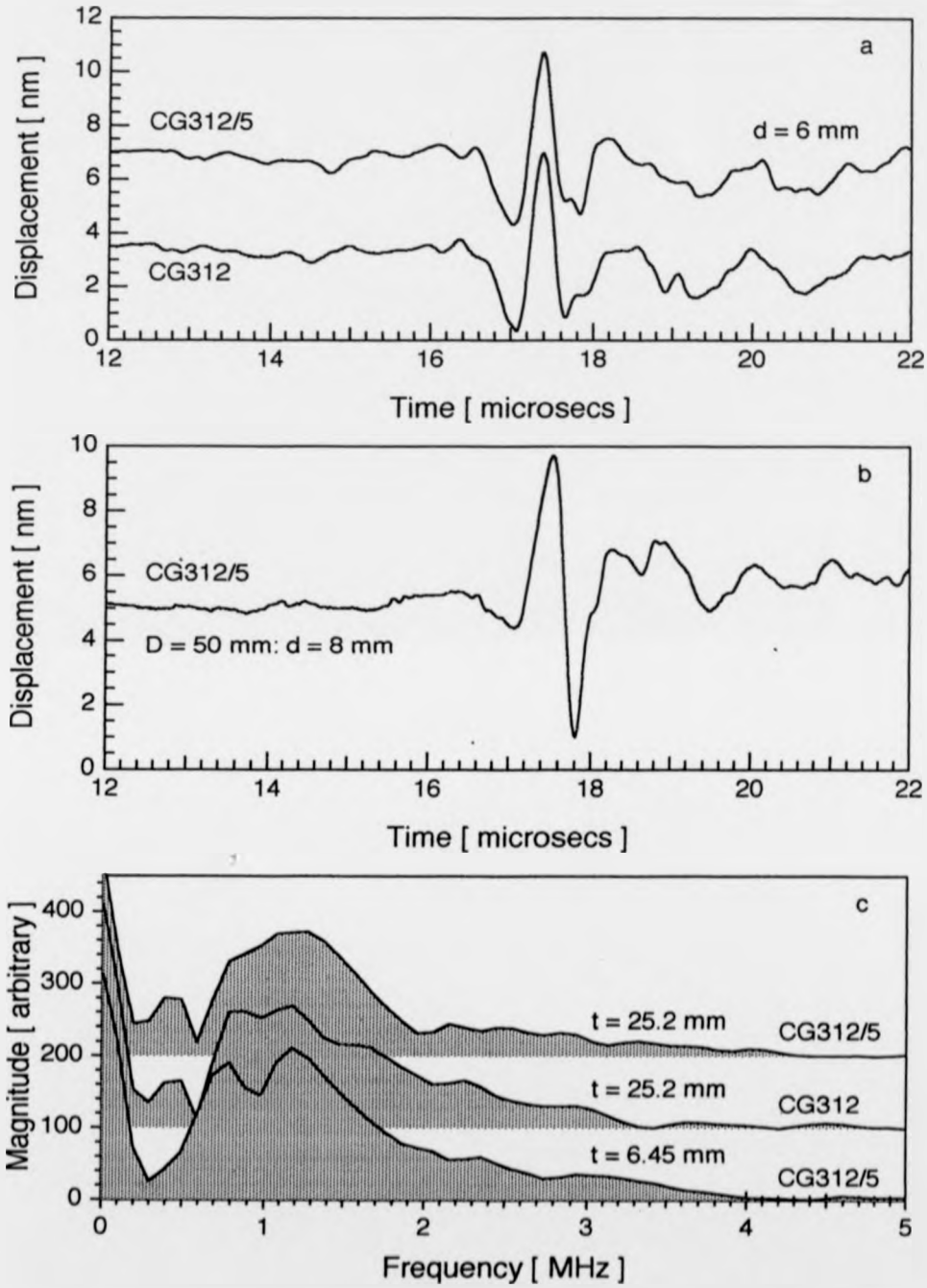

Figure 7.13 SIST waveforms transferring between adherends 25 mm and 6.5 mm thick, a). across epoxy with (/5) and without carrier, detected on 25 mm thick adherend, and b). on 6.5 mm side. c). Corresponding FFT magnitude spectra.

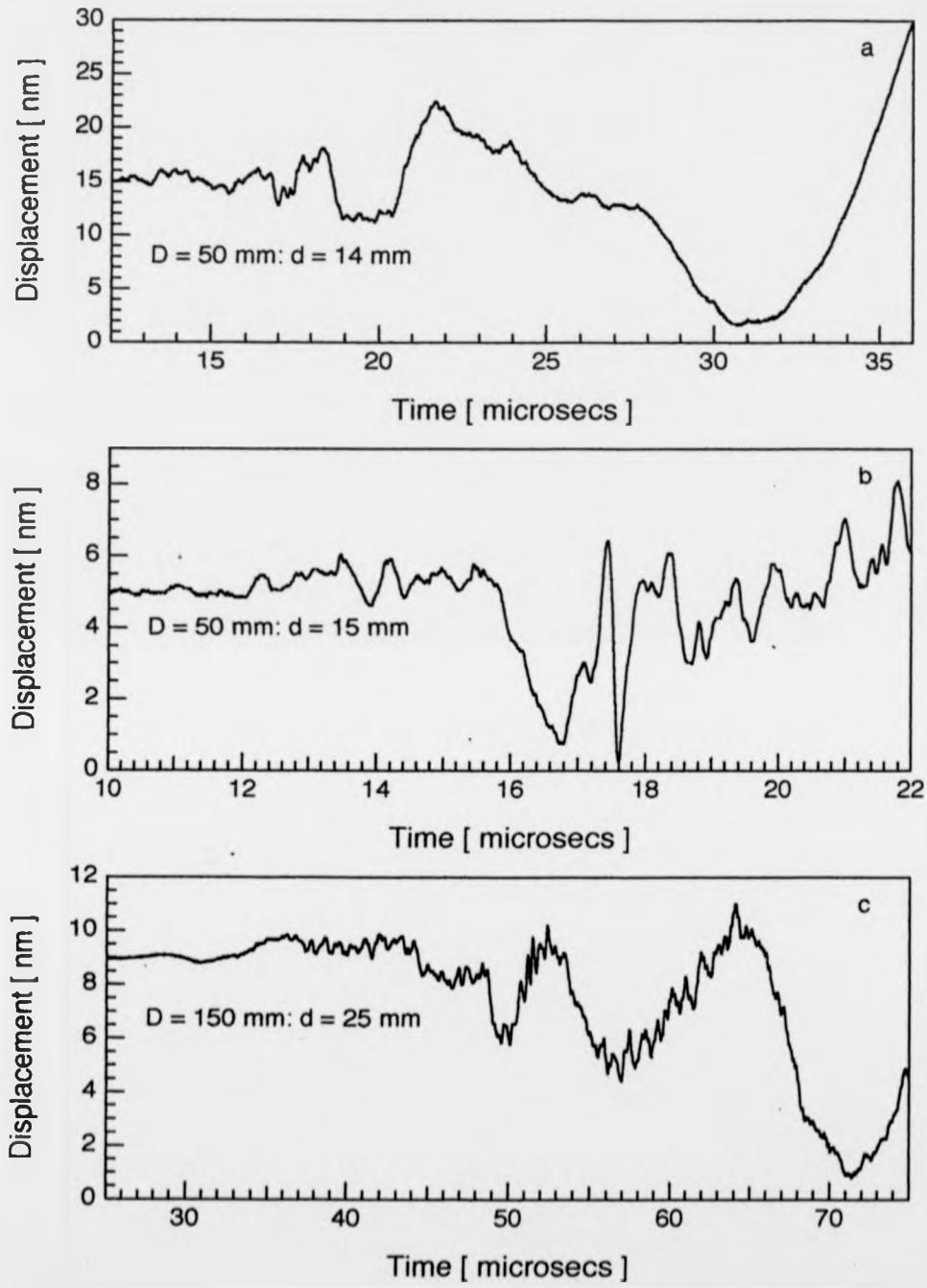

Figure 7.14 Transferred SIST acoustic waveforms generated by laser ablation line source on 3.3 mm thick adherend, detected at D = 50 mm on a). 0.57 mm thick and b). 3.3 mm thick adherends and at c). D = 150 mm on t = 3.3 mm adherend.

although frequency analysis should in principle separate adherend and adhesive resonances. However, as with reinforcement bonds, transmitted SIST waves are most useful on relatively thick adherends along which free surface acoustic pulses can propagate undispersed. The lap-shear detector configuration (Figure 7.11) has the advantage of allowing SIST wave observations with fixed apparatus, but is more useful on individual components than on complex structures, where access from both sides may be a problem.

In conclusion, while surface waves have been observed after reflection at the bond edge or diversion onto the second adherend's outer surfaces, they are low in amplitude and correspondingly hard to separate from noise or bulk-travelling waves. Detection of defects located in the bond fillet region using such surface waves therefore appears unfeasible. The absence of substantial amplitude reflected or diverted waves, however, supports observations on lap-shear joints that ultrasonic pulses, on encountering an epoxy bonded joint, convert efficiently into travelling waves which cause displacements in the neighbourhood of both adhesive layer interfaces. Such waves have considerable potential for detecting both cohesive and adhesive defects in epoxy-bonded lap-shear joints and further research into their properties is strongly recommended.

CHAPTER EIGHT

CONCLUSIONS

This thesis has described complementary experimental techniques for assessing adhesion quality at epoxy-bonded joint interfaces, using either ultrasonic pulses transmitted through the bond layer (Chapter 4) or surface-interface-surface travelling (SIST) waves directed along the bonded joint length (Chapters 5, 6, 7). Both techniques detected defects deliberately introduced into the bond region. However, results obtained from through transmitted ultrasound were more amenable to quantitative analysis, and promise to allow extraction of bond layer properties from pulse data, whereas SIST wave theory is currently only able to provide qualitative agreement with observation. More SIST wave work is needed to improve both theory (see Chapter 2) and the experimental basis upon which it rests. But although my results suggest that further research will be profitable, SIST wave techniques need this additional development before they can be seriously considered for defect analysis, especially on plates which are thin relative to the longest wavelengths in laser-generated ultrasonic pulses. Through transmission on-epicentre detection, in contrast, is ready for wider application to defect measurement problems. And clearly detected acoustic pulse reverberations in epoxy layers bonding 3 mm thick aluminium alloy adherends (chapter 4.2) imply a method appropriate to plates within the thickness range of interest to DRA (Aerospace).

8.1 Suggestions for Enhanced Quality Signal Processing.

I am concerned that despite careful experimental preparation, the epoxy data extracted from on-epicentre through-transmission waveforms (Chapter 4) appears to be seriously degraded, primarily due to the limited 8 bit digitized signal resolution. Above 5 MHz, dispersion curve analyses will only improve significantly with 16 bit resolution, most easily achieved by summing 256 traces (instead of the current 20) at a penalty of greatly increased wear and tear on the pulsed laser. Moreover, the procedure needs to be carried out manually, a time-consuming exercise, as the ablating source progressively alters sample surfaces and requires regular reduction of the source laser intensity to maintain a constant shape weak ablation pulse. Averaging may well be the only option, however, for squeezing the maximimum signal out of digitizers that

are fast at the expense of resolution. Loss of high frequency data, whether caused by digitizer resolution or by device bandwidth limitations (as with EMATs) can be compensated by improvements at low frequencies, which are more heavily dependent on signal processing methods than experimental procedure. Fourier transform resolution is inversely proportional to the window length, which can be increased by padding the trace preceding the direct longitudinal arrival with additional zero displacement points. Choosing the resolution is thus a trade-off between desired detail and computational expense. Higher resolution will only improve the low frequency signal, however, if the time window is chosen to minimize distortion. Phase spectra are most accurately determined when windowed signals are re-centred, about the window zero, prior to transformation and more work is needed to move from the current approach, centring a signal's maximum, to a more robust alignment about its pulse centroid. The centroid method should work better with EMATs than with the interferometer data where the finite amplitude tail of arbitrary length following the main weak ablation pulse has to be excluded in some way for any centroid calculation to be meaningful. Signal processing and the method for extracting individual reverberations from multiple reflection arrivals are therefore interlinked, with different fit functions acting to shift pulse centroids or govern the need for additional tapering to match up pulse amplitudes at the two window edges. Better theoretical understanding of laser generated pulse transmission through epoxy is needed to feed back, via improved descriptions of pulse shapes, into more accurate extrapolation of individual reverberations across overlap regions, and in turn ensure better depiction of low frequency viscoelastic dispersion relations in epoxy.

8.2 Improving Shear Wave Observations.

Given improved signal processing, laser-generated ultrasound's Achilles' heel is the lack of broad bandwidth, non-contacting detectors with the high sensitivities and low cost displayed by contact transducers. Improvements in laser acoustic test rigs are therefore most likely to result from upgraded detection systems. Laser technology advances are bringing continuous wave, solid state lasers like the ADLAS 300 (chapter 3.5) onto the market in increasing numbers, allowing cheaper and more stable optical detectors to be constructed. At Warwick, there is an ongoing effort directed towards improving non-optical, non-contact, EMAT detectors (chapter 3.6) as relatively low technology, practical replacements for laser

interferometry. One advantage which EMATs bring is the ability to construct, from the same basic materials, detectors with sensitivities optimized to different components of the ultrasonic surface motions. It is therefore possible to respond to the laser source flexibility by tailoring the relative geometry of EMAT magnets and detector coils. Take, for example, some results on an aluminium adherend 13 mm thick by 51 mm long, which was bonded to a 25.4 mm thick adherend. The base was painted prior to epoxy cure with a 1 cm wide Frekote stripe, creating a weakened adhesive region at the reinforcement joint centre. Laser-generated ultrasonic pulses examine the joint in on-epicentral configuration (Figure 4.1), transmitting through the bond layer to detectors placed on the opposite surface. Using a thermoelastic, laser ultrasonic point source generates shear motions about the epicentre which can transmit through bonds to in-plane motion sensitive detectors, such as the shear EMAT (Figure 8.1.a). Point sources generate axisymmetric waves radiating from the epicentre, where they produce a null displacement. The shear EMAT which I built (chapter 3.6) has coils wrapped round the NdFeB permanent magnet at its centre, forcing currents to flow in the same direction in all the wire sections nearest to the surface. Advancing radially polarized waves, however, induce currents in opposite directions in wires either side of the epicentre axis (Figure 8.1.a), which appproximately cancel. The shear EMAT therefore detects predominantly at the edges of its sensitive area, where magnetic field fringe effects allow signal contamination by out-of-plane motion, with the result that I have been unable to study on-epicentre shear motions. Dr. C. Edwards has developed a prototype compact spiral coil EMAT, however, in which induced currents either side of the epicentre flow in opposite directions (Figure 8.1.b), producing a maximimum sensitivity to axisymmetric motions. Since interface parallel displacements only transmit between samples in good acoustic contact, radially polarized shear waves are expected to respond much more clearly to adhesion defects than longitudinal waves detected on-epicentre.

There is still merit, however, in detecting on-epicentre longitudinal pulses, as perpendicular motion propagating across interfaces between surfaces in close contact, whether well-adhered or not, behaves more as if encountering a rigid bond. It may therefore be possible to deduce the cohesive properties and thickness of a bond under rigid assumptions from longitudinal wave observations which can be fed into adhesion property analyses conducted on shear motion data. A 532 nm laser Michelson interferometer, placed on-epicentre, senses

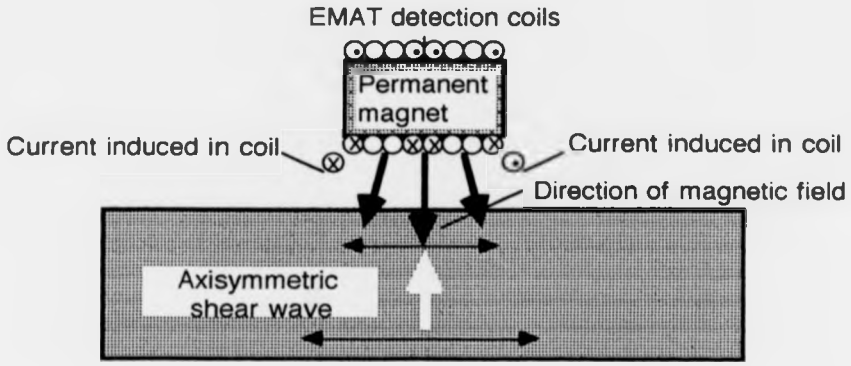

a). Ordinary shear EMAT positioned over epicentre detects null acoustic signal.

b). Spiral coil EMAT is sensitive to axisymmetric waves detected on epicentre.

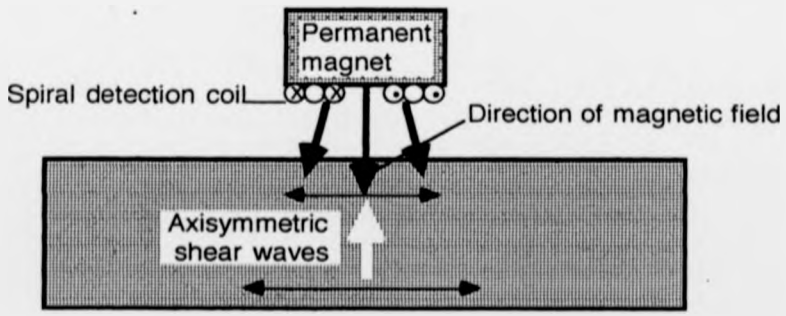

Figure 8.1 Observing on-epicentre transverse ultrasonic waves transmitted through an epoxy bonded joint.

out-of-plane displacements and detects a characteristic reverberating bond signal arriving from an ablating laser point source through the centre of the defect region (Figure 8.2.a). Pulses from the same source, again centred on the defect, are also detected by a normal EMAT under 200 gain preamplification, with signal voltage proportional to out-of-plane displacement rates of change (Figure 8.2.b). But it is reverberations between the interfaces detected by the spiral coil EMAT, again preamplified 200 times, that prove the presence of at least a partial bond in the defect region, in line with previous Frekote painted samples (chapter 4.4). That the spiral coil EMAT definitely detects shear motions rather than longitudinal, is seen from the direct arrival time and from the fact that the epoxy reverberation time is approximately double those of the other detectors.

Fast Fourier transform magnitude spectra of the traces, with low frequency peaks normalized to 1'00, reveal a corresponding halving of reverberation peak frequencies in the spiral coil EMAT data (Figure 8.3). The effects of different detector bandwidths are also noticeable on the FFT spectra, since the interferometer spectrum indicates resonant frequencies at 8.5 MHz and 17.5 MHz, while the normal EMAT detects little above 12 MHz and the spiral EMAT nothing significant above 8 MHz. The absence of a clear reverberation peak in the spiral EMAT spectrum is due partly to the lower reverberation frequencies associated with shear motion and partly to a relatively large detector area for the prototype. Tighter spiral coils allow EMATs with smaller sensitive areas and more rapid response times, which take full advantage of size reductions made possible by using NdFeB permanent magnets to generate the detectors' static magnetic fields. Certainly, as the detectors improve, additional information provided by in-plane motion ultrasonic waves will significantly enhance the analysis of through transmission pulses reverberating within epoxy-bonded joints.

8.3 Future Developments.

As ultrasonic through transmission pulses are sensitive to defects, the next logical step is to set up an X-Y stepping system, enabling gridwise scans over bonds, from which 2-dimensional defect maps can be constructed. Defect mapping leads into two main avenues of research. First there is the question of defect detection limits, which vary according to the nature and location of the defect and must be quantified before the technique can be adopted as

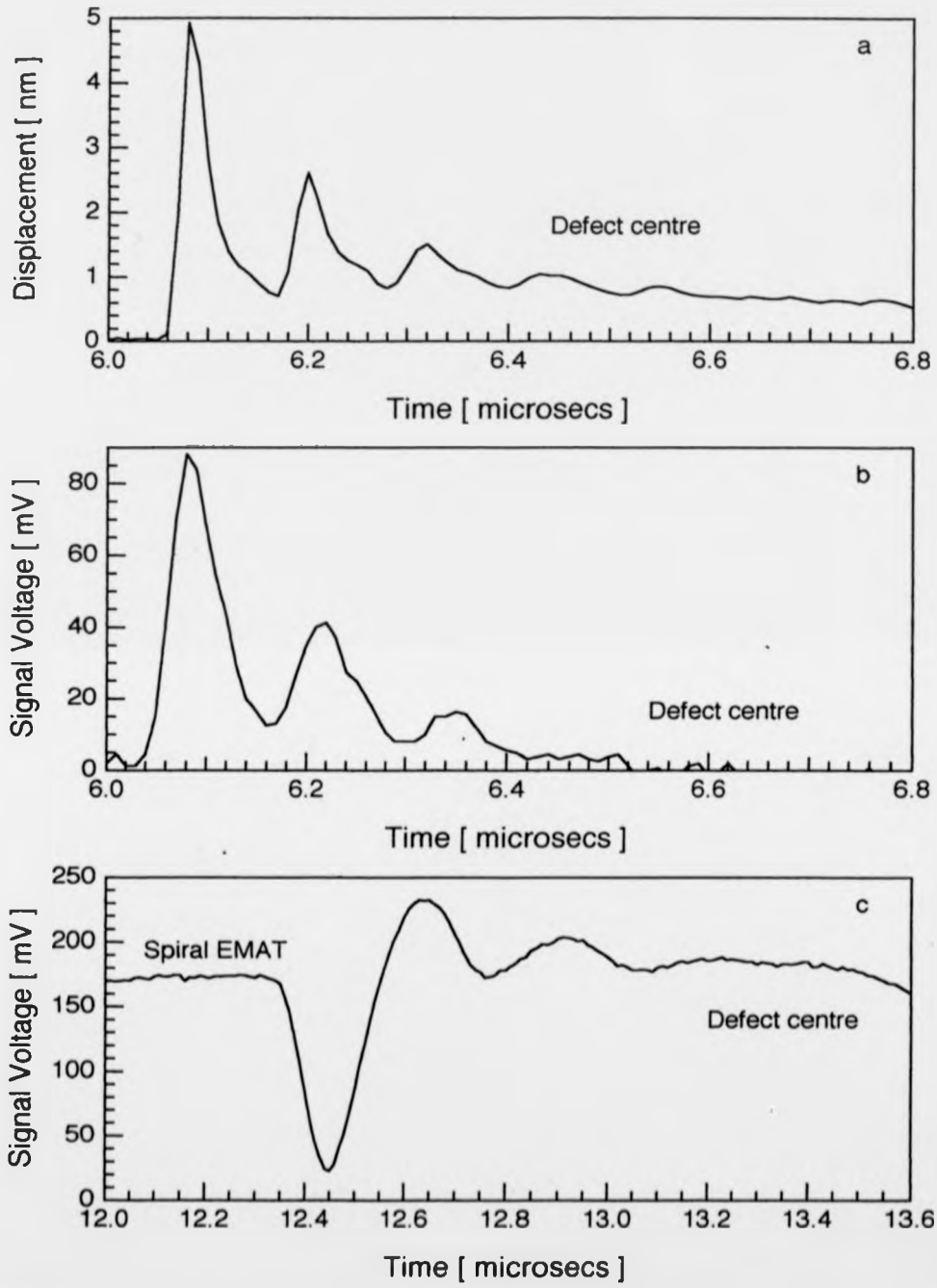

Figure 8.2 Laser-generated ultrasound transmitted through 0.2 mm thick CG312/5 epoxy layer weakened by Frekote stripe. Detected by a). 532 nm laser Michelson interferometer, b). normal (out-of-plane) EMAT. c). spiral coil EMAT .

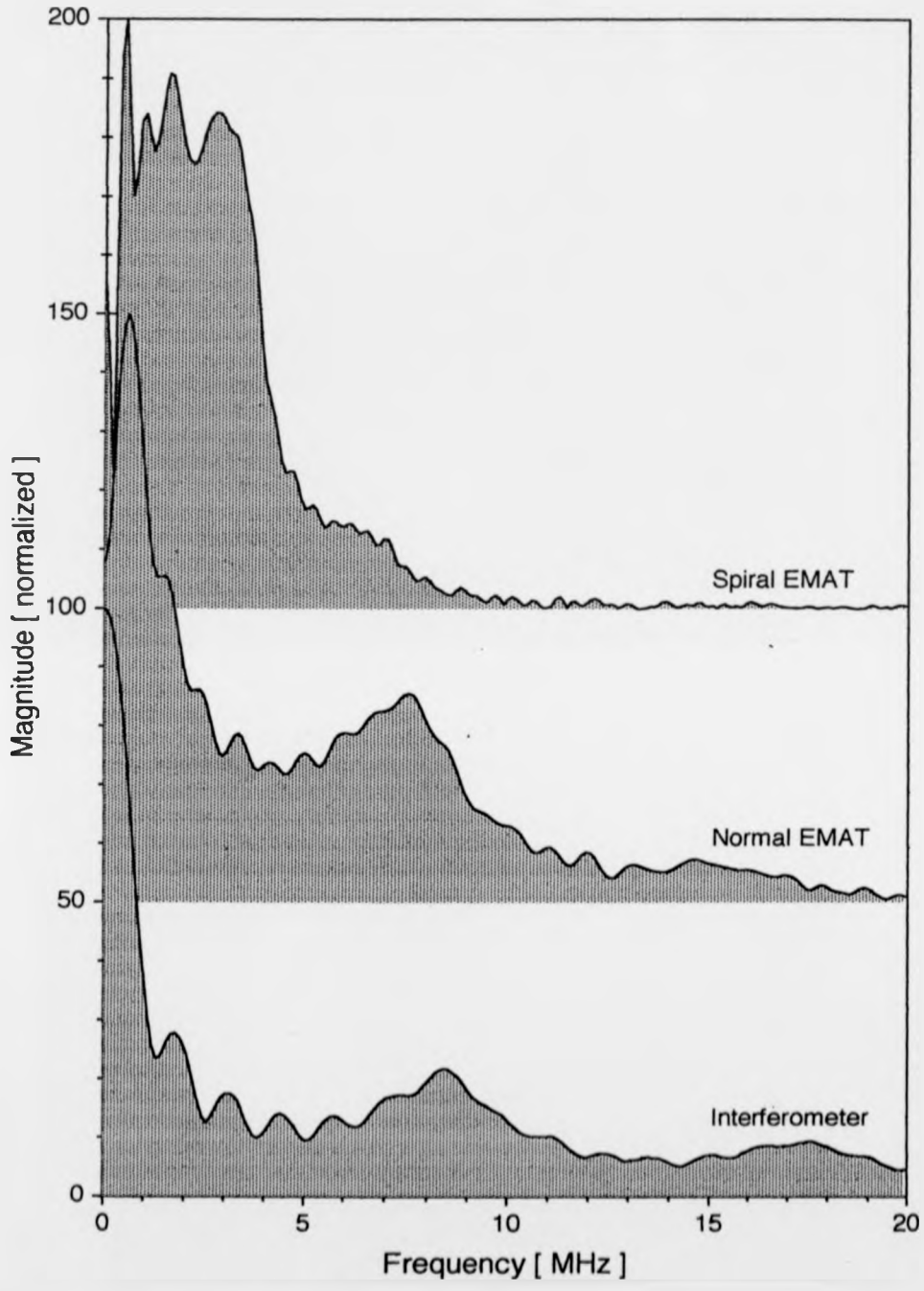

Figure 8.3 Fast Fourier transform magnitude spectra, normalized to low frequency maxima, of on-epicentre ultrasonic signals transmitted through Frekote stripe defect and detected by interferometer, normal & spiral coil EMATs.

standard. Detection limits also depend upon the chosen detectors (and the source for that matter, if alternative laser arrangements are available), a link which needs to be explored before advice on preferred options is issued. Secondly, as touched upon in Chapter 1, the relation between detected defects and adhesive, or cohesive, bond strengths remains to be tackled. For meaningful comparison between destructive tests, conditions under which bonded joints are destroyed must be carefully controlled, as peel strengths are markedly lower than strengths deduced from extension, and in turn from shear or compression of the sample [Adams & Cawley, 1988]. By implication, therefore, the bonded joints themselves have to be designed specifically for the task, requiring a carefully planned experimental programme to ensure standard destructive tests. Such work can be carried out alongside adaptation of the present flexible experimental system into a robust industrial detector, calibration against other testers, and similar activities of a more developmental nature. Correlations between destructive and non-destructive tests are most easily obtained by examining groups of samples for defects ultrasonically before destroying them. However, a non-contacting laser generation, optical detection system should be able to monitor individual joint changes up to failure as long as the test can be paused, either between static load increments or at regular intervals over cycled loads, in order to let background sample surface motions die away. The main difficulty with in situ testing is that laser interferometer signals are very responsive to joint deformation, which will occur under stress and may well mask subtler changes due to defect growth within the adhesive layer.

The ultimate goal, an accurate, repeatable and reasonably robust system for revealing potential weaknesses in adhesively bonded structures, remains distant. But laser generated ultrasound can certainly be applied to defect detection in simple geometry epoxy-bonded joints and with continued improvements both to the detectors and to the underlying theoretical description of sandwiched epoxy layers, non-destructive laser acoustic pulse examinations are expected to become increasingly informative.

APPENDIX A.

THEORETICALLY DERIVED LAYER STRUCTURE MATRIX VALUES

This appendix contains a full description of the matrices used in Chapter Two to describe the passage of ultrasound through multiple layers. Properties specific to the ith layer are denoted with subscript i, those specific to the interface between i-1 and i with the subscript i-0.5. The following variables apply throughout:

C_{Li} longitudinal speed in layer i.

C_{Ti} shear speed in layer i.

ρ_i density in layer i.

θ_{Li} longitudinal plane wave angle to interface normal in layer i.

θ_{Ti} shear plane wave angle to interface normal in layer i.

$Z_{Li} = \rho_i C_{Li}$

$Z_{Ti} = \rho_i C_{Ti}$

ω angular frequency of ultrasonic waves.

2h epoxy layer thickness ($-h =< z <= +h$, for epoxy layer).

A.1 General Through Transmission Case. (Equation 2.4.2)

The matrices are formulated to describe radiation at arbitrary incoming angles θ_{Li} for amplitude u longitudinal waves and θ_{Ti} for amplitude v shear waves. It is convenient to define the following quantities:

$$C = \sin(\theta_{Li}) / C_{Li} = \sin(\theta_{Ti}) / C_{Ti} \quad \ldots \text{A.1.1}$$

$$b_{Li} = i\sqrt{(1 - (C^2 / C_{Li}^2))} \quad \text{and} \quad b_{Ti} = i\sqrt{(1 - (C^2 / C_{Ti}^2))} \quad \ldots \text{A.1.2}$$

C repesents the component of the plane wave velocity in the interface plane and becomes significant when it equals the interface wave velocity and can propagate energy along the interface as well as into transmitted or reflected beams.

Matrix $E_{i}(z_{i-0.5}) = E_{i}^{-1}(-z_{i-0.5})$

$E_{11} = \exp(i\,\omega\, z_{i-0.5}\cos(\theta_{1i}) / C_{1i}) \quad = \exp(i\,\omega\, z_{i-0.5} b_{1i} / C)$

$E_{22} = \exp(i\,\omega\, z_{i-0.5}\cos(\theta_{1i}) / C_{Ti}) \quad = \exp(i\,\omega\, z_{i-0.5} b_{1i} / C)$

$E_{33} = \exp(-i\,\omega\, z_{i-0.5}\cos(\theta_{1i}) / C_{1i}) \quad = \exp(-i\,\omega\, z_{i-0.5} b_{1i} / C)$

$E_{44} = \exp(-i\,\omega\, z_{i-0.5}\cos(\theta_{1i}) / C_{Ti}) \quad = \exp(-i\,\omega\, z_{i-0.5} b_{Ti} / C)$

$E_{12} = E_{13} = E_{14} = E_{21} = E_{23} = E_{24} = E_{31} = E_{32} = E_{34} = E_{41} = E_{42} = E_{43} = 0.$ ... A.1.3

Matrix J_{i}^{-1}

$j_{11} = 1 / (2 Z_{1i}) \quad = 1 / (2 \rho_{i} C_{1i})$

$j_{12} = -\sin(\theta_{1i}) / (2 Z_{1i}\cos(\theta_{1i})) \quad = -1 / (2 \rho_{i} b_{1i} C_{1i})$

$j_{14} = \cos(2\theta_{1i}) / (2\cos(\theta_{1i})) \quad = (C^{2} - 2 C_{Ti}^{2}) / (2 b_{1i} C C_{1i})$

$j_{22} = 1 / (2 Z_{1i}) \quad = 1 / (2 \rho_{i} C_{1i})$

$j_{24} = -\cos(2\theta_{1i}) / (2\cos(\theta_{1i})) \quad = -(C^{2} - 2 C_{Ti}^{2}) / (2 b_{1i} C C_{Ti})$

$j_{33} = C_{Ti}\sin(\theta_{1i}) / C_{1i} \quad = C_{Ti}^{2} / C C_{1i}$

$j_{44} = \sin(\theta_{1i}) \quad = C_{Ti} / C$

$j_{13} = j_{33} \qquad j_{21} = j_{32} = -j_{12} \qquad j_{24} = j_{44}$

$j_{31} = j_{11} \qquad j_{34} = -j_{14} \qquad j_{41} = j_{12}$

$j_{42} = j_{22} \qquad j_{43} = -j_{23}.$ ... A.1.4

Matrix $A_{i-0.5}^{-1}$

$a_{11} = a_{22} = a_{33} = a_{44} = 1$

$a_{12} = a_{13} = a_{14} = a_{21} = a_{23} = a_{24} = a_{31} = a_{34} = a_{42} = a_{43} = 0$

$a_{32} = -i\,\omega\,\eta_{I\,i-0.5} \qquad a_{41} = +i\,\omega\,\eta_{N\,i-0.5}$ ... A.1.5

The matrix inverts by setting $A_{32} = -a_{32} \qquad A_{41} = -a_{41}$

while all other terms $A_{ij} = a_{ij}.$ ... A.1.6

The eta terms are compliances which parametrize the interfacial adhesive strengths, varying in

the range $<10^{-18}$ (good bond) to $>10^{-14}$ (poor) for 0.1 mm layers and 0 to 25 MHz ultrasound.

Matrix J_1

$J_{11} = Z_{1,1} \cos(2\theta_{1,1})$ $= \rho_1 C_{1,1}(1 - (2C_1^2 / C^2))$

$J_{12} = Z_{1,1} \sin(2\theta_{1,1})$ $= 2\rho_1 b_{T1} C_{T1}(C_{T1}^2 / C^2)$

$J_{21} = -Z_{1,1} C_1 \sin(2\theta_{1,1}) / C_1$ $= -2\rho_1 b_{1,1} C_{1,1}(C_{T1}^2 / C^2)$

$J_{22} = Z_{1,1} \cos(2\theta_{1,1})$ $= \rho_1 C_{T1}(1 - (2C_1^2 / C^2))$

$J_{33} = \sin(\theta_{1,1})$ $= C_{1,1} / C$

$J_{32} = -\cos(\theta_{1,1})$ $= -b_{1,1} C_{T1} / C$

$J_{41} = \cos(\theta_{1,1})$ $= b_{1,1} C_{1,1} / C$

$J_{44} = \sin(\theta_{1,1})$ $= C_{T1} / C$

$J_{13} = J_{11}$ $J_{14} = -J_{12}$ $J_{23} = -J_{21}$

$J_{24} = J_{22}$ $J_{31} = J_{33}$ $J_{34} = -J_{32}$

$J_{42} = J_{44}$ $J_{43} = -J_{41}$ ... A.1.7

A.2 On-Epicentre Through Transmission Case. (Equation 2.4.3)

Setting $\theta_{1,1} = \theta_{T1} = 0$ reduces many of the terms in A.1 to 0. The matrix equation 2.4.3 decouples as a result to give two pairs of simultaneous equations, relating to the longitudinal and shear components of motion respectively:

$$[(Z_{1,1} / Z_{1,2}) + 1 - i F_3]\, t_1 = e^{i2\omega h C_1} ([(Z_{1,1} / Z_{1,2}) + 1 + i F_1]\, u + [(Z_{1,1} / Z_{1,2}) - 1 + i F_1]\, r_1)$$

$$[(Z_{1,1} / Z_{1,2}) - 1 + i F_3]\, t_1 = e^{i2\omega h C_1} ([(Z_{1,1} / Z_{1,2}) - 1 - i F_1]\, u + [(Z_{1,1} / Z_{1,2}) + 1 - i F_1]\, r_1)$$

where, $F_1 = \omega \eta_{\kappa 1,s} Z_{1,1}$ $F_3 = \omega \eta_{\kappa 2,s} Z_{1,1}$. ... A.2.1

$$[(Z_{T1} / Z_{T2}) + 1 - i G_3]\, t_1 = e^{i2\omega h C_1} ([(Z_{T1} / Z_{T2}) + 1 + i G_1]\, u + [(Z_{T1} / Z_{T2}) - 1 + i G_1]\, r_T)$$

$$[(Z_{T1} / Z_{T2}) - 1 + i G_3]\, t_1 = e^{i2\omega h C_1} ([(Z_{T1} / Z_{T2}) - 1 - i G_1]\, v + [(Z_{T1} / Z_{T2}) + 1 - i G_1]\, r_T)$$

where, $G_1 = \omega \eta_{T1,s} Z_{T1}$ $G_3 = \omega \eta_{T2,s} Z_{T1}$. ... A.2.2

Given the assumptions for viscoelastic behaviour described in chapter 2.4, C_{visc} the viscoelastic phase velocity and a_{visc} the attenuation may be calculated in terms of frequency (f):-

$$C_{visc} = C_0 \sqrt{|\ (1 + A^2 T^2 f^2\ ) / (1 + T^2 f^2\ )\ |} \qquad \ldots A.2.3$$

$$a_{visc} = \pi\ |\ (A - A^{-1}\ ) T f / (1 + T^2 f^2\ )\ | \qquad \ldots A.2.4$$

where, C_0 is the zero frequency phase velocity, A is the attenuation strength and $T = 2\pi t$, with t the relaxation time.

A.3 Case for Waves Travelling Parallel to the Interface. (Equation 2.5.2)

The matrices are formulated to describe displacements travelling along the layer with velocity = v. It is convenient to define the following quantities:

$$b_{l_i} = i\sqrt{(1 - (v^2 / C_{l_i}^2))} \quad \text{and} \quad b_{T_i} = i\sqrt{(1 - (v^2 / C_{T_i}^2))} \qquad \ldots A.3.1$$

Matrix $E_i(z_{i-0.5}) = E_i^{-1}(-z_{i-0.5})$

$$E_{11} = \exp(-\omega z_{i-0.5}(1 - (v^2 / C_l^2))^{1/2} / v\ )$$

$$E_{22} = \exp(-\omega z_{i-0.5}(1 - (v^2 / C_l^2))^{1/2} / v\ )$$

$$E_{33} = \exp(+\omega z_{i-0.5}(1 - (v^2 / C_l^2))^{1/2} / v\ )$$

$$E_{44} = \exp(+\omega z_{i-0.5}(1 - (v^2 / C_l^2))^{1/2} / v\ )$$

$$E_{12} = E_{13} = E_{14} = E_{21} = E_{23} = E_{24} = E_{31} = E_{32} = E_{34} = E_{41} = E_{42} = E_{43} = 0. \qquad \ldots A.3.2$$

Matrix J_i^{-1}

$$j_{11} = C_T^2 / v^2$$

$$j_{12} = (1 / b_{l_i})\ (\ C_T^2 / v^2\ )\ ((v^2 / 2 C_{l_i}^2\ ) - 1)$$

$$j_{14} = -(1 / 2 \rho_i C_T^2\ )(C_{T_i}^2 / v^2\ )$$

$$j_{21} = (1 / b_{T_i})\ (\ C_T^2 / v^2\ )\ (1 - (v^2 / 2 C_{T_i}^2\ ))$$

$$j_{33} = -(1 / 2 \rho_i C_{T_i}^2 b_{l_i})\ (\ C_{T_i}^2 / v^2\ )$$

$$j_{44} = (1 / 2 \rho_i C_{T_i}^2 b_{T_i})\ (\ C_{T_i}^2 / v^2\ )$$

$j_{13} = -j_{33}$ $\qquad$ $j_{22} = j_{31} = j_{42} = j_{11}$ $\qquad$ $j_{23} = j_{34} = j_{43} = j_{14}$

$j_{24} = -j_{44}$ $\qquad$ $j_{32} = -j_{12}$ $\qquad$ $j_{41} = -j_{21}$ $\qquad \ldots A.3.3$

Matrix $A_{i+0.5}^{-1}$

$a_{11} = a_{22} = a_{33} = a_{44} = 1$

$a_{12} = a_{13} = a_{14} = a_{21} = a_{23} = a_{24} = a_{31} = a_{34} = a_{42} = a_{43} = 0$

$a_{13} = i\,\omega\,\eta_{I\,i+0.5} / v$ $\qquad$ $a_{24} = i\,\omega\,\eta_{X\,i+0.5} / v$ $\qquad$ ... A.3.4

The matrix inverts by setting $\qquad A_{13} = -a_{13} \qquad A_{24} = -\,a_{24}$

while all other terms $\qquad A_{ij} = a_{ij}$. $\qquad$ ... A.3.5

The eta terms are again compliances which parametrize the interfacial adhesive strengths.

Matrix J_i

$J_{11} = 1$

$J_{12} = -\,b_{Ti}$

$J_{21} = b_{Li}$

$J_{33} = -\,2\,Z_{Ii}\,C_{Ii}\,b_{Ii} \qquad = -\,2\,\rho_i\,C_{Ti}^{\,2}\,b_{Ii}$

$J_{32} = Z_{Ii}\,C_{Ii}\,(2 - (v^2 / C_{Ii}^{\,2})) \qquad = \rho_i\,C_{Ti}^{\,2}\,(2 - (v^2 / C_{Ti}^{\,2}))$

$J_{41} = \cos(\theta_{Ii}) \qquad = b_{Ii}\,C_{Ii} / C$

$J_{44} = 2\,Z_{Ii}\,C_{Ti}\,b_{Ti} \qquad = 2\,\rho_i\,C_{Ti}^{\,2}\,b_{Ti}$

$J_{13} = J_{22} = J_{24} = J_{11}$ $\qquad$ $J_{14} = -J_{12}$ $\qquad$ $J_{23} = -J_{21}$

$J_{31} = -\,J_{33}$ $\qquad$ $J_{34} = J_{41} = J_{43} = J_{32}$ $\qquad$ $J_{42} = -\,J_{44}$ $\qquad$ ... A.3.6

A.4 Eigenmatrix Determinant Assuming Rigid Bonds. (Equation 2.5.3)

Referring to A.3 and using the following:

$j_{11a} = 1 - ((\mu_A / \mu_L)\,(1 - (v^2 / 2\,C_{LA}^{\,2})))$

$j_{11b} = ((\mu_A / \mu_L) - 1 + (v^2 / 2\,C_{TI}^{\,2}))\,(1 - (v^2 / C_{LA}^{\,2}))^{1/2} / (1 - (v^2 / C_{LI}^{\,2}))^{1/2}$

$j_{12a} = i\,(1 - (v^2 / C_{LA}^{\,2}))^{1/2}\,((\mu_A / \mu_L) - 1)$

$j_{12b} = (((\mu_A / \mu_L)\,(1 - (v^2 / 2\,C_{LA}^{\,2}))) - 1 + (v^2 / 2\,C_{TL}^{\,2})) / (i\,(1 - (v^2 / C_{LI}^{\,2}))^{1/2})$

$j_{21a} = (1 - ((\mu_A / \mu_L)\,(1 - (v^2 / 2\,C_{TA}^{\,2}))) - (v^2 / 2\,C_{TI}^{\,2})) / (i\,(1 - (v^2 / C_{TI}^{\,2}))^{1/2})$

$j_{21b} = i\,(1 - (v^2 / C_{LA}^{\,2}))^{1/2}\,(1 - (\mu_A / \mu_L))$

$j_{22b} = ((\mu_A / \mu_L) - 1 + (v^2 / 2\,C_{TI}^{\,2}))\,(1 - (v^2 / C_{TA}^{\,2}))^{1/2} / (1 - (v^2 / C_{TL}^{\,2}))^{1/2}$

where, A and E denote aluminium and epoxy respectively, and $\mu_i = \rho_i C_{Ti}^2$. ... A.4.1

The determinant from which the velocity v is deduced then becomes:

$$2 (j_{11a} j_{12b} - j_{11b} j_{12a}) (j_{21b} j_{22b} - j_{11a} j_{21a}) + 2 [((j_{11a} j_{12b} + j_{11b} j_{12a}) \cos L$$
$$+ i (j_{11a} j_{12a} + j_{11b} j_{12b}) \sin L) ((j_{11a} j_{21a} + j_{21b} j_{22b}) \cos T + i (j_{21a} j_{22b} - j_{11a} j_{21b}) \sin T)]$$
$$- (2 j_{11a} j_{22b} \cos T + i (j_{11a}^2 + j_{22b}^2) \sin T) (2 j_{11a} j_{11b} \cos L + i (j_{11a}^2 + j_{11b}^2) \sin L)$$
$$- (2 j_{21a} j_{21b} \cos T + i (j_{21a}^2 + j_{21b}^2) \sin T) (2 j_{12a} j_{12b} \cos L + i (j_{12a}^2 + j_{12b}^2) \sin L) = 0 \quad \text{... A.4.2}$$

where $\cos L = \cos(2 h \omega ((C_{L1}^{-2} - v^{-2})^{1/2})$ and $\sin L = \sin(2 h \omega ((C_{L1}^{-2} - v^{-2})^{1/2})$

$\cos T = \cos(2 h \omega ((C_{T1}^{-2} - v^{-2})^{1/2})$ and $\sin T = \sin(2 h \omega ((C_{T1}^{-2} - v^{-2})^{1/2})$ ... A.4.3

The expression A.4.2 does not appear to yield an analytical solution for the travelling wave velocity.

APPENDIX B.

PREPARATION OF BONDED LAYER STRUCTURES

B.1 Preparing Adhesively Bonded Joints for Cure.

Appendix B outlines the procedure used to construct the bonded joints in this thesis. Many factors have to be controlled during the manufacture of an adhesive bond, if it is not to suffer from any of the defects mentioned at the beginning of Chapter 3. All the joints were prepared from standard cross-section aluminium aerospace alloy L102 by DRA(Aerospace), following a detailed step-by-step procedure, with treatment in batches limited by the capacity of various processing tanks. At intervals throughout the process, samples are put through a two tank rinse, for 1.5 minutes in one tank followed immediately by 20 minutes in a second tank, both retaining continuously-flowing tap-water. After any two tank rinse, batch processing can be halted by drying the samples in air for 20 minutes, before oven drying for 30 minutes at 50°C, and the batches can be stored in a desiccator until all the components for a set of joints are ready.

Step One — Preliminary vapour degreasing, before cutting the alloy into sample lengths, to strip the surface of any grease or other contaminant, which can act as a releasing agent during bonding. The pieces are then fixed to cradles for easy handling, and to reduce the likelihood of putting grease marks back on surfaces during processing.

Step Two — MINCO 3410 alkaline degrease for 5 minutes, followed by two tank rinse.

Step Three — Chromic-sulphuric acid etch at 60°C to 65°C for 30 minutes, followed by two tank rinse.

Step Four — Three alternative options have been examined, of which the second is preferred and most generally used to provide a surface key for bonding adhesive to alloy.

4.1 Proceed to next step.

4.2 BAC 5555 phosphoric acid anodize at 25 (±1) °C, increasing voltage from 0 to 10 V in 30 seconds, maintaining 10 V for 22 minutes. Two tank rinse.

4.3 Chromic acid anodize to produce 1 to 3 μm thick aluminium oxide layer. Two tank rinse.

Step Five Dry in air for 20 minutes. Dry in oven for 30 minutes at 50 °C. Desiccate.

B.2 Curing Thermosetting Epoxy Adhesive Bonds.

Two thermosetting epoxy resin adhesives were used, CG312/5 and CG312, manufactured by Ciba-Geigy. The two are distinguished by the presence of woven polymer carrier in the CG312/5 adhesive which is absent from CG312. The prepared adherends are bonded between temperature-controlled plattens in a pneumatic press. At this stage, the surfaces to be bonded should be clean, and the main problem is the exclusion of water, which can vaporize during the temperature cycle and cause porosity in the cured adhesive. The adherends are thus kept in desiccators and the rolls of adhesive prepreg, sealed with desiccating gel, are stored deep-frozen until it is time for them to be brought up to room temperature and cut to shape. For parallel plattens to apply an even pressure, sets of bonds must be made up from samples with identical total thickness, although minor adjustments can be made with metal shims. For complicated geometries, or mass-produced items, jigs are generally used.

Step One Sandwich the adhesive between the adherends at approximately 700 kPa pressure.

Step Two Raise temperature by 8 °C per minute to 120 °C in order to melt the epoxy.

Step Three Maintain temperature at 120 (±2) °C for 30 minutes to cure epoxy.

Step Four Lower temperature at 10 °C per minute to below 40 °C.

When the final temperature is reached, pressure on the plattens is released and the samples removed and stored in a desiccator. Storage in this way minimizes the absorption of atmospheric water vapour into the glue layer, which can effect its mechanical properties.

BIBLIOGRAPHY

The set of guidelines used in the preparation of this thesis is PHYS/ PG/ 3.

Text and diagrams were prepared using the Nisus 3.06 Br word-processing package, produced by Paragon Concepts, inc.. Graphical analysis and presentation was carried out within Wavemetrics' Igor package, which acknowledges use of W. H. Press et al., Numerical Recipes in C, Cambridge (1988).

Publications resulting from work presented in this thesis are as follows:

As primary author.

1991. A. C. Bushell, C. Edwards and S. B. Palmer, British Journal of Non-Destructive Testing 33, (4), pp. 177-182.

1991. A. C. Bushell, C. Edwards and S. B. Palmer, Review of Progess in Quantitative Nondestructive Evaluation 11, pp. 569-576.

1991. A. C. Bushell, C. Edwards, S. B. Palmer and H. Nakano, Review of Progess in Quantitative Nondestructive Evaluation 11, pp. 1315-1322.

As supporting author

1991. C. Edwards, A. C. Bushell, S. B. Palmer and H. Nakano, Nondestructive Testing and Evaluation, 10, (1), pp. 15-23.

REFERENCES

The following abbreviations are used for journals commonly encountered in the reference sections:-

Appl. Phys. Lett.	Applied Physics Letters.
IEEE Trans.	Transactions of the Institute of Electrical & Electronic Engineers.
J. Acoust. Soc. Am.	Journal of the Acoustic Society of America.
J. Appl. Mech.	Journal of Applied Mechanics.
J. Appl. Phys.	Journal of Applied Physics.
Phil. Trans. Roy. Soc.	Philosophical Transactions of the Royal Society of London.
Proc. London Maths. Soc.	Proceedings of the London Mathematics Society.
Proc. Roy. Soc.	Proceedings of the Royal Society of London.

R.1 CHAPTER ONE.

1983. S. I. Rokhlin, J. Composite Materials 17, pp. 15-25.

1987. R. J. Dewhurst, C. E. Edwards, A. D. W. McKie and S. B. Palmer, Ultrasonics 25, pp. 315-321.

1987. S. I. Rokhlin, Nondestructive Characterization of Materials II, Ed. J. F. Bussière, J-P. Monchalin, C. O. Rund, R. E. Green Jr., pp. 105-113.

1988. D. A. Hutchins, Physical Acoustics XVIII. Ed. Mason and Thurston, Chapter 2, pp. 21-123.

1991. R. E. Challis, T. Alper, R. P. Cocker, A. K. Holmes and J. D. H. White, Ultrasonics 29, pp. 22-28.

1993. M. H. Noray, D. Royer and M. Fink, J. Acoust. Soc. Am. 94, pp. 1934-1943.

R.2 CHAPTER TWO.

1889. Lord Rayleigh, Proc. London Maths. Soc. 20, pp. 225-234.

1904. H. Lamb, Phil. Trans. Roy. Soc. A203, pp. 1-42.

1956. W. W. Garvin, Proc. Roy. Soc. A234, pp. 528-541.

1957. C. L. Pekeris and H. Lifson, J. Acoust. Soc. Am. 29, (11), pp. 1233-1238.

1958. L. Knopoff, J. Appl. Phys. 29, (4), pp. 661-670.

1967. I. A. Victorov, Rayleigh and Lamb Waves, New York: Plenum Press.

1972. G. W. Farnell and E. L. Adler, Physical Acoustics IX, Ed. Warren and Thurston, Chapter 2, pp. 35-127.

1978. W. Sachse and Y.-H. Pao, J. Appl. Phys. 49, (8), pp. 4320-4327.

1979. Y.-H. Pao, R. R. Gajewski and A. N. Ceranoglu, J. Acoust. Soc. Am. 65, (1), pp. 96-105.

1979. W. L. Pilant, Elastic Waves in the Earth, Elsevier, Amsterdam, Ch. 11, pp.103-126.

1980. S. I. Rokhlin, M. Hefets and M. Rosen, J. Appl. Phys. 51, (7), pp. 3579-3582.

1980. M. Schoenberg, J. Acoust. Soc. Am. 68, (5), pp. 1516-1521.

1981. S. I. Rokhlin, M. Hefets and M. Rosen, J. Appl. Phys. 52, (4), pp. 2847-2851.

1982. S. I. Rokhlin and M. Rosen, Thin Solid Films, 89, pp. 143-148.

1982. R. L. Weaver and Y.-H. Pao, J. Appl. Mech. 49, pp. 821-836.

1983. R. J. Dewhurst, D. A. Hutchins, S. B. Palmer and C. B. Scruby, Ultrasonics 21, pp. 79-84.

1985. J. A. Cooper, Laser-Generated Ultrasound with Applications to Non-Destructive Evaluation, Ph.D. Thesis, Department of Applied Physics, University of Hull.

1985 A. Pilarski, Proc. 11th World Conference on NDT (Las Vegas), pp. 768-775.

1986. A. M. Aindow, Characteristics of a Laser-Generated Acoustic Source in Solids, Ph.D. Thesis, Department of Applied Physics, University of Hull.

1986. P. A. Doyle, J. Physics D: Appl. Phys. 19, pp. 1613-1623.

1987. A. H. Nayfeh and T. W. Taylor, Review of Progess in Quantitative NDE, pp. 919-926.

1988. L. F. Bresse, M.Sc. Thesis, Queen's University, Kingston, Ontario, Chapter V, pp. 90-104.

1988.a A. H. Nayfeh and T. W. Taylor, Acousto-Ultrasonics:- Theory and Applications, Ed. J. C. Duke Jr., Plenum Press New York, pp. 23-34.

1988.b A. H. Nayfeh and T. W. Taylor, J. Acoust. Soc. Am. 84, (6), pp. 2187-2191.

1988. T. D. K. Ngoc, K. W. Ng and J. W. Hirsh, New Directions in NDE of Advanced Materials: Winter Annual Meeting of ASME, Chicago, Illinois, pp. 17-22.

1988. A. Pilarski and J. L. Rose, J. Appl. Phys. 63, (2), pp. 300-307.

1989. L. F. Bresse and D. A. Hutchins, J. Appl. Phys. 65, (4) pp. 1441-1446.

1989. A. C. Smith and H. Yang, Materials Evaluation 47, pp. 1396-1400.

1991. R. E. Challis, T. Alper, R. P. Cocker, A. K. Holmes and J. D. H. White, Ultrasonics 29, pp. 22-28.

1991. J. B. Spicer, Ph. D. Thesis, Johns Hopkins University, Baltimore, Maryland.

1992. R. E. Challis, R. P. Cocker, A. K. Holmes and T. Alper, J. Applied Polymer Sci. 44, (1), pp. 65-81.

R.3 CHAPTER THREE.

1958. L. Knopoff, J. Appl. Phys. 29, (4), pp. 661-670.

1963. R. M. White, J. Appl. Phys. 34, (12), pp. 3559-3567.

1965. J. F. Ready, J. Appl. Phys. 36, (2), pp 462-468.

1976. K. Kawashima, J. Acoust. Soc. Am. 60, (5), pp. 1089-1099.

1977. L. E. Drain, J. H. Speake and B. C. Moss, Proc. 1st Eur. Congress on Optics Applied to Metrology SPIE 136, pp. 52.

1977. R. J. von Gutfeld and R. L. Melcher, Appl. Phys. Lett. 30, (6), pp. 257-259.

1979. H. M. Ledbetter and J. C. Moulder, J. Acoust. Soc. Am. 65, (3), pp. 840-842.

1979. H. M. Frost, Physical Acoustics XIV, [Eds. W. P. Mason & R. N. Thurston] Academic Press, London, pp. 179-275.

1980. A. M. Aindow, R.J. Dewhurst, D. A. Hutchins and S. B. Palmer, European Conference on Optical Systems and Applications (Utrecht) SPIE 236, pp. 478-485.

1980. S. I. Rokhlin, M. Hefets and M. Rosen, J. Appl. Phys. 51, (7), pp. 3579-3582.

1981. S. I. Rokhlin, M. Hefets and M. Rosen, J. Appl. Phys. 52, (4), pp. 2847-2851.

1981. A. M. Aindow, R.J. Dewhurst, D. A. Hutchins and S. B. Palmer, J. Acoust. Soc. Am. 69, (2), pp. 449-455.

1981.a D. A. Hutchins, R.J. Dewhurst, S. B. Palmer, and C. B. Scruby, Appl. Phys. Lett. 38, (9), pp. 677-679.

1981.b D. A. Hutchins, R. J. Dewhurst and S. B. Palmer, Ultrasonics 19, pp. 103-108.

1982. R. J. Dewhurst, D. A. Hutchins, S. B. Palmer and C. B. Scruby, J. Appl. Phys. 53, (6), pp. 4064-4071.

1982. C. B. Scruby, R. J. Dewhurst, D. A. Hutchins and S. B. Palmer, Research Techniques in NDT, V, chapter 8, pp. 281-327.

1983. R. J. Dewhurst, D. A. Hutchins, S. B. Palmer and C. B. Scruby, Ultrasonics 21, pp. 79-84.

1983. S. I. Rokhlin, J. Composite Materials 17, pp. 15-25.

1984. K. Kawashima, IEEE Trans. on Sonics & Ultrasonics SU-31, (2), pp. 83-94.

1984. L. R. F. Rose, J. Acoust. Soc. Am., 75, pp. 723

1985. J. A. Cooper, Laser-Generated Ultrasound with Applications to Non-Destructive Evaluation, Ph.D. Thesis, Department of Applied Physics, University of Hull.

1985. D. A. Hutchins, D. E. Wilkins and G. Luke, Appl. Phys. Lett. 46, (7), pp 634-635.

1985. A. D. W. McKie, Applications of Laser-Generated Ultrasound Using an Interferometric Sensor, Ph.D. Thesis, Dept. of Applied Physics, University of Hull.

1985. H. Sontag and A. C. Tam, Appl. Phys. Lett. 46, (8), pp. 725-727:

1986. A. M. Aindow, Characteristics of a Laser-Generated Acoustic Source in Solids, Ph.D. Thesis, Department of Applied Physics, University of Hull.

1986 J. A. Cooper, R. J. Dewhurst and S. B. Palmer, Phil. Trans. Roy. Soc. 320A, pp. 319-328.

1986. P. A. Doyle, J. Phys. D: Appl. Phys. 19, pp. 1613-1623.

1986. C. C. H. Guyott, P. Cawley and R. D. Adams, J. Adhesion 20, pp. 129-159.

1986. D. Hutchins, J. Hu and K. Lundgren, Materials Evaluation 44, pp. 1244-1253.

1986. R. A. Kline, C. P. Hsiao and M. A. Fidaali, ASME Trans., J. Engineering Materials & Technology 108, (3), pp. 214-217.

1986. J. P. Monchalin, IEEE Trans. on Ultrasonics, Ferroelectrics and Frequency Control UFFC-33, pp. 485-499.

1987. A. Aharoni, M. Tur and K. M. Jassby, Appl. Phys. Lett., 51, (20), pp. 1569-1571.

1987. E. V. Dan'shchikov, V. A. Dymshakov, A. M. Dykhne, F. V. Lebedev and B. P. Rysev, Soviet Physics Acoustics 33, (6), pp. 602-605.

1987. R. J. Dewhurst, C. E. Edwards, A. D. W. McKie and S. B. Palmer, Ultrasonics 25, pp. 315-321.

1987. P. Dickstein, Y. Segal and E. Segal, Non-Destructive Testing [Proceedings of the 4th European Conference], Ed. J. M. Farley, R. W. Nichols, pp. 1668-77.

1987. F. He, S. I. Rokhlin and L. Adler, Review of Progress in Quantitative Non-Destructive Evaluation, pp. 911-918.

1987. R. D. Weglein and A. K. Mal, Ultrasonic Symposium Proceedings.

1988. R. D. Adams and P. Cawley, NDT International 21, pp. 208-221.

1988. L. F. Bresse, M.Sc. Thesis, Queen's University, Kingston, Ontario, Chapter V, pp. 90-104.

1988. R. J. Dewhurst, C. Edwards, A. D. W. McKie and S. B. Palmer, J. of Appl. Phys. 63, (4), pp. 1225-1227.

1988. C. C. H. Guyott and P. Cawley, NDT International 21, (4), pp. 233-240.

1988. D. A. Hutchins, Physical Acoustics XVIII, Ed. Mason and Thurston, Chapter 2, pp. 21-123.

1988. P. J. Latimer and H. L. Whaley, Acousto-Ultrasonics: Theory and Applications. [Ed. J. C. Duke Jr.] Plenum, New York, pp. 209-220.

1988. A. D. W. McKie and J. W. Wagner, Appl. Phys. Lett., 53, (12), pp. 1043-1044.

1988. A. Pilarski and J. L. Rose, J. Appl. Phys., 63, (2), pp. 300-307.

1988. A. Pilarski, J. L. Rose, K. Balasubramaniam and J. Da-Le, Acousto-Ultrasonics: Theory and Applications, Ed. J. C. Duke Jr., Plenum New York, pp. 79-91.

1989. A. Pilarski and J. L. Rose, Ultrasonics 27, (4), pp. 226-233.

1989. C. M. Teller, K. J. Diercks, Y. Bar-Cohen and A. K. Mal, J. Adhesion 30, pp. 243-261. ALSO 1988 US Army Materials Technology Mat. Research Conf. pp. 1-20.

1989. C. Edwards and S. B. Palmer, Nondestructive Testing & Evaluation 5, pp. 203-212.

1989. D. A. Hutchins, K. Lundgren and S. B. Palmer, J. Acoust. Soc. Am. 85, (4), pp. 1441-1448.

1989. C. M. Scala and P. A. Doyle, J. Acoust. Soc. Am. 85, (4), pp. 1569-1576.

1990. C. Edwards and S. B. Palmer, IEEE Trans. on Magnetics MAG-26, (5), pp 2080-2084.

1990. F. A. McDonald, Appl. Phys. Lett. 56, (3), pp. 230-232.

1990. L. Noui and R. J. Dewhurst, Appl. Phys. Lett. 57, (6), pp. 551-553.

1990. C. B. Scruby and L. E. Drain, Laser Ultrasonics: Techniques and Applications, Adam Hilger, Bristol, pp 63-147.

1990. G. S. Taylor, Ph.D. Thesis, Department of Physics, University of Warwick.

1991. A. C. Bushell, C. Edwards and S. B. Palmer, British Journal of Non-Destructive Testing 33, (4), pp. 177-182.

1991. D. E. Chimenti and R. W. Martin, Ultrasonics 29, pp. 13-21.

1991. C. Edwards, A. C. Bushell, S. B. Palmer and H. Nakano, Nondestructive Testing and Evaluation, 10, (1), pp. 15-23.

1991. D. A. Hutchins, M. D. C. Moles, G. S. Taylor and S. B. Palmer, Ultrasonics 29, pp. 294-301.

1991.a K. Yamanaka, Y. Nagata and T. Koda, Appl. Phys. Lett. 58, (15), pp. 1591-1593.

1991.b K. Yamanaka, Y. Nagata and T. Koda, Review of Progess in Quantitative NDE, II.

1992. P. Fraisse, F. Schmit and A. Zarembowitch, J. Appl. Phys., 72, (8), pp. 3264-3271.

1993. T. M. Hsieh and M. Rosen, Ultrasonics 31, (1), pp. 45-51.

R.4 CHAPTER FOUR.

1988.a C. C. H. Guyott and P. Cawley, J. Acoust. Soc. Am. 83, (2), pp. 623-631.

1988.b C. C. H. Guyott and P. Cawley, J. Acoust. Soc. Am. 83, (2), pp. 632-640.

1991. R. E. Challis, T. Alper, R. P. Cocker, A. K. Holmes and J. D. H. White, Ultrasonics 29, pp. 22-28.

1991. D. A. Hutchins, M. D. C. Moles, G. S. Taylor and S. B. Palmer, Ultrasonics 29, pp. 294-301.

1992. T. Pialucha and P. Cawley, Review of Progess in Quantitative NDE, II, pp. 1261-1266.

1993. R. J. Freemantle, T. Alper and R. E. Challis, Meas. Sci. Technol. 4, (10), pp. 1129-1137.

R.5 CHAPTER FIVE.

1917. H. Lamb, Proc. Royal Soc. A 93, pp. 114-128.

1885. Lord Rayleigh, Proc. London Maths. Soc. 17, pp. 4-11.

1967. I. A. Viktorov, Rayleigh and Lamb Waves, Plenum Press, New York.

1978. W. Sachse and Y-H. Pao, J. Appl. Phys. 49, (8), pp. 4320-4327.

1987. R. J. Dewhurst, C. Edwards, A. D. W. McKie and S. B. Palmer, Appl. Phys. Lett. 51, pp. 1066-1068.

1989. C. Edwards and S.B. Palmer, Nondestructive Testing & Evaluation 5, pp. 203-212.

1989. D. Hutchins, K. Lundgren and S. B. Palmer, J. Acoust. Soc. Am. 85, pp. 1441-1448.

1989. M. Lorenz, A. J. A. Bruinsma, U. Stelwagen, J. A. Vogel and A. J. Berkhout, Proceedings of the 12th World Conf. on NDT., ed. J. Boogard and G. M. van Dijk. Elsevier Science Publishers B.V., Amsterdam, pp. 1449-1455.

1989. J. C. H. Yu, C. K. Jen, E. L. Adler, J-D. Aussel, J-P. Monchalin and R. Bernier, Ultrasonics International Conference Proceedings, pp. 205-210.

1990. M. Lorenz, J. A. Vogel, A. J. A. Bruinsma, A. J. Berkhout, Nondestructive Testing and Evaluation 5, (2-3), pp. 187-202.

1990. J. B. Spicer, A. D. W. McKie and J. W. Wagner, Appl. Phys. Lett. 57, (18), pp. 1882-1884.

1991. B. J. Jarosz, Ultrasonics 29, pp. 53-57.

R.6 CHAPTER SIX.

1968. R. E. Lee and R. M. White, Appl. Phys. Lett. 12, (1), pp. 12-14.

1970. G. Cachier, Appl. Phys. Lett. 17, (10), pp. 419-421.

1980. R. O. Claus and C. H. Palmer, IEEE. Trans. on Sonics and Ultrasonics SU-27, (3), pp. 97-103.

1980. S. I. Rokhlin, M. Hefets and M. Rosen, J. Appl. Phys. 51, (7), pp. 3579-3582.

1981. S. I. Rokhlin, M. Hefets and M. Rosen, J. Appl. Phys. 52, (4), pp. 2847-2851.

1982. K. A. Nelson, R. J. Dwayne Miller, D. R. Lutz and M. D. Fayer, J. Appl. Phys. 53, (2), pp. 1144-1149.

1988. A. Pilarski and J. L. Rose, J. Appl. Phys. 63, (2), pp. 300-307.

1989. A. Pilarski, J. L. Rose and J. Da-Le, Non-Destructive Testing (Proc. 12th World Conference), ed. J. Boogaard and G. M. van Dijk (Elsevier Science Publishers B.V. Amsterdam), Vol.1, pp. 836-841.

1990. K. J. Faran, R. J. Dwayne Miller and S. M. Gracewski, ASME J. Appl. Mech. 57, pp. 415-418.

1990. A. Harata, H. Nishimura and T. Sawada, Appl. Phys. Lett. 57, (2), pp. 132-134.

1991. A. C. Bushell, C. Edwards, S. B. Palmer and H. Nakano, Review of Progess in Quantitative NDE, II, pp. 1315-1322.

1991. J. B. Deaton Jr., J. W. Wagner and J. B. Spicer, Review of Progess in Quantitative NDE, II, pp. 601-608.

1991. C. Edwards, A. C. Bushell, S. B. Palmer and H. Nakano, Nondestructive Testing and Evaluation, 10, (1), pp. 15-23.

1991. M. J. Lowe and P. Cawley, unpublished communication.

1991. H. Nakano and S. Nagai, Ultrasonics, 29, pp. 230-234.

1991. T. Pialucha and P. Cawley, Review of Progess in Quantitative NDE, II, pp. 1261-1266.

R.7 CHAPTER SEVEN.

1986. J. A. Cooper, R. A. Crosbie, R. J. Dewhurst, A. D. W. McKie and S. B. Palmer, IEEE Trans. Ultrasonics Ferroelectrics & Freq. Control UFFC-33, (5), pp. 462-470.

1989. A. Pilarski and J. L. Rose, Ultrasonics 27, (4), pp. 226-233.

R.8 CHAPTER EIGHT.

1988. R. D. Adams and P. Cawley, NDT International 21, (4), pp. 208-222.